UNIVERSIDAD AUTÓNOMA DE MADRID

FACULTAD DE CIENCIAS

Departamento de Química Inorgánica

TESIS DOCTORAL

Diseño seguro de partículas de aluminato de cobalto nanoestructuradas y sus potenciales aplicaciones

MEMORIA PARA OPTAR AL GRADO DE DOCTORA EN QUÍMICA APLICADA

PRESENTADA POR

Carmen María Álvarez Docio

Directores

Dr. Julián Jiménez Reinosa

Prof. José Francisco Fernández Lozano

Madrid, 2020

UNIVERSIDAD AUTÓNOMA DE MADRID

FACULTAD DE CIENCIAS

Departamento de Química Inorgánica

Tesis doctoral

Diseño seguro de partículas de aluminato de cobalto nanoestructuradas y sus potenciales aplicaciones

Memoria para Optar al Grado de Doctora en Química Aplicada

Carmen María Álvarez Docio

Dirigida por:

Dr. Julián Jiménez Reinosa

Prof. José Francisco Fernández Lozano

Madrid, 2020

Instituto de Cerámica y Vidrio

Consejo Superior de Investigaciones Científicas

A mi familia

"*En un súbito impulso se abrazaron, se abrazaron, se abrazaron. Metiendo cada uno en su pecho el del otro hasta besarse con los corazones*"

José Luis Sampedro, La sonrisa etrusca

Agradecimientos

Me considero una persona feliz, lo tengo casi todo en esta vida. Pero esta vida plena y hermosa no sería nada sin vosotros, todos aquellos que me acompañáis en los buenos y malos momentos. Esta etapa de doctorado, en algunas ocasiones no ha sido fácil, pero creo que la he disfrutado todo lo que he podido y más. De nuevo aparece vuestra luz, poniendo sabiduría, cariño y amistad al servicio de esta loca doctoranda que un día decidió embarcarse en esta aventura. Por esta razón, quiero expresar mi más profundo y sincero agradecimiento a todas aquellas personas del ámbito académico y no académico, que con su ayuda han colaborado en la realización de esta tesis doctoral. He de decir que esto me va a resultar más difícil que escribir la "Intro", pues son numerosas las emociones que me abordan cuando me paro a pensar en todo lo que hemos vivido a lo largo de estos años…

En primer lugar, agradecer a mis directores de tesis, el Profesor José Francisco Fernández Lozano y el Doctor Julián Jiménez Reinosa, por la oportunidad brindada para realizar esta tesis. Mis palabras de agradecimiento por su ayuda, supervisión y dedicación, sin los cuales la realización de la presente tesis hubiera sido imposible. Gracias a los dos por permitirme ver la grandeza del mundo "nano".

Al Profesor Vincenzo Buscaglia y a la Doctora María Teresa Buscaglia, les quiero agradecer la buena acogida y toda la ayuda prestada durante mi estancia en Génova (Institute of Energetics and Interphases, National Research Council of Italy). Eternamente agradecida a mi compañera de despacho, Giovanna, nunca olvidaré lo mucho que te implicaste para hacerme sentir como en casa, siempre atenta y dispuesta a todo. A Doriana, por todos esos atardeceres junto al mar, por los paseos a Portofino juntas, por enseñarme todos los rincones. ¡Qué bien lo pasamos y cómo extraño tu amistad!

Muchas gracias al Profesor Miguel Ángel Bañares, por permitirme realizar mis experimentos catalíticos en el Laboratorio de Espectroscopia Catalítica, del Instituto de Catálisis y Petroleoquímica. Gracias, en particular, a la Doctora Raquel Portela, por tu disponibilidad durante la etapa experimental y tu inestimable ayuda con la escritura de los artículos.

Mi agradecimiento también a mi tutora académica, la Catedrática Isabel Cuadrado, por el seguimiento de la tesis durante todo este tiempo. Siempre es un placer mantener una charla animada contigo, has sido una de las mejores profesoras que he tenido a lo largo de mi carrera académica. Tras estas palabras me acuerdo de todos esos maestros que he tenido a lo largo de mi vida… en el Olivar: Resu (todavía guarda mis dibujos), Pili (llegamos juntas, siempre me lo recuerdas), Toñi e Isabel (erais estrictas, sí, pero siempre cariñosas), Isaac (nunca me diste clase, pero fuiste maestro de vida), sois tantos con los que he dado vueltas y vueltas alrededor de la Ondarreta… En el Montpe encarrilaron mi adolescencia como pudieron, creo que no fue tan mal. Gracias a Carlos y a Alicia, por inculcarme vuestra pasión por las Mates y la Química.

Y así llegue al Instituto de Cerámica y Vidrio, a hacer ciencia. Aquí me he encontrado con mucho más que meros compañeros de trabajo. Decidido, sois amigos. Gracias a Rocío, esta oportunidad vino de tu mano, ojalá tuviésemos todos un poco más de tu compromiso, haríamos del mundo un lugar mejor. Gracias a Fernando, espero que, tras estos años a tu lado, se me haya pegado un poquitín de tu gusto para hacer gráficas, pero también algo de tu bondad y honestidad. Gracias a Esther, no eres una acelga, eres la viva imagen del empoderamiento de la mujer, admiración y respeto es lo que siento por ti. Gracias a Víctor, como voy a echar de menos esa sonrisa perfecta, espero que logres todo lo que te propongas porque te lo mereces. Gracias a Manu, por ser el que unió a los "Caraculos", aunque la dieta ha sido más fácil sin tus galletitas. Gracias a Sara, por todas esas conversaciones intentando arreglar el mundo. Por supuesto, gracias a Julián, protagonista de los mejores momentos del ICV. Gracias por casi todo. Por tu dedicación, tu interés, y lo más importante… por tu tiempo… gracias por cada segundo que me has regalado sin esperar nada a cambio. Gracias también por esos ánimos cuando más los he necesitado. Gracias por tus bromas, aunque alguna no te la perdono. Gracias por lidiar con paciencia mi cabezonería. Gracias a todos, desde el personal de mantenimiento (siempre dispuestos a "echarme un cable"), hasta el resto de compañeros: Aida, Cecilia, Adrián, Alberto, Adolfo, Eva, Pili, Isma, Sara, Jesús ("Titi"), Patricia, Carlitos, Isa, Marco, Teresa, David y Gumiel. De todos ellos he aprendido. Gracias por el apoyo constante. Me siento orgullosa de lo que hemos construido estos años y orgullosa de todas las personas que lo han construido.

A mis amigos de fuera del ICV que, aunque algunos dicen que no soy muy social, sois unos cuantos. A Maroto, da igual el tiempo que pase, siempre presente. A María, ojalá pudiésemos volver atrás y disfrutar de nuevo esa niñez compartida. A Raquel, contigo alucino, con lo que te hace sufrir la vida y siempre sonriente, siempre dispuesta a ayudar, te quiero. A los eternos ponferradinos, después de tantos años, parte de mi familia. A los "periquitos", Hilda y Dani, sois un amor, os deseo lo mejor en esta nueva etapa que comenzáis. A los "norteños", Bueicho y Bego, mil gracias por alojarnos todos los veranos, por soportar mis jornadas maratonianas de playa y por todas las risas compartidas. A Óscar, siempre con las puertas de Rusia abiertas para todos, fiel a tus principios y amigo perfecto. A Jorge y a Tania, ejemplos de coraje y valentía, os echamos de menos. A Carlos y Rocío, por todas las aventuras vividas junto a vosotros, por las locuras de Carlos y la generosidad de Rocío.

No me puedo olvidar de mi familia. A mi tía Tere, porque parte de esta tesis es por ti y para ti, por ser la fuerza que nos aglutina a todos ahora que la abuela ya no está. A todos mis primos, pero sobre todo a Teresa y Alberto, porque somos como hermanos, desde pequeños haciendo gamberradas juntos. A mi hermana Eli, por ser la persona más buena que conozco y por perdonármelo todo. También quiero acordarme de mi familia política… Tali, Encarna, Ventura, Rubén, Raquel y Pablo. Pero sobre todo de mis sobrinos Mateo y Samuel ¡la vida es mucho más divertida y emocionante con vosotros!

A Jesús, porque he crecido junto a ti, y pienso envejecer a tu lado. Elisa dijo en nuestra boda que tú siempre agarras mi cuerda, pero yo creo que tiras de ella, para ayudarme a subir a donde sea. Contigo al fin del mundo, eso sí, ¡off-road!

A mis padres. Sin palabras. Por darme todas las herramientas para construir mi felicidad. Por preocuparos y ocuparos de mi educación personal y profesional. Papá, admiro casi todo de ti, pero sobre todo tu inteligencia casi infinita y tu honestidad. Mamá, gracias por la dedicación absoluta que tienes con nosotros y por querernos sin límites. Os imagino agarrados de la mano, como siempre, y orgullosos de lo que habéis construido: una familia feliz.

La realización de este trabajo ha sido posible gracias a la financiación del Ministerio de Economía y Competitividad (MINECO) de los proyectos MAT2013-48009-C4-1-P y MAT2017-86450-C4-1-R. También agradecer al Consejo Superior de Investigaciones Científicas por la financiación del proyecto NANOMIND CSIC 201560E068.

Carmen María Álvarez Docio quiere expresar su agradecimiento Ministerio de Economía y Competitividad (MINECO) por la concesión de la Beca Predoctoral FPI (BES-2014-069779) para la realización de esta tesis doctoral. Al Consejo de Investigaciones científicas, CSIC, y a la dirección del Instituto de Cerámica y Vidrio, ICV, por permitir la realización de la presente tesis doctoral.

Índice de contenido

Índice de Figuras

Índice de Tablas

Resumen

En esta memoria se recogen los resultados más relevantes sobre el diseño, el procesamiento, la caracterización y la aplicabilidad de materiales nanoestructurados de aluminato de cobalto ($CoAl_2O_4$). La reactividad de las superficies nanoestructuradas obtenidas, en las cuales las nanopartículas se encuentran organizadas jerárquicamente, se ha modulado mediante el diseño de dos rutas de procesamiento diferentes.

En la primera aproximación, se han anclado nanopartículas de Co_3O_4 sobre partículas micrométricas de α-Al_2O_3, mediante un proceso de dispersión en seco de baja energía. Mediante la reacción en estado sólido a alta temperatura de estos precursores se generan nanocristales de $CoAl_2O_4$ en la superficie de las micropartículas de alúmina que actúan como soporte. De esta forma se obtienen micropartículas tipo coraza-núcleo donde la coraza está formada por nanocristales de $CoAl_2O_4$ y el núcleo se mantiene como α-Al_2O_3.

A partir de los resultados de la caracterización de las diferentes nanoestructuras de $CoAl_2O_4$ presentes en la coraza de la micropartícula, se estableció su mecanismo de cristalización. Se demostró que el estado de agregación de las nanopartículas de Co_3O_4 y su saturación, son factores determinantes en la morfología final de las nanoestructuras de $CoAl_2O_4$. Estos aspectos ponen de manifiesto el reto de desarrollar metodologías adecuadas para la caracterización de los materiales nanoestructurados. En esta memoria, a través de la Microscopia Raman Confocal, se han correlacionado diferentes parámetros estructurales y funcionales con la micro-nanoestructura, tanto de los precursores de partida como de las micropartículas coraza-núcleo desarrolladas.

En cuanto a la aplicabilidad del material, señalar que a través del pigmento obtenido se abren nuevas posibilidades para los materiales nanoestructurados basados en aluminato de cobalto. Las micropartículas coraza-núcleo presentan unas propiedades colorimétricas semejantes a las de los pigmentos

convencionales con una reducción considerable del contenido en cobalto (emplean un 9 % en peso del óxido de cobalto, CoO, frente al 42 % en peso requerido para un material estequiométrico). De esta forma se reducen las implicaciones negativas del cobalto en cuanto a su alto coste, impacto medioambiental y toxicidad. Finalmente, este material presenta una alta reflectividad en el intervalo espectral del infrarrojo cercano, que posibilita su incorporación en recubrimientos o pinturas, aportándoles el color y el efecto térmico deseados.

La segunda aproximación realizada en esta memoria, para el desarrollo de un material nanoestructurado de $CoAl_2O_4$, se llevó a cabo mediante un proceso de micromolienda en etanol. Así, se produce una disminución del tamaño de partícula y el consecuente aumento en la superficie específica. Sin embargo, el aspecto más relevante consiste en la activación de la superficie mediante la formación de nanorugosidad y exposición de planos cristalinos de menor estabilidad que el plano cristalino (111). Los materiales nanoestructurados de $CoAl_2O_4$ presentan así un incremento notable de los sitios ácidos superficiales. De esta forma las nanoestructuras desarrolladas han mostrado una alta eficiencia como catalizador en la reacción de oxidación de carbonilla, derivada de la combustión de combustibles de gasoil. Los catalizadores presenta las siguientes características: 1) aumentan las zonas de contacto entre el catalizador y la carbonilla, facilitando el acceso a las especies gaseosas reactivas; 2) los sitios ácidos generados interaccionan con las partículas de carbonilla, permitiendo su activación y facilitando así su combustión y 3) existe una sinergia entre el mecanismo de oxidación asistido por NO_2 y el mecanismo de oxidación asistido por vacantes de oxígeno. La importancia de este proceso radica en el escenario actual de la industria automovilística. Los motores diésel generan elevadas emisiones de materiales particulados (carbonilla), lo cual resulta altamente perjudicial, por lo que se ha implementado una legislación cada vez más restrictiva a su respecto. El desarrollo de tecnologías de tratamiento de post-combustión es imprescindible para disminuir el nivel de emisiones de este contaminante. Los catalizadores propuestos en la presente memoria representan

una alternativa de menor coste que las soluciones actuales y con una alta eficiencia.

En su conjunto, en este trabajo se ha propuesto el empleo de materiales nanoestructurados, en los que las nanopartículas se encuentran organizadas jerárquicamente, depositadas sobre una matriz con un tamaño de grano mayor o formando aglomerados de tamaño micrométrico. De esta forma se establece un equilibrio entre el desarrollo de nuevas funcionalidades para materiales industriales potenciado las propiedades beneficiosas de los materiales en la nanoescala y minimizando su posible impacto negativo mediante soluciones nanoestructuradas.

Abstract

This report contains the most relevant results on the design, processing, characterization and applicability of nanostructured cobalt aluminate materials ($CoAl_2O_4$). The reactivity of the nanostructured surfaces obtained, in which the nanoparticles are organized hierarchically, has been modulated by designing two different processing paths.

In the first approach, Co_3O_4 nanoparticles were anchored on micrometric particles of α-Al_2O_3, by means of a low energy dry dispersion process. Through the high-temperature solid-state reaction of these precursors, nanocrystals of $CoAl_2O_4$ were generated on the surface of the alumina microparticles that acted as support. In this way, core-shell microparticles were obtained where the shell was formed by $CoAl_2O_4$ nanocrystals and the core was maintained as α-Al_2O_3.

From the results of the characterization of the different nanostructures of $CoAl_2O_4$ present in the shell of the microparticle, a crystallization mechanism was established. It was shown that the aggregation state of the Co_3O_4 nanoparticles and their degree of saturation are determining factors in the final morphology of the $CoAl_2O_4$ nanostructures. These aspects highlight the challenge of developing appropriate methodologies for the characterization of nanostructured materials. In this report, through Confocal Raman Microscopy, different structural and functional parameters were correlated with the micro-nanostructure, both of the starting precursors and of the developed core-shell microparticles.

Regarding the applicability of the material, note that through the pigment obtained new possibilities are opened for nanostructured materials based on cobalt aluminate. The core-shell microparticles showed similar colorimetric properties to those of conventional pigments, but the obtained core-shell particles presented a considerable reduction in cobalt content (they use 9% by weight of cobalt oxide, CoO, compared to 42% by weight required for a stoichiometric

material). This reduces the negative implications of cobalt in terms of its high cost, environmental impact and toxicity. Finally, this material had a high reflectivity in the near infrared spectral range, which means achieving eco-efficient coatings thought its incorporation into coatings or paints, giving them the desired color and thermal effect.

The second approach made in this report consisted of the development of a nanostructured material of $CoAl_2O_4$ and was carried out following a milling process in ethanol. Thus, a decrease in particle size was generated, as well as the consequent increase in the specific surface. However, the most relevant aspect was the activation of the surface through the formation of nanoroughness and the exposition of crystalline planes with less stability than the crystalline plane (111). The nanostructured materials of $CoAl_2O_4$ presented a notable increase in surface acid sites. In this way, the developed nanostructures showed a high efficiency as a catalyst in the oxidation reaction of soot, which was generated in diesel combustion engines. The catalysts have the following characteristics: 1) to increase the contact areas between the catalyst and the carbon, facilitating access to reactive gaseous species; 2) the acid sites generated could interact with the soot particles, allowing their activation and facilitating their combustion and 3) a synergy between the oxidation mechanism assisted by NO_2 and the oxidation mechanism assisted by oxygen vacancies appeared. The importance of this process lies in the current scenario of the car industry. Diesel engines generate high emissions of particulate materials (soot), which is highly damaging, and therefore more and more restrictive legislation has been implemented in this regard. The development of post-combustion treatment technologies is essential to reduce the level of emissions of this pollutant. The catalysts proposed herein represent an alternative of lower cost than current solutions and with high efficiency.

As a whole, this work has proposed the use of nanostructured materials, in which the nanoparticles are organized hierarchically, deposited on a matrix with a larger grain size or forming agglomerates of micrometric size. In this way, a

balance is established between the development of new functionalities for industrial materials that enhances the beneficial properties of the materials in the nanoscale and minimizing their possible negative impact through nanostructured solutions.

Capítulo 1. Introducción

El aluminato de cobalto: Estructura, propiedades y aplicaciones

"No hay azul sin amarillo y sin naranja"

Vincent Van Gogh

1.1. El aluminato de cobalto ($CoAl_2O_4$)

La espinela aluminato de cobalto ($CoAl_2O_4$) es uno de los pigmentos cerámicos más destacados, debido a su intenso color azul. Es conocido que en la Edad Media ya se usaban minerales que contenían cobalto para colorear cerámica y vidrio. Incluso, se ha detectado la presencia de aluminato de cobalto en objetos correspondientes a civilizaciones antiguas procedentes de China o Egipto [1,2]. Sin embargo, el compuesto sintético de aluminato de cobalto no se comercializó hasta principios del siglo XIX. El químico Louis Jacques Thénard fue el encargado de buscar un sustituto económico para el color azul ultramar, que se elaboraba con lapislázuli, motivado por el excesivo precio de éste [3]. Thénard obtuvo el llamado azul cobalto calentando arsenato de cobalto y fosfato de cobalto con alúmina [4].

1.1.1. Descripción estructural

El $CoAl_2O_4$ presenta una estructura de tipo espinela normal, perteneciente al grupo espacial $Fd\bar{3}m$ (O^7_h; n° 227 en las tablas internacionales [5]). La fórmula general es AB_2O_4 y la celda unidad contiene 32 átomos de oxígeno dispuestos en un empaquetamiento cúbico centrado en las caras, de modo que la fórmula de la celda unidad es $A_8B_{16}X_{32}$ (***Figura 1. 1***).

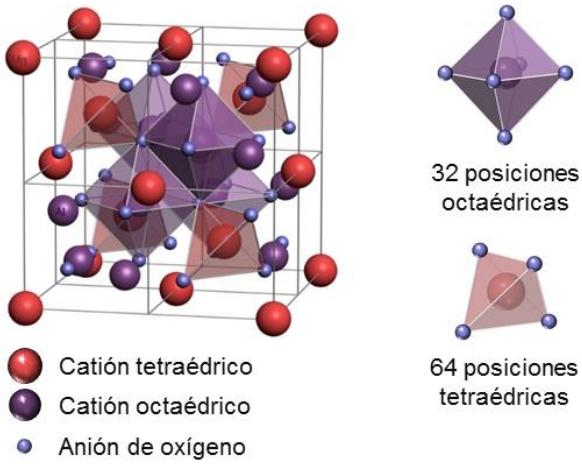

Figura 1. 1 *Celda unidad de la estructura espinela normal y sus posiciones octaédricas y tetraédricas. Imagen adaptada de la referencia [6].*

Es ampliamente conocido que el aluminato de cobalto es una espinela normal, por lo que los cationes Al^{3+} se encuentran ocupando la mitad de las posiciones octaédricas disponibles, mientras que los cationes Co^{2+} ocupan la octava parte de las posiciones tetraédricas disponibles [7]. Sin embargo, según el tamaño de los cationes (r_{Al} = 0.52 Å < r_{Co} = 0.78 [8]), los valores de electronegatividad (χ_{Co} = 1.47 < χ_{Al} = 1.54 [9]) y por el efecto de estabilización del campo cristalino [10], los cationes de Co^{2+}, deberían presentar una fuerte preferencia por las posiciones octaédricas. Sin embargo, los estudios realizados han revelado que, si el $CoAl_2O_4$ presentase una estructura espinela inversa (la mitad de los cationes Al^{3+} se desplazan hacia posiciones tetraédricas y los cationes Co^{2+} pasan a ocupar únicamente posiciones octaédricas), las longitudes de enlace en las posiciones tetraédricas serían anormalmente largas y la repulsión entre los cationes de las posiciones octaédricas serían considerablemente grandes [11]. Estos factores de desestabilización de la estructura cristalina pueden evitarse mediante la configuración de espinela normal.

1.1.2. Morfología de las cristalizaciones

A partir de monocristales de este compuesto se revela el hábito de crecimiento cristalino, dominado por la anisotropía de la energía superficial que favorece la presencia de las caras cristalinas de menor energía [12]. Para un material con un empaquetamiento cúbico centrado en las caras, la secuencia de energía superficial es: $\gamma\{111\} < \gamma\{100\} < \gamma\{110\}$ [13]. De modo que, siguiendo el principio de minimización de energía superficial, en un monocristal de espinela de fórmula general AB_2O_4 la morfología más favorable se corresponde con un octaedro cuyas caras son paralelas a los planos cristalográficos (111) [14], como se muestra en la ***Figura 1. 2***.

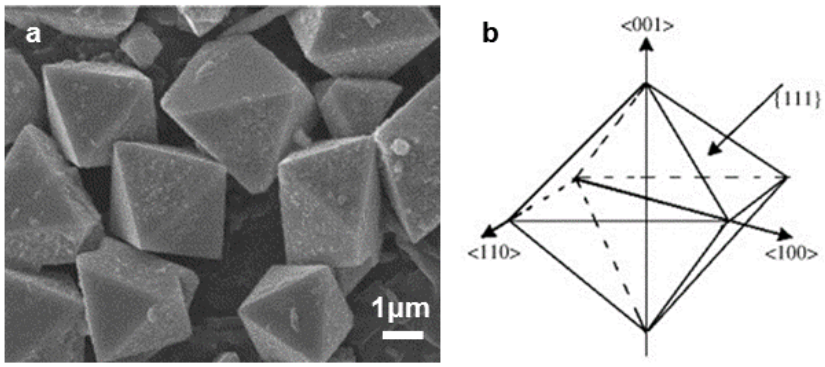

Figura 1. 2 *a) Cristalizaciones de la espinela $CoFe_2O_4$ con forma de octaedro y un tamaño aproximado de 4 µm. b) Esquema de los planos cristalográficos correspondientes a las partículas. Imágenes de las referencias [14,15].*

A pesar de esta dirección de crecimiento preferencial, el patrón de difracción de rayos-X del $CoAl_2O_4$ para muestras en polvo no presenta una cristalización preferente en los planos de menor energía (111), (222), (333) [16], como se corresponde con su naturaleza policristalina y la orientación aleatoria. Únicamente se obtienen materiales orientados en el plano (111) para películas delgadas de $CoFe_2O_4$ [17], espinela isomorfa del aluminato de cobalto (***Figura 1. 3***).

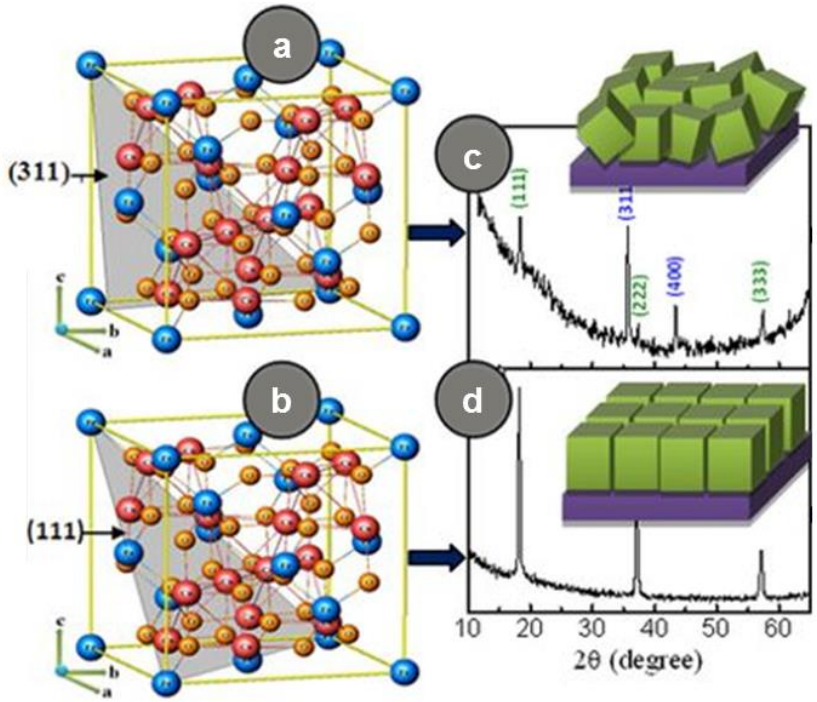

Figura 1. 3 *Esquema mostrando el ordenamiento catiónico en una espinela cúbica de $CoFe_2O_4$ a) Plano (311), b) plano (111). Difractograma de rayos X y esquema de la textura de la película delgada c) $CoFe_2O_4$ orientado aleatoriamente, d) orientado en la dirección [111]. Imágenes adaptadas de la referencia [17].*

1.1.3. Terminaciones de las superficies

Aunque la morfología más favorable para la espinela sea el crecimiento en forma de octaedro, se han obtenido otras morfologías diferentes [18], comprendiendo desde partículas en forma de cubo con las caras paralelas al plano (100), hasta octaedros truncados con caras paralelas al plano (111) y al plano (100).

Las diferentes morfologías son importantes en términos de la estabilidad química de las espinelas, donde las terminaciones atómicas que constituyen las principales superficies de la espinela juegan un papel relevante. Así, el plano cristalino (110) presenta dos terminaciones posibles [19]: una que expone los cationes tetraédricos y octaédricos, y otra que únicamente expone los cationes octaédricos. Por el contrario, cuando la superficie es paralela al plano cristalino (100), los cationes coordinados de forma tetraédrica son las especies terminales, debido a la ruptura de un menor número de enlaces [20]. De forma contraria, la superficie cristalográfica (111), presenta hasta seis posibles terminaciones [21], como se puede observar en la ***Figura 1. 4***. La naturaleza de los diferentes enlaces químicos va a determinar la reactividad de los materiales con estructura cristalina tipo espinela.

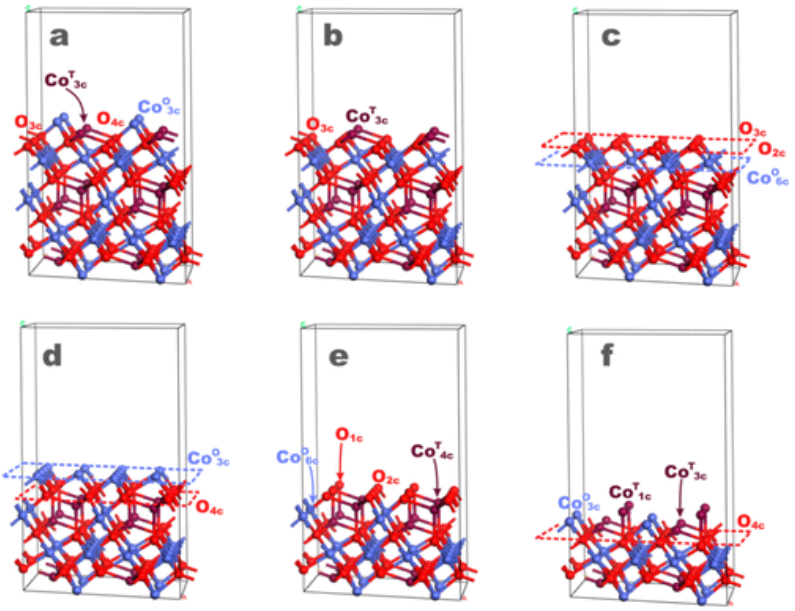

Figura 1. 4 *Principales terminaciones atómicas para el plano cristalográfico (111) de la espinela Co_3O_4. Imágenes de la referencia [21].*

1.2. Aluminato de cobalto: Pigmento cerámico

1.2.1. El color azul en la cerámica

El aluminato de cobalto se usa ampliamente como pigmento azul en el campo de la cerámica, debido principalmente a sus propiedades: intenso color, alto índice de refracción, y alta estabilidad térmica, química y fotoquímica [22,23]. Es interesante destacar que, la fuente tradicional e inevitable de reflexión de la luz en el rango de longitudes de onda correspondientes al color azul (~ 427-476 nm) en el aluminato de cobalto es el catión cobalto [24]. Los pigmentos cerámicos azules conocidos actualmente con la excepción del azul de vanadio-zircón, contienen cobalto, como por ejemplo: el olivino Co_2SiO_4, la willemita $(Co,Zn)_2SiO_4$, y las espinelas de cobalto $CoAl_2O_4$, Co_2SnO_4, $(Co,Zn)Al_2O_4$ y $Co(Al,Cr)_2O_4$. El color azul es más estable en los pigmentos basados en cobalto, mientras que el azul de vanadio-zircón presenta problemas de estabilidad por reducción del V^{5+} a V^{4+} a alta temperatura [25].

Concretamente, el color azul del aluminato de cobalto es el resultado de que se elimine la regla de selección de Laporte, permitiéndose las transiciones d-d [24,26,27]. Por esta razón, el espectro Ultravioleta-Visible (UV-Vis) del aluminato de cobalto presenta un triplete de bandas centradas en torno a: 540, 580 y 625 nm (absorción de las longitudes de onda de la luz verde y roja), que es característico de la presencia de los iones Co^{2+} en la coordinación tetraédrica y correspondiente a la transición $^4A_2$ (F) → $^4T_1$(P) [28]. El desdoblamiento de las bandas se debe al efecto Jahn-Teller, por la distorsión de la geometría tetraédrica, debido a la degeneración de los estados t_{2g} [29]. Además, la presencia de cationes de Co^{3+} en posiciones octaédricas hace que aparezcan bandas de transferencia de carga y el material presente una coloración verdosa [28].

A partir del espectro Ultravioleta-Visible se pueden obtener los parámetros cromáticos CIE-Lab que definen un color: el valor de L* indica la claridad (mayor o menor brillo) y puede oscilar de $L^*=0$ (negro) a $L^*=100$ (blanco), mientras que los valores de a^* y b^* indican la tonalidad: $a^* < 0$ verde, $a^* > 0$ rojo; $b^* > 0$ amarillo

y $b^* < 0$ azul. El conjunto (a^*, b^*) recibe el nombre de cromaticidad, y junto con la claridad definen el color de un estímulo. Así, en la ***Figura 1. 5***, se muestra la correlación entre la intensidad del color azul y el aumento de la temperatura de calcinación de pigmentos de aluminato de cobalto, correspondientes a una mayor proporción de cationes de Co^{2+} en posiciones tetraédricas.

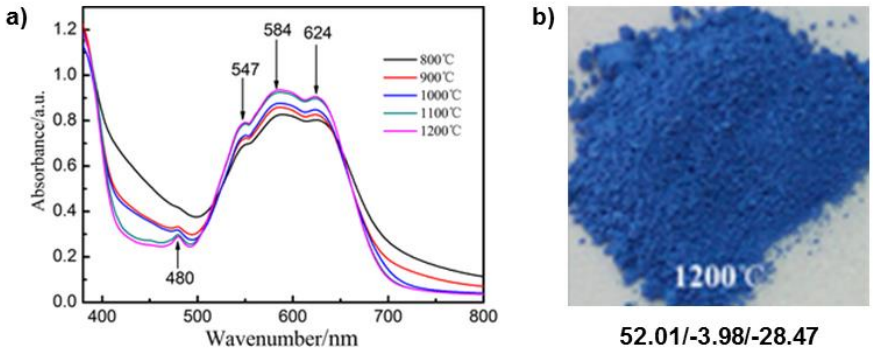

Figura 1. 5 *a) Espectros de absorción Uv-Vis de pigmentos de $CoAl_2O_4$ calcinados a diferentes temperaturas. b) Imagen fotográfica y coordenadas cromáticas L*/a*/b* del $CoAl_2O_4$ calcinado a 1200 ºC. Imágenes adaptadas de la referencia [23].*

1.2.2. Síntesis del pigmento $CoAl_2O_4$ por la vía cerámica

El aluminato de cobalto, generalmente, se sinteriza a alta temperatura por reacción en estado sólido entre dos óxidos [30,31]. Dicha vía se sigue prefiriendo por la industria debido a su bajo coste y fácil procesado, a pesar de que, actualmente, existe una amplia variedad de métodos de preparación [32].

En la bibliografía existe un número elevado de estudios que utilizan el método cerámico para la preparación del aluminato de cobalto. Srisawad y col. [33] sinterizaron el aluminato de cobalto mediante reacción por estado sólido a partir de cloruro de cobalto hexahidratado y Gibbsita (Hidróxido de aluminio $Al(OH)_3$) con diferente tamaño de partícula. Demostraron que la disminución en el tamaño de partícula del precursor de óxido de aluminio, resulta en una disminución de la temperatura de cristalización del $CoAl_2O_4$. La temperatura de calcinación se reduce mediante el uso de mineralizadores o agentes fundentes, generalmente basados en haluros de alcalinos o alcalinotérreos, que ayudan a la

difusión iónica, creando fases fluidas de baja viscosidad en torno a la temperatura de reacción de las fases cristalinas [34,35]. Sin embargo, la utilización de estos compuestos puede provocar serios problemas medioambientales, debido a la evaporación de compuestos tóxicos durante los tratamientos térmicos [36,37].

Otra línea de investigación se ha centrado en aumentar el rendimiento del color del aluminato de cobalto en esmaltes cerámicos. Melo y col. [38] utilizaron como precursores oxalato de cobalto y alúmina, estudiando diferentes temperaturas de calcinación. Por otro lado, se ha investigado la posibilidad de emplear otras estructuras de espinela, como el aluminato de cinc o de magnesio, que presentan unas tonalidades azules muy intensas, para utilizar cantidades de cobalto menores que en el aluminato de cobalto [24,34]. Sin embargo, el rendimiento del color obtenido fue inferior.

1.2.3. Nanopigmentos de $CoAl_2O_4$

La principal innovación realizada en pigmentos cerámicos en los últimos 20 años ha consistido en su aplicación en forma de nanopigmentos, mediante los sistemas de impresión por chorro de tinta (*inkjet*, en inglés) o la decoración digital de cerámica. En el proceso de decoración digital se emplea una tinta que consiste en una suspensión de nanopigmentos cerámicos en un medio líquido, y que pasa a través de los cabezales de impresión a altas velocidades [39,40]. Las gotas de la tinta cerámica se rocían sobre el sustrato para producir una capa con un espesor < 10 µm [41]. Esta tecnología se ha implantado muy rápidamente en el sector cerámico de azulejos ya que hace posible reducir el coste en la decoración de baldosas, digitalizar la decoración y obtener una mayor definición de la imagen.

Un factor determinante para la aplicabilidad de la tinta de inyección conteniendo nanopigmentos consiste en ajustar el tamaño de partícula del pigmento a valores < 300 nm, para evitar obturar los cabezales de impresión [42]. La reducción del tamaño de partícula de los pigmentos se realiza mediante molienda en medio húmedo empleando microbolas [43]. El uso de

nanopartículas de aluminato de cobalto en la decoración digital de azulejos cerámicos ha implicado la mejora de algunas de sus propiedades, como la obtención de un mayor poder cubriente [44] y una mayor dispersión de la luz [42].

La demanda de partículas nanométricas de $CoAl_2O_4$ ha planteado la búsqueda de nuevas rutas sintéticas para la obtención de este material, entre las cuales destacan: el método sol-gel [45], la síntesis hidrotermal [46,47], la síntesis por combustión [48], el método Pechini [49], la coprecipitación [50] y el método de poliol [51]. Sin embargo, su desarrollo a escala industrial aún no resulta competitivo para la mayoría de estos métodos en comparación con la molienda en microbolas.

1.3. Retos tecnológicos del aluminato de cobalto

El emergente uso del cobalto en nuevas aplicaciones tecnológicas, así como su escasez en la naturaleza, ha generado un aumento considerable del precio de los compuestos de cobalto. La explosión científica de la nanotecnología abre nuevas posibilidades en las aplicaciones de nanomateriales basados en aluminato de cobalto. Sin embargo, unidas a las nuevas posibilidades, se encuentran nuevos retos relacionados con las dudas generalizadas sobre el uso masivo de las nanopartículas y sus posibles efectos nocivos tanto para el ser humano como para el medio ambiente. En este contexto, la comunidad científica es consciente de que las nuevas aplicaciones en nanotecnología deben abordar el empleo de materiales con una base de conocimiento más horizontal, donde los procesos de obtención, los métodos de caracterización y los usos de los nanomateriales, estén contrastados en comparación con los materiales más "convencionales" (macroscópicos).

1.3.1. La abundancia del cobalto

El cobalto es un elemento muy escaso, se estima que en la corteza terrestre hay solo un 0,001% [52]. Actualmente se extrae en 20 países, pero más de la mitad de la producción mundial de cobalto corresponde a la República Democrática del Congo (RDC), donde solo las cuatro minas más importantes son responsables del 43% de la extracción mundial, estimada actualmente en unas 160.000 toneladas anuales [53].

La situación es algo más acuciante en la Unión Europa, donde hay una producción muy baja y la demanda anual de cobalto ya es aproximadamente nueve veces superior a la producción interna, que se sitúa en torno a las 2.300 toneladas anuales [54]. En la actualidad, Finlandia es el único productor minero de cobalto de la Unión Europea y, aunque también se han identificado depósitos en Suecia y en España, todos ellos tienen una concentración muy baja de cobalto [55].

La minería submarina supone uno de los proyectos futuros para poder atender la demanda de algunos de los minerales más codiciados, entre los cuales se encuentra el cobalto. La escasez del cobalto en tierra y la demanda cada vez mayor hace que el medio marino se posicione como una alternativa viable para la obtención de éste y otro tipo de metales [56].

Ante la escasez de cobalto en la naturaleza, es necesaria una política de sostenibilidad de las aplicaciones que requieren cobalto. Esto implica una reducción del uso, una reutilización de los productos con cobalto y una aproximación de economía circular que involucre a los materiales que contienen cobalto en sus composiciones. Estos aspectos van a condicionar el desarrollo e implantación de nuevas tecnologías que empleen cobalto.

1.3.2. Limitaciones de la nanotecnología

Los nanomateriales ya se encuentran en productos de uso cotidiano como pinturas, materiales de construcción, cosméticos o en la industria alimentaria, ejerciendo un gran impacto en la sociedad de hoy en día [57–59]. Sin embargo, se plantean una serie de inconvenientes, como son: la necesidad de obtener nanopartículas dispersas, la dificultad de su caracterización y la toxicidad de las mismas.

a) Dispersión de las nanopartículas

El principal problema que presentan los óxidos en forma de nanopartículas consiste en su extrema dificultad de manipulación y su fuerte tendencia a aglomerarse, debido a su pequeño tamaño y a su elevada superficie específica [60]. Las fuerzas atractivas de Van der Waals son responsables, en gran medida, del estado de aglomeración de las nanopartículas [61]. Los procesos de aglomeración modifican considerablemente las propiedades específicas de los nanomateriales. Esto afecta directamente a su empleo en determinadas aplicaciones, donde el carácter individual de las nanopartículas es crucial. Además, la aglomeración de las nanopartículas dificulta el estudio de las

propiedades estructurales y funcionales de las mismas como entidades individuales [62].

Para superar estas dificultades es necesario que las nanopartículas se encuentren en un estado de dispersión controlado. A escala industrial, la molienda en vía líquida es el principal proceso empleado para obtener nanopartículas dispersas, tal y como ocurre en las tintas de colores para inyección cerámica. Para evitar su reaglomeración, normalmente, se mantienen en el medio líquido en una suspensión estable, mediante el ajuste del pH o mediante la adición de polímeros dispersantes [44]. Por otro lado, en múltiples ocasiones, se requieren las nanopartículas en forma seca. Sin embargo, la eliminación del solvente y la presencia de los aditivos genera la reaglomeración de las nanopartículas y la modificación de sus propiedades.

Por tanto, el estado de aglomeración es un parámetro muy relevante para el empleo de materiales como el aluminato de cobalto y, tanto la optimización de aplicaciones existentes, como la generación de nuevas aplicaciones, precisa del control sobre el estado de aglomeración de las nanopartículas.

b) Caracterización de las nanopartículas

Como se ha indicado, en la actualidad, se preparan muchos más tipos de nanomateriales que hace tan solo una década, y en mayores cantidades, lo que requiere el desarrollo de protocolos más precisos para su caracterización. Sin embargo, tal caracterización es a veces incompleta debido a las dificultades inherentes de los materiales a nanoescala para ser analizados adecuadamente [63]. El carácter multidisciplinar de la nanotecnología requiere un enfoque integral de los métodos de caracterización, mediante la combinación de técnicas de manera complementaria [64].

Actualmente, son numerosas las técnicas analíticas que se emplean, por ejemplo, la fotoluminiscencia (PL, del inglés *Photoluminescence*), la electroluminiscencia (EL) y la espectroscopía ultravioleta-visible (UV-vis) proporcionan información sobre la composición y sobre la interacción de la luz

con las nanopartículas [65–67]. Las técnicas de imagen como el microscopio electrónico de barrido (SEM, del inglés *Scanning Electron Microscopy*) o el microscopio electrónico de transmisión de trasmisión (TEM, del inglés *Transmission Electron Microscopy* o HRTEM, del inglés *High-Resolution Transmission Electron Microscopy*), la microscopía Confocal Raman (CRM, del inglés *Confocal Raman Microscopy*) proporcionan información morfológica y estructural [68]. Algunas de las técnicas anteriormente mencionadas (SEM, TEM, UV-vis), junto a la dispersión dinámica de la luz (DLS, del inglés *Dynamic Light Scattering*) y la electroforesis de zona capilar (CZE, del inglés *Capillary Zone Electrophoresis*), permiten medir el tamaño de las nanopartículas [69,70]. Otras técnicas, como la difracción de rayos X (XRD, del inglés *X-Ray Powder Diffraction*) y la espectroscopia de fotoelectrones de rayos X (XPS, del inglés *X-Ray photoelectron spectrometry*) proporcionan información sobre la cristalinidad y la composición de las nanopartículas [71,72]. Sin embargo, en el caso de los nanomateriales, las técnicas anteriormente mencionadas presentan limitaciones en cuanto al análisis estructural de las regiones nanométricas; debido a la aparición de fases múltiples, aglomerados, fenómenos de interacción entre las diferentes fases o, simplemente, por la limitada resolución de las técnicas [63].

Respecto a la caracterización estructural de los nanomateriales de $CoAl_2O_4$, es importante destacar la similitud estructural con otras espinelas composicionalmente diferentes, como por ejemplo con uno de sus precursores el óxido de cobalto (Co_3O_4), dificultando su caracterización individual, pues únicamente presentan sutiles diferencias en la celdilla unitaria de la red cristalina [73,74]. Además, es necesario tener en cuenta que el aluminato de cobalto presenta un color oscuro. De modo que, cuando se le hace incidir la luz láser, en ciertas técnicas de caracterización estructural como la espectroscopia Raman, se produce una fuerte absorción con los efectos de calentamiento asociados [75]. Otra de las dificultades añadidas para la caracterización de estos materiales es las diferencias entre autores a la hora de interpretar los resultados de las técnicas. Esto es debido, entre otros factores, a la falta de control del estado de

aglomeración. A modo de ejemplo, se consigna la controversia existente en la asignación de los modos Raman del propio aluminato de cobalto [76–80].

c) Toxicidad de las nanopartículas

Por otro lado, mientras que la nanotecnología y la producción de nanopartículas crecen exponencialmente, quedan muchos aspectos por investigar sobre su impacto toxicológico y el posible peligro que suponen para la salud humana y el medio ambiente [81–83]. La gran relación superficie/volumen de las nanopartículas se traduce en un aumento de la reactividad de las mismas [84], de particular importancia en los mecanismos de interacción con los sistemas biológicos, que están lejos de ser completamente dilucidados dada su complejidad. Incluso, se ha planteado que materiales aparente inofensivos deberían tratarse con la misma precaución que los carcinógenos conocidos debido a los cambios en las propiedades potenciadas por el tamaño nanométrico [85]. La penetración de las nanopartículas en el organismo afecta a los pulmones, el cerebro, el hígado o los riñones causando diferentes enfermedades [86].

Concretamente, los nanomateriales que contienen cobalto también presentan una elevada toxicidad. Los efectos nocivos para la salud humana por una exposición excesiva a nanopartículas de cobalto se caracterizan por un síndrome clínico complejo con un conjunto variable de déficits neurológicos, cardiovasculares y endocrinos, directamente relacionados con la absorción de iones de cobalto en los tejidos y en la circulación sanguínea [87].

d) Reactividad

Finalmente, gracias a la alta reactividad de las nanopartículas de compuestos basados en cobalto, este tipo de materiales pueden promover la actividad catalítica de una gran variedad de reacciones. En parte, el rendimiento catalítico de estos materiales depende estrechamente de su tamaño. La disminución del tamaño de partícula provoca que una gran cantidad de átomos estén disponibles, como sitios activos, en la superficie de las partículas [88]. Esto genera

catalizadores altamente activos, pues la actividad química es proporcional al número de especies activas accesibles a los reactivos [89].

Por otro lado, la actividad catalítica de los catalizadores basados en cobalto también depende de su composición. Entre todos los óxidos de cobalto existentes, el Co_3O_4 es el que se investiga con mayor frecuencia, debido a su excelente estabilidad térmica y a sus propiedades físicas y químicas excepcionales [90]. Las investigaciones destacan que, los catalizadores de Co_3O_4, ofrecen el mejor equilibrio entre coste y actividad catalítica: su comportamiento resulta ser muy similar al de los metales nobles [91], mientras que la selectividad es mayor que la de otros óxidos de metales de transición (como Mn_2O_3 o V_2O_5) [92]. Wang y col. [93] determinaron los factores clave para la alta actividad catalítica, en la reacción de oxidación del CO, de los catalizadores basados en Co_3O_4: la fuerza de adsorción del CO, la barrera de reacción del CO con el oxígeno de la red y las propiedades redox del Co_3O_4. Harrison y col. [94] demostraron la gran actividad y selectividad del sistema catalítico CoO/CeO_2 para la oxidación de la carbonilla generada por los motores diésel, lo cual también está íntimamente ligado a la fuerte capacidad redox del CoO_x [95,96].

También se ha observado que la morfología de las nanopartículas o el plano cristalino expuesto de los nanocristales de Co_3O_4 pueden alterar notablemente su rendimiento catalítico [91]. En este sentido, la síntesis controlada de nano o micropartículas de óxidos metálicos con diferentes morfologías ha alcanzado un notable interés dentro de la comunidad científica en el uso de catalizadores [97–100]. Este control de la morfología ofrece una gran versatilidad en la modulación de las propiedades catalíticas de un nanocristal, especialmente cuando las superficies que se exponen poseen diferentes actividades. Por ejemplo, Xiaowei y col. [101] investigaron la oxidación catalítica del CO sobre nanopartículas catalíticas de Co_3O_4. Mediante un delicado control del tamaño y la topología, encontraron que una estructura de nanohilos de Co_3O_4, en la cual un 40 % de las caras se encuentran orientadas en la dirección [110], presenta una actividad catalítica 10 veces mayor que los catalizadores convencionales de Co_3O_4. Estos

estudios se han realizado también para otros materiales, Aneggi y col. [102] demostraron que la actividad de combustión de la carbonilla depende de la forma de las nanopartículas de CeO_2 y de la superficie expuesta: nanocubos de CeO_2 con las caras paralelas al plano (100) y nanohilos con las caras paralelas a los planos (100), (110) y (111) exhibieron una actividad mucho más alta en comparación con materiales de CeO_2 policristalinos o con forma de octaedros, con las caras orientadas en la dirección [111].

La alta eficiencia catalítica del Co_3O_4 contrasta claramente con la del $CoAl_2O_4$. Pese a ello, el $CoAl_2O_4$, se ha propuesto como catalizador en numerosas reacciones, como por ejemplo: la oxidación de CO [103], la hidrogenación de CO [104], el reformado de metano [105], la deshidrogenación de propano [106] y la combustión de carbonilla en presencia de NO_x/O_2 [107]. Sin embargo, hasta la fecha, la eficiencia testada del $CoAl_2O_4$ reacciones catalíticas ha sido limitada. Básicamente, las investigaciones se han centrado en la mejora de las propiedades catalíticas del $CoAl_2O_4$ mediante el aumento de la superficie específica, a través del desarrollo de nanoestructuras [108], o de estructuras mesoporosas [109]. El efecto de la morfología sobre las propiedades fisicoquímicas del aluminato de cobalto en las reacciones catalíticas permanece inexplorado, lo cual dificulta la comprensión del mecanismo de reacción y restringe el diseño de catalizadores basados en $CoAl_2O_4$ de alto rendimiento con gran actividad y selectividad.

1.4. Motivación y objetivos

El emergente uso del cobalto en nuevas aplicaciones tecnológicas, así como su escasez en la naturaleza, justifica la necesidad de desarrollar materiales de aluminato de cobalto sostenibles, en los que también se eliminen las posibles implicaciones negativas asociadas a la toxicidad del cobalto, pero sin comprometer las propiedades de este material.

La nanotecnología abre nuevas opciones para la aplicación del aluminato de cobalto a escala nanométrica, donde el estado de aglomeración y el control de la reactividad permiten resolver, o al menos estudiar, nuevas rutas para una mayor eficiencia en su uso.

Entre las posibilidades que abre la nanotecnología destacan los materiales nanoestructurados, que se caracterizan por una disposición organizada de las nanopartículas. Las rutas más frecuentes en nanotecnología se realizan siguiendo dos aproximaciones: la generación de nanopartículas a partir de unidades químicas más pequeñas (Abajo-Arriba o *Bottom-Up*), o la reducción en tamaño desde unidades mayores (Arriba-Abajo o *Top-Down*). El empleo de estas aproximaciones para diseñar soluciones específicas permite sintonizar sus propiedades, a la vez que manipular las nanopartículas de forma adecuada para evitar los riesgos de aglomeración e, incluso, su toxicidad si el tamaño de la matriz es lo suficientemente grande.

En este contexto, uno de los desafíos tecnológicos más importantes en el ámbito de la nanotecnología es el desarrollo de técnicas correlacionadas que permitan la caracterización de las propiedades físicas y químicas, durante las distintas etapas de producción y uso de los materiales nanoestructurados. Una técnica que se encuentra en el eje de las técnicas correlativas de caracterización de nanomateriales es la Microscopía Raman Confocal.

Por otro lado, el desarrollo de un nuevo material debería estar ligado a la resolución de los problemas que tiene planteada la sociedad, tales como la búsqueda del bienestar humano orientado a la mejora de la salud, la

comunicación, la sostenibilidad o el suministro de energía. En este contexto, el rápido crecimiento económico, el aumento de la población y los altos estándares de vida, han generado un incremento del consumo energético que ha tenido consecuencias directas en la contaminación y en el cambio climático. Por esta razón, se plantea la posibilidad de contribuir a la sostenibilidad mediante la búsqueda de aplicaciones avanzadas para estos materiales nanoestructurados.

El objetivo de este trabajo de tesis consiste en la obtención y estudio de sistemas nanoestructurados basados en la espinela de aluminato de cobalto ($CoAl_2O_4$) mediante diferentes rutas de síntesis. En este sentido, el control de las metodologías de síntesis llevadas a cabo han sido un aspecto delimitante de las propiedades finales obtenidas por los nanomateriales y, consecuentemente, de sus aplicaciones finales.

Se plantean así una serie de objetivos específicos para poder alcanzar el objetivo general:

- ✓ Síntesis de materiales nanoestructurados con arquitectura de tipo coraza-núcleo donde la superficie externa está formada por cristales nanométricos de $CoAl_2O_4$ y el núcleo está formado por α-Al_2O_3.
- ✓ Estudiar exhaustivamente la estabilidad térmica de los materiales nanoestructurados tipo coraza-núcleo, mediante técnicas correlacionadas de microscopía y espectroscopia avanzadas.
- ✓ Optimización de la composición de los materiales precursores, así como del proceso de sinterización llevado a cabo, con el fin de obtener una elevada estabilidad de las nanopartículas de $CoAl_2O_4$, que maximice las propiedades colorimétricas para su aplicación como pigmento.
- ✓ Diseño de un material nanoestructurado de $CoAl_2O_4$, con potenciación de la reactividad mediante técnicas de arriba-abajo.
- ✓ Estudio de la influencia de la estructura-microestructura en la actividad catalítica de materiales nanoestructurados de aluminato de cobalto para su aplicación en la combustión selectiva de carbonilla.

- ✓ Optimización de la eficiencia y estabilidad de catalizadores basados en materiales nanoestructurados activados de aluminato de cobalto empelados como como soporte de nanopartículas metálicas.

1.5. Bibliografía

1. Doerner, M., and Hoppe, T. (2001) *Los materiales de pintura y su empleo en el arte*, Reverté, Barcelona.

2. Nicholson, P.T., and Shaw, I. (2000) *Ancient Egyptian materials and technology*, Cambridge University Press, Cambridge.

3. Ball, P., and Vitier, J.A. (2012) *La invención del color*, Turner, Madrid.

4. Thénard, L.J. (1799) Considérations générales sur les Couleurs, suivies d'un procédé pour préparer une couleur bleue aussi belle que l'outremer. *J. des mines*, **15** (2), 128–136.

5. Henry, N.F.M., and Lonsdale, K. (1952) *International tables for X-ray crystallography*, The Kynoch Press, Birmingham.

6. Márquez, G. (2015) Síntesis y caracterización de nanopartículas magnéticas de ferritas y cromitas de Co, Mn y Ni.

7. Sickafus, K.E., Wills, J.M., and Grimes, N.W. (1999) Structure of spinel. *J. Am. Ceram. Soc.*, **82** (12), 3279–3292.

8. Horsfall, M., and Spiff, A.I. (2005) Equilibrium sorption study of Al^{3+}, Co^{2+} and Ag^{+} in aqueous solutions by fluted pumpkin (Telfairia Occidentalis HOOK f) waste biomass. *Acta Chim. Slov.*, **52** (9), 174–181.

9. Sanderson, R.T. (1954) Electronegativities in inorganic chemistry. *J. Chem. Educ.*, **31** (1), 539–544.

10. Matheus, P.R., Abad, J.M., Fernández, L., et al. (2008) Influencia del estado de oxidación del ión cobalto en la estabilidad de electrodos modificados con monocapas SAM-TOA-ANTA-Co^{n+}-HRP-N_{His}. *Av. en Química*, **3** (2), 69–77.

11. Nakatsuka, A., Ikeda, Y., Yamasaki, Y., et al. (2003) Cation distribution and bond lengths in $CoAl_2O_4$ spinel. *Solid State Commun.*, **128** (2–3), 85–90.

12. Xia, Y., Xiong, Y., Lim, B., and Skrabalak, S.E. (2009) Shape-controlled synthesis of metal nanocrystals: Simple chemistry meets complex physics? *Angew. Chemie - Int. Ed.*, **48** (1), 60–103.

13. Wang, Z.L., and Feng, X. (2003) Polyhedral shapes of CeO_2 nanoparticles. *J. Phys. Chem. B*, **107** (49), 13563–13566.

14. Zhang, D.E., Zhang, X.J., Ni, X.M., et al. (2006) Synthesis and characterization of $CoFe_2O_4$ octahedrons via an EDTA-assisted route. *J. Magn. Magn. Mater.*, **305** (1), 68–70.

15. Liu, X.M., Fu, S.Y., and Zhu, L.P. (2007) High-yield synthesis and characterization of monodisperse sub-microsized $CoFe_2O_4$ octahedra. *J. Solid State Chem.*, **180** (2), 461–466.

16. Gao, H., Yang, H., Wang, S., et al. (2018) A new route for the preparation of $CoAl_2O_4$ nanoblue pigments with high uniformity and its optical properties. *J. Sol-Gel Sci. Technol.*, **86** (1), 206–216.

17. Shirsath, S.E., Liu, X., Yasukawa, Y., et al. (2016) Switching of magnetic easy-axis using crystal orientation for large perpendicular coercivity in $CoFe_2O_4$ thin film. *Sci. Rep.*, **6** (2), 1–11.

18. Zhao, L., Zhang, H., Xing, Y., et al. (2008) Morphology-controlled synthesis of magnetites with nanoporous structures and excellent magnetic properties. *Chem. Mater.*, **20** (1), 198–204.

19. Chen, J., and Selloni, A. (2012) Electronic states and magnetic structure at the Co_3O_4 (110) surface: A first-principles study. *Phys. Rev. B - Condens. Matter Mater. Phys.*, **85** (8), 1–9.

20. Ritter, M., and Weiss, W. (1999) Fe_3O_4 (111) surface structure determined by LEED crystallography. *Surf. Sci.*, **432** (1), 81–94.

21. Zasada, F., Gryboś, J., Piskorz, W., and Sojka, Z. (2018) Cobalt spinel (111) facets of various stoichiometry - DFT+U and ab initio thermodynamic investigationssdafsfas. *J. Phys. Chem. C*, **122** (5), 2866–2879.

22. Tang, Q., Zhu, H., Chen, C., et al. (2017) Preparation and characterization of nanoscale cobalt blue pigment for ceramic inkjet printing by sol-gel self-propagating combustion. *Mater. Res.*, **20** (5), 1340–1344.

23. He, X., Wang, F., Liu, H., et al. (2018) Synthesis and color properties of the TiO_2@$CoAl_2O_4$ blue pigments with low cobalt content applied in ceramic glaze. *J. Am. Ceram. Soc.*, **101** (6), 2578–2588.

24. Llusar, M., Forés, A., Badenes, J.A., et al. (2001) Colour analysis of some cobalt-based blue pigments. *J. Eur. Ceram. Soc.*, **21** (8), 1121–1130.

25. Demiray, T., Nath, D.K., and Hummel, F.A. (1970) Zircon-Vanadium blue pigment. *J. Am. Ceram. Soc.*, **53** (1), 1–4.

26. Mimani, T., and Ghosh, S. (2000) Combustion synthesis of cobalt pigments: Blue and pink. *Curr. Sci.*, **78** (7), 892–896.

27. Weller, M., Overton, T., Armstrong, F., and Rourke, J. (2018) *Inorganic chemistry*, Oxford University Press, Oxford.

28. Taguchi, M., Nakane, T., Hashi, K., et al. (2013) Reaction temperature variations on the crystallographic state of spinel cobalt aluminate. *Dalt. Trans.*, **42** (19), 7167–7176.

29. Pradhan, S.K., Dalal, B., Sarkar, A., and De, S.K. (2019) Spectroscopic and magnetic investigations of a spin-frustrated Mn-doped $CoAl_2O_4$ spinel. *Phys. Chem. Chem. Phys.*, **21** (2), 842–850.

30. Bolt, P.H., Habraken, F.H.P.M., and Geus, J.W. (1998) Formation of nickel, cobalt, copper, and iron aluminates from α- and γ-alumina-supported oxides: A comparative study. *J. Solid State Chem.*, **135** (1), 59–69.

31. Fernández Colinas, J.M., and Otero Areán, C. (1994) Kinetics of solid-state spinel formation: Effect of cation coordination preference. *J. Solid State Chem.*, **109** (1), 43–46.

32. Zhao, Q., Yan, Z., Chen, C., and Chen, J. (2017) Spinels: Controlled preparation, oxygen reduction/evolution reaction application, and beyond. *Chem. Rev.*, **117** (15), 10121–10211.

33. Srisawad, N., Chaitree, W., Mekasuwandumrong, O., et al. (2012) Formation of $CoAl_2O_4$ nanoparticles via low-temperature solid-state reaction of fine gibbsite and cobalt precursor. *J. Nanomater.*, **2012** (10), 1–8.

34. Forés, A., Llusar, M., Badenes, J.A., et al. (2000) Cobalt minimisation in willemite ($Co_xZn_{2-x}SiO_4$) ceramic pigments. *Green Chem.*, **2** (1), 93–100.

35. Pfaff, G. (2017) *Inorganic pigments*, De Gruyter, Berlin.

36. Tomas, G.M., and Monrós, G. (2003) El color de la cerámica: Nuevos mecanismos en pigmentos para los nuevos procesados de la industria cerámica, Athenea, Castelló de la Plana.

37. Pommier, C., Chhor, K., Bocquet, J.F., and Barj, M. (1990) Reactions in supercritical fluids, a new route for oxide ceramic powder elaboration, synthesis of the spinel $MgAl_2O_4$. *Mater. Res. Bull.*, **25** (2), 213–221.

38. Melo, D.M.A., Cunha, J.D., Fernandes, J.D.G., et al. (2003) Evaluation of $CoAl_2O_4$ as ceramic pigments. *Mater. Res. Bull.*, **38** (9–10), 1559–1564.

39. Prasad, P.S.R.K., Reddy, A.V., Rajesh, P.K., et al. (2006) Studies on rheology of ceramic inks and spread of ink droplets for direct ceramic ink jet printing. *J. Mater. Process. Technol.*, **176** (1–3), 222–229.

40. Safari, A., Allahverdi, M., and Akdogan, E.K. (2007) Solid freeform fabrication of piezoelectric sensors and actuators. *Front. Ferroelectr. A Spec. Issue J. Mater. Sci.*, **41** (1), 177–198.

41. Rahul, S.H., Balasubramanian, K., and Venkatesh, S. (2017) Optimizing inkjet printing process to fabricate thick ceramic coatings. *Ceram. Int.*, **43** (5), 4513–4519.

42. Wang, Y., Wang, Q., Chang, Q., et al. (2018) Effect of particle size on the blue chromate pigment $CoAl_2O_4$. *J. Ceram. Sci. Technol.*, **9** (1), 43–46.

43. Güngör, G.L., Kara, A., Blosi, M., et al. (2015) Micronizing ceramic pigments for inkjet printing: Part I. Grindability and particle size distribution. *Ceram. Int.*, **41** (5), 6498–6506.

44. Peymannia, M., Soleimani-Gorgani, A., Ghahari, M., and Najafi, F. (2014) Production of a stable and homogeneous colloid dispersion of nano $CoAl_2O_4$ pigment for ceramic ink-jet ink. *J. Eur. Ceram. Soc.*, **34** (12), 3119–3126.

45. Kurajica, S., Popović, J., Tkalčec, E., et al. (2012) The effect of annealing temperature on the structure and optical properties of sol-gel derived nanocrystalline cobalt aluminate spinel. *Mater. Chem. Phys.*, **135** (2–3), 587–593.

46. Chen, Z., Shi, E., Li, W., et al. (2002) Hydrothermal synthesis and optical property of nano-sized $CoAl_2O_4$ pigment. *Mater. Lett.*, **55** (5), 281–284.

47. Chen, Z., Shi, E., Li, W., et al. (2010) Particle size comparison of hydrothermally synthesized cobalt and zinc aluminate spinels. *J. Am. Ceram. Soc.*, **85** (12), 2949–2955.

48. Ali, A.A., El Fadaly, E., and Ahmed, I.S. (2018) Near-infrared reflecting blue inorganic nano-pigment based on cobalt aluminate spinel via combustion synthesis method. *Dye. Pigment.*, **158** (4), 451–462.

49. Gama, L., Ribeiro, M.A., Barros, B.S., et al. (2009) Synthesis and characterization of the $NiAl_2O_4$, $CoAl_2O_4$ and $ZnAl_2O_4$ spinels by the polymeric precursors method. *J. Alloys Compd.*, **483** (2), 453–455.

50. Baker, J.E., Bruch, R., and Niu, Y. (1991) Investigation of cobalt aluminum oxide ($CoAl_2O_4$), copper/cobalt aluminum oxide and cobalt/cobalt aluminum oxide catalysts for the formation of oxygenates from a carbon monoxide-carbon dioxide-hydrogen mixture. *Appl. Catal.*, **73** (1), 135–152.

51. Merikhi, J., Jungk, H.O., and Feldmann, C. (2000) Sub-micrometer $CoAl_2O_4$ pigment particles - Synthesis and preparation of coatings. *J. Mater. Chem.*, **10** (6), 1311–1314.

52. Hazen, R.M., Hystad, G., Golden, J.J., et al. (2017) Cobalt mineral ecology. *Am. Mineral.*, **102** (1), 108–116.

53. Zeuner, B. (2018) An obsolescing bargain in a rentier state: Multinationals, artisanal miners, and Cobalt in the Democratic Republic of Congo. *Front. Energy Res.*, **6** (21), 1–6.

54. Schmidt, T., Buchert, M., and Schebek, L. (2016) Investigation of the primary production routes of nickel and cobalt products used for Li-ion batteries. *Resour. Conserv. Recycl.*, **112** (9), 107–122.

55. Albanese, S., Sadeghi, M., Lima, A., et al. (2015) GEMAS: Cobalt, Cr, Cu and Ni distribution in agricultural and grazing land soil of Europe. *J. Geochemical Explor.*, **154** (7), 81–93.

56. Somoza, L., and González, F. (2011) Minería submarina: se inicia la explotación de los fondos oceánicos. *Enseñanza las ciencias la tierra Rev. la Asoc. Española para la Enseñanza las Ciencias la Tierra*, **19** (1), 115–118.

57. Vance, M.E., Kuiken, T., Vejerano, E.P., et al. (2015) Nanotechnology in the real world: Redeveloping the nanomaterial consumer products inventory. *Beilstein J. Nanotechnol.*, **6** (1), 1769–1780.

58. Perez Espitia, P.J., Ferreira Soares, N. de F., dos Reis Coimbra, J.S., et al. (2012) Zinc oxide nanoparticles: Synthesis, antimicrobial activity and food packaging applications. *Food Bioprocess Technol.*, **5** (5), 1447–1464.

59. Weir, A., Westerhoff, P., Fabricius, L., et al. (2012) Titanium dioxide nanoparticles in food and personal care products. *Environ. Sci. Technol.*, **46** (4), 2242–2250.

60. Ashraf, M.A., Peng, W., Zare, Y., and Rhee, K.Y. (2018) Effects of size and aggregation/agglomeration of nanoparticles on the

interfacial/interphase properties and tensile strength of polymer nanocomposites. *Nanoscale Res. Lett.*, **13** (11), 1–7.

61. Hartley, P.A., Parfitt, G.D., and Pollack, L.B. (1985) The role of the van der Waals force in the agglomeration of powders containing submicron particles. *Powder Technol.*, **42** (1), 35–46.

62. Lorite, I., Romero, J.J., and Fernandez, J.F. (2015) Influence of the nanoparticles agglomeration state in the quantum-confinement effects: Experimental evidences. *AIP Adv.*, **5** (3), 1–7.

63. Mourdikoudis, S., Pallares, R.M., and Thanh, N.T.K. (2018) Characterization techniques for nanoparticles: Comparison and complementarity upon studying nanoparticle properties. *Nanoscale*, **10** (27), 12871–12934.

64. Khan, I., Saeed, K., and Khan, I. (2017) Nanoparticles: Properties, applications and toxicities. *Arab. J. Chem.*, **5** (1), 1–24.

65. Rojas-Hernandez, R.E., Rubio-Marcos, F., Serrano, A., et al. (2017) Precise tuning of the nanostructured surface leading to the luminescence enhancement in Sr_2O_4 based core/chell structure. *Sci. Rep.*, **7** (1), 462.

66. Jafarzadeh, M., Rahman, I.A., and Sipaut, C.S. (2010) Optical properties of amorphous organo-modified silica nanoparticles produced via co-condensation method. *Ceram. Int.*, **36** (1), 333–338.

67. Reinosa, J.J., Leret, P., Álvarez-Docio, C.M., et al. (2016) Enhancement of UV absorption behavior in ZnO-TiO_2 composites. *Bol. la Soc. Esp. Ceram. y Vidr.*, **55** (2), 55–62.

68. Lucas-Gil, E., Fernández, J.F., and Rubio-Marcos, F. (2017) One more step against nanotoxicity: Hierarchical particles designed to antifungal properties. *Mater. Des.*, **134** (11), 188–195.

69. Jitkang, L., Pin, Y.S., Xin, C.H., and Chun, L.S. (2013) Characterization of magnetic nanoparticle by dynamic light scattering. *Nanoscale Res. Lett.*, **8** (1), 381.

70. Vanifatova, N.G., Spivakov, B.Y., Mattusch, J., et al. (2005) Investigation of iron oxide nanoparticles by capillary zone electrophoresis. *Talanta*, **66** (3), 605–610.

71. Rojas-Hernandez, R.E., Rubio-Marcos, F., Gonçalves, R.H., et al. (2015) Original synthetic route to obtain a $SrAl_2O_4$ phosphor by the molten salt method: Insights into the Reaction Mechanism and enhancement of the persistent luminescence. *Inorg. Chem.*, **54** (20), 9896–9907.

72. Bernardi, F., Fecher, G.H., Alves, M.C.M., and Morais, J. (2010) Unraveling the formation of core-shell structures in nanoparticles by S-XPS. *J. Phys. Chem. Lett.*, **1** (6), 912–917.

73. Mazza, D., Delmastro, A., and Ronchetti, S. (2000) Co, Ni, Cu aluminates supported on mullite precursors via a solid state reaction. *J. Eur. Ceram. Soc.*, **20** (6), 699–706.

74. Yoneda, M., Gotoh, K., Nakanishi, M., et al. (2019) Solid-state synthesis and characterization of cobalt blue core-shell pigment particles. *J. Am. Ceram. Soc.*, **102** (6), 3468–3476.

75. Najmaei, S., Liu, Z., Ajayan, P.M., and Lou, J. (2012) Thermal effects on the characteristic Raman spectrum of molybdenum disulfide (MoS_2) of varying thicknesses. *Appl. Phys. Lett.*, **100** (1).

76. D'Ippolito, V., Andreozzi, G.B., Bersani, D., and Lottici, P.P. (2015) Raman fingerprint of chromate, aluminate and ferrite spinels. *J. Raman Spectrosc.*, **46** (12), 1255–1264.

77. Shirai, H., Morioka, Y., and Nakagawa, I. (1982) Infrared and raman spectra and lattice vibrations of some oxide spinels. *J. Phys. Soc. Japan*, **51** (2), 592–597.

78. Bouchard, M., and Gambardella, A. (2010) Raman microscopy study of synthetic cobalt blue spinels used in the field of art. *J. Raman Spectrosc.*, **49** (2), 1477–1485.

79. Preudhomme, J., and Tarte, P. (1971) Infrared studies of spinels—III: The normal II–III spinels. *Spectrochim. Acta Part A Mol. Spectrosc.*, **2** (9), 1817–1835.

80. Cava, S., Tebcherani, S.M., Pianaro, S.A., et al. (2006) Structural and spectroscopic analysis of γ-Al_2O_3 to α-Al_2O_3-$CoAl_2O_4$ phase transition. *Mater. Chem. Phys.*, **97** (1), 102–108.

81. Jain, A., Ranjan, S., Dasgupta, N., and Ramalingam, C. (2018) Nanomaterials in food and agriculture: An overview on their safety concerns and regulatory issues. *Crit. Rev. Food Sci. Nutr.*, **58** (2), 297–317.

82. Chattopadhyay, S., Dash, S.K., Kar Mahapatra, S., et al. (2014) Chitosan-modified cobalt oxide nanoparticles stimulate TNF-α-mediated apoptosis in human leukemic cells. *J. Biol. Inorg. Chem.*, **19** (3), 399–414.

83. Malard, V., Perrin, L., Carmona, A., et al. (2014) Low-solubility particles and a Trojan-horse type mechanism of toxicity: the case of cobalt oxide on human lung cells. *Part. Fibre Toxicol.*, **11** (1), 14.

84. Li, Z.H., and Truhlar, D.G. (2014) Nanothermodynamics of metal nanoparticles. *Chem. Sci.*, **5** (7), 2605–2624.

85. Spruit, S.L. (2017) Choosing between precautions for nanoparticles in the workplace: Complementing the precautionary principle with caring. *J. Risk Res.*, **20** (3), 326–346.

86. Buzea, C., Pacheco, I.I., and Robbie, K. (2007) Nanomaterials and nanoparticles: Sources and toxicity. *Biointerphases*, **2** (4), 17–71.

87. Simonsen, L.O., Harbak, H., and Bennekou, P. (2012) Cobalt metabolism and toxicology-A brief update. *Sci. Total Environ.*, **432** (8), 210–215.

88. Zanella, R. (2014) Aplicación de los nanomateriales en catálisis. *Mundo Nano*, **7** (12), 66–82.

89. Corain, B., Schmid, G., and Toshima, N. (2011) *Metal nanoclusters in catalysis and materials science: The issue of size control*, Elsevier Science, Amsterdam.

90. Tang, C.W., Wang, C. Bin, and Chien, S.H. (2008) Characterization of cobalt oxides studied by FT-IR, Raman, TPR and TG-MS. *Thermochim. Acta*, **473** (1–2), 68–73.

91. Liotta, L.F., Wu, H., Pantaleo, G., and Venezia, A.M. (2013) Co_3O_4 nanocrystals and Co_3O_4-MO_x binary oxides for CO, CH_4 and VOC oxidation at low temperatures: A review. *Catal. Sci. Technol.*, **3** (12), 3085–3102.

92. Todorova, S., Blin, J.L., Naydenov, A., et al. (2019) Co_3O_4-MnO_x oxides supported on SBA-15 for CO and VOCs oxidation. *Catal. Today*, **5** (1), 1–11.

93. Wang, H.F., Kavanagh, R., Guo, Y.L., et al. (2012) Origin of extraordinarily high catalytic activity of Co_3O_4 and its morphological chemistry for CO oxidation at low temperature. *J. Catal.*, **296** (12), 110–119.

94. Harrison, P.G., Ball, I.K., Daniell, W., et al. (2003) Cobalt catalysts for the oxidation of diesel soot particulate. *Chem. Eng. J.*, **95** (9), 47–55.

95. Liu, J., Zhao, Z., Wang, J., et al. (2008) The highly active catalysts of nanometric CeO_2-supported cobalt oxides for soot combustion. *Appl. Catal. B Environ.*, **84** (1–2), 185–195.

96. Natile, M.M., and Glisenti, A. (2005) CoO_x/CeO_2 nanocomposite powders: Synthesis, characterization, and reactivity. *Chem. Mater.*, **17** (13), 3270–3280.

97. Saputra, E., Muhammad, S., Sun, H., et al. (2014) Shape-controlled activation of peroxymonosulfate by single crystal α-Mn_2O_3 for catalytic phenol degradation in aqueous solution. *Appl. Catal. B Environ.*, **154–155** (8), 246–251.

98. Wu, Z., Li, M., and Overbury, S.H. (2012) On the structure dependence of CO oxidation over CeO_2 nanocrystals with well-defined surface planes. *J. Catal.*, **285** (1), 61–73.

99. Li, Y., and Shen, W. (2014) Morphology-dependent nanocatalysts: Rod-shaped oxides.

100. González-Prior, J., López-Fonseca, R., Gutiérrez-Ortiz, J.I., and de Rivas, B. (2016) Oxidation of 1,2-dichloroethane over nanocube-shaped Co_3O_4 catalysts. *Appl. Catal. B Environ.*, **199** (12), 384–393.

101. Xie, X., Li, Y., Liu, Z.Q., et al. (2009) Low-temperature oxidation of CO catalysed by Co_3O_4 nanorods. *Nature*, **458** (7239), 746–749.

102. Aneggi, E., Wiater, D., De Leitenburg, C., et al. (2014) Shape-dependent activity of ceria in soot combustion. *ACS Catal.*, **4** (1), 172–181.

103. Thormählen, P., Fridell, E., Cruise, N., et al. (2001) The influence of CO_2, C_3H_6, NO, H_2, H_2O or SO_2 on the low-temperature oxidation of CO on a cobalt-aluminate spinel. *Appl. Catal. B Environ.*, **31** (1), 1–12.

104. Rojanapipatkul, S., and Jongsomjit, B. (2008) Synthesis of cobalt on cobalt-aluminate via solvothermal method and its catalytic properties for carbon monoxide hydrogenation. *Catal. Commun.*, **10** (2), 232–236.

105. Xu, L., Zhang, J., Wang, F., et al. (2015) One-step synthesis of ordered mesoporous $CoAl_2O_4$ spinel-based metal oxides for CO_2 reforming of CH_4. *RSC Adv.*, **5** (60), 48256–48268.

106. Hu, B., Kim, W.G., Sulmonetti, T.P., et al. (2017) A mesoporous cobalt aluminate spinel catalyst for nonoxidative propane dehydrogenation. *ChemCatChem*, **9** (17), 3330–3337.

107. Wang, J., Yang, G., Cheng, L., et al. (2015) Three-dimensionally ordered macroporous spinel-type MCr_2O_4 (M = Co, Ni, Zn, Mn) catalysts with highly enhanced catalytic performance for soot combustion. *Catal. Sci. Technol.*, **5** (9), 4594–4601.

108. Fino, D., Russo, N., Saracco, G., and Specchia, V. (2006) Catalytic removal of NO_x and diesel soot over nanostructured spinel-type oxides. *J. Catal.*, **242** (1), 38–47.

109. Zawadzki, M., Walerczyk, W., López-Suárez, F.E., et al. (2011) $CoAl_2O_4$ spinel catalyst for soot combustion with NO_x/O_2. *Catal. Commun.*, **12** (13), 1238–1241.

Capítulo 2. Resultados

"Un científico en su laboratorio no es un simple técnico: también es un niño que se enfrenta a fenómenos naturales que lo impresionan como si fueran cuentos de hadas."

Marie Curie

Artículo 1

2D particles forming a nanostructured shell: A step forward cool NIR reflectivity for $CoAl_2O_4$ pigments

C.M. Álvarez-Docio, J.J. Reinosa, A. del Campo, J.F. Fernández.

Dyes and Pigments, 137, 2017, 1-11.

Factor de impacto: 3.767 (según JCR Edition Science 2017).

Dyes and Pigments 137 (2017) 1–11

Contents lists available at ScienceDirect

Dyes and Pigments

journal homepage: www.elsevier.com/locate/dyepig

2D particles forming a nanostructured shell: A step forward cool NIR reflectivity for $CoAl_2O_4$ pigments

C.M. Álvarez-Docio*, J.J. Reinosa, A. del Campo, J.F. Fernández

Instituto de Cerámica y Vidrio, CSIC, C/Kelsen 5, 28049, Madrid, Spain

ARTICLE INFO

Article history:
Received 13 July 2016
Received in revised form
19 September 2016
Accepted 29 September 2016
Available online 30 September 2016

Keywords:
$CoAl_2O_4$ spinel
Dry dispersion
Core-shell
Infra red reflection
Cool colored coatings

ABSTRACT

Blue $CoAl_2O_4$ are inorganic pigments with impressive optical effects and a high chemical stability. However, this spinel type structure has two main drawbacks: cobalt is scarce and expensive, and the dark pigment absorbs the solar spectra resulting in undesirable heating. In this work a new type of cool NIR blue pigment is attained by in-situ forming of a shell of 2D $CoAl_2O_4$ nanoparticles on α-Al_2O_3 microparticles. Nanodispersion of Co_3O_4 nanoparticles on the surface of α-Al_2O_3 microparticles has been carried out by means of a low energy dry mixing method and further in-situ thermal treatment at 1200 °C forms a nanostructured shell. $CoAl_2O_4$ nanocrystals are controlled in size by the frequency site of the previously dispersed Co_3O_4 nanoparticles. 2D particles form to fill the distance between Co_3O_4 nanoparticles on the alumina surface. The new shell structure makes it possible to obtain a high efficient NIR pigment with a solar reflectance SR>70% and a large cobalt content reduction. A sample containing only 10 wt% of cobalt shows similar chromatic coordinates to standard bulk pigments, which means a significant saving of raw materials.

1. Introduction

The use of pigments is highly prevalent in today's society. The application fields cover different areas such as textiles, printing, polymers, interior and exterior coatings, etc. Inorganic pigments enable high durability and colour stability under extreme conditions such as UV radiation, temperature or chemical attack. Among others, spinel-type oxides are an important family of compounds with the general formula AB_2O_4, where A and B stand for two different cations of comparable ionic sizes. The crystal lattice of the normal spinel consists of a cubic close packing of oxygen atoms and A^{2+} and B^{3+} cations occupy two different crystallographic sites, tetrahedral and octahedral, respectively [1]. Owing to their physicochemical properties and that they are a class of chemically and thermally stable materials, they are suitable for a wide range of applications of extensive use such as ceramics materials [2], magnetics [3], electronics [4], and catalysis [5].

Among spinel materials, cobalt aluminate, $CoAl_2O_4$, is widely used in several fields as a pigment because of its intense blue colour [6], which is commonly known as Thenard's blue. Today's pigments face new challenges owing to higher yields, sustainability and new functionalities. One such technology is the use of specialty infrared reflective pigments which are applied to impart colour to an object and to reflect the invisible heat from the object, in order to minimize heat build-up when the objects are exposed to solar radiation [7]. Ultimately the reflection of solar energy lowers the heat build-up resulting in a reduction on the load of the cooling system and therefore a cost saving [8]. There are currently a number of cool materials commercially available for buildings and other surfaces in the urban environment. Most of these materials are white or light-coloured [9]. However, there is a need for cool non-white products because in many cases the aesthetics of darker colours is preferred. Our cobalt aluminate is a dark pigment and has high near infrared (NIR) reflectance. Hence, by using this material we can keep the coated surface of roofs cool while enhancing the aesthetics of the built environment.

The use of nanoparticles improves the functionality of the materials; for instance, nano-pigments enhance mechanical properties such as scratch, abrasion resistance, hardness and strain-to-failure [10] or allow the use of mild temperatures in synthesis [11]. However, smaller particles as nanoparticles have higher specific surface and reactivity that could potentially cause toxic health effects through human exposure [6,12]. Therefore, the increase of the industrial use of cobalt nanoparticles has led to many recent

* Corresponding author.
E-mail address: carmenma.docio@icv.csic.es (C.M. Álvarez-Docio).

http://dx.doi.org/10.1016/j.dyepig.2016.09.061
0143-7208/

in vitro toxicological studies [13]. These studies have shown that cobalt is genotoxic [14], induces oxidative stress [15], apoptosis [16], and is a hypoxia-simulating agent [17]. Moreover, cobalt particular limitation is related to scarcity and cost. In this sense, the solution of the harmful collateral effect of nanotechnology could be addressed by using nanostructured microparticles.

In recent years, the study of core-shell composite particles has attracted increasing attention because of their potential applications, especially in the biomedical [18] and electronics fields [19]. The resulting composite particles often combine large particles with nanoparticles; for example, silica and metal nanoparticles have been applied widely for the development of various core-shell materials [20]. Complex pigments obtained through chemical routes consist of a core rutile TiO_2 and a spinel $CoAl_2O_4$ shell that exhibit good colour properties with enhanced NIR reflectance [21] but still have a limited Al^{3+} to Co^{2+} ratio of 3 as standard spinel [22]. Several techniques have been demonstrated for depositing metal nanoparticles onto inorganic cores, including seed methods [23], thermal evaporation techniques [24], self-assembly methods [25], electroless plating [26], and sol-gel methods [27]. However, these approaches are really expensive and almost always result in non-uniform or low particle densities in the shell area.

Previous studies have shown a methodology to effectively disperse Co_3O_4 nanoparticles onto α-Al_2O_3 microparticles by using a dry dispersion process [28,29]. Nanoparticle dispersion and anchoring effects occur at room temperature through an electrochemical reaction between these materials due to the high initial reactivity of the Co_3O_4 [30]. This procedure to de-agglomerate nanoparticles has also been applied previously in different systems [28,31,32], producing novel properties at the interfaces.

The aim of this work is to design a safety method to obtain a core-shell structure, where the shell is nanostructured. In this study, further thermal treatment of dispersed Co_3O_4 nanoparticles on α-Al_2O_3 microparticles provides 2D nanoparticles of $CoAl_2O_4$ spinel type. So we prepared core-shell particles by assembling a layer of 2D $CoAl_2O_4$ nanoparticles using a facile and massive method. The core-shell structure reduces notably the amount of required cobalt and minimizes its potential toxicity effects. Moreover, solar reflectivity is enhanced by achieving values higher than 70% in the NIR range with the same chromatic coordinated as standard bulk pigments. These materials represent a step forward towards designing an efficient and sustainable pigment that could act as cool pigment under solar radiation applications.

2. Experimental procedure

2.1. Nanodispersion procedure of α-Al_2O_3/Co_3O_4 mixtures and thermal treatment procedure

Compositions with 1, 5, 10, 20 and 30 wt % of Co_3O_4 nanoparticles on α-Al_2O_3 microparticles (hereafter named as 99Al1Co, 95Al5Co, 90Al10Co, 80Al20Co and 70Al30Co, respectively) were prepared by incorporating the appropriate amounts of Co_3O_4 nanoparticles by a previously described dry solid state method. The dry dispersion process consisted of shaking the materials' mixture using an acoustic-type mixer. The raw materials used in this study were 20 nm nanoparticles of cobalt oxide (Co_3O_4, Aldrich, Wadena, MN, USA) having high purity (>99.9%), forming large agglomerates of >5 μm in average diameter, and ~6.0 μm size microparticles of aluminium oxide (α-Al_2O_3, Vicar, S.A. Manises, Spain) having a purity of >99.5%. The powders were dried at 80 °C for 24 h before dry mixing. It was carried out the thermal treatments at different temperatures in the 850 °C to 1300 °C range with a heating rate of 3°C/min.

2.2. Characterization

Thermal behaviour of materials was studied by means of differential thermal (TDA) and thermogravimetric (TG) analysis using a Thermo-Analyzer Netzch STA 409 with a temperature controller Netzch TASC 414/2. It was carried out in the range 20–1300 °C with the same heating rate as in the synthesis process (3°C/min).

UV-Vis diffuse reflectance spectra of the samples were recorded using a Perkin Elmer Lambda 650 UV-Vis spectrophotometer with an integrated sphere attachment. The Kubelka-Munk function was used to transform the results from diffuse reflectance to absorbance. The points were measured every 2 nm each second. The solar reflectance (*SR*) in the wavelength range from 700 to 2500 nm was calculated according to ASTM standard number E891-87, where the reflectivity spectrum is integrated with the considered spectra of solar irradiance AM1GH in accordance with the formula:

$$SR = \frac{\int_{700}^{2500} r_\lambda i_\lambda \mathrm{d}\lambda}{\int_{700}^{2500} i_\lambda \mathrm{d}\lambda}$$

where r_λ is the experimentally obtained spectral reflectance ($W°m^{-2}$) and i_λ is the solar spectral irradiance ($W°m^{-2}°nm^{-1}$).

In order to assure the optical properties of the prepared pigments, the CIE-L*a*b* colour measurements were also performed using a spectrophotometer (Konica Minolta CM 2600d/2500d) in the 300–800 nm range. This method used the reflectance data in the visible region to obtain the three relevant parameters, L*a*b*, indicating the brightness, red-green, and yellow-blue hue intensities, respectively. The parameter C^* (chroma) represents the saturation of the colour and is defined as $C^* = \sqrt{(a^*)^2 + (b^*)^2}$. For comparison purposes a commercial blue pigment of $CoAl_2O_4$ composition (Manuel Riesgo) has been evaluated and used as reference.

For the study of the morphology and the corrected dispersion of the nanoparticles over the microparticles, the new micro-nano composite was observed by using a Field Emission Scanning Electronic Microscope, FESEM, S-4700 from Hitachi. In addition, the nanostructure was studied by atomic force microscope, AFM, in non-contact mode with a WITec 300 microscope.

The Raman study was carried out with the use of a confocal micro-Raman coupled with the AFM (Witec alpha – 300R, Witec, Ulm, Germany). Raman spectra were obtained using a micro-Raman system with a 532 nm excitation laser and a 100× objective lens (NA = 0.9). The incident laser power was 5 mW for the samples and 0.5 mW for the $CoAl_2O_4$ pigment used as reference. The system allows studying of the same area of the sample by selecting the adequate objective of the microscope. Samples were deposited on a microscopy glass slice. Collected spectra were analyzed by using Witec Control Plus Software (Witec, Ulm, Germany).

3. Results and discussion

3.1. Morphology of the nanodispersed α-Al_2O_3/Co_3O_4 mixtures

The morphology of a mixture of α-Al_2O_3 with 5 wt % of Co_3O_4 nanoparticles (95Al5Co sample) is shown in Fig. 1. Fig. 1a shows the α-Al_2O_3 morphology consisting mainly of plate type particles characteristic of this material, due to crystal growth in the ab plane. The Co_3O_4 nanoparticles are intuited on the α-Al_2O_3 microparticles surface. Fig. 1b shows dispersed Co_3O_4 nanoparticles having diameters of 10–30 nm. The nanoparticles form agglomerates of

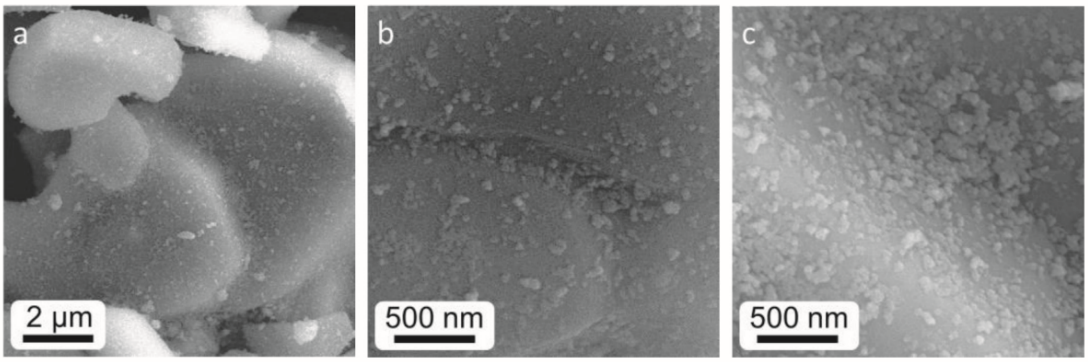

Fig. 1. FESEM micrographs of Co_3O_4 nanoparticles dispersed on α-Al_2O_3 microparticles. a) and b) 95Al5Co and c) 90Al10Co.

several tens of nanometers as the Co_3O_4 amount increases, as shown in Fig. 1c (90Al10Co sample).

The micrographs show that former Co_3O_4 agglomerates disappear and individual nanoparticles are adhered to the α-Al_2O_3 surface (Fig. 1b). For Co_3O_4 contents <10 wt % nanoparticles are completely dispersed over the surface of the α-Al_2O_3 particles, whereas for higher Co_3O_4 contents nanoparticle agglomerates started to appear (Fig. 1c). This means that there is a "saturation amount" of Co_3O_4 nanoparticles. In all of the samples there is an alumina surface that is free of nanoparticles. The higher the amount of Co_3O_4 the lower the alumina surface is.

3.2. Thermal evolution of mixtures

In order to evaluate the thermal evolution of the different samples, DTA/Tg curves of the mixtures and of Co_3O_4 as a raw material are shown in Fig. 2. The temperature range of 600–1300 °C is selected to show relevant changes. In a first approach, an endothermic reaction with a mass loss of the cobalt (II) (III) oxide occurs at ca. 930 °C. The mass losses correspond to the oxygen release to produce CoO [33]. By comparison of the mass losses in the mixture with the pure Co_3O_4, higher temperatures are required to complete the mass loss that indicates a plausible stabilization of the nanoparticles. However, the differences in scale mass losses could mask this effect. In a second approach, the DTA shows a more relevant change with the cobalt amount (details shown in Fig. 2g). Both the peak shape and the temperatures at which the reaction takes place depend on the Co_3O_4 amount. Pure Co_3O_4 (Fig. 2f) shows an asymmetric endothermic peak (peak marked as 4′) with an onset at 900 °C and extents up to 955 °C. Peak asymmetry is attributed to the high agglomeration state of pure nanoparticles. In these agglomerates, external nanoparticles are preferentially exposed to both atmosphere and temperature; meanwhile the oxygen diffusion is more difficult through the nanoparticles into the agglomerate. Hence, inner cobalt nanoparticles into the agglomerate require a longer time and a higher temperature to complete the reduction process than the external ones. As the amount of Co_3O_4 decreases, the endothermic peak content occurs at a lower temperature (peak marked as 4) and the process takes place in a short range of temperatures with a higher onset temperature. This effect is in agreement with the large agglomerate size reduction due the attrition effect of the α-Al_2O_3 microparticles during the dry dispersion. Down to 10 wt % of Co_3O_4 the endothermic peak splits into two peaks (marked as 1 and 2) that are related to the appearance of cobalt nanoparticles in contact with the alumina surface and small agglomerates.

Co_3O_4 nanoparticles anchored on α-Al_2O_3 microparticles are partially reduced due to the electrochemical reaction during the dry dispersion process, as was previously described [30]. Moreover, the Co–O bond strength slightly varies with the amount of nanoparticles in an agglomerate [29] and thereby the lower the number of nanoparticles the higher the temperature to produce the reduction. Peaks 1 and 2 are also present in the DTA/Tg curves of 80Al20Co and 70Al30Co samples, but the high presence of Co_3O_4 agglomerates limited their resolution.

At higher temperatures than the exothermic peak region, a trend of the DTA base line to increase as an indication of the mass transport processes. There is an inflexion at ~1017 °C for mixture samples (marked as 3) that can be attributed to the spinel $CoAl_2O_4$ formation according to the reaction:

$$Al_2O_3 + CoO \rightarrow CoAl_2O_4$$

As the reaction occurs in solid state regime, it is expected that the active Co-cations enter into the more stable alumina crystal lattice and the diffusion mechanism controls this reaction [34]. It is worth mentioning that the lower the amount of nanoparticles the higher the energy increase in terms of μV after the inflexion point marked as 3. This fact could be associated with low site presence of former cobalt nanoparticles at the surface and indicates a large requirement of heat absorption for low cobalt content. A further inflexion point is observable at ca. 1060 °C that is present in all the samples including the pure Co_3O_4. At this temperature coarsening of cobalt nanoparticles is expected as the mass transport mechanism responsible for increasing of the ATD base line in this system. This indicates that in addition to the spinel reaction at ~1017 °C, there is a residual amount of CoO during the non-isothermal treatment.

To sum up, according to the thermal measurements performed in the mixtures, two different behaviours took place due to the elimination of oxygen from the Co_3O_4 reduction: lower temperature (914 °C) for isolated Co_3O_4 nanoparticles on α-Al_2O_3 microparticles and higher temperatures (927 °C) from Co_3O_4 agglomerates. These differences on the Co_3O_4 distribution will cause differences in the spinel reaction pathway.

In order to evaluate the effect of the iso-thermal treatment on the phases evolution, the mixture of α-Al_2O_3 with 10 wt % of Co_3O_4 were thermally treated at 850, 1000, 1100, 1200 and 1300 °C for 1 h. The identification of crystalline phases by XRD is shown in Fig. 3a. The XRD diffractograms are normalized to the (104) crystallographic plane of α-Al_2O_3 at $2\theta \approx 35°$. No evidence of metallic Co, CoO or any additional phases different to α-Al_2O_3, Co_3O_4 or $CoAl_2O_4$ are found at any temperature within the XRD resolution limit. The expected reaction between Co_3O_4 and α-Al_2O_3 is the formation of a $CoAl_2O_4$ spinel-type solid solution. However this phase is isostructural with Co_3O_4, both of them present a space group Fd3m

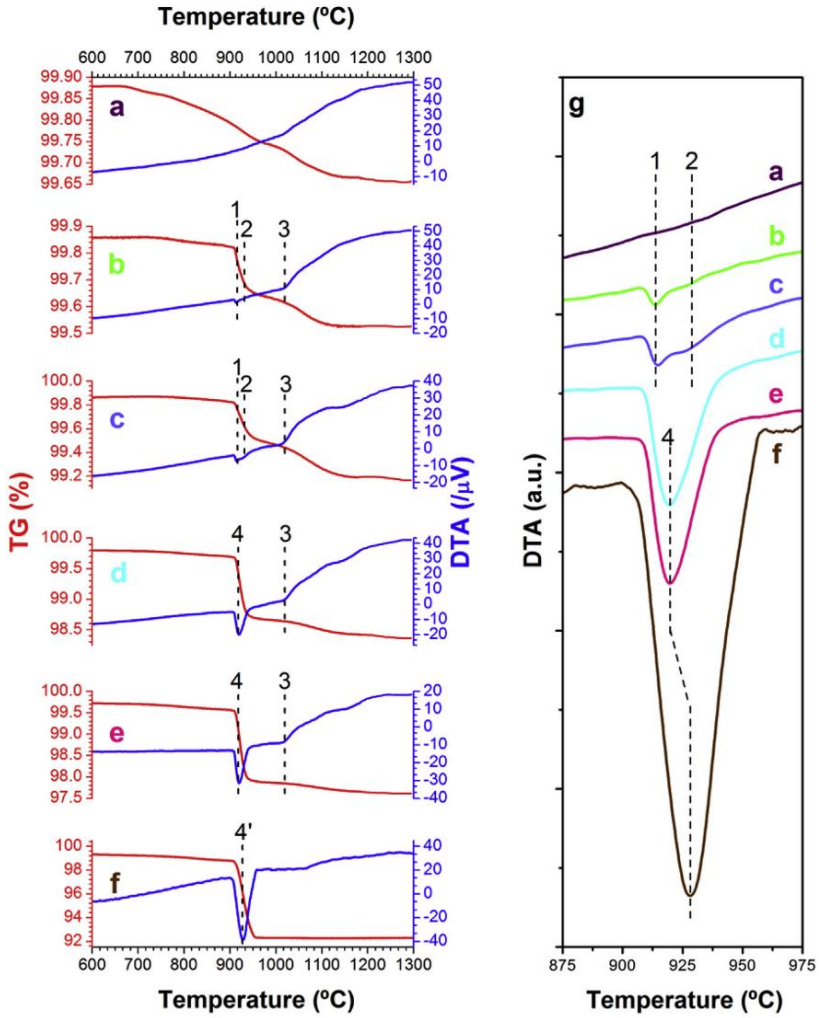

Fig. 2. DTA/Tg curves up to 1200 °C at a 3ºC/min rate of the precursor mixtures: a) 99Al1Co, b) 95Al5Co, c) 90Al10Co, d) 80Al20Co, e) 70Al30Co and f) reference Co_3O_4. (g) Detail of the endothermic signal in DTA curve for samples with different Co_3O_4 amounts. The numbers next to the peaks represent different endothermic and/or exothermic processes which occurred during the thermal analysis of the mixtures.

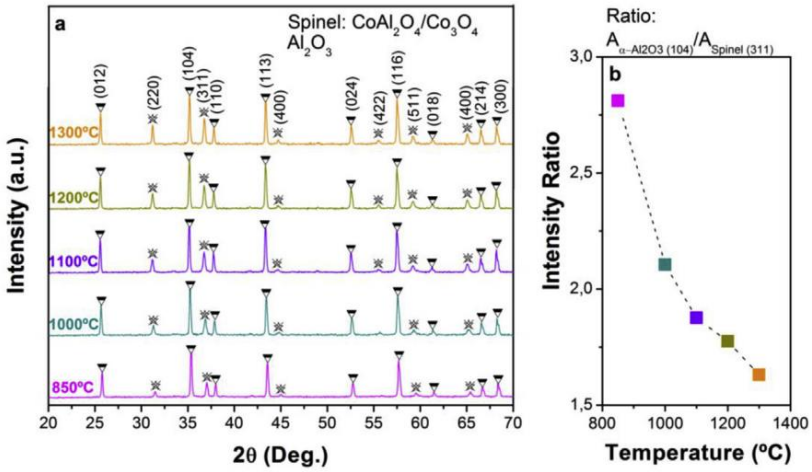

Fig. 3. a) XRD patterns corresponding to the mixture of 90Al10Co iso-thermally treated at different temperatures (850-1300 °C). b) Ratio between the (104) peak area corresponding to α-Al_2O_3 phase and the (311) peak area corresponding to the spinel phase.

symmetry [22], and therefore X-ray diffraction patterns fail to determine whether the $CoAl_2O_4$ spinel forms.

The area of the (104) peak corresponding to the α-Al_2O_3 phase is then compared with the area of the signal at $2\theta \approx 37°$ corresponding to the (311) peak of the spinel phase (Fig. 3b). The ratio between the areas of both peaks decreases significantly when the temperature increases, as an indication of the spinel reaction is favoured at a higher temperature. For every 3 mol of $CoAl_2O_4$ formed, 1 mol of Co_3O_4 is reduced, so the spinel amount should increase due to the reaction stoichiometry and this fact is verified by XRD. For all temperatures, the presence of alumina in the sample is joined to the presence of spinel phase. This experimental evidence is in concordance with the reaction processes described by DTA points and is related to the possibility of a core-shell formation.

3.3. Optical response of synthesized pigments

Fig. 4a shows ultraviolet–visible spectra for pigments having 90Al10Co synthesized at different temperatures (changes in colour for 90Al10Co sample as a function of the iso-thermal treatment temperature are appreciable in Fig. 4b). The pigments synthesized at temperatures <1000 °C show a green colour and pigments synthesized >1000 °C show blue. The blue colour is described to be due to Co^{2+} in tetrahedral sites, while the green colour is observed for Co^{3+} in octahedral coordination. In order to determine the temperature at which the cobalt aluminate formation takes place the presence of the species Co^{2+} and Co^{3+} allow for the phase development.

The products treated at lower temperatures ($T \leq 1000$ °C) progress with the increase of temperature. The sample treated at 850 °C is dark green and it has two wide bands, one at 800-580 nm and the other at 580–250 nm. Both bands are related to charge transfer (CT) process [35]. The band at 800–580 nm is a ligand to metal charge transfer (LMCT) band, which is assigned to the electron transference from O^{2-} to Co^{3+} in octahedral position. The band at higher energy (580–250 nm) is another ligand to metal charge transfer (LMCT) band related to the electron transference from O^{2-} to Co^{2+} in tetrahedral position. The spectrum of sample at 850 °C is similar to the Co_3O_4 one [36] and no reaction took place, in agreement with DTA/Tg analysis. The pigment treated at 1000 °C presents more Co^{2+} because of the reduction reaction at 914 °C. The wide band at 800–580 nm splits into several bands because of the d-d transitions of Co^{2+} in tetrahedral position. In addition, a wide band appears nearly 720 nm related to the Co^{3+} in octahedral sites.

The spectra of the samples iso-thermally treated at temperatures of ≥1100 °C are similar between them. In addition they are similar to the $CoAl_2O_4$ spectrum [37]. These spectra are composed of bands corresponding to the allowed transitions of Co^{2+} electrons at $3d^7$ orbitals in a tetrahedral coordination, $^4A_2$ (F) → $^4T_1$ (P). These transitions correspond to the bands at 554, 584 and 622 nm [35]. The blue colour is due to the absorption of light at this range. The higher the synthesis temperature, the stronger the blue colour the sample presents. It suggests that a higher amount of Co^{2+} at tetrahedral positions is observed when temperature increases and so more spinel is formed with temperature [38]. This is in agreement with XRD results and confirms the coexistence of $CoAl_2O_4$ and α-Al_2O_3 but the core-shell formation required further proofs. Two bands at 480 and 408 nm are also observed which are assigned to

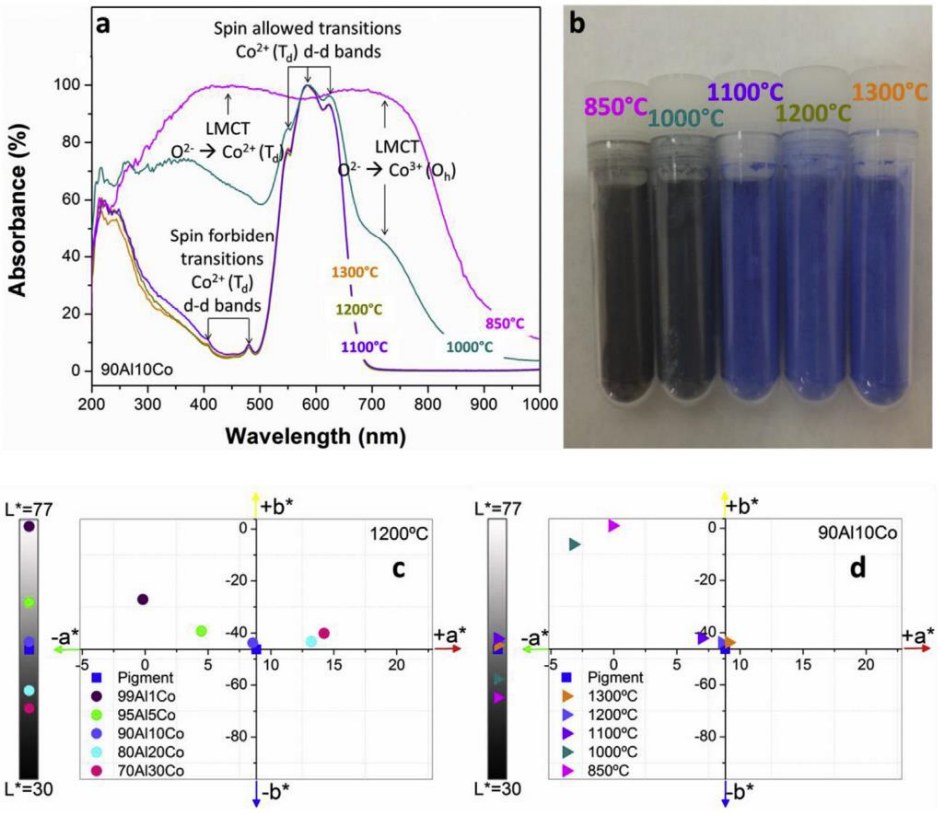

Fig. 4. a) UV-Visible spectra of 90Al10Co mixture iso-thermally treated at different temperatures. b) Representative image of 90Al10Co pigments synthesized at different temperatures. c) CIE-L*a*b* coordinates of 90Al10Co pigments iso-thermally treated at different temperatures. d) CIE-L*a*b* colorimetric coordinates of different cobalt content compositions. A reference cobalt aluminate commercial pigment is used as reference for the colorimetric coordinates.

the forbidden spin transitions d-d of Co^{2+} in tetrahedral positions $^4A_2$ (F) → ^2T (G) [22,35,37]. For this reason, the intensities of both bands are low in comparison with the rest of bands.

UV-Vis spectroscopy determines the optimum temperature for the synthesis of the $CoAl_2O_4$ spinel. The pigment treated at 1100 °C for 1 h shows similar behaviour to a reference stoichiometric pigment (not included in the graph for the sake of clarity), although the band associated with metal charge transfer (LMCT) related to the electron transference from O^{2-} to Co^{2+} in tetrahedral position is still appreciated. In addition, the pigment treated at 1300 °C for 1 h shows similar behaviour to the pigment treated at 1200 °C. So taking into account these results, 1200 °C seems to be the more suitable temperature for the synthesis of $CoAl_2O_4$ spinel by a solid-state reaction.

In Fig. 4c, it is compared the CIE-L*a*b* colorimetric study of 90Al10Co pigments treated at different temperatures and a commercial $CoAl_2O_4$ blue pigment used as reference, in the centre of the colorimetric. Two trends are clearly differentiated by colour: samples treated at 850 and 1000 °C whose colour coordinates tend to green and yellow, and present more darkness; whereas, the colour coordinates of the samples thermally treated at ≥1100 °C are quite close to the reference spinel. In fact, 1200 °C and 1300 °C seem to be the most similar samples although only less than 23% of the cobalt amount necessary to form the cobalt aluminate phase (the stoichiometric cobalt aluminate required an equivalent content of 44 wt % of Co_3O_4) has been used. According to the UV-Vis spectroscopy results, it was chosen 1200 °C as optimum temperature for the synthesis of this compound. Owing to the possibility to transfer this technical to the industry, 100 °C of difference involves a considerably energy saving. Moreover, the blue colour is an indication that the spinel formation occurs at the surface of the alumina microparticles and thereby a core-shell is developed. The chroma value C* that represents the richness of the colour hue is very high for the 90Al10Co pigment, with a value of 44.3 that does not change remarkable respect to the reference pigment with a value of 47.7. The chroma value is considerably high if compared with other chroma values obtained in $CoAl_2O_4$ nanopigments 35.2 [39] or even with the large values of recent new blue nanopigments such as $Yin_{0.9}Mn_{0.1}O_3$–ZnO that reaches a chroma value of 42.2 [40]. An evolution of CIE-L*a*b* coordinates is observed in the colorimetric diagram of pigments treated at 1200 °C for 1 h with cobalt amounts, Fig. 4d. In spite of the higher cobalt content the 90Al10Co pigment is still the most similar to the reference pigment. The samples synthesized with <10 wt % of cobalt nanoparticles increase b* coordinate and reduce a* coordinate in addition to large increases of whitening, as the cobalt amount decreases. The reduction of cobalt amount accounts for a reduced reaction with alumina and thus the alumina contributed to the colour response. Nevertheless, samples synthesized with >10 wt % of nanoparticles increase the b* coordinate and show a tendency towards higher darkness as the cobalt amount increases. The presence of nanoparticle agglomerates in the precursor seems to limit the development of the cobalt aluminate.

To sum up, a complete formation of the cobalt aluminate has been stated for pigment with <23 wt % content of cobalt oxide than the stoichiometric counterpart. The colorimetric analysis showed that a highly rich blue chroma is achieved for this pigment that accounts for a core-shell formation in which the cobalt aluminate forms the shell. The pigment is obtained from the thermal treatment of dispersed Co_3O_4 nanoparticles on the surface of alumina microparticles. As the precursor showed alumina surface free of cobalt nanoparticles, the formation of a cobalt aluminate shell requires high mobility of cobalt cations along the alumina surface. Hence an in-depth study on the microstructure of the new pigment is required.

3.4. Shell structure and microstructure

In order to determine the structure of the spinel phase a Confocal Raman Microscopy analysis is attempted. Fig. 5a shows an Optical Microscopy micrograph of a single particle of 90Al10Co composition treated at 1200 °C for 1 h. The same observed area serves to generate a Raman image of the surface (Fig. 5b).

Fig. 5c shows the Raman spectrum which corresponds to the 90Al10Co pigment and for comparison purposes the Raman spectra of α-Al_2O_3 and $CoAl_2O_4$ particles as references. Concerning α-Al_2O_3,

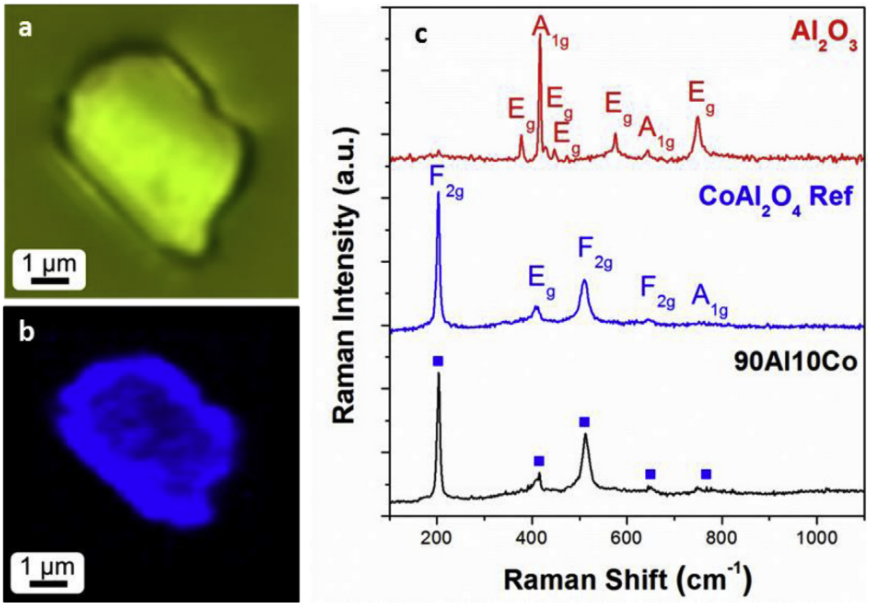

Fig. 5. Confocal Raman Microscopy of an isolated single pigment particle 90Al10Co synthesized at 1200 °C for 1 h: a) Optical microscopy micrograph. b) Raman image in which colour intensity evidences Raman intensity of the main F2g Mode for $CoAl_2O_4$ phase (c) Raman spectra of 90Al10Co pigment and Raman spectra of α-Al_2O_3 and $CoAl_2O_4$ references.

it has been reported that α-Al_2O_3 (corundum) is based on D^6_{3d} symmetry with seven Raman-active phonon modes, $2A_{1g} + 5E_g$, at 378, 418, 429, 448, 576, 645, and 750 cm^{-1} [41]. $CoAl_2O_4$ pigment used as reference has a spinel structure and, considering that spinel structure belongs to the Fd3m (O^7_h) space group, it exhibits five Raman active modes: A_{1g} (764 cm^{-1}); F_{2g} (644, 511 and 203 cm^{-1}) and E_g (413 cm^{-1}) [42]. The main phase identified by Raman in the 90Al10Co sample is the spinel $CoAl_2O_4$ (signalled in blue colour). This sample also exhibits the five expected Raman active modes which correspond to $CoAl_2O_4$ in this spectral range: A_{1g} (775 cm^{-1}); F_{2g} (646, 513 and 204 cm^{-1}) and E_g (417 cm^{-1}). All modes exhibit a blue-shift compared to the reference pigment, this fact indicates that the constant force is higher and could attribute to crystal stress in the spinel particles. This effect cannot be attributed to differences in heating by the incident laser because for the 90Al10Co sample the laser power was 5 mW, whereas for the pigment used as reference the laser power was 0.5 mW. The difference in laser power is due to the efficiency in power dissipation of heat from the sample 90Al10Co, possibly through the core-shell structure. Moreover, a higher laser power could heat the sample more and as a result a red-shift would occur, which has not been the case. There is even a small controversy between the coefficients of thermal expansion, CTE. In the literature data, the CTE of alumina is slightly higher (9.09×10^{-6} K^{-1}) [43], than the CTE of $CoAl_2O_4$ (8.7×10^{-6} K^{-1}) [44]. This difference could contribute to the compression stress of the supported 2D spinel particles as indicated by the Raman blue-shift.

The Raman intensity of the spinel is higher at the edges of the particles. This fact could be associated to the evanescent field which was concentrated there. The Raman intensity of the α-Al_2O_3 phase is rather lower than the Raman intensity of the spinel phase so the presence of alumina is difficult to determine. It is worth remarking that the laser spot has ca. 500 nm in diameter and 700 nm in depth. As the average thickness of pigment particles is 1 μm the laser spot should cover the alumina core. However the presence of a cobalt aluminate shell absorbs effectively the 534 nm laser as stated from the absorbance UV-Vis spectra.

Fig. 6a shows the FESEM micrographs of the 90Al10Co sample which was treated at 1200 °C. FESEM micrographs illustrate the presence of 2D surface crystallizations having different morphologies that cover the whole α-Al_2O_3 surface (Fig. 6b). A high proportion of these nanocrystals have a triangular shape and present strikingly flat surfaces with low thickness and straight edges, as shown in Fig. 6c. Additionally, Fig. 6d reveals other features of 2D particles, which present a triangular hole in the middle. Several irregular particles could also be seen in which the triangular shaped crystallizations are restricted and resemble an earlier stage of the sintering between former cobalt oxide nanoparticles. These irregular particles are more protruded from the alumina surface than the triangular ones. The surface has particles with different heights and spinel crystallization seems to extend the covering beyond the sites in which former Co_3O_4 nanoparticles are initially anchored. However the FESEM micrographs fail in resolution to determine if the alumina surface is completely covered by the cobalt aluminate particles.

The surface of the particles is studied by Atomic Force Microscopy, Fig. 7. The first observation is that the whole surface of the microparticle is covered by nanocrystals (Fig. 7a). Specifically, well-defined triangular particles and irregular small nanoparticles form a continuous shell over the α-Al_2O_3 surface. The roughness profiles from AFM of selected regions (Fig. 7b–d) confirms that the highly protruded regions are <50 nm, and correspond to former small agglomerates of Co_3O_4. The triangular shaped particles present a flat surface with a height down the 15 nm (see point 2 and 3 in Fig. 7c). Initial Co_3O_4 presents a particle size ranging between 10 and 30 nm and this value is in accordance with the height of the AFM profile in which protruded regions lie down the two former nanoparticle heights. The triangular shaped flat particle implies a surface diffusion of cobalt cations to react with the other layer of alumina. The effective formation of a shell is based on a correct dispersion of Co_3O_4 nanoparticles and the 10 wt % is the optimal amount to obtain a corrected yield for the formation of a $CoAl_2O_4$ shell in α-Al_2O_3 microparticles.

3.5. Schematic diagram of the shell formation mechanism

In order to propose a mechanism about the formation of a 2D shell, a schematic model has been developed and represented in

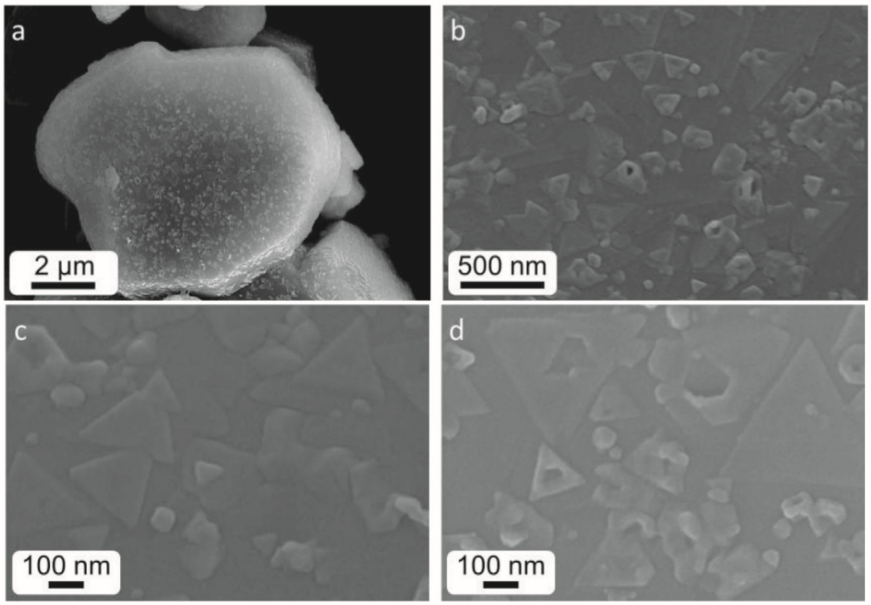

Fig. 6. FESEM of the 90Al10Co pigment treated at 1200 °C: a) general view of 90Al10Co in order to show that the coating is complete, b) enlarged general view of 90Al10Co sample with triangular nanoparticles, c) detail of triangular shaped 2D particles, and d) detail of surface coalescence which shows 2D structures with a hole in the middle.

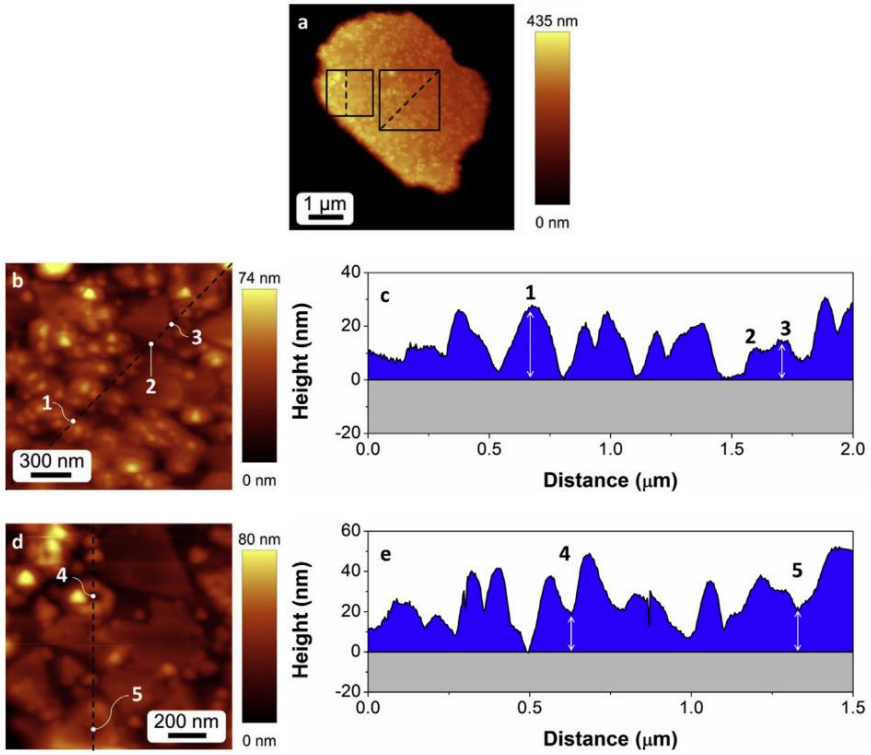

Fig. 7. Atomic force microscopy images of 90Al10Co sample (a), detail of 90Al10Co sample (b, d) and roughness (c, e).

Fig. 8. The results of the previous observations have been taken into account and are depicted on the scheme.

The dry dispersion procedure provides Co_3O_4 nanoparticles anchored to the α-Al_2O_3 surfaces. Isolated nanoparticles and small agglomerates are observed in conjunction with uncovered alumina spaces for the optimum amount of 10 wt % of Co_3O_4. The small agglomerates consist of a few nanoparticles that do not protrude in excess from the alumina surface. On the other hand, FESEM images show that there is a "saturation amount" of Co_3O_4; so Co_3O_4 nanoparticles can be effectively dispersed over α-Al_2O_3

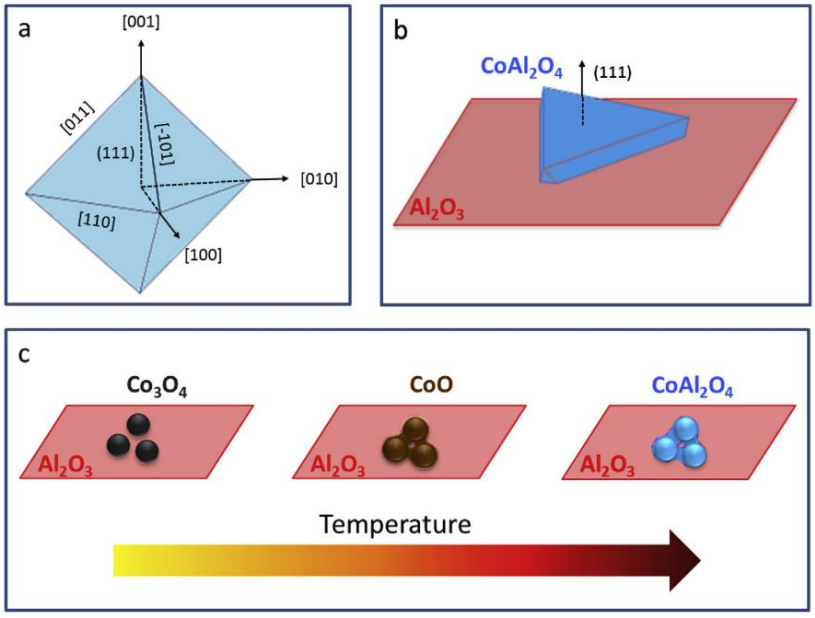

Fig. 8. a) Schematic of the lowest energy surfaces of the $CoAl_2O_4$ crystal. b) Schematic of morphology of the $CoAl_2O_4$ triangular shaped particles on α-Al_2O_3 surface. c) Schematic evolution of the cobalt nanoparticles coalescence before the spinel formation.

microparticles before a large presence of agglomerates. Definitively, two different scenarios of dispersion exist: well dispersed isolated nanoparticles and agglomerates with different nanoparticle content. The larger the amount of cobalt nanoparticles is, the larger the number of agglomerates there are and as a consequence their size increases. Regarding the DTA/Tg analysis, it was stated that the well-dispersed nanoparticles produce higher heat during the spinel formation than the agglomerated nanoparticles. This amount of heat is considerably higher if it is taken into account that the amount of well-dispersed nanoparticles is limited by the available alumina surface sites. In addition, the agglomerates show a trend to stabilize the CoO and therefore there is a competition between the spinel formation and the sintering of CoO nanoparticles. Consequently two different crystallization pathways could occur during the thermal treatment. It has been reported that the spinel crystal prefers to form an octahedron with eight (111) surfaces, as shown in Fig. 8a, because of the lower energy at these planes [45]. Depending on the octahedron orientation the structure seems to be different. For instance, the triangle shaped particles correspond to a 111-oriented octahedron [46,47], Fig. 8b. The formation of 2D particles as flat shaped triangles corresponds to the isolated nanoparticles on the alumina surface. The spinel crystallization requires the mass transportation by surface diffusion of cobalt cations according to their epitaxial relationship with the substrate. This mechanism is possible because to form spinels from oxides a non-equilibrium interdiffusion is always involved during the reactions [48]. In this case, the in-diffusion of the shell material is faster than the out-diffusion of the core material, so the particle growth following the alumina surface in one of the facile spinel orientations.

Appearances of void between different triangular shaped particles during growing (Fig. 8c) represent evidence of such a surface diffusion to form 2D particles on the alumina surface. The reason is that cobalt nanoparticle agglomerates allow the mass transport to form sintering necks and then to coalesce in larger particles. It is worth noting that surface diffusion to form the sintering neck does not imply crystal reorientation and therefore the large particles possess different crystal orientations. Afterwards, the spinel reaction takes place and the existence of different crystal orientations with lower surface energy than the former nanoparticles limits the spinel reaction mechanism. Holes inside these particles are an indication that the spinel formation slows the sintering process between the cobalt nanoparticles. The appearance of agglomerates is thus a limitation of the formation of planar 2D particles.

Whatever the mechanism of crystallization of $CoAl_2O_4$ from Co_3O_4 nanoparticles at the surface of α-Al_2O_3 microparticles was, a core-shell is formed. These core-shell particles are composed by a core of α-Al_2O_3 and a shell of $CoAl_2O_4$ nanocrystallizations.

3.6. *Effective solar reflectivity of 2D shell pigments*

Cool pigments is one of the most challenging topics to counteract urban heat island [49,50]. The core-shell concept having 2D particles here developed produces a high chroma value of the blue colour in the visible region of the electromagnetic spectrum. However, 52% of the irradiance of the solar energy lies in the near infrared region (700–2500 nm) [51]. On other hand, NIR irradiance penetration is deeper than visible irradiance, so the effectiveness of the shell in visible response could be combined with the good NIR reflection of the alumina core.

Fig. 9 shows the NIR response of 2D shell pigments with different cobalt content. Both the R^* (Reflectance) and the SR (Solar Reflectance) enhanced >40% and >10%, respectively, in the 90Al10Co pigment by comparison with the commercial. The obtained values for $R^* = 77\%$ are quite large when compared with current literature data in cool NIR pigment for $CoAl_2O_4$ as 47% [39] or new compositions that reach 67% [40]. It is worth mentioning that the commercial pigment that we use as standard possesses a

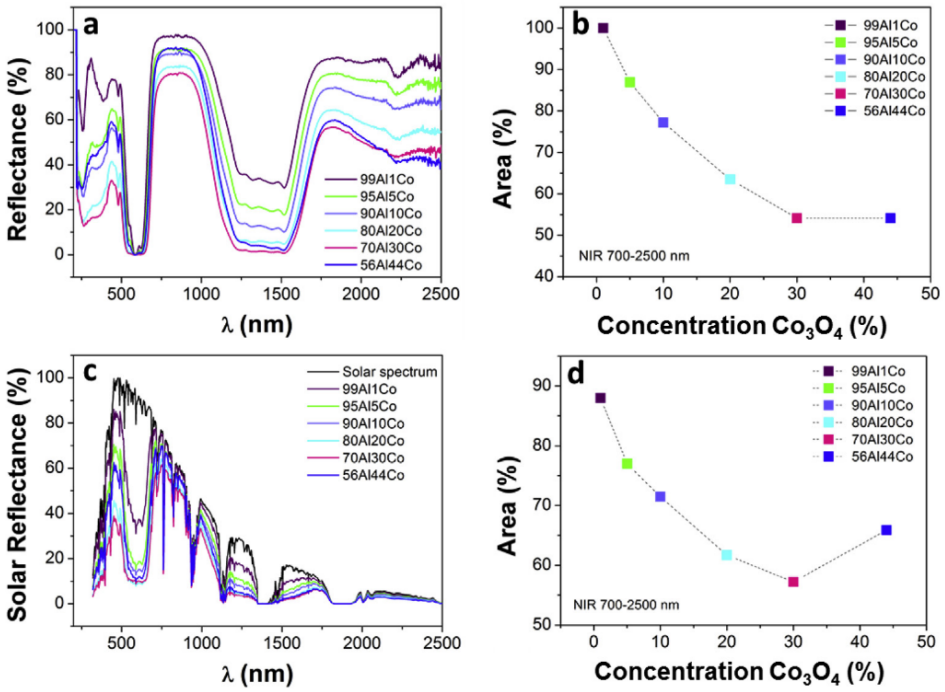

Fig. 9. NIR response of 2D shell pigments with different cobalt content: a) UV-VIS NIR reflectance. b) R* in the spectral range 700–2500 nm c) Solar reflectance spectra. d) SR in the spectral range 700–2500 nm. The representation of R* and SR is considered versus the formulated Co_3O_4 wt. % amount. The commercial pigment used as reference corresponds to an equivalent 44 wt % of Co_3O_4.

large R* of 55%, in addition to their colour yield, that corresponds to an optimized industrial pigment. In terms of SR, the values of the 2D shell composition are 72%, again superior to the commercial pigment. The advantage of the core-shell pigment is related to the effectiveness of the 2D particles that reach high crystallinity due to their surface growth mechanism. The presence of protruded spinel nanocrystals originated in agglomerates of formed Co_3O_4 limited in that sense the effectiveness and a more refined procedure to maximize the planar particle represents a challenge for core-shell pigments.

To sum up, we have obtained a $CoAl_2O_4$ blue pigment, using less amount of cobalt oxide (10 wt %) than the amount required to form the stoichiometric cobalt aluminate (44 wt %). This is due to the formation of a core-shell structure consisting of a 2D $CoAl_2O_4$ nanoparticles shell over a α-Al_2O_3 core. The mentioned structure allows improving the yield of the colour generated by the pigment despite the cobalt oxide decrease. In addition, the results revealed that the formation of the composite Al_2O_3–$CoAl_2O_4$ not only reduced the cost but also increased near-infrared solar reflectance ($R^* > 77\%$) with respect to the conventional pigments ($R^* > 47$–67%). These facts express the potential of the $CoAl_2O_4$ core-shell pigment to be employed in cool coatings and opens new study fields.

4. Conclusions

An effective dry dispersion method was used to obtain Co_3O_4 nanoparticles dispersed over α-Al_2O_3 microparticles. Co_3O_4 isolated nanoparticles and agglomerates are deposited on the α-Al_2O_3 microparticles surface. The different dispositions of Co_3O_4 promote variations at its reduction temperature because of the different ways oxygen diffuses. A correct dispersion was observed up to 10 wt % of Co_3O_4 nanoparticles and 1200 °C seems to be the more suitable temperature for the synthesis of $CoAl_2O_4$ spinel by a solid-state reaction. Hence, core-shell particles of Al_2O_3–$CoAl_2O_4$ are achieved.

Two mechanisms of 2D $CoAl_2O_4$ crystallization over an α-Al_2O_3 surface are observed: arrangement of Co_3O_4 agglomerated nanoparticles on the surface of α-Al_2O_3, and diffusion mechanism of isolated nanoparticles on the surface of α-Al_2O_3. The correct formation of the core shell was demonstrated by Raman Spectroscopy and by colorimetric and UV-Vis spectroscopy studies. The colorimetric study shows that the new core-shell pigment presents a high chroma blue value which is similar to a reference $CoAl_2O_4$ pigment. Finally, the effective solar reflectivity of the new core-shell pigment is superior to the commercial one due to the high crystallinity of the 2D $CoAl_2O_4$ because of its surface growth mechanism.

Acknowledgements

The authors express their thanks to the MINECO (Spain) project MAT2013-48009-C4-1-P for their financial support. C.M.D. is also indebted to MINECO for a Predoctoral Grant (BES-2014-069779), which is co-financed with FEDER funds.

References

[1] Sickafus KE, Wills JM, Grimes NW. Structure of spinel. J Am Ceram Soc 1999;82:3279–92. http://dx.doi.org/10.1111/j.1151-2916.1999.tb02241.x.
[2] Melo DMA, Cunha JD, Fernandes JDG, Bernardi MI, Melo MAF, Martinelli AE. Evaluation of $CoAl_2O_4$ as ceramic pigments. Mater Res Bull 2003;38:1559–64. http://dx.doi.org/10.1016/S0025-5408(03)00136-3.
[3] Gul IH, Maqsood A, Naeem M, Ashiq MN. Optical, magnetic and electrical investigation of cobalt ferrite nanoparticles synthesized by co-precipitation route. J Alloy Compd 2010;507:201–6. http://dx.doi.org/10.1016/j.jallcom.2010.07.155.
[4] Tielens F, Calatayud M, Franco R, Recio JM, Pérez-Ramírez J, Minot C. Periodic DFT study of the structural and electronic properties of bulk $CoAl_2O_4$ spinel. J Phys Chem B 2006;110:988–95. http://dx.doi.org/10.1021/jp053375l.
[5] Dandapat A, De G. Host-mediated synthesis of cobalt aluminate/γ-alumina nanoflakes: a dispersible composite pigment with high catalytic activities. ACS Appl Mater Interfaces 2012;4:228–34. http://dx.doi.org/10.1021/am201283c.
[6] Luo R, editor. Encyclopedia of color science and technology. first ed. New York: Springer Berlin Heidelberg; 2016. http://dx.doi.org/10.1007/978-3-642-27851-8.
[7] Sarasamma Vishnu V, Lakshmipathi Reddy M. Near-infrared reflecting inorganic pigments based on molybdenum and praseodymium doped yttrium cerate: synthesis, characterization and optical properties. Sol Energy Mater Sol Cells 2011;95:2685–92. http://dx.doi.org/10.1016/j.solmat.2011.05.042.
[8] Synnefa A, Santamouris M, Livada I. A study of the thermal performance of reflective coatings for the urban environment. Sol Energy 2006;80:968–81. http://dx.doi.org/10.1016/j.solener.2005.08.005.
[9] Gao Q, Wu X, Fan Y. Solar spectral optical properties of rutile TiO_2 coated mica-titania pigments. Dye Pigm 2014;109:90–5. http://dx.doi.org/10.1016/j.dyepig.2014.04.028.
[10] Perera DY. Effect of pigmentation on organic coating characteristics. Prog Org Coat 2004;50:247–62. http://dx.doi.org/10.1016/j.porgcoat.2004.03.002.
[11] Karmaoui M, Silva NJO, Amaral VS, Ibarra A, Millan A, Palacio F. Synthesis of cobalt aluminate nanopigments by a non-aqueous sol-gel route. Nanoscale 2013;5:4277–83. http://dx.doi.org/10.1039/C3NR34229H.
[12] Lewinski N, Colvin V, Drezek R. Cytotoxicity of nanoparticles. Small 2008;4:26–49. http://dx.doi.org/10.1002/smll.200700595.
[13] Sabbioni E, Fortaner S, Farina M, Del Torchio R, Olivato I, Petrarca C, et al. Cytotoxicity and morphological transforming potential of cobalt nanoparticles, microparticles and ions in Balb/3T3 mouse fibroblasts: an in vitro model. Nanotoxicology 2014;8:455–64. http://dx.doi.org/10.3109/17435390.2013.796538.
[14] De Boeck M, Kirsch-Volders M, Lison D. Cobalt and antimony: genotoxicity and carcinogenicity. Mutat Res Fund Mol Mech Mut 2003;533:135–52. http://dx.doi.org/10.1016/j.mrfmmm.2003.07.012.
[15] Salnikow K, Su W, Blagosklonny MV, Costa M. Carcinogenic metals induce hypoxia-inducible factor-stimulated transcription by reactive oxygen species-independent mechanism. Cancer Res 2000;60:3375–8. http://dx.doi.org/10.1016/j.physe.2011.04.021.
[16] Pulido MD, Parrish AR. Metal-induced apoptosis: mechanisms. Mutat Res Fund Mol Mech Mut 2003;533:227–41. http://dx.doi.org/10.1016/j.mrfmmm.2003.07.015.
[17] Bruick RK. Oxygen sensing in the hypoxic response pathway: regulation of the hypoxia-inducible transcription factor. Genes Dev 2003;17:2614–23. http://dx.doi.org/10.1101/gad.1145503.
[18] Chatterjee K, Sarkar S, Jagajjanani Rao K, Paria S. Core/shell nanoparticles in biomedical applications. Adv Colloid Interface Sci 2014;209:8–39. http://dx.doi.org/10.1016/j.cis.2013.12.008.
[19] Zhang X, Xie S, Fan Y, Wang Z, Zhang H, Zhao M. Structural and electronic properties of ZnS/ZnO heteronanotubes. Phys E Low Dimens Syst Nanostruct 2011;43:1522–7. http://dx.doi.org/10.1016/j.physe.2011.04.021.
[20] Jankiewicz BJ, Jamiola D, Choma J, Jaroniec M. Silica–metal core–shell nanostructures. Adv Colloid Interface Sci 2012;170:28–47. http://dx.doi.org/10.1016/j.cis.2011.11.002.
[21] Zheng W, Zou J. Synthesis and characterization of blue TiO_2/$CoAl_2O_4$ complex pigments with good colour and enhanced near-infrared reflectance properties. RSC Adv 2015;5:87932–9. http://dx.doi.org/10.1039/C5RA17418J.
[22] Zayat M, Levy D. Blue $CoAl_2O_4$ particles prepared by the sol-gel and citrate-gel methods. Chem Mater 2000;12:2763–9. http://dx.doi.org/10.1021/cm001061z.
[23] Hofmeister H, Miclea P-T, Mörke W. Metal nanoparticle coating of oxide nanospheres for core-shell structures. Part Part Syst Char 2002;19:359–65. http://dx.doi.org/10.1002/1521-4117(200211)19. 5<359::AID-PPSC359>3.0.CO;2-B.
[24] Chhikara D, Senthil Kumar M, Srivatsa KMK. On the synthesis of Zn/ZnO core–shell solid microspheres on quartz substrate by thermal evaporation technique. Superlattices Microstruct 2015;82:368–77. http://dx.doi.org/10.1016/j.spmi.2015.02.036.
[25] Yuan W, Yuan J, Xie J, Li CM. Polymer-mediated self-assembly of TiO_2@Cu_2O core–shell nanowire array for highly efficient photoelectrochemical water oxidation. ACS Appl Mater Interfaces 2016;8:6082–92. http://dx.doi.org/10.1021/acsami.6b00030.
[26] Uysal M, Karslioğlu R, Alp A, Akbulut H. The preparation of core-shell Al_2O_3/Ni composite powders by electroless plating. Ceram Int 2013;39:5485–93. http://dx.doi.org/10.1016/j.ceramint.2012.12.060.
[27] Milde M, Dembski S, Osvet A, Batentschuk M, Winnacker A, Sextl G. Polymer-assisted sol-gel process for the preparation of photostimulable core/shell structured SiO_2/Zn_2SiO_4:Mn^{2+} particles. Mater Chem Phys 2014;148:1055–63. http://dx.doi.org/10.1016/j.matchemphys.2014.09.017.
[28] Fernández JF., Lorite I., Rubio-Marcos F., Romero JJ., García MÁ, Quesada A, et al. Method for the dry dispersion of nanoparticles and the production of hierarchical structures and coatings, Patent Numbers WO2010010220–A1; ES2332079-A1, 2010, to Consejo Superior de Investigaciones Científicas, CSIC.
[29] Lorite I, del Campo A, Romero JJ, Fernández JF. Isolated nanoparticle Raman spectroscopy. J Raman Spectrosc 2012;43:889–94. http://dx.doi.org/10.1002/jrs.3112.

[30] Martin-González MS, García MA, Lorite I, Costa-Krämer JL, Rubio-Marcos F, Carmona N, et al. A solid-state electrochemical reaction as the origin of magnetism at oxide nanoparticle interfaces. J Electrochem Soc 2010;157:E31–5. http://dx.doi.org/10.1149/1.3272638.
[31] Rubio-Marcos F, Calvino-Casilda V, Bañares MA, Fernandez JF. Novel hierarchical Co_3O_4/ZnO mixtures by dry nanodispersion and their catalytic application in the carbonylation of glycerol. J Catal 2010;275:288–93. http://dx.doi.org/10.1016/j.jcat.2010.08.009.
[32] Rubio-Marcos F, Manzano CV, Reinosa JJ, Lorite I, Romero JJ, Fernández JF, et al. Modification of optical properties in ZnO particles by surface deposition and anchoring of NiO nanoparticles. J Alloy Compd 2011;509:2891–6. http://dx.doi.org/10.1016/j.jallcom.2010.11.149.
[33] Tomić-Tucaković B, Majstorović D, Jelić D, Mentus S. Thermogravimetric study of the kinetics of Co_3O_4 reduction by hydrogen. Thermochim Acta 2012;541:15–24. http://dx.doi.org/10.1016/j.tca.2012.04.018.
[34] Bi Z, Zhang R, Wang X, Gu S, Shen B, Shi Y, et al. Synthesis of zinc aluminate spinel film through the solid-phase reaction between zinc oxide film and α-alumina substrate. J Am Ceram Soc 2003;86:2059–62. http://dx.doi.org/10.1111/j.1151-2916.2003.tb03609.x.
[35] Taguchi M, Nakane T, Hashi K, Ohki S, Shimizu T, Sakka Y, et al. Reaction temperature variations on the crystallographic state of spinel cobalt aluminate. Dalt Trans 2013;42:7167–76. http://dx.doi.org/10.1039/C3DT32828G.
[36] Jiang C-M, Baker LR, Lucas JM, Vura-Weis J, Alivisatos AP, Leone SR. Characterization of photo-induced charge transfer and hot carrier relaxation pathways in spinel cobalt oxide (Co_3O_4). J Phys Chem C 2014;118:22774–84. http://dx.doi.org/10.1021/jp5071133.
[37] Angeletti C, Pepe F, Porta P. Structure and catalytic activity of $Co_xMg_{1-x}Al_2O_4$ spinel solid solutions. Part 1.-Cation distribution of Co^{2+} ions. J Chem Soc Faraday Trans 1977;73:1972–82. http://dx.doi.org/10.1039/F19777301972.
[38] Meyer F, Hempelmann R, Mathur S, Veith M. Microemulsion mediated sol-gel synthesis of nano-scaled MAl_2O_4 (M=Co, Ni, Cu) spinels from single-source heterobimetallic alkoxide precursors. J Mater Chem 1999;9:1755–63. http://dx.doi.org/10.1039/A900014C.
[39] Hedayati HR, Sabbagh Alvani AA, Sameie H, Salimi R, Moosakhani S, Tabatabaee F, et al. Synthesis and characterization of $Co_{1-x}Zn_xCr_{2-y}Al_yO_4$ as a near-infrared reflective color tunable nano-pigment. Dye Pigm 2015;113:588–95. http://dx.doi.org/10.1016/j.dyepig.2014.09.030.
[40] Jose S, Jayaprakash A, Laha S, Natarajan S, Nishanth KG, Reddy MLP. $YIn_{0.9}Mn_{0.1}O_3$–ZnO nano-pigment exhibiting intense blue color with impressive solar reflectance. Dye Pigm 2016;124:120–9. http://dx.doi.org/10.1016/j.dyepig.2015.09.014.
[41] Munisso MC, Zhu W, Pezzotti G. Raman tensor analysis of sapphire single crystal and its application to define crystallographic orientation in polycrystalline alumina. Phys Status Solidi B 2009;246:1893–900. http://dx.doi.org/10.1002/pssb.200945137.
[42] D'Ippolito V, Andreozzi GB, Bersani D, Lottici PP. Raman fingerprint of chromate, aluminate and ferrite spinels. J Raman Spectrosc 2015;46:1255–64. http://dx.doi.org/10.1002/jrs.4764.
[43] Gladysz GM, Chawla KK. Coefficients of thermal expansion of some laminated ceramic composites. Compos Part A 2001;32:173–8. http://dx.doi.org/10.1016/S1359-835X(00)00144-5.
[44] Petric A, Ling H. Electrical conductivity and thermal expansion of spinels at elevated temperatures. J Am Ceram Soc 2007;90:1515–20. http://dx.doi.org/10.1111/j.1551-2916.2007.01522.x.
[45] Liao S-C, Tsai P-Y, Liang C-W, Liu H-J, Yang J-C, Lin S-J, et al. Misorientation control and functionality design of nanopillars in self-assembled perovskite-spinel heteroepitaxial nanostructures. ACS Nano 2011;5:4118–22. http://dx.doi.org/10.1021/nn200880t.
[46] Martín-García L, Quesada A, Munuera C, Fernández JF, García-Hernández M, Foerster M, et al. Atomically flat ultrathin cobalt ferrite islands. Adv Mater 2015;27:5955–60. http://dx.doi.org/10.1002/adma.201502799.
[47] Zheng H, Zhan Q, Zavaliche F, Sherburne M, Straub F, Cruz MP, et al. Controlling self-assembled perovskite-spinel nanostructures. Nano Lett 2006;6:1401–7. http://dx.doi.org/10.1021/nl060401y.
[48] Yin Y, Rioux RM, Erdonmez CK, Hughes S, Somorjai GA, Alivisatos AP. Formation of hollow nanocrystals through the nanoscale Kirkendall effect. Science 2004;304:711–4. http://dx.doi.org/10.1126/science.1096566.
[49] Ferrari C, Muscio A, Siligardi C, Manfredini T. Design of a cool color glaze for solar reflective tile application. Ceram Int 2015;41:11106–16. http://dx.doi.org/10.1016/j.ceramint.2015.05.058.
[50] Santamouris M. Cooling the cities - a review of reflective and green roof mitigation technologies to fight heat island and improve comfort in urban environments. Sol Energy 2014;103:682–703. http://dx.doi.org/10.1016/j.solener.2012.07.003.
[51] Levinson R, Berdahl P, Akbari H. Solar spectral optical properties of pigments-Part II: survey of common colorants. Sol Energy Mater Sol Cells 2005;89:351–89. http://dx.doi.org/10.1016/j.solmat.2004.11.013.

Artículo 2

Investigation of thermal stability of 2D and 3D $CoAl_2O_4$ particles in core-shell nanostructures by Raman spectroscopy

C.M. Álvarez-Docio, J.J. Reinosa, A. del Campo, J.F. Fernández.

Journal of Alloys and Compounds, 779, 2019, 244-254

Factor de impacto: 4.175 (según JCR Edition Science 2018).

Journal of Alloys and Compounds 779 (2019) 244–254

Contents lists available at ScienceDirect

Journal of Alloys and Compounds

journal homepage: http://www.elsevier.com/locate/jalcom

Investigation of thermal stability of 2D and 3D $CoAl_2O_4$ particles in core-shell nanostructures by Raman spectroscopy

C.M. Álvarez-Docio*, J.J. Reinosa, A. Del Campo, J.F. Fernández

Instituto de Cerámica y Vidrio, CSIC, C/Kelsen 5, 28049, Madrid, Spain

ARTICLE INFO

Article history:
Received 15 June 2018
Received in revised form
19 November 2018
Accepted 20 November 2018
Available online 22 November 2018

Keywords:
$CoAl_2O_4$ spinel
Dry dispersion
Core-shell
Confocal Raman microscopy

ABSTRACT

We are studying the formation of a nanostructured spinel $CoAl_2O_4$ layer on α-Al_2O_3 giving rise to a core-shell composite. In the final product, two mechanisms of $CoAl_2O_4$ crystallization onto a α-Al_2O_3 microparticle surface are observed, depending on the dispersion grade of Co_3O_4: a 3D nanostructure from the arrangement of Co_3O_4 agglomerated nanoparticles; 2D nanoparticles from the diffusion mechanism of isolated Co_3O_4 nanoparticles. As a consequence, two different crystallization pathways may occur during the thermal treatment. In order to understand the formation mechanisms a Raman Confocal Study is performed. The features of the Raman spectra of the samples depend strongly on the morphology of the nanoparticles located in the shell of the microparticle. Average spectra of the samples show a variation in the Raman shift between the different samples. The differences between 3D or 2D structures is associated with the transmission of phonons among the nanoparticles. The high absorbance of the cobalt species could mask the Raman shift displacement by local heating, so both the temperature and the laser source power are considered in the Raman study. The evolution of the Raman spectra with applied temperature indicates a decoupling of the Raman modes. This fact is more relevant for the 3D aggregates in which nanoparticles produced a larger scattering of phonons and a higher sensitivity to temperature variation. These results clearly indicate that extrinsic parameters such as the size of the crystals and their aggregation state affects their Raman properties.

1. Introduction

At nanoscale, materials often possess physical and functional properties that are dramatically different from their corresponding bulk crystals [1]. This is one of the main reasons why the research on nanoscale materials; such as nanowires, nanoparticles and quantum dots; has made great progress in the last few years. For practical applications, nanomaterials are integrated into heterostructures [2] or dispersed into different supports. One of the approaches that is useful to avoid negative effects of nanoparticles is the use of a core-shell type nanostructure that corresponds to biphasic materials, which have an inner core and an outer shell made of different components. These particles are of interest, as they can exhibit unique properties arising from the combination of dissimilar core and shell materials, geometry and design [3–5]. Several techniques have been investigated for depositing nanoparticles onto the cores, including seed methods [6], thermal evaporation techniques [7], self-assembly methods [8], electroless plating [9], sol-gel methods [10], molten salts synthesis [11] and dry-dispersion procedures [12–14].

In a recent study, dry-dispersion of $CoAl_2O_4$ nanoparticles onto α-Al_2O_3 microparticles with a further thermal treatment showed two different pathways for $CoAl_2O_4$ crystallization [15]. Materials with different nanostructures are formed depending on the dispersion grade of Co_3O_4: 3D nanostructure regions from the arrangement of Co_3O_4 agglomerated nanoparticles; 2D nanoparticles from the diffusion mechanism of isolated Co_3O_4 nanoparticles [15]. Therefore, the difficulties in characterizing these types of compounds are a current challenge in understanding nanostructured materials [16].

Attached to the appearance of unusual functional properties, the crystalline parameters are able to be modified at nanoscale. However, the structural studies at nanoscale are complex and require high-resolution techniques. Generally speaking, common techniques with enough resolution to determine structural parameters in nanometric materials are X-Ray Diffraction (XRD) and Transmission Electron Microscopy (TEM). However, in the case of core-

* Corresponding author.
E-mail address: carmenma.docio@icv.csic.es (C.M. Álvarez-Docio).

https://doi.org/10.1016/j.jallcom.2018.11.263
0925-8388/

shell nanostructured microparticles, there are limitations in the structural analysis of nanoregions because of the appearance of multiple phases, interface phenomena, agglomeration state or even simply the limited resolution of the techniques. The problem to be addressed is to combine the structural and microstructural characterization in a single procedure. Confocal Raman microscopy is a powerful non-destructive technique with high spectral and spatial resolution that is able to resolve structure–microstructure of a wide variety of materials and composites [17–19]. Raman spectroscopy reveals information about the crystal structure, electronic structure and lattice vibrations; it can be used to probe thickness, strain, structural stability, defects or charger effects. For these reasons, it is an efficient tool for the characterization of 2D materials [20].

Therefore, the aim of this work is to differentiate among dissimilar nanostructures in a core-shell microparticle by using Confocal Raman Spectroscopy. Both 2D particles and 3D nanostructures have the same composition, $CoAl_2O_4$, which presents high laser absorption and is therefore suitable for heating. We look at the differences in Raman spectra related to the shell $CoAl_2O_4$ nanoparticles on α-Al_2O_3 core microparticles. In addition, the nature of the 2D and 3D nanoparticles affects the phonons' density through the transmission and reflection processes of phonons, showing that particle-to-particle interphases modify the thermal response of the nanostructure.

1.1. Raman spectra of $CoAl_2O_4$

$CoAl_2O_4$ is a normal spinel, which exhibits a cubic structure, with Fd3m space group (Z = 8). In this structure, the oxygen anions form a cubic close-packed (ccp) sub-lattice surrounded by Co^{2+} and Al^{3+} cations occupying tetrahedral and octahedral sites, respectively. The cations occupy only $^1/_8$ of the tetrahedral sites (8a Wyckoff position) and ½ of the octahedral sites (16d Wyckoff position) [21]. Anisotropy of the surface energy provokes $CoAl_2O_4$ into adopting a face-centred cubic crystal structure, and the general sequence for the surface energies of the spinel structure is $\gamma\{111\} < \gamma\{100\} < \gamma\{110\}$ [22]. Based on the principle of surface free energy minimization, the equilibrium morphology of the spinel is expected to be an octahedron, and indeed, this is the most common form in which a nanocrystalline spinel is observed [22–24].

Although 56 atoms are present within the spinel's unit cell, only 14 atoms are necessary to construct the simplest primitive cell. The factor group analysis shows that the 42 normal modes of spinel, 3 acoustic modes and 39 optical modes belong to the symmetry modes [25].

$$\Gamma(AB_2O_4) = A_{1g}(R) + Eg(R) + F_{1g}(in) + 3F_{2g}(R) + 2A_{2u}(in) + 2E_u(in) + 4F_{1u}(IR) + 2F_{2u}(in)$$

The (R) and (IR) identify Raman- and infrared-active vibrational modes, respectively, and the rest of the modes marked as (in) are silent. The E_g and F_{2g} modes are doubly and triply degenerate, respectively. The three acoustic modes belong to a single F_{1u} mode. A common notation exists in most of the literature to distinguish between the Raman and IR modes belonging to the same representation, and will be used in the present study. The three Raman-active F_{2g} modes are labelled F_{2g} (1), F_{2g} (2), and F_{2g} (3), where F_{2g} (1) is the lowest-energy F_{2g} mode and F_{2g} (3) is the highest-energy mode of this vibrational modes. Conversely, the four IR-active F_{1u} modes are labelled ν_1, ν_2, ν_3, and ν_4 in descending value of energy.

In detail, the irreducible representations that describe the normal modes of vibration associated with each atomic species in their Wyckoff positions are:

$$8a\,[T]{:}F_{1u}(IR)+F_{2g}(R)$$

$$16d[M]{:}A_{2u}(in)+E_u(in)+F_{2u}(in)+2F_{1u}(IR)$$

$$32e[X]{:}A_{1g}(R)+A_{2u}(in)+E_u(in)+E_g(R) +2F_{2g}(R)+F_{1g}(in)+F_{2u}(in)+2F_{1u}(IR)$$

The literature is inconsistent with regard to the assignment of the specific atomic motions within the spinel lattice during the Raman-active vibrations. Accordingly, it is necessary to summarize the common atomic motions assigned to the vibrations of the spinel (Table 1). The Raman band at ca. 705 cm^{-1}, A_{1g} mode, is assigned as the symmetric A^{2+}-O stretching vibration of the AO_4 unit within the spinel lattice [26–28]. The oxygen atoms move away from the tetrahedral cation along the direction of the bonds. Neither the tetrahedral nor octahedral cations are in motion during this vibration [29,30]. However, some authors demonstrated that exchanging the octahedral cation has a much greater effect upon the wavenumber of this mode than exchanging the tetrahedral cation [31], so the A_{1g} mode is mostly independent of the divalent metal occupying the tetrahedral site. This fact justifies that A_{1g} mode is viewed as the symmetric B–O stretching vibration of BO_6 groups, and it is assigned to the A_{1g} mode in the octahedral spectroscopic symmetry [32–35]. The literature also disagrees about the assignment of atomic motions during the vibration for the F_{2g} (3) mode, which has been reported as either the antisymmetric stretching mode of the AO_4 unit [28], or as an asymmetric bending motion of the oxygen bonded to the tetrahedral cation [36]. Furthermore, by comparing the Raman shift of F_{2g} (3) in MgB_2O_4 and FeB_2O_4 spinels (B = Cr, Al, Fe^{3+}), a linear decreasing trend with increase of the octahedral cation radio was observed [26]. Generally speaking, this mode has been assigned to the asymmetric stretching of oxygen with respect to the tetrahedral cation [26–28], but the observed trend indicates that the F_{2g} (3) mode is related to the octahedral cation itself. Additionally, the F_{2g} (2) mode has been assigned to the A-O asymmetric stretching vibration in the tetrahedral sites [26,27], T-sites. A very good correlation was found between the peak position of the E_g mode and the tetrahedral cation radius [26]. Thus, E_g mode has been assigned to the symmetric

Table 1
Overview of Raman modes for $CoAl_2O_4$.

Raman Band (cm^{-1})	Symmetry Mode	Assignment	References
705	A_{1g}	Stretching symmetric AO_4	[26–28]
		Stretching BO_6	[32–35]
615	F_{2g} (3)	Stretching antisymmetric AO_4	[26–28]
		Bending antisymmetric AO_4	[36]
		BO_6	[26]
516	F_{2g} (2)	Stretching asymmetric AO_4	[26,27]
406	E_g	Bending symmetric AO_4	[26,27]
201	F_{2g} (1)	Complete Translation AO_4	[26–28,30,33]

bending motion of the oxygen atoms within the T-sites [27]. Hence, despite the movement affecting mainly the oxygen atoms, the presence of different divalent cations in the T-sites influences the E_g mode [26]. Finally, most of the authors agree that the F_{2g} (1) mode is assigned to a complete translation of AO_4 within the spinel structure [26–28,30,33].

2. Experimental

2.1. Nanodispersion procedure of α-Al_2O_3/Co_3O_4 mixtures and thermal treatment procedure

Compositions with 1, 5, 10, 20 and 30 wt % of Co_3O_4 nanoparticles on α-Al_2O_3 microparticles (hereafter named as 99Al1Co, 95Al5Co, 90Al10Co, 80Al20Co and 70Al30Co, respectively) were prepared by incorporating the appropriate amounts of Co_3O_4 nanoparticles as previously described [15]. Samples were thermally treated at 1200 °C with a heating rate of 3 °C/min. For comparison purposes, a standard $CoAl_2O_4$ micrometric pigment (Manuel Riesgo SA, Madrid, Spain) has been used.

2.2. Characterization

The crystalline phases were characterized by X-ray diffraction (XRD, D8, Bruker) using a Lynx Eye detector and Cu $K\alpha_{1,2}$ radiation. The X-Ray data were analysed by standard Rietveld refinement using the CHEKCELL program, assuming a face-centred cubic spinel structure with the space group Fd3m (JCPDS 00-038-0814) for $CoAl_2O_4$ phase and a hexagonal corundum structure with the space group R-3c (JCPDS 00-011-0661) for α-Al_2O_3 phase.

The surface composition was performed using an X-ray Photoelectron Spectrometer (XPS, K-Alpha, Thermo Scientific). It utilizes a monochromated Al Kα (1486.6 eV) source running at a voltage of 12 KV with a pass energy of 40 eV used for high resolution region scans and 200 eV for survey scans. Finally, for charge correction a 1 point scale with the C 1s peak shifted to 284.6 eV was used.

Core-shell microparticles were observed by using a Field Emission Scanning Electronic Microscope, FESEM, Hitachi S-4700. Additionally, the nanostructure was studied by atomic force microscope, AFM, with the Witec system (Witec ALPHA 300RA) where the AFM is coupled to the confocal microscope. AFM images were taken at RT using silicon tips (with a resonant frequency of 200–300 kHz) in non-contact mode. This system allows studying the same area of an isolate microparticle in both the Raman and the AFM studies. For this purpose, the samples were deposited on a microscopy glass slice. This sample preparation does not allow us to use the intermittent contact mode, because the microparticles can move during the assay.

The Raman study was carried out with the use of a confocal micro-Raman coupled with the AFM (Witec alpha – 300R, Witec, Ulm, Germany). Raman spectra were obtained using a micro-Raman system with a 532 nm excitation laser and a 100x objective lens (NA = 0.9). The incident laser power was about 5 mW on the core-shell samples and 0.5 mW on the $CoAl_2O_4$ pigment used as reference. The final spectrum is the result of an average of 6 spectra integrating 30 s each spectrum. Collected spectra were analysed by using Witec Control Plus Software (Witec, Ulm, Germany).

Temperature Raman measurements between 300 K (RT) and 848 K were carried out in a temperature chamber (LinkamSystem) on compacted powders, for which argon gas was used in order to purge the sample chamber and avoid condensation in the upper lid of the window surface. This chamber is used to provide a homogeneous temperature for the whole sample under study. For each measurement point, the temperature was stabilized for 10 min before acquiring a spectrum for 3 min. All the Raman spectra were obtained under the same experimental conditions, and the Raman band positions and widths were obtained by fitting them with a Lorentzian function.

3. Results and discussion

3.1. Micro-nanostructural characterization of shell nanostructures

Fig. 1(a and b) shows the FESEM micrographs of the 95Al5Co and 70Al30Co samples. FESEM micrographs illustrate the presence of crystallizations having different morphologies that cover the whole α-Al_2O_3 surface. A high proportion of these nanocrystals have a triangular shape and presents strikingly flat surfaces with low thickness and straight edges, so hereafter they will be called 2D particles. Irregular particles could also be seen, which have a hole in the middle. These particles protrude further from the alumina surface than the flat triangular ones, they are the result of the agglomeration of former nanoparticles, so we will name them 3D particles [15].

The surface roughness of the 2D and 3D structures is confirmed by AFM characterization, Fig. 1(c and d) (For more detailed information see Supplementary Info, Fig. S1). Hence, samples with lower amounts of Co_3O_4 in their composition allow the presence of flat $CoAl_2O_4$ 2D particles. On the other hand, 3D rough structures are highly present in samples with a higher percentage of the former Co_3O_4 and an increase in the surface roughness of the core-shell nanostructure particles occurs with a corresponding increase of the initial cobalt oxide amount, Fig. S1 (b). In fact, the height of the $CoAl_2O_4$ structures increases from ≈20 nm for 99Al1Co samples to ≈100 nm for 70Al30Co samples.

Fig. 2 shows the XRD patterns of the core-shell nanostructured microparticles made with various cobalt contents. The reaction between Co_3O_4 and α-Al_2O_3, according to the phases diagram [37] results in the formation of a $CoAl_2O_4$ spinel-type solid solution. The diffraction patterns are compared with that of a commercial $CoAl_2O_4$ used as reference. $CoAl_2O_4$ and Co_3O_4 have the same spinel cubic (Fd3m) crystallographic structure with slight differences in the *a* lattice constant: 8.1040 Å for $CoAl_2O_4$ and 8.0840 Å for Co_3O_4. They therefore, have a similar peak pattern, and the positions of the XRD peaks are nearly the same, so no relevant differences between

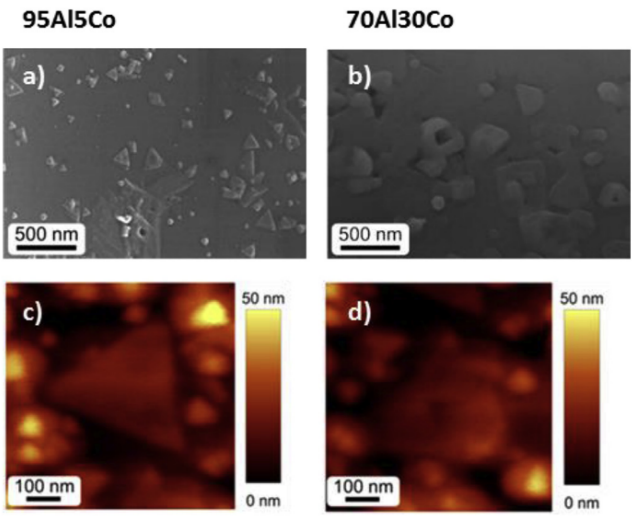

Fig. 1. Micro-nanostructural analysis of core-shell nanostructured microparticles: FESEM micrographs of a) 95Al5Co and b) 70Al30Co samples; AFM topographical images of c) 95Al5Co and d) 70Al30Co samples.

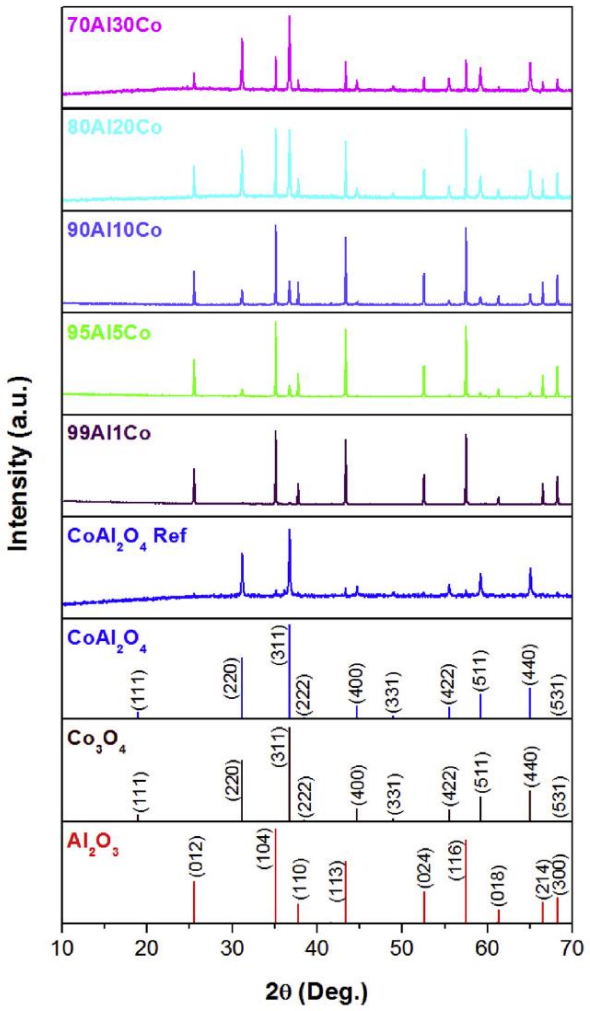

Fig. 2. XRD diffraction patterns of 100-xAlxCo series of core-shell nanostructured microparticles, $CoAl_2O_4$ reference, and corresponding JCPD patterns for $Co_2Al_2O_4$, Co_3O_4 and Al_2O_3.

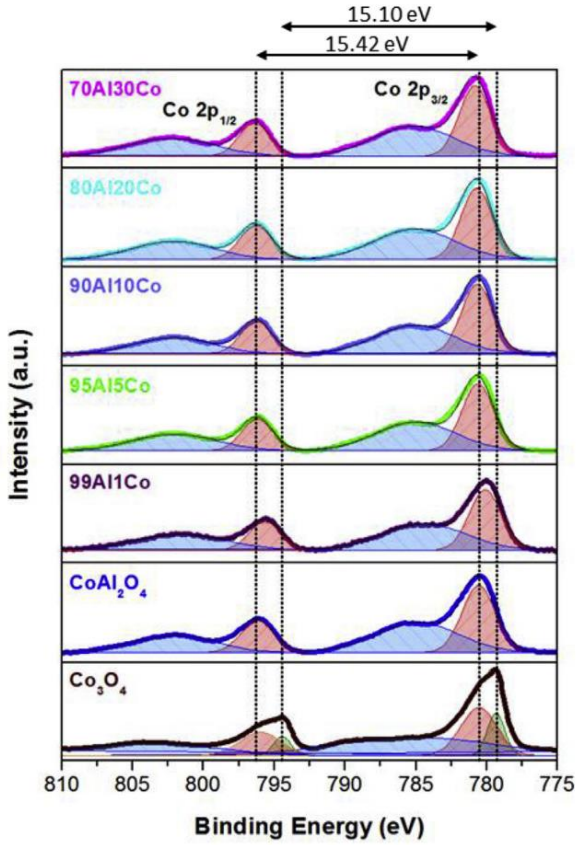

Fig. 3. XPS spectra of Co 2p core levels of pure Co_3O_4 and $CoAl_2O_4$ samples. The vertical dot lines are binding energy for the reference compounds: For the Co $2p_{3/2}$ peak the values are 779.7 and 780.9 eV for the Co_3O_4 and 780.6 eV for the $CoAl_2O_4$, whereas for the Co $2p_{1/2}$ peak the values are 794.8 and 796.1 eV for the Co_3O_4 and 795.6 eV for the $CoAl_2O_4$.

their phases could be determined by XRD. Moreover, the presence of un-reacted Co_3O_4 could not be dismissed from this technique. In any case, no evidence of metallic Co, CoO or secondary phases different from α-Al_2O_3, Co_3O_4 or $CoAl_2O_4$ is found at any composition within the XRD resolution limit.

3.2. Structural characterization of core-shell nanostructures

In order to confirm the absence of a Co_3O_4 spinel at the surface of the platelets of α-Al_2O_3, an additional study was performed by XPS. The high-resolution photoelectron spectra of Co 2p for the different samples are displayed in Fig. 3. The binding energies (BE) of Co core levels of the samples are listed in Table 2. For comparison, the XPS data of raw materials (Co_3O_4 and $CoAl_2O_4$) are also listed in Table 2. The XPS spectra of all the samples annealed at 1200 °C, as well as the references (Al_2O_3, Co_3O_4 and $CoAl_2O_4$), indicating that in addition to the raw materials and contaminated carbon, sodium is detected as a contaminant specie (as shown in Supplementary Info, Fig. S2). As indicated by the XPS spectrum of α-Al_2O_3 the presence of sodium comes from the α-Al_2O_3 particles [38]. In addition, the C1s peak at 284.6 eV of contaminated carbon is used as reference.

Pure Co_3O_4 exhibits two oxidation states. On a molar basis, there are two Co^{3+} ions in octahedral symmetry and one Co^{2+} ion in tetrahedral symmetry, which are distributed on the A and B sites as $[Co^{2+}]A[2Co^{3+}]BO_4$. The combination of the two oxidation states results in the asymmetric shape of the Co $2p_{3/2}$ and $2p_{1/2}$ peaks [39] as observed in Fig. 3. Hence, the XPS data for Co_3O_4 spinel clearly shows the presence of a doublet of peaks, which are centred at 779.34 eV and at 780.54 eV, and a shake-up satellite peak at 784.94 eV for the Co $2p_{3/2}$ level. A doublet is also observed for the Co $2p_{1/2}$ level at 794.84 eV and 795.96 eV, and the satellite at 803.75 eV. Note too, that the energy splitting (ΔE) between the two levels, due to spin-orbit coupling, should be different for the Co^{2+} and Co^{3+} configurations: the differences in energy therefore are ΔE = 15.10 eV for Co^{3+} and ΔE = 15.42 eV for Co^{2+}. These results confirm the presence of Co^{3+} and Co^{2+} in Co_3O_4 and are in good agreement with the previously reported data [40–42].

The cobalt atoms in $CoAl_2O_4$ are in a +2 oxidation state with tetrahedral coordination. Cobalt aluminate has also a spinel structure like cobalt oxide, but the aluminium atoms occupy the octahedral coordination. The Co $2p_{3/2}$ peak presents a significantly higher binding energy in cobalt aluminate than in cobalt oxide and the peak is more symmetric in cobalt aluminate because cobalt only has a single oxidation state [43]. In the case of the samples with different cobalt content, small changes are observed in both the Co $2p_{3/2}$ and Co $2p_{1/2}$ peaks positions; they are displaced to higher binding energies as the amount of cobalt increases (Table 2). For these samples, the data give an energy splitting ΔE = 15.6 eV, which

Table 2
Binding energies of Co 2p core level (eV) for 100-xAlxCo series of samples, $CoAl_2O_4$ and Co_3O_4 as references depending on "T_d" (tetrahedral) and "O_h" (octahedral) structures.

Sample	Co $2p_{3/2}$			Co $2p_{1/2}$		
	Co^{2+} T_d (eV)	Co^{3+} O_h (eV)	Sat (eV)	Co^{2+} O_h (eV)	Co^{3+} T_d (eV)	Sat (eV)
99Al1Co	780,11		784,40	795,67		801,57
95Al5Co	780,62		785,01	796,20		802,03
90Al10Co	780,68		785,07	796,26		802,06
80Al20Co	780,70		785,10	796,29		802,11
70Al30Co	780,83		785,17	796,42		802,29
$CoAl_2O_4$	780,56		784,92	796,17		802,01
Co_3O_4	779,34	780,55	784,94	794,44	795,96	803,75

is characteristic of Co^{2+} only, and no additional signatures for the Co^{3+} state are noticed. Moreover, these structures clearly show two intense satellites which are representative of tetrahedral coordinated Co^{2+} cations as they occur in $CoAl_2O_4$ [44]. The satellites are attributed to the transition of an electron from an occupied 3d orbital to the empty 4s orbital during the ejection of the core 2p photoelectron [45,46]. From the XPS study, the atomic percentages resulting from the quantitative analysis of the XPS spectra of the species presented in the formulated samples and in references are shown in Table 3. Reference $CoAl_2O_4$ presents a value for a Co:Al ratio of 1:7. This value is initially in concordance with a $CoAl_2O_4$ structure that ends with Aluminium atoms in octahedral positions. The aforementioned ratio is similar for samples 90Al10Co, 80Al20Co and 70Al30Co so it confirms that the core-shell is formed in these samples. In the case of 95Al5Co and 99Al1Co, the amount of Aluminium cations is slightly higher, so the surface is not completely covered by $CoAl_2O_4$, as observed in the FESEM study. These results confirm the coexistence of $CoAl_2O_4$, α-Al_2O_3 and the core-shell formation.

Fig. 4 (a) shows the Raman average spectra for the five samples and for comparison purposes the Raman spectra of α-Al_2O_3 and $CoAl_2O_4$ as references. Concerning α-Al_2O_3, it has been reported that α-Al_2O_3 (corundum) is based on D63d symmetry with seven Raman-active phonon modes, A_{1g} (418 and 645 cm^{-1}) and E_g (378, 429, 448, 576 and 750 cm^{-1}) [47]. $CoAl_2O_4$ pigment which is used as reference has a spinel structure and, considering that this spinel structure belongs to the Fd3m space group, it exhibits five Raman active modes: A_{1g} (764 cm^{-1}); F_{2g} (644, 511 and 203 cm^{-1}) and E_g (413 cm^{-1}) [26]. The main phase identified by Raman spectroscopy in the samples is the spinel $CoAl_2O_4$. In the 99Al1Co sample, α-Al_2O_3 is identified because its surface is not completely covered by $CoAl_2O_4$ nanoparticles in agreement with the XPS study. Fig. 4 (b) and Fig. 4 (c) show Raman redshift variation for the most intense Raman peaks of the $CoAl_2O_4$ phase, F_{2g} (1) and F_{2g} (2), as the amount of starting Co_3O_4 increases in the composition. The Raman redshift is more pronounced for 80Al20Co and 70Al30Co samples. Moreover, a broadening of the Raman modes occurs in addition to the Raman redshift.

With the aim to elucidate the origin of the redshift of Raman modes, taking into account the concentration of starting Co_3O_4, both the possible heating of the sample due to the laser irradiation and the morphology of the surface nanostructures must be considered [48–50].

In Fig. 5 (a) representative Optical Microscopy images of a core-shell nanostructured particle of each composition are shown. The characteristic platelet type of the starting α-Al_2O_3 is preserved in the core-shell particle and it is used to locate the isolated microparticles onto the glass slide support. The microparticles are aligned with the larger face perpendicular to the Raman beam ensuring both the stability of the microparticle and its homogenous observation under Confocal Raman Microscopy. For the Raman study, the displacement of the F_{2g} (1) active Raman mode is represented by a colour code following the Raman shift colour bar (Fig. 5 (b)). A gradient in the Raman shift is observed for the different microparticles between the edges and the centre of the microparticles. Moreover, the Raman intensity for the aluminate phase is higher at the edge of the microparticles (Fig. S3 (d)). In addition, Fig. 5 (c) represents the full width at half maximum (FWHM) of the F_{2g} (1) active Raman mode, in a colour code following the FWHM colour bar. Once again, a gradient of the FWHM is observed depending on the starting Co_3O_4 amount. Differences between centre and edge areas of the core-shell particles are also detected. Two effects could cause the origin of the higher intensity of the Raman signals for the cobalt aluminate at the particle edge: a) the presence of a higher amount of $CoAl_2O_4$ (see Fig. S3e), which can also be related to thermal effect due to irradiation [48–50]; and b) the evanescence field generated in the edge of the platelet. Both of these factors could contribute simultaneously to the redshift. In any case, to evaluate structural changes by Raman analysis, a better approach results when Raman shifts are used instead of Raman intensities.

With the data obtained from Fig. 5 (b) for Raman shift and from Fig. 5 (c) for FWHM, a statistical analysis is possible by using the histograms of the different regions, where each pixel of the Raman image contains the full Raman spectrum (Fig. S4). From the histograms, the main values of the Raman shift (Fig. 5 (d)) and FWHM (Fig. 5 (e)) for the different core-shell nanostructured microparticles are compared as a function of the centre and edge location. The study is also performed for F_{2g} (2) active Raman mode. The histograms obtained for samples with a higher amount of cobalt show a red-shift for the Raman modes with a larger broadening as the amount of cobalt increases. In addition, the higher the Raman redshift is, the higher FMHW is. Moreover, Raman red-shift is more pronounced at the edge region, but the FWHM is slightly higher in the centre region. This indicates that the heating process of the shell under laser irradiation provokes differences in both the centre and the edge regions that are not consistent. The $CoAl_2O_4$ shell is supported on α-Al_2O_3, which is an insulating material with a wide band gap (absorption edge below 200 nm) and high reflectivity in the visible region. The alumina core of the microparticles acts as a heat sink for the heat generated at the absorbing shell. The sample with the higher amount of cobalt in its composition shows

Table 3
Element contents (%) of the samples based on XPS analysis.

Sample	At % C	At % O	At % Al	At % Co	Co:Al
Al_2O_3	8,78	47,77	43,44		
Co_3O_4	12,42	57,35		30,23	
99Al1Co	9,84	47,74	41,25	1,17	1:35
95Al5Co	7,38	49,72	38,88	4,02	1:10
90Al10Co	8,57	49,56	36,28	5,59	1:6
80Al20Co	13,18	46,94	34,49	5,39	1:6
70Al30Co	10,41	48,33	35,76	5,50	1:7
$CoAl_2O_4$	6,13	52,18	36,62	5,07	1:7

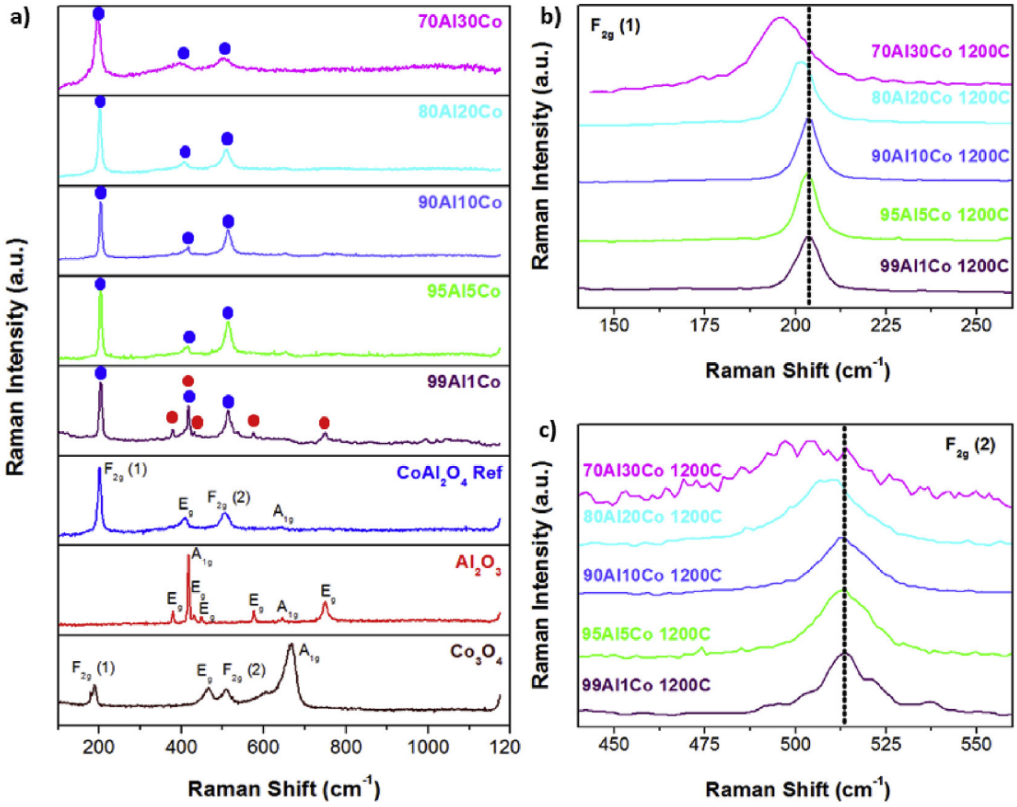

Fig. 4. a) Raman spectra for core-shell nanostructured microparticles of the 100-xAlxCo series, and for comparison Raman spectra of $CoAl_2O_4$ and Co_3O_4 as references are also included. b) Detail of the Raman shift of F_{2g} (1) mode an c) F_{2g} (2) mode. (In figures b) and c), the dashed lines serve as a visual guide).

increasing roughness and grain size, which are indicative of thicker shells. The higher the volume of the cobalt aluminate shell and the lower the alumina core is, the more laser absorption occurs. However, the morphology of the particles in the shell is dissimilar for the samples with a low cobalt content, which possess higher amounts of 2D particles; meanwhile a large content of starting Co_3O_4 produce the appearance of 3D nanostructures. So the heating behaviour plays a relevant role in the determination of the structural characteristics of the core-shell nanostructured material and, as a consequence, the thermal evolution of Raman spectra must be evaluated.

3.3. *Thermal stability of shell Raman modes*

Taking into account the relevance of the laser power on the Raman properties of core-shell nanostructured microparticles, the Raman spectra of all samples under different output laser powers have been measured. The study was attempted to the most characteristic sample representatives of the 2D particles in the shell, 95AlCo5, and of the 3D nanostructures in the shell, 70Al30Co. Fig. 6 presents the evolution of the Raman shift and FWHM for F_{2g} (1) and F_{2g} (2) Raman modes for the different samples. The laser power for Raman acquisition was increased stepwise until irreversible modifications on the Raman spectra were produced, that is, the original spectrum was not recovered by reducing the output laser power to the minimum. The minimum excitation laser power was chosen as the one that produced a reproducible Raman signal of the spinel structure with a signal to noise ratio of >10 units of intensity (Supplementary Info Fig. S5).

Fig. 6 shows the values of the Raman shift and FWHM versus the laser power that caused differences in evolution for each sample, in good agreement with the results in Fig. 5. Moreover, the 70Al30Co sample presents the largest red-shift and broadening at low incident laser power, >7 mW, that produces irreversible change in the structure. Meanwhile, the 95Al5Co sample shows a large range of stability, up to 40 mW: the maximum output laser power available in our experimental setup. In order to determine the evolution of the Raman spectra with the temperature, a study into a temperature chamber follows.

Fig. 7 shows the dependence of the Raman shift and FWHM of the F_{2g} (1) and F_{2g} (2) modes versus measurement temperature. As can be observed, an increase of temperature produces both a Raman red-shifting and a FWHM broadening: The Raman shifts are slightly different than the previously observed by varying the incident laser power. This effect is owing to the different sample preparation. In the case of the laser power studies the measurements are followed over isolated particles, whereas the temperature study are carried out on compacted powders, that is agglomerated state powders. The agglomeration of nanoparticles modifies the quantum confinement that is associated with a Raman shift red-shift and an increase of FWHM of Raman modes [19,51]. These modifications of the Raman spectrum with the agglomeration are comparable with the ones produced by the temperature. Both samples showed a linear behaviour with slight differences in their slopes until 500 K. For temperatures higher than 500 K, the 70Al30Co sample experiences a sudden increase of the FWHM. The thermal treatment at 500 K does not change the average particle size for the $CoAl_2O_4$ crystallizations as an indication that the morphology of the particles remained unaltered. By the contrary, such surface has a relevant roughness that accounts for surface

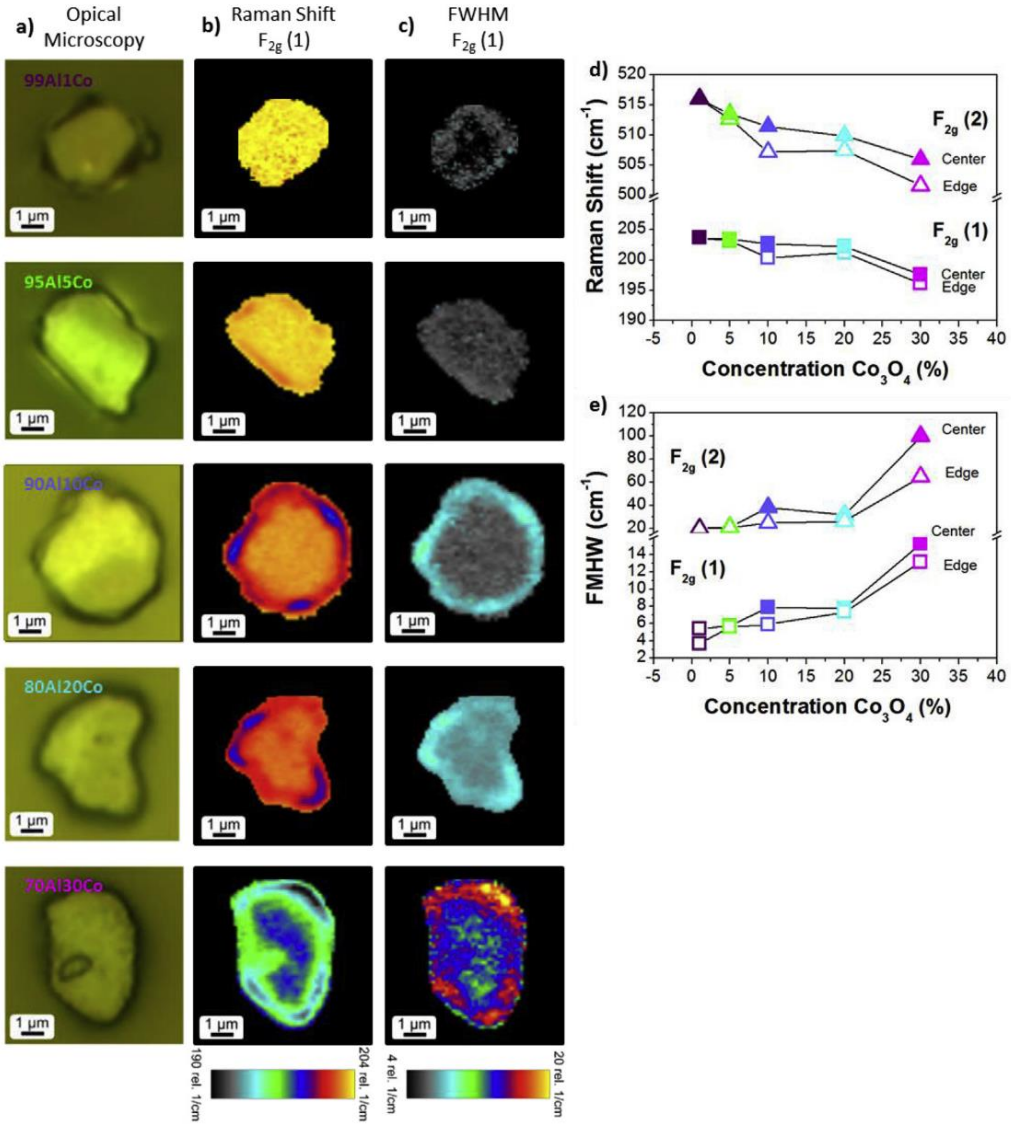

Fig. 5. a) Micrographs by Confocal Optical Microscopy of core-shell nanostructure microparticles for 100-xAlxCo series. b) Raman image representation of the Raman shift of the F_{2g} (1) mode of the same particles present in **a**. Bar at the bottom of the figure incorporates the colour code scale of the Raman shift. c) FWHM of the F_{2g} (1) mode of the same particles present in **a** and **b**. Bar at the bottom of the figure incorporates the colour code scale of the FWHM. d) Raman shift of the F_{2g} (1) mode as a function of the starting Co_3O_4 content. e) FWHM of the F_{2g} (1) mode as a function of the starting Co_3O_4 content. (For interpretation of the references to colour in this figure legend, the reader is referred to the Web version of this article.)

water absorption, mainly in capillary sites of the spinel nanostructure. The presence of surface water modifies the energy of the polarizability of the surface [52] and therefore the Raman spectra due to the proximity effect. Once the samples are cooled, Fig. 7, the Raman Shift is completely reversible, whereas the FWHM remains enhanced for the 70Al30Co sample as indication of the modification of the surface charge. However, after two days at RT in ambient conditions, the Raman spectra return to the initial values. In the case of the 90Al10Co sample, these effects are not observed due to the low surface roughness.

The temperature dependence of the Raman shift in the linear regions can be adjusted by considering the following Equation (1) [53].

$$\omega = \omega_0 + \omega_0\left(e^{-3\alpha\gamma T} - 1\right) + A\left(1 + \frac{2}{e^{\frac{\hbar\omega_0}{2kT}} - 1}\right) \quad (1)$$

where ω_0 is the natural phonon energy at 0 K; the second term on the right-hand side is the correction due to thermal expansion where α is the thermal expansion coefficient and γ is the thermodynamic equation of Gruneinsen; the third term describes the coupling of the optical phonon to two lower energy acoustic phonons to describe the anharmonic processes occurring at high temperature where $\hbar$ is Planck's constant and K is Boltzman's constant.

The observed variation of Raman Shift of the F_{2g} (1) and F_{2g} (2) modes has been fitted to Equation (1), taking into consideration that thermal expansion should be negligible regarding the

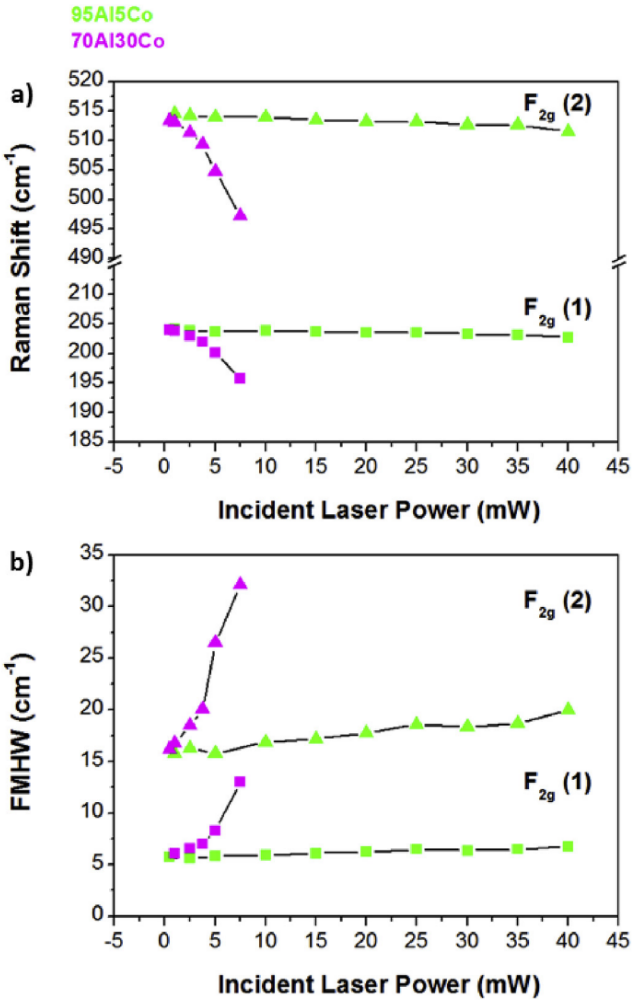

Fig. 6. Evolution of the F_{2g} (1) and F_{2g} (2) Raman mode as a function of the incident laser power for the 95Al5Co and 70Al30Co samples: a) Raman Shift and b) FWHM. (Measurements are made at Room Temperature).

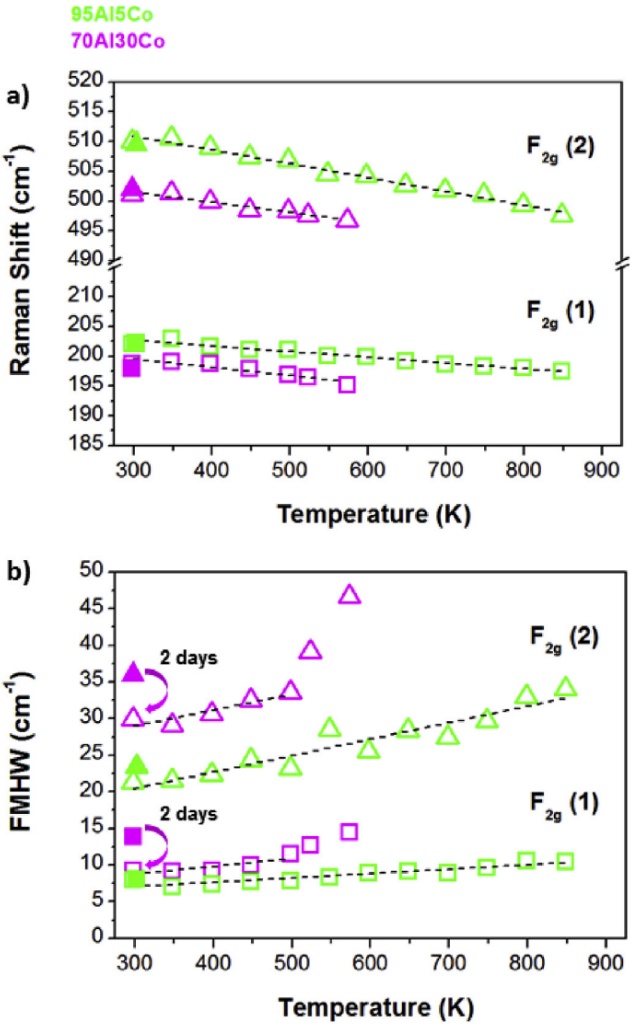

Fig. 7. Evolution of the main Raman parameter vs temperature for the 95Al5Co and 70AlCo30 samples. a) Raman Shift dependence of F_{2g} (1) and F_{2g} (2) modes as function of the temperature; b) FWHM dependence of F_{2g} (1) and F_{2g} (2) modes as function of the temperature. (The laser power on sample is about 5 mW). The filled points corresponds to the measurements performed after cooling the samples.

anharmonic processes [51,54–56]. The fitting is included in Fig. 7 as dashed lines for all samples and the values of the different fitting parameters are summarized in Table 4.

The temperature dependence of the FWHM can be fitted using Equation 2.

$$\Gamma_T = \Gamma_0 + B\left(1 + \frac{2}{e^{\frac{\hbar\omega_0}{2kT}} - 1}\right) \quad (2)$$

where Γ_0 is the natural line-width broadening which is produced by effects not related to the thermal population of phonons [53]. This broadening could be produced by extrinsic sources, such as experimental artefacts introduced by the equipment, or intrinsic, due to variations of the anharmonicity of the atoms vibration in the crystal which are not dependant on the temperature, like an inhomogeneous strain [51]. The second term on the right-hand side of the equation describes the coupling of the optical phonon to two lower energy acoustic phonons [57].

Taking into account the parameters obtained from the fitting of Equation (1), the linewidths of the F_{2g} (1) and F_{2g} (2) modes are fitted to Equation (2). The fitting is shown in Fig. 7 and the obtained values of Γ_0 and B are also included in Table 4.

The study of the F_{2g} (1) and F_{2g} (2) active Raman modes with temperature confirms the different slopes and therefore these Raman modes are temperature decoupled. The large variation of B values in Table 4 confirms the Raman modes' decoupling. This fact could be explained by the differences in the photon-phonon coupling due to their dissimilar $CoAl_2O_4$ crystallizations. It is well known that for bulk materials only, vibration modes at the Brillouin centre zone are allowed, whereas in the case of the nanoparticles, the interruption of phonon propagation at the nanomaterial surface produces a relaxation of this selection rule and allows vibration modes far from the Brillouin zone centre [58]. These new available vibration modes produce a strongly particle-size dependent displacement and broadening of the Raman spectrum [59]. In the 95Al5Co sample the predominated crystallizations are $CoAl_2O_4$ 2D particles. These 2D particles are large particles in diameter but thinner in thickness. The phonon reflects against the boundaries of the plane (Fig. 8 (a)) and remains in a confined state within the particle thickness owing to their dimension (Fig. 8 (b)). In 2D particles the life time mechanism of phonon-coupling with the

Table 4
Values of the fitting parameters of equations (1) and (2) for the Raman shift and the FWHM of the F_{2g} (1) and F_{2g} (2) modes as a function of the temperature.

	ω_0 (cm^{-1})	A (cm^{-1})	Γ_0 (cm^{-1})	B (cm^{-1})
95Al5Co F_{2g} (1)	205,452	−0,111	4525	0,083
70Al30Co F_{2g} (1)	207,673	−0,260	0051	0,298
95Al5Co F_{2g} (2)	518,712	−0,724	13,372	0,674
70Al30Co F_{2g} (2)	506,744	−0,500	15,762	1081

$CoAl_2O_4$ atom network is different depending on the space direction of phonon propagation. Differences in the mean free path for the phonons in the network results in different types and different frequencies of vibrations of the atoms around their equilibrium position; the associated thermal energy is different in each space direction, which is translated to the decoupling of Raman modes. In the case of the 70Al30Co sample, the predominant shell crystallizations are $CoAl_2O_4$ 3D nanostructured particles, which are the result of the sintering of several $CoAl_2O_4$ nanoparticles forming aggregates (Fig. 8 (c)). In this configuration phonons can be partially reflected at the particle's surface or can be transmitted to other systems as phonon bottlenecks [60]. Partially reflected phonons seem to present a slower decay, which allows a larger addition of modes out of the Brillouin zone centre than those given for the total reflected phonon in a single nanoparticle [61]. This effect produces a larger red shift and FWHM broadening for aggregated nanoparticles, which is not presented for the isolated ones. Again, the decoupling of the Raman modes is attributed to the differences in the phonon motion because of differences in crystalline structures. The mean free path of phonons is thus different for 2D and 3D nanostructures, so the anharmonicity in phonon coupling with temperature is consistent with the differences in crystallinity of the material.

As previously mentioned in Table 1, F_{2g} (1) mode is assigned to a complete translation of the AO_4 units within the spinel structure (Fig. 8 (d)); whereas F_{2g} (2) mode corresponds to the asymmetric stretch in AO_4 units (Fig. 8 (e)). F_{2g} (1) occurrence is qualitatively higher than F_{2g} (2), so it is more favorable that F_{2g} (1) occurs. Additionally, Raman shift of F_{2g} (2) mode also indicates a lower energy absorption of the crystal lattice. The clear differences between both modes related to their thermal evolution indicate that the phonon transmission between adjacent particles is more likely to occur in the lower energy vibration mode, translation of AO_4 units in F_{2g} (1). The aggregation of the 3D nanoparticles area is associated with a redshift of the Raman modes, so these vibration modes are easy to heat, as occurs in the 70Al30Co sample. On the other hand, 2D particles are constrained by the alumina support as indicated by their higher bond constant force, sample 95Al5Co. The differences on the heating ratio between Raman modes F_{2g} (1) and F_{2g} (2) could be attributed to the energy difference ceded by the photons to the crystal lattice. This aspect is related to the nature of each Raman mode where the A-O asymmetric stretching in AO_4 tetrahedrons (F_{2g} (2)) is favoured versus AO_4 translation (F_{2g} (1)). For this reason, F_{2g} (2) mode is more affected by heating from the incident laser power. This effect is less relevant for the 95Al5Co sample because of the reduced volume of material due to the lower thicknesses of 2D nanostructures and, in addition, to the higher laser reflectivity of α-Al_2O_3 core support.

FMHW is wider for the 70Al30Co sample as a result of their relaxed crystal structure in the aggregation state (Fig. 7 (b)). In the 95Al5Co sample, the FMHW maintains its value and the sample removes the heat efficiently. In this sense, the presence of 2D particles in the shell is more favorable - to ensure the thermal stability of core-shell particles - than the presence of 3D nanostructures. These findings open the design of new pigments with superior performance under extreme operating conditions.

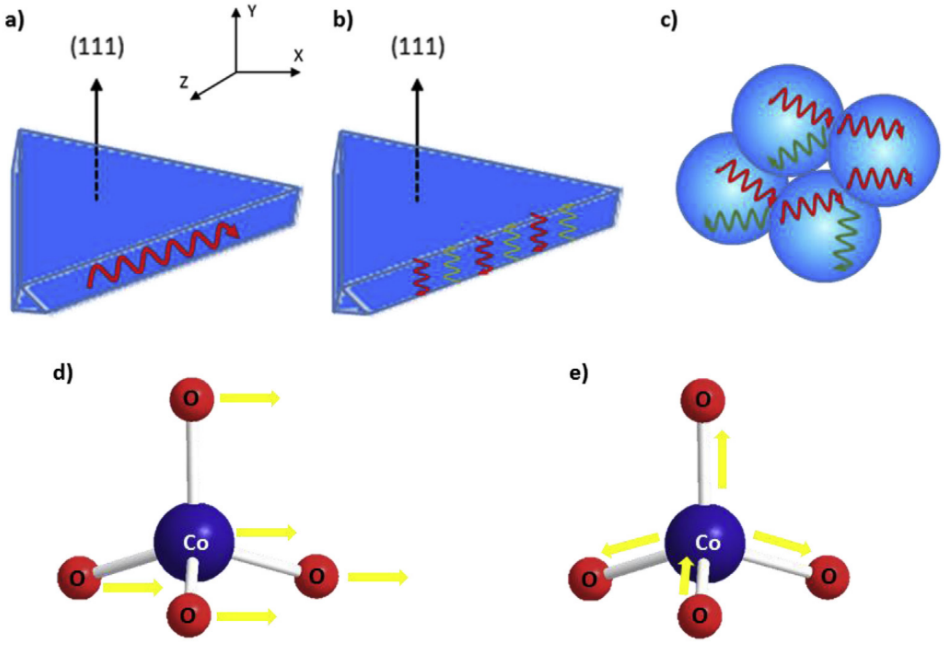

Fig. 8. Representation of phonon movement depending on the type of $CoAl_2O_4$ particle: a) phonon transversal to the (111) crystallographic orientation in 2D particles; b) confinement of phonons along (111) crystallographic orientation in 2D particles; and c) phonon behaviour in aggregate nanoparticles. (Phonons are represented in red and scattered phonons in green). Schematic diagram of the Raman modes: d) F_{2g} (1) corresponds to a complete translation of the AO_4 units and e) F_{2g} (1) mode has been assigned to the Co–O asymmetric stretching vibration in the tetrahedral coordinated sites. (For interpretation of the references to colour in this figure legend, the reader is referred to the Web version of this article.)

4. Conclusions

The formation of a $CoAl_2O_4$ shell of isolated 2D or 3D nanoparticle aggregates onto α-Al_2O_3 core microparticles has been demonstrated. An AFM study confirmed an increase of the roughness over α-Al_2O_3 platelets due to the presence of $CoAl_2O_4$ having different morphologies. XPS characterization indicated the effective formation of a $CoAl_2O_4$ shell in samples having $\geq$10 wt% of Co_3O_4. Confocal Raman microscopy revealed the structural differences between core-shell microparticles with 2D $CoAl_2O_4$ particles (95Al5Co) and with aggregates of 3D nanoparticles (70Al30Co). Depending on the $CoAl_2O_4$ nanostructure morphology, the shift and FWHM was different. In 3D the phonon confinement was correlated with a crystal structure relaxation that favoured the thermal heating. The Raman modes also decoupled with temperature for F_{2g} (1) and F_{2g} (2) modes, as consequence of their differences in energy and occurrence. The complete translation of AO_4 units in the spinel structure was limited in 2D nanostructures and the heating of the particles is accordingly limited. The thermal stability of core-shell microparticles by using the approach of 2D nanostructures opens thus an opportunity to design better pigments based on inorganic materials.

Conflicts of interest

The authors declare no competing financial interest.

Acknowledgment

The authors wish to express their thanks to the projects NANOMIND CSIC201560E068 and MAT2017-86450-C4-1-R for their financial support. C.M. Álvarez-Docio is also indebted to MINECO for a Predoctoral Grant (BES-2014-069779).

Appendix A. Supplementary data

Supplementary data to this article can be found online at https://doi.org/10.1016/j.jallcom.2018.11.263.

References

[1] D. Guo, G. Xie, J. Luo, Mechanical properties of nanoparticles: basics and applications, J. Phys. D Appl. Phys. 47 (2014), 013001, https://doi.org/10.1088/0022-3727/47/1/013001.
[2] E. de Lucas-Gil, J.F. Fernández, F. Rubio-Marcos, One more step against nanotoxicity: hierarchical particles designed to antifungal properties, Mater. Des. 134 (2017) 188–195, https://doi.org/10.1016/j.matdes.2017.08.038.
[3] V. V Srdić, B. Mojić, M. Nikolić, S. Ognjanović, Recent progress on synthesis of ceramics core/shell nanostructures, Process. Appl. Ceram. 7 (2013) 45–62, https://doi.org/10.2298/PAC1302045S.
[4] R.G. Chaudhuri, S. Paria, Core/shell nanoparticles: classes, properties, synthesis mechanisms, characterization, and applications, Chem. Rev. 112 (2012) 2373–2433, https://doi.org/10.1021/cr100449n.
[5] A. Aguilar-Elguézabal, M. Román-Aguirre, L. De la Torre-Sáenz, P. Pizá-Ruiz, M. Bocanegra-Bernal, Synthesis of CoAl2O4/Al2O3 nanoparticles for ceramic blue pigments, Ceram. Int. 43 (2017) 15254–15257, https://doi.org/10.1016/j.ceramint.2017.08.062.
[6] H. Hofmeister, P.-T. Miclea, W. Mörke, Metal nanoparticle coating of oxide nanospheres for core-shell structures, Part. Part. Syst. Char. 19 (2002) 359–365. https://doi.org/10.1002/1521-4117(200211)19:5<359::AID-PPSC359>3.0.CO;2-B.
[7] D. Chhikara, M.S. Kumar, K.M.K. Srivatsa, Superlattices and Microstructures on the synthesis of Zn/ZnO core – shell solid microspheres on quartz substrate by thermal evaporation technique, Superlattice. Microst. 82 (2015) 368–377, https://doi.org/10.1016/j.spmi.2015.02.036.
[8] W. Yuan, J. Yuan, J. Xie, C.M. Li, Polymer-mediated self-assembly of TiO2@Cu2O core – shell nanowire array for highly efficient photoelectrochemical water oxidation, Appl. Mater. Interfaces (2016), https://doi.org/10.1021/acsami.6b00030.
[9] M. Uysal, R. Karslioğlu, A. Alp, H. Akbulut, The preparation of core-shell Al2O3/Ni composite powders by electroless plating, Ceram. Int. 39 (2013) 5485–5493. https://doi.org/10.1016/j.ceramint.2012.12.060.
[10] M. Milde, S. Dembski, A. Osvet, M. Batentschuk, A. Winnacker, G. Sextl, Polymer-assisted sol-gel process for the preparation of photostimulable core/shell structured SiO2/Zn2SiO4:Mn2+ particles, Mater. Chem. Phys. 148 (2014) 1055–1063. https://doi.org/10.1016/j.matchemphys.2014.09.017.
[11] R.E. Rojas-Hernandez, F. Rubio-Marcos, A. Serrano, A. Del Campo, J.F. Fernandez, Precise tuning of the nanostructured surface leading to the luminescence enhancement in SrAl2O4 based core/shell structure, Sci. Rep. 7 (2017) 462, https://doi.org/10.1038/s41598-017-00541-w.
[12] J.J. Reinosa, P. Leret, C.M. Álvarez-Docio, A. del Campo, J.F. Fernández, Enhancement of UV absorption behavior in ZnO–TiO2 composites, Boletín La Soc. Española Cerámica y Vidr. 55 (2016) 55–62, https://doi.org/10.1016/j.bsecv.2016.01.004.
[13] F. Rubio-Marcos, V. Calvino-Casilda, M.A. Bañares, J.F. Fernandez, Novel hierarchical Co3O4/ZnO mixtures by dry nanodispersion and their catalytic application in the carbonylation of glycerol, J. Catal. 275 (2010) 288–293. https://doi.org/10.1016/j.jcat.2010.08.009.
[14] F. Rubio-marcos, C. V Manzano, J.J. Reinosa, J.J. Romero, P. Marchet, M.S. Martin-Gonzalez, J.F. Fernandez, Mechanism of Ni(1-x)ZnxO formation by thermal treatments on NiO nanoparticles dispersed over ZnO, J. Phys. Chem. C (2011) 13577–13583.
[15] C.M. Álvarez-Docio, J.J. Reinosa, A. del Campo, J.F. Fernández, 2D particles forming a nanostructured shell: a step forward cool NIR reflectivity for CoAl2O4 pigments, Dyes Pigments 137 (2017) 1–11, https://doi.org/10.1016/j.dyepig.2016.09.061.
[16] J. López-Sánchez, A. Serrano, A. Del Campo, M. Abuín, O. Rodríguez De La Fuente, N. Carmona, Sol-gel synthesis and micro-Raman characterization of ε-Fe2O3 micro- and nanoparticles, Chem. Mater. 28 (2016) 511–518, https://doi.org/10.1021/acs.chemmater.5b03566.
[17] F. Rubio-Marcos, A. Del Campo, P. Marchet, J.F. Fernández, Ferroelectric domain wall motion induced by polarized light, Nat. Commun. 6 (2015) 6594, https://doi.org/10.1038/ncomms7594.
[18] E. Enríquez, M.A. De Rubia, A. Del Campo, J.F. Ferna, Characterization of carbon nanoparticles in thin-film nanocomposites by confocal Raman microscopy, J. Phys. Chem. C 118 (2014) 10488–10494, https://doi.org/10.1021/jp502403r.
[19] I. Lorite, A. del Campo, J.J. Romero, J.F. Fernández, Isolated nanoparticle Raman spectroscopy, J. Raman Spectrosc. 43 (2012) 889–894. https://doi.org/10.1002/jrs.3112.
[20] Z.J. Zhang, Q.C. Zheng, L. Sun, Synthesis of 2-D nanostructured BiVO4: Ag hybrid as an e fficient electrode material for supercapacitors 43 (2017) 16217–16224, https://doi.org/10.1016/j.ceramint.2017.08.200.
[21] K.E. Sickafus, J.M. Wills, N.W. Grimes, Structure of spinel, J. Am. Ceram. Soc. 82 (1999) 3279–3292. https://doi.org/10.1111/j.1151-2916.1999.tb02241.x.
[22] H. Zheng, Q. Zhan, F. Zavaliche, M. Sherburne, F. Straub, M.P. Cruz, L.-Q. Chen, U. Dahmen, R. Ramesh, Controlling self-assembled perovskite-spinel nanostructures, Nano Lett. 6 (2006) 1401–1407. https://doi.org/10.1021/nl060401y.
[23] L. Zhao, H. Zhang, Y. Xing, S. Song, S. Yu, W. Shi, X. Guo, J. Yang, Y. Lei, F. Cao, Morphology-controlled synthesis of magnetites with nanoporous structures and excellent magnetic properties, Chem. Mater. 20 (2008) 198–204, https://doi.org/10.1021/cm702352y.
[24] F. Wang, H. Wu, Z. Lin, S. Han, D. Wang, Y. Xue, Y. Sun, J. Sun, B. Li, Shape evolution of Cu-doped Mn3O4 spinel microcrystals: influence of copper content, Mater. Res. Bull. 45 (2010) 1567–1573, https://doi.org/10.1016/j.materresbull.2010.07.022.
[25] W.B. White, B.A.D. Anoelis, Interpretation of the vibrational spectra of spinels, Spectrochim. Acta 25 (1967).
[26] V. D'Ippolito, G.B. Andreozzi, D. Bersani, P.P. Lottici, Raman fingerprint of chromate, aluminate and ferrite spinels, J. Raman Spectrosc. 46 (2015) 1255–1264. https://doi.org/10.1002/jrs.4764.
[27] O.N. Shebanova, P. Lazor, Raman spectroscopic study of magnetite (FeFe2O4): a new assignment for the vibrational spectrum, J. Solid State Chem. 174 (2003) 424–430, https://doi.org/10.1016/S0022-4596(03)00294-9.
[28] T. Yamanaka, I. Motohiko, Raman Scattering and Lattice Vibrations of Ni2SiO4 Spinel at Elevated Temperature, 1986, pp. 156–160.
[29] C.M. Julien, M. Massot, Lattice vibrations of materials for lithium rechargeable batteries I . Lithium manganese oxide spinel 97 (2003).
[30] B.D. Hosterman, Raman Spectroscopic Study of Solid Solution Spinel Oxides, University of Nevada, Las Vegas, 2011.
[31] H. Shirai, Y. Morioka, I. Nakagawa, Infrared and Raman spectra and lattice vibrations of some oxide spinels, J. Phys. Soc. Jpn. 51 (1982) 592–597.
[32] M. Bouchard, A. Gambardella, Raman microscopy study of synthetic cobalt blue spinels used in the field of art, J. Raman Spectrosc. 49 (2010) 1477–1485, https://doi.org/10.1002/jrs.2645.
[33] S. Kumar, M. Christy, N. Park, E. Suh, S. Anand, Y. Yu, Hydrothermal synthesis of single-crystalline nanocubes of Co3O4, Mater. Lett. 62 (2008) 1006–1009, https://doi.org/10.1016/j.matlet.2007.07.037.
[34] Z.V. Marinkovic Stanojevi, N. Romcevi, B. Stojanovic, Spectroscopic study of spinel ZnCr2O4 obtained from mechanically activated ZnO – Cr2O3 mixtures 27 (2007) 903–907, https://doi.org/10.1016/j.jeurceramsoc.2006.04.057.
[35] J. Preudhomme, P. Tarte, Infrared studies of spinels—III: the normal II–III spinels, Spectrochim. Acta Part A Mol. Spectrosc. 2 (1971) 1817–1835.
[36] H. Cynn, S.K. Sharma, T.F. Cooney, M. Nicol, High-temperature Raman investigation of order-disorder behavior in the MgAl2O4 spinel, Phys. Rev. B 45 (1992) 500–502.
[37] S. Cava, S.M. Tebcherani, S.A. Pianaro, C.A. Paskocimas, E. Longo, J.A. Varela,

Structural and spectroscopic analysis of γ-Al2O 3 to α-Al2O3-CoAl2O4 phase transition, Mater. Chem. Phys. 97 (2006) 102–108, https://doi.org/10.1016/j.matchemphys.2005.07.057.
[38] S. Hashimoto, A. Yamaguchi, Synthesis of α–Al2O3 platelets using sodium sulfate flux, J. Mater. Res. 14 (1996) 4667–4672.
[39] T. Aghavnian, J.B. Moussy, D. Stanescu, R. Belkhou, N. Jedrecy, H. Magnan, P. Ohresser, M.A. Arrio, P. Sainctavit, A. Barbier, Determination of the cation site distribution of the spinel in multiferroic CoFe2O4/BaTiO3 layers by X-ray photoelectron spectroscopy, J. Electron. Spectrosc. Relat. Phenom. 202 (2015) 16–21, https://doi.org/10.1016/j.elspec.2015.02.006.
[40] S. Nayak, S. Thota, D.C. Joshi, M. Krautz, A. Waske, A. Behler, J. Eckert, T. Sarkar, M.S. Andersson, R. Mathieu, V. Narang, M.S. Seehra, Magnetic compensation, field-dependent magnetization reversal, and complex magnetic ordering in Co2TiO4, Phys. Rev. B 92 (2015) 214434, https://doi.org/10.1103/PhysRevB.92.214434.
[41] Y. Tang, C. Wu, Y. Song, Y. Zheng, K. Zhao, Effects of colouration mechanism and stability of CoAl2O4 ceramic pigments sintered on substrates, Ceram. Int. 44 (2018) 1019–1025, https://doi.org/10.1016/j.ceramint.2017.10.038.
[42] X. Duan, M. Pan, F. Yu, D. Yuan, Synthesis, structure and optical properties of CoAl2O4 spinel nanocrystals, J. Alloys Compd. 509 (2011) 1079–1083, https://doi.org/10.1016/j.jallcom.2010.09.199.
[43] G. Jacobs, J.A. Chaney, P.M. Patterson, T.K. Das, B.H. Davis, Fischer-Tropsch synthesis: study of the promotion of Re on the reduction property of Co/Al2O3 catalysts by in situ EXAFS/XANES of Co K and Re LIII edges and XPS, Appl. Catal. A Gen. 264 (2004) 203–212, https://doi.org/10.1016/j.apcata.2003.12.049.
[44] S.C. Petitto, M. a. Langell, Cu2O (110) formation on Co3O4 (110) induced by copper impurity segregation, Surf. Sci. 599 (2005) 27–40, https://doi.org/10.1016/j.susc.2005.09.034.
[45] Z. Zhou, Y. Zhang, Z. Wang, W. Wei, W. Tang, J. Shi, R. Xiong, Electronic structure studies of the spinel CoFe2O4 by X-ray photoelectron spectroscopy, Appl. Surf. Sci. 254 (2008) 6972–6975, https://doi.org/10.1016/j.apsusc.2008.05.067.
[46] L. Yin, I. Adler, T. Tsang, L.J. Matienzo, S.O. Grim, Paramagnetism and shake-up satellites in X-ray photoelectron spectra, Chem. Phys. Lett. 24 (1974) 81–84.
[47] M.C. Munisso, W. Zhu, G. Pezzotti, Raman tensor analysis of sapphire single crystal and its application to define crystallographic orientation in polycrystalline alumina, Phys. Status Solidi 246 (2009) 1893–1900, https://doi.org/10.1002/pssb.200945137.
[48] H.A. Girard, S. Perruchas, C. Gesset, M. Chaigneau, L. Vieille, J.C. Arnault, P. Bergonzo, J.P. Boilot, T. Gacoin, Electrostatic grafting of diamond nanoparticles: a versatile route to nanocrystalline diamond thin films, ACS Appl. Mater. Interfaces 1 (2009) 2738–2746, https://doi.org/10.1021/am900458g.
[49] Y. El Mendili, J.-F. Bardeau, N. Randrianantoandro, A. Gourbil, J.-M. Greneche, A.-M. Mercier, F. Grasset, New evidences of in situ laser irradiation effects on γ-Fe2O3 nanoparticles: a Raman spectroscopic study, J. Raman Spectrosc. 42 (2011) 239–242, https://doi.org/10.1002/jrs.2762.
[50] A. Ahlawat, V.G. Sathe, Raman study of NiFe2O4 nanoparticles, bulk and films: effect of laser power, J. Raman Spectrosc. 42 (2011) 1087–1094, https://doi.org/10.1002/jrs.2791.
[51] I. Lorite, J.J. Romero, J.F. Fernández, Effects of the agglomeration state on the Raman properties of Co3O4 nanoparticles, J. Raman Spectrosc. (2012), https://doi.org/10.1002/jrs.4098.
[52] I. Lorite, M.S. Martín-González, J.J. Romero, M.A. García, J.L.G. Fierro, J.F. Fernández, Electrostatic charge dependence on surface hydroxylation for different Al2O3 powders, Ceram. Int. 38 (2012) 1427–1434, https://doi.org/10.1016/j.ceramint.2011.09.024.
[53] J.E. Spanier, R.D. Robinson, F. Zhang, S. Chan, I.P. Herman, Size-dependent properties of CeO2 – y nanoparticles as studied by Raman scattering, Phys. Rev. B 64 (2001), 245407, https://doi.org/10.1103/PhysRevB.64.245407.
[54] T. M, D.J. Late, Temperature dependent phonon shifts in single-layer WS2, Appl. Mater. Interfaces 6 (2014) 1158–1163, https://doi.org/10.1021/am404847d.
[55] N. Peimyoo, J. Shang, W. Yang, Y. Wang, C. Cong, T. Yu, Thermal conductivity determination of suspended mono- and bilayer WS2 by Raman spectroscopy, Nano Res. 8 (2015) 1210–1221, https://doi.org/10.1007/s12274-014-0602-0.
[56] I. Calizo, A.A. Balandin, W. Bao, F. Miao, C.N. Lau, Temperature dependence of the Raman spectra of graphene and graphene multilayers, Nano Lett. 7 (2007) 2645–2649, https://doi.org/10.1021/nl071033g.
[57] K.R. Zhu, M.S. Zhang, Q. Chen, Z. Yin, Size and phonon-confinement effects on low-frequency Raman mode of anatase TiO2 nanocrystal, Phys. Lett. Sect. A Gen. At. Solid State Phys. 340 (2005) 220–227, https://doi.org/10.1016/j.physleta.2005.04.008.
[58] S. Tsunekawa, R. Sahara, Y. Kawazoe, A. Kasuya, Origin of the blue shift in ultraviolet absorption spectra of nanocrystalline CeO2-x particles, Mater. Trans., JIM 41 (2000) 1104–1107, https://doi.org/10.2320/matertrans1989.41.1104.
[59] H. Richter, Z.P. Wang, L. Ley, The one phonon Raman spectrum in microcrystalline silicon, Solid State Commun. 39 (1981) 625–629, https://doi.org/10.1016/0038-1098(81)90337-9.
[60] A.K. Arora, M. Rajalakshmi, T.R. Ravindran, V. Sivasubramanian, Raman spectroscopy of optical phonon confinement in nanostructured materials, J. Raman Spectrosc. 38 (2007) 604–617, https://doi.org/10.1002/jrs.1684.
[61] I. Lorite, J.J. Romero, J.F. Fernandez, Influence of the nanoparticles agglomeration state in the quantum-confinement effects: experimental evidences, AIP Adv. 5 (2015), https://doi.org/10.1063/1.4914107.

Supplementary material

Investigation of Thermal Stability of 2D and 3D $CoAl_2O_4$ Particles in Core-Shell Nanostructures by Raman Spectroscopy

C.M. Álvarez-Docio*, J. J. Reinosa, A. del Campo, J. F. Fernández.

Instituto de Cerámica y Vidrio, CSIC, C/Kelsen 5, 28049, Madrid, Spain.

*E-mail address: carmenma.docio@icv.csic.es (Carmen Álvarez)

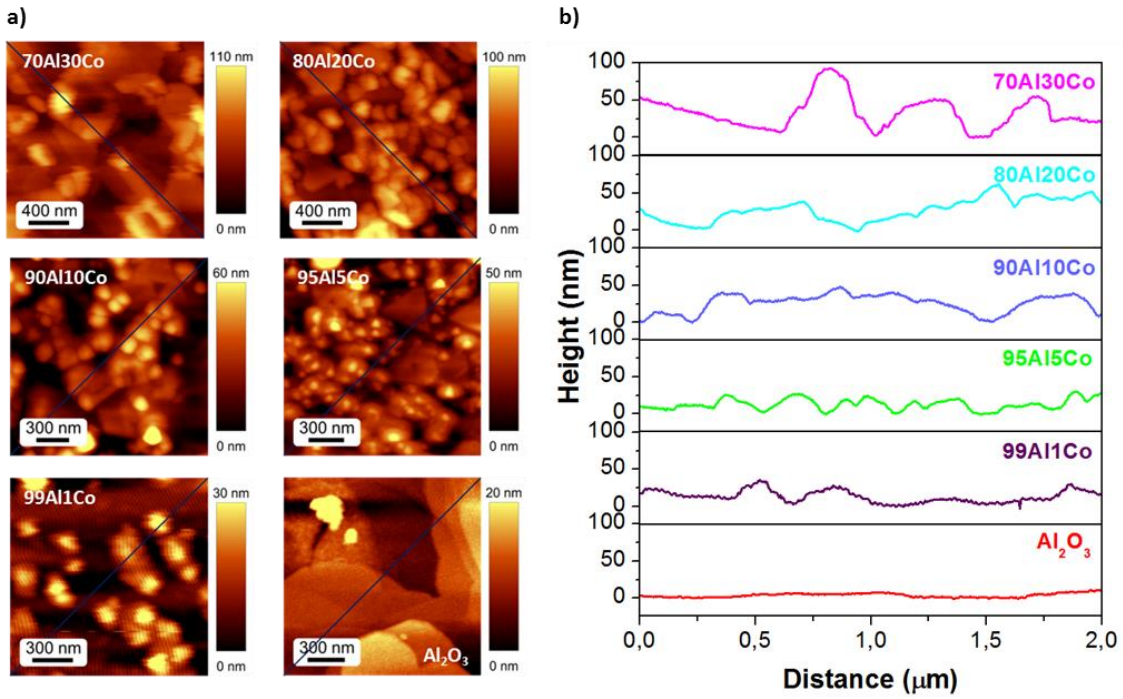

Figure S.1 *a) Two dimensional (2D) AFM topographical images of different samples showing the surface of the microparticle covered by nanocrystals. The black line corresponds the place where the roughness profile was calculated. b) Roughness profiles for the complete range of compositions.*

The surface roughness of the 2D and 3D structures is confirmed by AFM characterization (***Fig. S.1***). The roughness of the core-shell nanostructured particles varies depending on the starting amount of Co_3O_4. Hence, samples with lower amount of Co_3O_4 in composition allow the presence of isolated Co_3O_4 nanoparticles, so 2D $CoAl_2O_4$ particles predominate. Whereas, agglomerates are present in samples with higher percentages of Co_3O_4 and 3D particles are in the majority. The α-Al_2O_3 sample shows the typical morphology consisting mainly on plate type particles characteristic of this material, due to crystal growth in the ab plane.

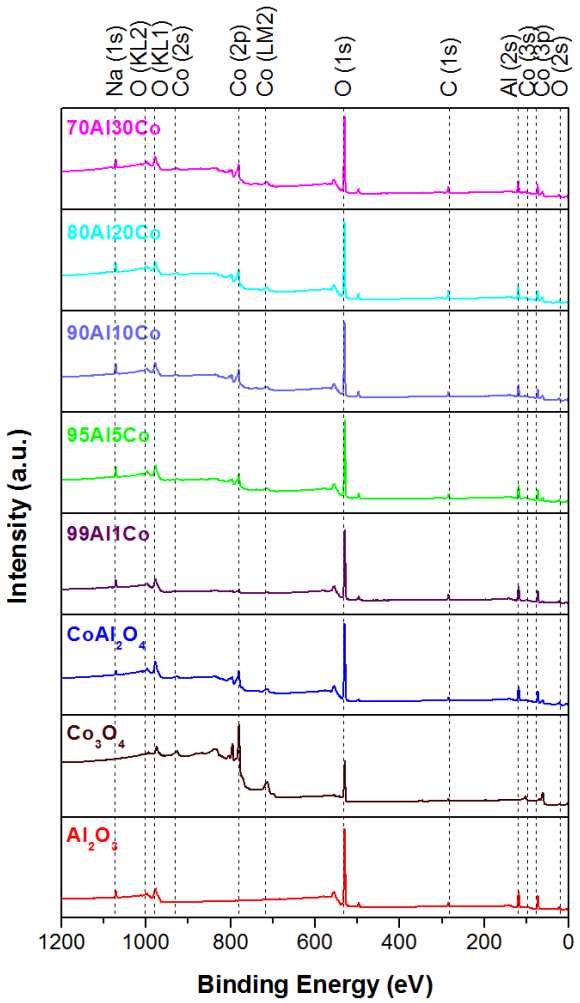

Figure S.2 *Survey XPS spectrum of the samples.*

In order to confirm the absence of a Co_3O_4 spinel at the surface of the platelets of α-Al_2O_3, an XPS study was performed (***Fig. S.2***). The XPS spectra of all the samples annealed at 1200ºC, as well as the references (Al_2O_3, Co_3O_4 and $CoAl_2O_4$), indicating that, in addition to the raw materials and contaminated carbon, sodium was detected as a contaminant specie. As indicated by the XPS spectrum of α-Al_2O_3, the presence of sodium comes from the α-Al_2O_3 particles. In addition, the C1s peak at 284.6 eV of contaminant carbon is used as reference.

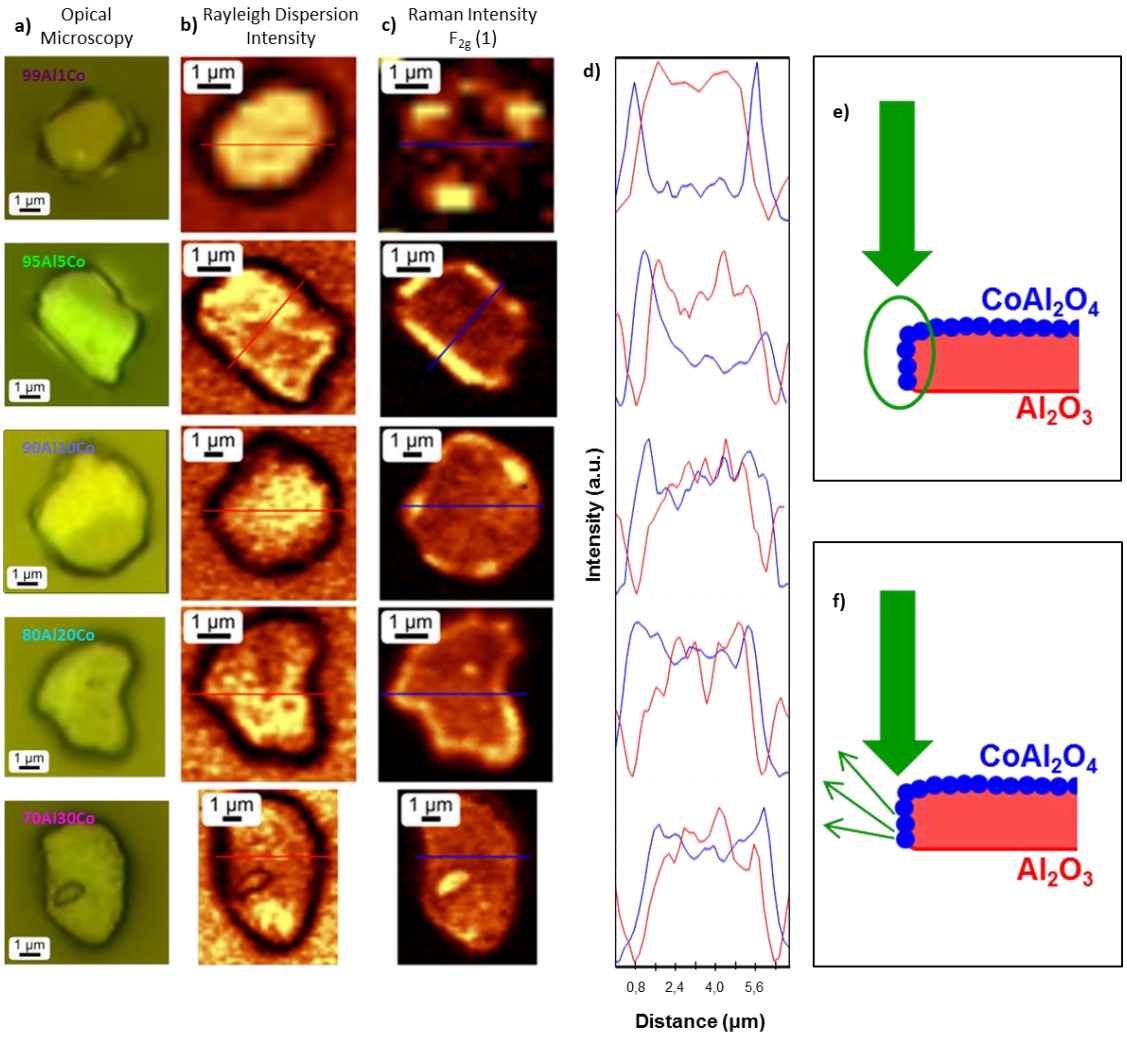

Figure S.3 *a) Confocal Optical Microscopy micrographs of core-shell nanostructured microparticles for 100-xAlxCo series. b) Raman image representation of the Rayleigh dispersion intensity of the particles presented in a. c) Raman image representation of the Raman intensity of the F_{2g} (1) mode of the particles presented in a. d) Graphical representation of the Rayleigh dispersion intensity and the Raman intensity of the F_{2g} (1) mode of the particles presented in a. e and f) Explicative model for higher heating of particles at the edge than in the centre.*

For the Raman study, differences in the Raman Rayleigh Dispersion intensity are observed for the different microparticles between the edges and the centre of the microparticles (***Fig. S.3b***). This situation is due to the morphology of α-Al_2O_3. The edges of the platelets present more structural elements that favour light dispersion. Moreover, the Raman intensity for the aluminate phase is higher at the edge of the microparticles (***Fig. S.3d***). This effect is due to the measure procedure, again because of the morphology of α-Al_2O_3. On the external part, the Raman laser beam falls on more $CoAl_2O_4$ nanoparticles than in the case of the

interior area of the core-shell (see ***Fig. S.3e***). So, in the external area the intensity Raman Shift increases because the laser beam interacts with higher amounts of $CoAl_2O_4$ nanoparticles.

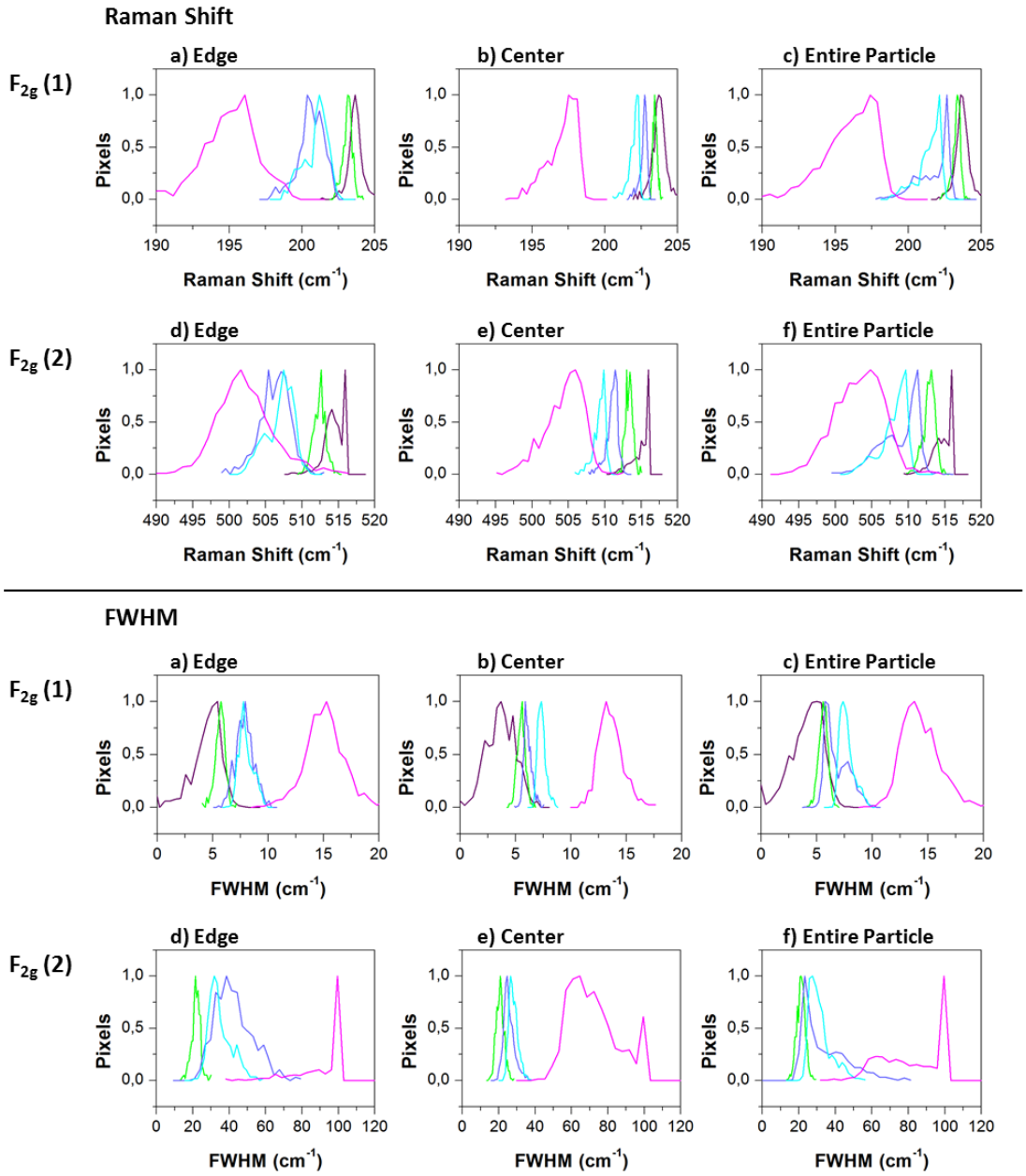

Figure S.4 *Statistical analysis obtained from Raman study.*

A statistical analysis of Raman shift and FWHM of Raman signal are represented as histograms. In this study, it was taken into account that each pixel of the Raman images contains the full Raman spectrum (***Fig. S.4***). From the histograms, the main values of Raman shift and FWHM for the different core-shell nanostructured microparticles were extracted as a function of the centre and edge location. The study was performed for F_{2g} (1) and F_{2g} (2) active Raman modes.

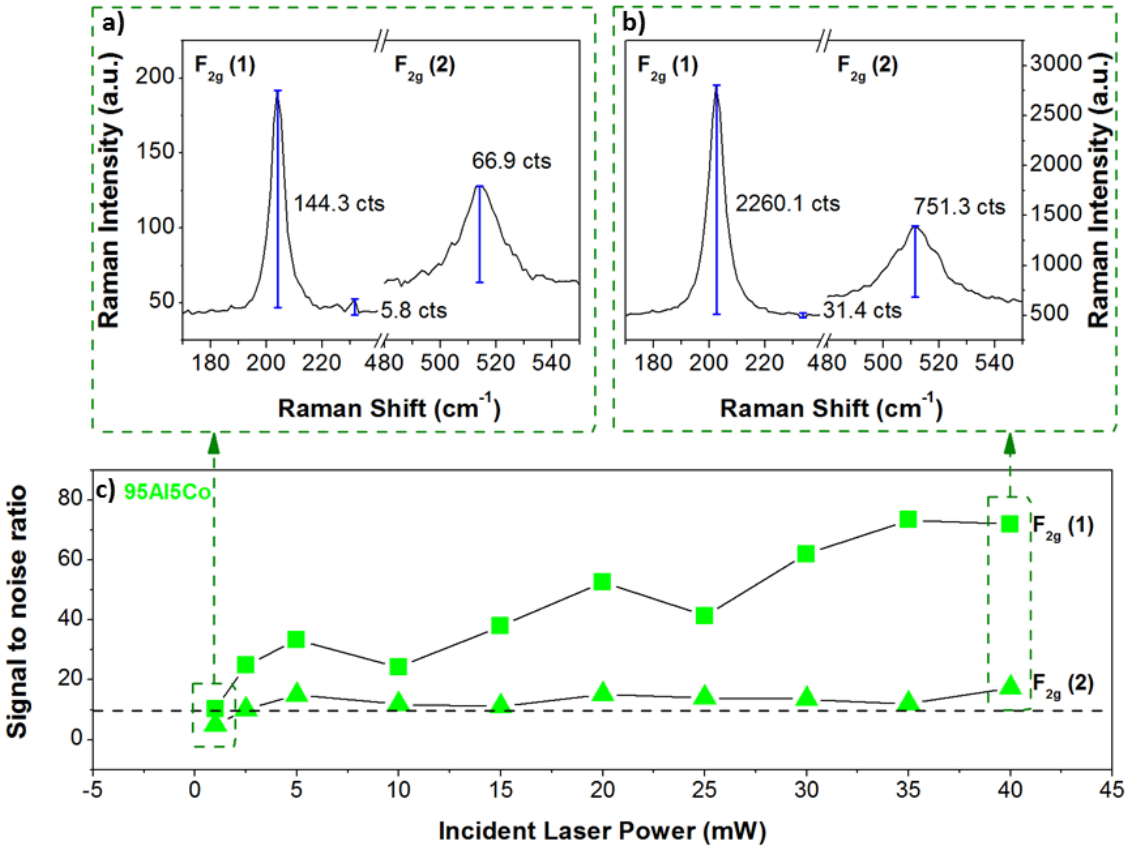

Figure S.5 *F_{2g} (1) and F_{2g} (2) Raman active modes in spectrum for the 95Al5Co sample: a) with a output laser power of 1 mW and b) with a output laser power of 40 mW. c) Signal to noise ratio as a function of the laser power.*

Raman acquisition procedure: For the Raman study, the minimum excitation laser power was chosen as the one that produced a reproducible Raman signal of the spinel structure with a signal to noise ratio of >10 units of intensity (***Fig. S.5***). Thus interference, i.e. heating of the sample or modifications to the structure, was highly avoided because only the minimum laser beam power necessary for obtaining accurate results was applied.

Artículo 3

Revealing the Role of the Intermediates during the Synthesis of $BaTi_5O_{11}$

Carmen María Álvarez Docio, Julián Jiménez Reinosa, Giovanna Canu, María Teresa Buscaglia, Vincenzo Buscaglia, José Francisco Fernández.

Inorganic Chemistry, 58, 2019, 8120-8129.

Factor de impacto: 4.850 (según JCR Edition Science 2018).

Inorganic Chemistry
Cite This: Inorg. Chem. 2019, 58, 8120−8129
Article
pubs.acs.org/IC

Revealing the Role of the Intermediates during the Synthesis of $BaTi_5O_{11}$

Carmen María Álvarez-Docio,*[,†] Julián Jiménez Reinosa,[†] Giovanna Canu,[‡] María Teresa Buscaglia,[‡] Vincenzo Buscaglia,[‡] and José Francisco Fernández[†]

[†]Ceramics for Smart Systems Group, Ceramic and Glasses Institute (ICV-CSIC), C/Kelsen 5, Madrid, Spain
[‡]Synthesis of Advanced Functional Oxides Group, Institute of Condensed Matter Chemistry and Technologies for Energy (IENI-CNR), Via de Marini 6, Genoa, Italy

Supporting Information

ABSTRACT: $BaTi_5O_{11}$ has been extensively studied because of their microwave dielectrics properties. Traditionally, it is difficult to achieve this material as single-phase. Here, we report an effective method to obtain $BaTi_5O_{11}$ powder with nanometer-scale crystals, by solid-state reaction at moderate temperatures and using as precursors nanostructured particles consisting of $BaTiO_3$ and TiO_2. The main advantage is the intimate contact between the $BaTiO_3$ and TiO_2 that ensure, when the solid-state reaction takes place, the formation of complex solid compounds from three or more constituents. The formation mechanism of $BaTi_5O_{11}$ has been studied as a function of both the thermal treatment and the time reaction. The reaction was monitored by Raman spectroscopy combined with Confocal microscopy, the aim of this characterization technique is to provide the description of the general strategy and design principles to obtain $BaTi_5O_{11}$ powder. Consequently, this work is a challenging task for the compositional and structural study of complex inorganic nanoparticles.

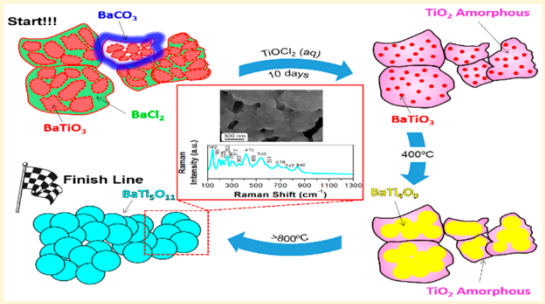

INTRODUCTION

The different crystalline phases present in the binary system of $BaTiO_3$−TiO_2 exhibit excellent microwave properties.[1] Specifically, $BaTi_5O_{11}$ ceramic has demonstrated potent functional dielectric characteristics, resulting in an interesting advanced material for microwave communications.[2−4] Owing to its high interest, $BaTi_5O_{11}$ powder as a single-phase has been the subject of research, and a great number of researchers have tried to produce this material in a variety of ways. O'Bryan and Thomson[5] synthesized $BaTi_5O_{11}$ by the traditional ceramic method, such as the solid-state reaction of $BaCO_3$ and TiO_2 at high temperatures (1100−1400 °C); however, this method could not produce single-phase material. Ritter et al.[6] produced the $BaTi_5O_{11}$ compound by a controlled hydrolysis. They relied on O'Bryan's study to predict the excellent dielectric properties of the $BaTi_5O_{11}$ material. Other chemical processes were effectively used to obtain the fine powder of $BaTi_5O_{11}$ as a single-phase. Fukui et al.[7] reported the effects of the thermal treatment on the sintering of $BaTi_5O_{11}$ ceramics from an alkoxide-derived powder. Employing a liquid-mix method, Javadpour and Eror[8] obtained $BaTi_5O_{11}$ by calcining the mixture obtained after the reaction of tetraisopropyl titanate, barium carbonate, and an ethylene glycolcitric acid solution. Lu et al.[9] and Tangjuank et al.[10] obtained $BaTi_5O_{11}$ powder using a sol−gel process; in both cases, the precursors were sintered at temperatures from 700 to 1200 °C. In addition, the evolution in the structure of intermediates, the mechanism involved during the reaction, and the final morphology of $BaTi_5O_{11}$ material, because of the thermal processing, are still not clearly defined.[10]

Chemical reactions may be optimized by reaction monitoring because it provides information about the chemical development at every stage of the reaction system.[11] Transmission Electron Microscopy (TEM) and X-ray Diffraction (XRD)[12] are currently used to structurally determine the reaction phases. However, reaction in nanostructured materials still represents a challenge because the structural analysis of nanoregions is limited in multiple phases systems. Confocal Raman microscopy is a powerful tool for research, which may introduce significant enhancements over other common analytical techniques. It is a nondestructive, noninvasive, and contact- and label-free technique and discloses evidence about the stress and strain states, crystal structure, electronic properties, and lattice vibrations. Consequently, it permits detecting the different phases present in the materials.[13] Moreover, the combination of confocal Raman spectroscopy and confocal microscopy, allows us to systematically study the structure−microstructure of a wide variety of materials and composites, as well as to resolve the spatial distribution of the compounds, owing to the high spectral and spatial resolution of this technique.[14−16] In this sense, Raman

Received: March 27, 2019
Published: June 4, 2019

DOI: 10.1021/acs.inorgchem.9b00865
Inorg. Chem. 2019, 58, 8120−8129

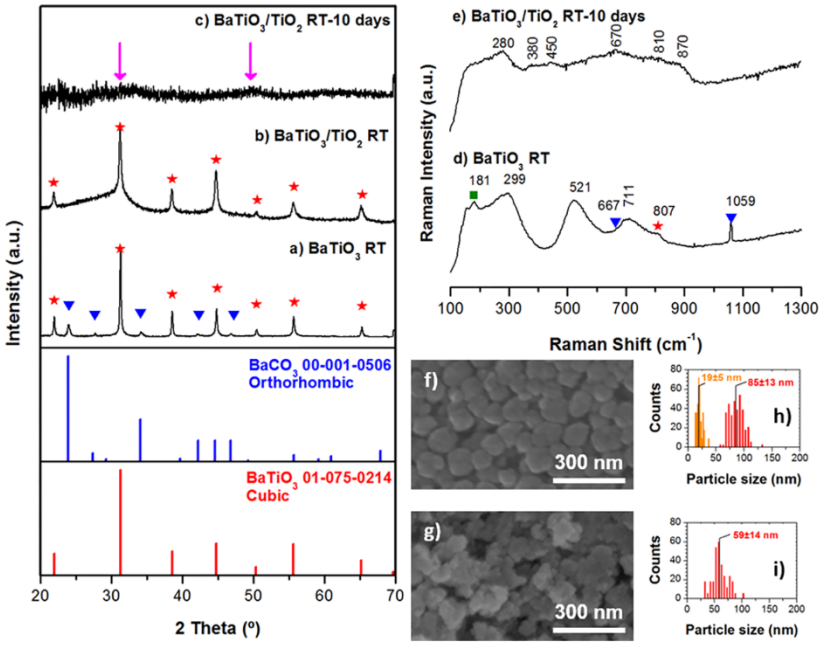

Figure 1. Diffraction patterns of (a) as-obtained $BaTiO_3$ particles, (b) fresh $BaTiO_3/TiO_2$ composite particles, and (c) 10 days aged $BaTiO_3/TiO_2$ composite particles (the arrow indicates the peaks of amorphous titania). Raman spectrum obtained for (d) as-obtained $BaTiO_3$ particles and (e) 10 days aged $BaTiO_3/TiO_2$ composite particles (peaks signaled as blue triangles, green squares, and red stars correspond to $BaCO_3$, $BaCl_2$, and internal defects, respectively). FESEM micrographs of (f) as obtained $BaTiO_3$ particles and (g) 10 days aged $BaTiO_3/TiO_2$ composite particles. Particle size distribution of (h) as-obtained $BaTiO_3$ particles and (i) 10 days aged $BaTiO_3/TiO_2$ composite particles.

spectroscopy is an effective technique for the characterization of the different phases obtained during a solid-state reaction.

In conclusion, this work will contribute to study the thermal evolution of core−shell $BaTiO_3/TiO_2$ nanoparticles to obtain single-phase $BaTi_5O_{11}$ particles. $BaTiO_3$ nanoparticles were synthesized through a hydrothermal method and consequently coated accordingly with a TiO_2 shell. Therefore, the samples were characterized by Raman spectroscopy, X-ray Photoelectron Spectroscopy (XPS) and XRD; in order to evaluate the behavior of the reagents used for the preparation of the core−shell particles and its effects in the solid-state reaction during the thermal treatments.

EXPERIMENTAL PROCEDURE

Synthesis. The synthesis of barium titanate particles was accomplished following this chemical reaction:[17]

$$BaCl_2(aq) + TiOCl_2(aq) + 4NaOH(aq) \rightarrow BaTiO_3(s) + 4NaCl(aq) + 2H_2O \quad (1)$$

where (aq) designates an aqueous solution.

The reaction was performed in a continuous Segmented Flow Tubular Reactor (SFTR), similar to that used by Jongen et al.[18] The reaction was carried out at 95 °C, and the residence time in the tubular reactor (length, 12 m; inner diameter, 4 mm) was 10 min. The $BaTiO_3$ precipitate obtained after reaction was centrifuged, it should be washed with water until it was free from chloride ions, and finally dried. Additional details about the preparation and properties of the barium titanate particles used as templates can be found at the Supporting Information.[19,20]

The previous obtained $BaTiO_3$ particles were introduced in a peroxotitanium(IV) solution (prepared as described in the Supporting Information) under continuous slow stirring at room temperature. The amount of Ti(IV) solution spent for the coating process was calculated to have an overall stoichiometry corresponding to Ti/Ba = 5. The suspension was maintained at 95 °C for 1 h. The resulting yellow powder, was then filtrated, washed with water until it was free from chloride ions, and finally dried.

Finally, the resulting $BaTiO_3/TiO_2$ powders were introduced in a cylindrical steel body of 1 cm in diameter, and they were compacted by isostatic cold pressing. Then, sintering was carried out, in a conventional muffle furnace, at different temperatures between 400 to 1000 °C with a heating rate of 5 °C/min. The hold time at the maximum temperature was 1 min in each treatment.

Characterization. The crystalline structure of the samples was studied by XRD in a D8 Bruker diffractometer with Cu Kα radiation and a Lynx Eye detector.

Differential thermal (DTA) analysis joined to thermogravimetric (TG) analysis was carried out to study the thermal behavior of the materials by using a Netzch STA 409 Thermo-Analyzer. The assay conditions correspond to the synthesis process: 20−1400 °C with heating rate of 5 °C/min.

A XPS study determined the surface composition of the samples in a K-Alpha, Thermo Scientific equipment applying pass energy of 200 eV for survey scans and 40 eV for high resolution scans, and shifting the C 1s peak to 285 eV.

The morphology of the particles was observed by using a Field Emission Scanning Electronic Microscope, FESEM, S-4700 from Hitachi. The morphological parameters were obtained by processing FESEM micrographs with Leica Qwin Image software. The obtained results consisted of a statistical study of values from more than 150 measured particles.

A confocal micro-Raman Witec α 300R equipment equipped with 532 nm excitation laser was using to achieve a Raman study of the samples by applying an incident laser power of 40 mW. The results treatment was carried out with a Witec Control Plus Software.

DOI: 10.1021/acs.inorgchem.9b00865
Inorg. Chem. 2019, 58, 8120−8129

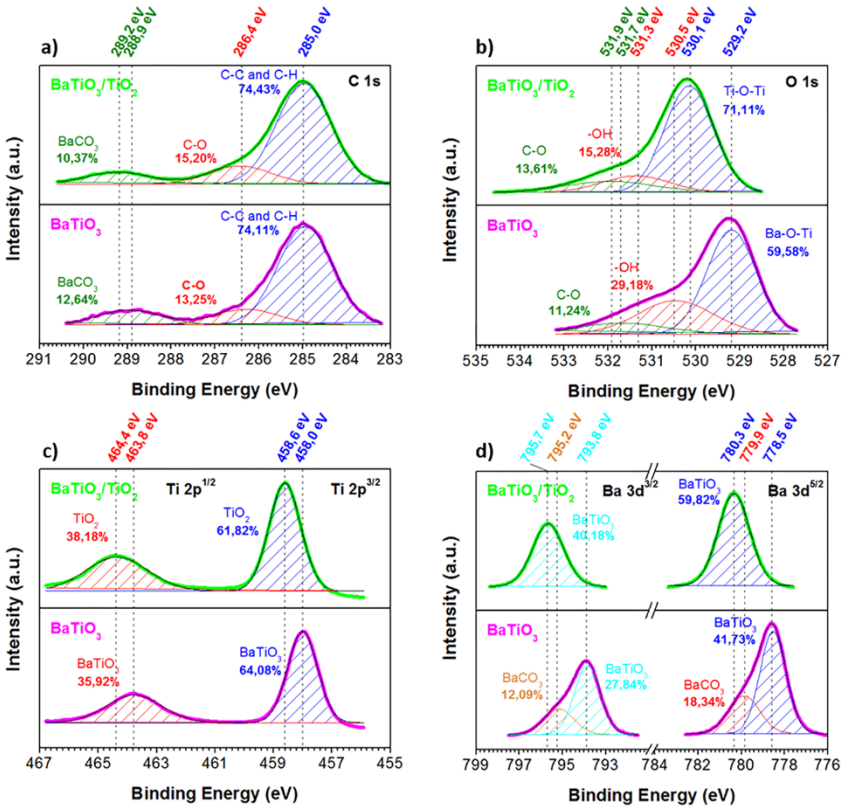

Figure 2. XPS spectra of as-prepared $BaTiO_3$ (pink line) and aged $BaTiO_3/TiO_2$ (green line) composite particles: (a) C_{1s}, (b) O_{1s}, (c) Ti_{2p}, and (d) Ba_{3d} elements.

■ RESULTS AND DISCUSSION

The crystalline structure of the precursors is determined by XRD (Figure 1). Figure 1a shows that the as-precipitated $BaTiO_3$ particles possess the typical pseudocubic structure of hydrothermal particles (JCPDS 01-075-0214). In addition, it is possible to distinguish the presence of $BaCO_3$ (JCPDS 00-001-0506), despite the precautions taken during the synthesis. Figure 1b,c shows the XRD patterns of the $BaTiO_3/TiO_2$ particles, both as prepared and after 10 days aging. The diffractogram of the freshly prepared sample are characterized by the superposition of narrow diffraction peaks corresponding to the cubic $BaTiO_3$ and a broad hump at 25−35° 2θ that could be associated with the amorphous titania phase.[21,22] After 10 days of aging, the diffraction peaks of $BaTiO_3$ almost disappear, leaving only the characteristic diffraction spectrum of amorphous hydrated titania, which does not reveal any crystal characteristics; it only shows two wide bands, one centered at ~32° 2θ and the other at ~50° 2θ.[23] According to the previous studies,[24−27] the amorphous phase of peroxo-titanium hydrate with a unknown structure is generated when the spontaneous hydrolysis at room temperature of the peroxo-titanium solution occurs.[23] In the temperature range of 80−100 °C, the peroxo-titanium hydrate evolves toward the formation of an amorphous hydrated titania.[25−27] Consequently, we suggest that the amorphous layer achieved in this work consists mainly of an amorphous titania comprising hydration water.[23,28]

The Raman spectrum for the as-precipitated $BaTiO_3$ sample shows the typical spectrum for $BaTiO_3$ in a pseudocubic phase (Figure 1d). This polymorph is based on cubic $Pm3m$ (O_h^1) symmetry and the phonon modes are represented by $3F_{1u} + F_{2u}$.[29] Although no Raman-active mode is predicted for the cubic phase, it has been reported that it typically shows two wide Raman bands at around 250 and 520 cm^{-1}.[29−32] The as-precipitated $BaTiO_3$ presents Raman bands centered at about 299 and 521 cm^{-1}, which indicates local disorder of titanium atoms in a nominally pseudocubic phase. Raman bands at 667 and 1059 cm^{-1} are also detected in the samples and are assigned to the $BaCO_3$ phase,[30,33,34] while the Raman band at 181 cm^{-1} is attributed to the $BaCl_2$ phase[35−37] (a complete assignment of the $BaCl_2$ spectrum is given in the Supporting Information, Figure S1). The Raman band at 807 cm^{-1} should have been caused by the deformation of hydroxyl lattice groups, they are located in the $BaTiO_3$ structure as defects in oxygen sites.[38,39]

The Raman spectrum of the 10 days aged precipitate of $BaTiO_3/TiO_2$ sample shows several broad Raman features located at about 280, 380, 450, 670, 810, and 870 cm^{-1} (Figure 1e). These Raman bands correspond to the vibration modes of the Ti−O−Ti bonds.[23,27,40] It is also worth highlighting that the strong Raman band at 525 cm^{-1}, which is characteristic of the Ti−O−O groups in gels composed of peroxy-titanium, is not observed in the 10 days aged precipitate.[23,27] Thus, it could be excluded the existence of an important quantity of residual peroxy groups in the 10 days aged precipitated particles.

The morphology of as precipitates $BaTiO_3$ nanoparticles is shown in the Figure 1f. The stoichiometric particles are small in size (≈100 nm) and they have a nearly spherical shape.[41]

DOI: 10.1021/acs.inorgchem.9b00865
Inorg. Chem. 2019, 58, 8120−8129

Moreover, into Figure S2 it could be observed smaller primary particles (≈100 nm), that are aggregated to build up the so obtained $BaTiO_3$ particles.

According to similar previous studies,[42] the amorphous titania coating generated onto the surface of barium titanate nanoparticles is owing to the hydrolysis of the peroxotitanium solution. The formation of the coating is promoted by the differences in surface potential between the $BaTiO_3$ particles and the amorphous titania when the pH of the suspension was adjusted to 9. Thus, the amorphous titania self-assemble spontaneous at the barium titanate nanoparticle surface.[23] Furthermore, the morphology of the 10 days aged $BaTiO_3$/TiO_2 composite particles evidence the rearrangement of the primary particle of $BaTiO_3$ during the formation of the titania coating, Figure 1g. It may be noted that the size of the $BaTiO_3$/TiO_2 composite particles is slightly smaller than the $BaTiO_3$ nanoparticles (insets of Figure 1f,g), this fact confirms that the amorphous titania attacks the $BaTiO_3$ aggregates and therefore produces rearrangement. Moreover, the evolution of the crystallinity with the aging indicates that this attack also advance far from the disaggregation and promotes the reduction of crystallinity of the $BaTiO_3$ nanoparticles. This kind of chemical attack only could be justified if some reactant remains in the so obtained powder.

A systematic surface characterization study of the particles was carried out by XPS, which is an effective technique to understand the chemistry produced at the surface of materials, because it provides evidence about the local bonding environment of the samples.[43,44] Moreover, it is a powerful tool for characterizing the chemical structure of nanoparticles at the surface and bulk.[45,46] A survey scan from 1300 to 0 eV (shown in Supporting Information, Figure S3) indicated the existence of barium, titanium, oxygen, and carbon in both the as obtained $BaTiO_3$ and 10 days aged $BaTiO_3$/TiO_2 particles. Additional high-resolution scans (Figure 2a–d) were conducted in the selected binding energy ranges for C_{1s}, O_{1s}, Ti_{2p}, and Ba_{3d}, respectively, in order to quantify the elemental composition of the samples. The C_{1s} peak can be deconvoluted into two principal bands (see Figure 2a) with a peak centered at 285 eV, corresponding to the C–H/C–C species and the other one centered at 286.4 eV, due to C=O groups. The amount of the carbon atoms bonded as C–C/C–H and as C=O is 75% and 15%, respectively. These signals of carbon, owing to the environmental contamination, are assigned as absorbed carbon and absorbed CO_2. However, the C_{1s} peak displays a third component at 288.9 eV for the as prepared $BaTiO_3$ particles and at 289.2 eV for the 10 days aged $BaTiO_3$/TiO_2 particles having a ∼10% contribution and it has been assigned to CO_3^{2-} ions.[47,48] The O_{1s} signal displays also three components, as seen in Figure 2b. For the $BaTiO_3$ particles, there is an intense band near 529.2 eV assigned to oxygen atoms in the Ba–O–Ti structure.[49,50] In the case of the aged $BaTiO_3$/TiO_2 particles, this peak appears at 530.1 eV and it is attributed to the oxygen atoms in Ti–O–Ti structure.[49,50] The peak at 530.5 eV ($BaTiO_3$ particles) or at 531.3 eV (aged $BaTiO_3$/TiO_2 particles) corresponds to the hydroxyl group on the surface of nanoparticles.[47] The O_{1s} emission line at 531.7 eV ($BaTiO_3$ particles) or at 531.9 eV (aged $BaTiO_3$/TiO_2 particles) is assigned to the absorbed oxygen as O–C of CO_2. The fitted Ti_{2p} spectrum for the core $BaTiO_3$ nanoparticles, Figure 2c shows the main peaks assigned to $Ti_{2p}^{1/2}$ and $Ti_{2p}^{3/2}$, centered at 463.8 and 458.0 eV, respectively, which are in good agreement with the bonding energies of Ti^{4+} in $BaTiO_3$,[48] whereas the peaks detected at 464.4 and 458.6 eV in the XPS spectrum of Ti_{2p} for the aged $BaTiO_3$/TiO_2 particles is assigned to the Ti^{4+} in TiO_2.[51] Finally, the Ba_{3d} spectra in both samples $BaTiO_3$ and $BaTiO_3$/TiO_2 look slightly different, Figure 2d. In the case of the $BaTiO_3$ particles, there are two signals due to the Ba_{3d} species ($Ba_{3d}^{3/2}$ and $Ba_{3d}^{5/2}$) that can be deconvoluted into two peaks at around 793.8 and 795.2 eV, which is consistent to barium in titanate and in carbonate species, respectively. Moreover, for the $Ba_{3d}^{5/2}$ the two peaks located about 778.5 and 779.9 eV, also correspond to barium in titanate and in carbonate species, respectively. However, in the case of the aged $BaTiO_3$/TiO_2 particles the Ba_{3d} peak can be resolved into $Ba_{3d}^{3/2}$ at 795.7 eV and $Ba_{3d}^{5/2}$ at 780.3 eV that it is assigned to barium in $BaTiO_3$ without presence of $BaCO_3$. It is worth noting that for the $BaTiO_3$ sample there was no detected chlorine from $BaCl_2$, in contrast with Raman results, where the Cl_{2p} for the $BaCl_2$ should present a peak with a binding energy of 202 eV[52] that was not present in the samples. Furthermore, the $BaTiO_3$ precipitate was carefully washed with water. Accordingly, with the silver nitride test method,[53] the supernatant is chloride ion free. These two ideas may suggest that the $BaCl_2$ could be found between the $BaTiO_3$ aggregates.

Based on the XPS analysis, the weight percentages of Ti, Ba, O, and C were also calculated and listed in Table 1. The relative atomic percentages indicate that the Ba:Ti proportion of $BaTiO_3$ particles is 1:1, whereas for the $BaTiO_3$/TiO_2 composite particles, the Ba:Ti ratio is 1:4, which corresponds with the $BaTi_4O_9$ compound. These data evidence that the $BaTiO_3$/TiO_2 composite sample presents Ba^{2+} cations at the surface that could be related to two aspects: (a) diffusion effect during the synthesis process or (b) incomplete covering of nanoparticles by the amorphous titania shell.

Table 1. Element Contents (%) of Core $BaTiO_3$ and Aged $BaTiO_3$/TiO_2 Composite Particles Based on XPS Analysis

sample	At % Ti	At % Ba	At % O	At % C	Ba/Ti
$BaTiO_3$	13.70	14.34	48.85	23.11	1:1
$BaTiO_3$/TiO_2 (10 days)	16.71	4.54	47.38	31.37	1:4

Figure 3 shows the thermal evolution study of the different samples (DTA/TG). The TG curve of both samples shown a first weight loss in the 40–200 °C temperature range, related to the evaporation of absorbed water. These mass losses continue gradually in the range 200–600 °C related to the chemisorbed OH groups in the nanoparticle crystal lattice.[54] Besides, the $BaTiO_3$ nanoparticles shows two distinct mass losses at higher temperatures signaled by two DTG peaks. The first DTG peak, centered at ∼816 °C, is associated with the thermal decomposition of $BaCO_3$ and CO_2 elimination, in agreement of the endothermic peak observed at this temperature.[55] At higher temperature, the second DTG peak (∼911 °C) could be associated with the Cl^- removal, in spite of the fact that the melting point of $BaCl_2$ occurs at a higher temperature and it is an endothermic phenomena.[12] In the case of aged $BaTiO_3$/TiO_2 composite, the thermogravimetric curves show the loss of adsorption water at temperatures <200 °C and a weak exothermic peak at ∼750 °C without relevant mass variation, that could correspond to the phases crystallization. In order to determine the structural nature of such thermally activated reactions, a XRD and Raman characterization is afforded.

DOI: 10.1021/acs.inorgchem.9b00865
Inorg. Chem. 2019, 58, 8120–8129

Inorganic Chemistry Article

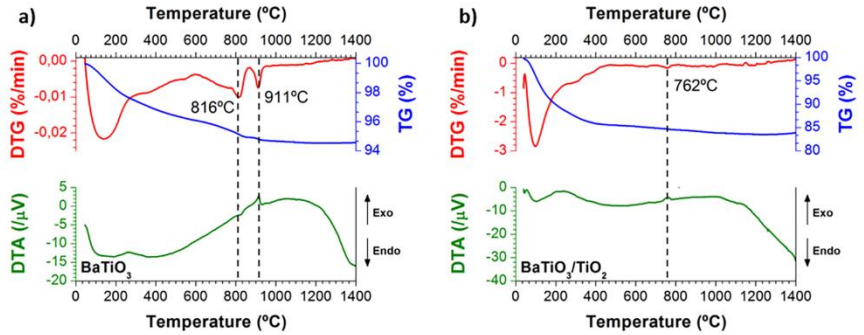

Figure 3. DTA/TG analysis at a 5 °C/min heating rate for the samples: (a) $BaTiO_3$ and (b) $BaTiO_3/TiO_2$ composite particles.

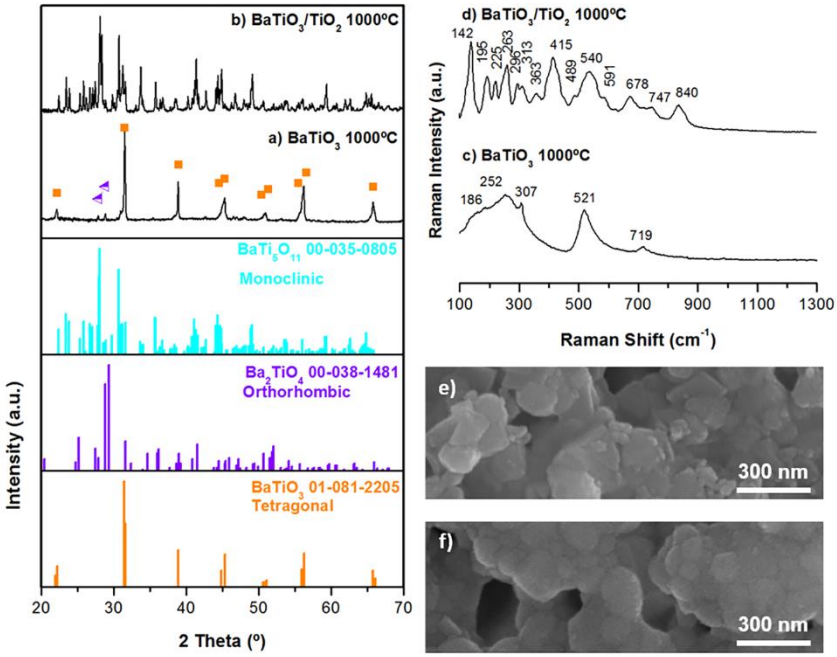

Figure 4. XRD patterns of 1000 °C thermally treated (a) $BaTiO_3$ and (b) $BaTiO_3/TiO_2$. Raman spectrum of 1000 °C thermally treated (c) $BaTiO_3$ and (d) $BaTiO_3/TiO_2$. FESEM micrographs of 1000 °C thermally treated (e) $BaTiO_3$ and (f) $BaTiO_3/TiO_2$.

A XRD study of the samples after a thermal treatment at 1000 °C is shown in Figure 4a,b. After thermal treatment at 1000 °C, the $BaTiO_3$ sample presents a main tetragonal structure (JCPDS 01-081-2205), with a minor secondary phase corresponding to the barium orthotitanate species, Ba_2TiO_4 (JCPDS 00-038-1481). The removal of barium carbonate observed in the precursor is in the origin of the appearance of such a secondary phase. The as-prepared coated powder ($BaTiO_3/TiO_2$ composite) was also calcined in air at 1000 °C, and the diffractogram is shown in Figure 4b. The diffraction pattern for the $BaTiO_3/TiO_2$ composite heat-treated at 1000 °C shows mostly the peaks of the $BaTi_5O_{11}$ phase, in spite of their low resolution (JCPDS 00-035-0805). No evidence of other titanate phases are detected within the XRD resolution limit (of the order of 1 wt %). Hence, it can be asserted that the amorphous titania reacts with $BaTiO_3$ nanoparticles, and the system evolves toward the formation of nanocrystalline $BaTi_5O_{11}$.

The Raman spectrum of the 1000 °C thermally treated $BaTiO_3$ sample is shown in Figure 4c. The Raman modes centered at about 186 and 521 cm^{-1} correspond to the transversal component of the mode with the A_1 symmetry (A_1 (TO)),[38] whereas the peak at about 719 cm^{-1} can be assigned to the longitudinal mode of A_1 symmetry (A_1 (LO)).[39] The Raman mode at about 307 cm^{-1} is related to the B_1 mode, indicating asymmetry within the TiO_6 octahedral.[56] Finally, the Raman characterization for the 1000 °C thermally treated $BaTiO_3/TiO_2$ sample indicates the formation of $BaTi_5O_{11}$ is complete (Figure 4d).[8,9,57] In addition, it is observed that a material densification in which grain boundaries and sintering necks appear in a nanostructured material having a grain size ranging from 40 to 200 nm (Figure 4e,f).

Despite obtaining the desired phase, the role of intermediate compounds and the evolution of phase composition with temperature is not adequately resolved by the use of XRD. To clarify this point, both precursors are isothermally treated at 400, 500, 600, 700, 800, 900, and 1000 °C for 1 h and Confocal Raman microscopy (CRM) has been used to determine the nature of intermediate chemical species and

DOI: 10.1021/acs.inorgchem.9b00865
Inorg. Chem. 2019, 58, 8120−8129

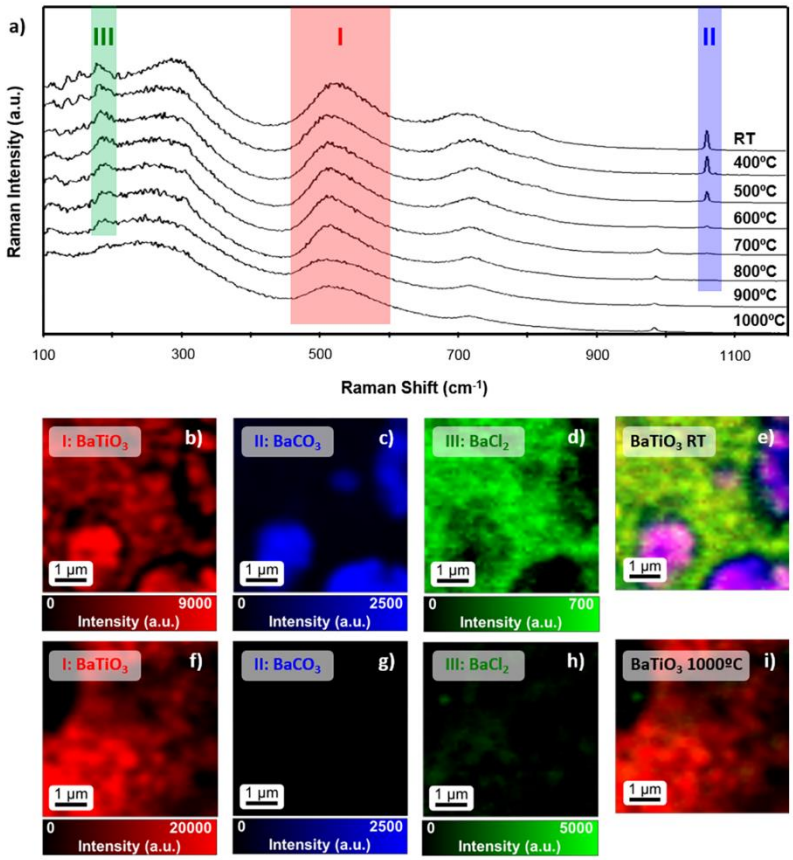

Figure 5. (a) Average Raman spectra for $BaTiO_3$ thermally treated at selected temperatures. The main Raman modes of the different phases are signaled by color-coding: $BaTiO_3$ in red; $BaCO_3$ in blue; and $BaCl_2$ in green. Raman images of the different phases for (b–e) untreated $BaTiO_3$ sample and (f–i) 1000 °C thermally treated $BaTiO_3$ sample.

the evolution with the thermal treatment of main crystalline phases.

The CRM study of the $BaTiO_3$ precursor at different temperatures has been carried out by mapping the surface of samples pressed into disks, Figure 5. Raman images of the untreated $BaTiO_3$ and 1000 °C thermally treated $BaTiO_3$ samples are depicted to show the distribution of the main phases, Figure 5b–e and f–i, respectively. The Raman images of the untreated $BaTiO_3$ sample, presented in Figure 5b–e, show three distinguishable phases: $BaTiO_3$ as the main phase (signaled by red regions, Figure 5b); $BaCO_3$ as disperse in agglomerates with a particle size of ~2 μm (signaled by blue region, Figure 5c); and unreacted $BaCl_2$ is distributed in the whole area where $BaTiO_3$ is present (signaled by green, Figure 5d). This fact, together with the convergence between $BaTiO_3$ and $BaCO_3$ in Figure 5b,c, indicates that the $BaCO_3$ could be at the surface of the agglomerates, while the existence of unreacted $BaCl_2$ protects the $BaTiO_3$ against the carbonation. Figure 5a shows the average Raman spectrum of the core $BaTiO_3$ samples treated at different temperatures. The $BaCO_3$ disappears at temperatures >700 °C (see Figure 5a), as signaled by the lack of the Raman signal at 1059 cm^{-1} (in concordance with DTA-Tg study). It is worth noting that the unreacted $BaCl_2$ coexists with $BaTiO_3$ for the whole range of temperatures.

The evolution of average Raman spectra obtained for $BaTiO_3/TiO_2$ composite sample treated at various temperatures is shown in Figure 6a. The Raman image of the aged and untreated $BaTiO_3/TiO_2$, Figure 6b, only shows a broad Raman band associated with Ti–O–Ti bonds, signaled by a magenta box. We study the Raman spectra as a function of the temperature treatment, between 400 and 700 °C (for the sake of brevity, this spectra is shown in the Supporting Information, Figure S4 and it shows Raman peaks at 116, 140, 228, 264, 271, 362, 424, 630, and 845 cm^{-1}). As it was reported before, these Raman peaks correlate with the orthorhombic structure of $BaTi_4O_9$.[57−59] In the Raman image (Figure 6e) it can be observed that the amount of the amorphous titanium decreases as the $BaTi_4O_9$ crystallizes, signaled as yellow. In addition, the increase of the thermal treatment temperature favors the appearance of $BaTi_5O_{11}$ (signaled in cyan regions, Figure 6f). Taking into account the results of the Raman spectra, the system seems to have almost entirely transformed into $BaTi_5O_{11}$, since this phase is observed from 800 °C and is correlated with the crystallization, which is denoted by an exothermic peak at ~750 °C in the DTA analysis (Figure 3b). The existence of crystalline $BaTi_5O_{11}$ is also in agreement with the XRD pattern of the 1000 °C thermally treated sample (Figure 4b).

From the above discussion, by combining the results of the thermal analysis with the XRD, XPS, and CRM analyses, the

DOI: 10.1021/acs.inorgchem.9b00865
Inorg. Chem. 2019, 58, 8120–8129

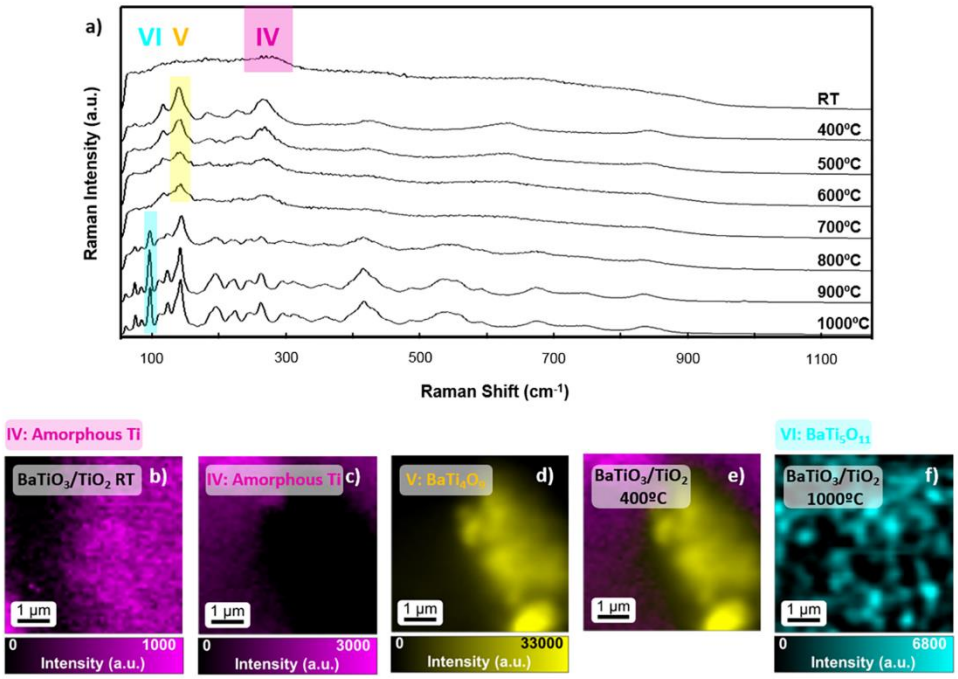

Figure 6. (a) Study of the Raman spectra evolution as a function of thermal treatment for the $BaTiO_3/TiO_2$ composite sample. The main Raman modes of the different phases are signaled by color-coding: amorphous Ti in magenta, $BaTi_4O_9$ in yellow, and $BaTi_5O_{11}$ in cyan. Raman images of the phase distribution for (b) an untreated sample of $BaTiO_3/TiO_2$ sample, (c–e) 400 °C thermally treated $BaTiO_3/TiO_2$ sample, and (f) 1000 °C thermally treated $BaTiO_3/TiO_2$ sample.

reaction mechanism of $BaTi_5O_{11}$ formation through solid-state reaction from core–shell $BaTiO_3$@TiO_2 nanoparticles can be schematically illustrated as shown in Figure 7. The first stage portrays the core $BaTiO_3$ raw materials at room temperature

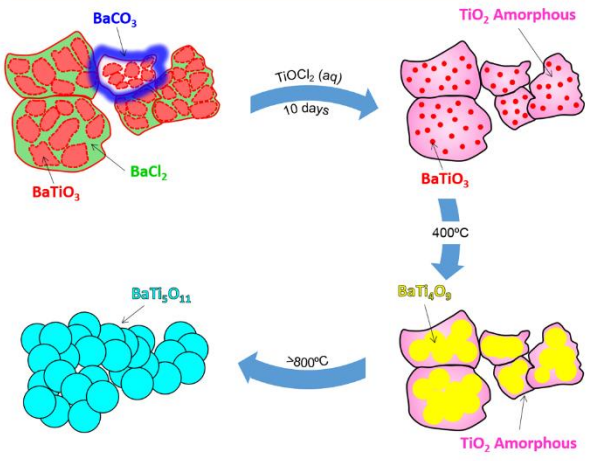

Figure 7. Scheme representing the main stages of the $BaTi_5O_{11}$ formation. Up-left scheme illustrates the former $BaTiO_3$ nanoparticle agglomerateas. The next up-right scheme represents the initial reaction between the core-$BaTiO_3$ aggregates and the peroxotitanium-(IV) solution, the final room temperature reaction of the core–shell $BaTiO_3/TiO_2$ to produce an amorphous titania with $BaTiO_3$ rests. The down-right scheme denotes the beginning of the formation of the $BaTi_4O_9$ particles surrounded by the amorphous Titania phase. Finally, the down-left scheme depicts the formation of the $BaTi_5O_{11}$ particles.

obtained by a hydrothermal synthesis in a Segmented Tubular Reactor. $BaTiO_3$ particles possess spherical shape morphology and they form aggregates (corresponding FE-SEM micrographs are included in Supporting Information, Figure S2). Raman images show that some $BaTiO_3$ nanoparticles are carbonated forming $BaCO_3$ at room temperature. In addition, the $BaCl_2$ precursor remains in contact with $BaTiO_3$ particles. Even when the precipitated was carefully washed with water and chloride ions are absent in the supernatant by the silver nitride test method, this compound is found in the $BaTiO_3$ aggregates. The second stage in the scheme illustrates the reaction when an amorphous TiO_2 is generated by coating the core $BaTiO_3$ from an aqueous solution of $TiOCl_2$. The presence of the amorphous titania phase produces three main effects: first, the elimination of $BaCO_3$; second, through the removal of $BaCl_2$ a rearrangement of the agglomerates; and, finally, the amorphization of $BaTiO_3$. XRD and Raman studies expose that $BaTiO_3$ is almost completely decomposed in the presence of amorphous TiO_2, which penetrates through the structure of $BaTiO_3$ by the $BaCl_2$ phase. According to the XPS data, it is also evident that the $BaTiO_3/TiO_2$ composite sample presents Ba^{2+} cations at the surface that could be related to the migration of the Ba^{2+} cations during the synthesis process. Thus, an amorphous TiO_2 is generated having a nucleus of $BaTiO_3$. At the third stage, evidence of the crystallization of $BaTi_4O_9$ phase appears in the presence of amorphous titania. Finally, at 800 °C, the excess of amorphous TiO_2 continues to penetrate the structure and form nanoparticles of the $BaTi_5O_{11}$ phase.

DOI: 10.1021/acs.inorgchem.9b00865
Inorg. Chem. 2019, 58, 8120–8129

CONCLUSIONS

In the attempt of obtaining a core−shell structure of TiO_2@ $BaTiO_3$, both the phases evolution and the role of the intermediate compounds during the synthesis of nanostructured $BaTi_5O_{11}$ have been studied. Core $BaTiO_3$ particles in the form of aggregates present precursor rests as $BaCl_2$ and local carbonation. The process of shell formation by an amorphous titania onto core $BaTiO_3$ provokes both the carbonates and the chlorides removal. The progressing of the reaction tooks 10 days and, as the chloride is completely removed, the $BaTiO_3$ particles are chemically attacked by the amorphous titania phase. The thermal treatment of the so obtained materials produces a single phase of $BaTi_5O_{11}$. The intermediate phases are identified by a combination of characterization methodologies as Raman confocal, XRD and XPS. This example shows a strategy to synthesize complex single-phase composition by controlling of the intermediate phase and, in particular, to the residues of the precursors that contributed to the reaction mechanism during the thermal treatment. Finally, the development of $BaTi_5O_{11}$ powders is attractive because this material exhibits excellent microwave properties that allow its use in monolithic microwave integrated circuits with reduced particle dimensions.

ASSOCIATED CONTENT

Supporting Information

The Supporting Information is available free of charge on the ACS Publications website at DOI: 10.1021/acs.inorgchem.9b00865.

Raman spectrum of as-obtained core $BaTiO_3$ particles, FESEM micrographs of core $BaTiO_3$ particles, survey XPS spectrum, and Raman spectrum of $BaTiO_3/TiO_2$ at 400 °C, showing the $BaTi_4O_9$ phase (PDF)

AUTHOR INFORMATION

Corresponding Author

*E-mail: carmenma.docio@icv.csic.es.

ORCID

Carmen María Álvarez-Docio: 0000-0002-3984-3078

Giovanna Canu: 0000-0003-0819-9352

José Francisco Fernández: 0000-0001-5894-9866

Notes

The authors declare no competing financial interest.

ACKNOWLEDGMENTS

The authors express their thanks to the projects NANOMIND CSIC201560E068 and MAT2017-86450-C4-1-R for their financial support. C.M.A.-D. is also indebted to MINECO for a Predoctoral Grant (BES-2014-069779), which is cofinanced with FEDER funds. C.M.A.-D. is grateful to MINECO for a short stay scholarship (EEBB-I-16-11587).

REFERENCES

(1) Zhou, H.; Wang, H.; Chen, Y.; Li, K.; Yao, X. Microwave Dielectric Properties of $BaTi_5O_{11}$ Ceramics Prepared by Reaction-Sintering Process with the Addition of CuO. *J. Am. Ceram. Soc.* **2008**, *91* (10), 3444−3447.

(2) Jang, B. Y.; Jeong, Y. H.; Lee, S. J.; Nahm, S.; Sun, H. J.; Lee, W. S.; Yoo, M. J.; Kang, N. K.; Lee, H. J. Microwave Dielectric Properties of the $BaTi_5O_{11}$ Thin Film Grown on the Poly-Si Substrate Using Rf Magnetron Sputtering. *J. Eur. Ceram. Soc.* **2006**, *26* (10−11), 2151−2154.

(3) Chen, Y.; Li, E.; Duan, S.; Zhang, S. Low Temperature Sintering Kinetics and Microwave Dielectric Properties of $BaTi_5O_{11}$ Ceramic. ACS Sustain. *ACS Sustainable Chem. Eng.* **2017**, *5* (11), 10606−10613.

(4) Hsu, C. H.; Chen, W. S.; Tung, H. H.; Yang, P. C.; Lin, J. Sen Dielectric Properties of $BaTi_5O_{11}$ Ceramics at Microwave Frequencies. *Adv. Mater. Res.* **2013**, *677*, 153−156.

(5) O'Bryan, H. M.; Thomson, J. Preparation of $BaTi_5O_{11}$ by Solid-State Reaction. *J. Am. Ceram. Soc.* **1975**, *58* (9), 454.

(6) Ritter, J. J.; Roth, R. S.; Blendell, J. E. Alkoxide Precursor Synthesis and Characterization of Phases in the Barium-titanium Oxide System. *J. Am. Ceram. Soc.* **1986**, *69* (2), 155−162.

(7) Fukui, T.; Sakurai, C.; Okuyama, M. Effects of Heating Rate on Sintering of Alkoxide-Derived $BaTi_5O_{11}$ Powder. *J. Mater. Res.* **1992**, *7* (1), 192−196.

(8) Javadpour, J.; Eror, N. G. Raman Spectroscopy of Higher Titanate Phases in the $BaTiO_3$-TiO_2 System. *J. Am. Ceram. Soc.* **1988**, *71* (4), 206−213.

(9) Lu, H. -c; Burkhart, L. E.; Schrader, G. L. Sol-Gel Process for the Preparation of $Ba_2Ti_9O_{20}$ and $BaTi_5O_{11}$. *J. Am. Ceram. Soc.* **1991**, *74* (5), 968−972.

(10) Tangjuank, S.; Tunkasiri, T. Effects of Heat Treatment on Structural Evolution and Morphology of $BaTi_5O_{11}$ Powder Synthesized by the Sol-Gel Method. *Mater. Sci. Eng., B* **2004**, *108* (3), 223−226.

(11) Wiss, J.; Zilian, A. Online Spectroscopic Investigations (FTIR/Raman) of Industrial Reactions: Synthesis of Tributyltin Azide and Hydrogenation of Chloronitrobenzene. *Org. Process Res. Dev.* **2003**, *7* (6), 1059−1066.

(12) Rojas-Hernandez, R. E.; Rubio-Marcos, F.; Gonçalves, R. H.; Rodriguez, M. Á.; Véron, E.; Allix, M.; Bessada, C.; Fernandez, J. F. Original Synthetic Route to Obtain a $SrAl_2O_4$ Phosphor by the Molten Salt Method: Insights into the Reaction Mechanism and Enhancement of the Persistent Luminescence. *Inorg. Chem.* **2015**, *54* (20), 9896−9907.

(13) Álvarez-Docio, C. M.; Reinosa, J. J.; Del Campo, A.; Fernández, J. F. Investigation of Thermal Stability of 2D and 3D $CoAl_2O_4$ Particles in Core-Shell Nanostructures by Raman Spectroscopy. *J. Alloys Compd.* **2019**, *779*, 244−254.

(14) Torres-Carrasco, M.; de la Rubia, M. A.; Moragues, A.; Fernández, J. F.; Reyes, E.; del Campo, A. New Insights in Weathering Analysis of Anhydrous Cements by Using High Spectral and Spatial Resolution Confocal Raman Microscopy. *Cem. Concr. Res.* **2017**, *100* (June), 119−128.

(15) Reinosa, J. J.; del Campo, A.; Fernández, J. F. Indirect Measurement of Stress Distribution in Quartz Particles Embedded in a Glass Matrix by Using Confocal Raman Microscopy. *Ceram. Int.* **2015**, *41* (10), 13598−13606.

(16) Enríquez, E.; De la Rubia, M. A.; Del Campo, A.; Rubio-Marcos, F.; Fernandez, J. F. Characterization of Carbon Nanoparticles in Thin-Film Nanocomposites by Confocal Raman Microscopy. *J. Phys. Chem. C* **2014**, *118* (19), 10488−10494.

(17) Bowen, P.; Donnet, M.; Testino, A.; Viviani, M.; Buscaglia, M. T.; Buscaglia, V.; Nanni, P. Synthesis of Barium Titanate Powders by Low-Temperature Aqueous Synthesis Using a New Segmented Flow Tubular Reactor. *Key Eng. Mater.* **2001**, *206−213*, 21−24.

(18) Jongen, N.; Donnet, M.; Bowen, P.; Lemaître, J.; Hofmann, H.; Schenk, R.; Hofmann, C.; Aoun-Habbache, M.; Guillemet-Fritsch, S.; Sarrias, J.; et al. Development of a Continuous Segmented Flow Tubular Reactor and the "Scale-out" Concept − In Search of Perfect Powders. *Chem. Eng. Technol.* **2003**, *26* (3), 303−305.

(19) Testino, A.; Buscaglia, M. T.; Buscaglia, V.; Viviani, M.; Bottino, C.; Nanni, P. Kinetics and Mechanism of Aqueous Chemical Synthesis of $BaTiO_3$ Particles. *Chem. Mater.* **2004**, *16* (8), 1536−1543.

(20) Testinon, A.; Buscaglia, M. T.; Viviani, M.; Buscaglia, V.; Nanni, P. Synthesis of BaTiO3 Particles with Tailored Size by Precipitation from Aqueous Solutions. *J. Am. Ceram. Soc.* **2004**, *87* (1), 79−83.

DOI: 10.1021/acs.inorgchem.9b00865
Inorg. Chem. 2019, 58, 8120−8129

(21) Sabzehparvar, M.; Kiani, F.; Tabrizi, N. S. Synthesis and Characterization of Black Amorphous Titanium Oxide Nanoparticles by Spark Discharge Method. *AIP Conf. Proc.* **2017**, 020046.
(22) Francisco-Santiago, P.; García-Macedo, J. A.; Valverde-Aguilar, G. Photoconductivity Studies on Amorphous and Crystalline TiO_2 and TiO_2:Eu^{3+} Thin Films Synthesized by Sol-Gel. *Proc. SPIE* **2012**, *8456*, 84560N.
(23) Buscaglia, M. T.; Buscaglia, V.; Alessio, R. Coating of $BaCO_3$ Crystals with TiO_2: Versatile Approach to the Synthesis of $BaTiO_3$ Tetragonal Nanoparticles. *Chem. Mater.* **2007**, *19* (4), 711−718.
(24) Mühlebach, J.; Müller, K.; Schwarzenbach, G. The Peroxo Complexes of Titanium. *Inorg. Chem.* **1970**, *9* (11), 2381−2390.
(25) Niesen, T. P.; Bill, J.; Aldinger, F. Deposition of Titania Thin Films by a Peroxide Route on Different Functionalized Organic Self-Assembled Monolayers. *Chem. Mater.* **2001**, *13* (5), 1552−1559.
(26) Tengvall, P.; Bertilsson, L.; Liedberg, B.; Elwing, H.; Lundstrom, I. Degradation of Dried Ti-Peroxy Gels Made from Metallic Titanium and Hydrogen Peroxide. *J. Colloid Interface Sci.* **1990**, *139* (2), 575−580.
(27) Tengvall, P.; Vikinge, T. P.; Lundstrom, I.; Liedberg, B. FT-Raman Spectroscopic Studies of the Degradation of Titanium Peroxy Gels Made from Metallic Titanium and Hydrogen Peroxide. *J. Colloid Interface Sci.* **1993**, *160*, 10−15.
(28) Buscaglia, M. T.; Buscaglia, V.; Viviani, M.; Dondero, G.; Röhrig, S.; Rüdiger, A.; Nanni, P. Ferroelectric Hollow Particles Obtained by Solid-State Reaction. *Nanotechnology* **2008**, *19* (22), 225602.
(29) Shiratori, Y.; Pithan, C.; Dornseiffer, J.; Waser, R. Raman Scattering Studies on Nanocrystalline $BaTiO_3$. Part I − Isolated Particles and Aggregates. *J. Raman Spectrosc.* **2007**, *38* (10), 1538−1553.
(30) Gajović, A.; Plešťina, J. V.; Žagar, K.; Plodinec, M.; Šturm, S.; Ceh, M. Temperature-Dependent Raman Spectroscopy of $BaTiO_3$ Nanorods Synthesized by Using a Template-Assisted Sol-Gel Procedure. *J. Raman Spectrosc.* **2013**, *44* (3), 412−420.
(31) Smith, M. B.; Page, K.; Siegrist, T.; Redmond, P. L.; Walter, E. C.; Seshadri, R.; Brus, L. E.; Steigerwald, M. L. Crystal Structure and the Paraelectric-to-Ferroelectric Phase Transition of Nanoscale $BaTiO_3$. *J. Am. Chem. Soc.* **2008**, *130* (22), 6955−6963.
(32) Venkateswaran, U. D.; Naik, V. M.; Naik, R. High-Pressure Raman Studies of Polycrystalline BaTiO3. *Phys. Rev. B: Condens. Matter Mater. Phys.* **1998**, *58* (21), 14256−14260.
(33) Pasierb, P.; Komornicki, S.; Rokita, M.; Rękas, M. Structural Properties of Li_2CO_3-$BaCO_3$ System Derived from IR and Raman Spectroscopy. *J. Mol. Struct.* **2001**, *596* (1), 151−156.
(34) Yamashita, Y.; Tada, M.; Kakihana, M.; Osada, M.; Yoshida, K. Synthesis of RuO_2-Loaded $BaTi_nO_{2n+1}$ (n = 1, 2 and 5) Using a Polymerizable Complex Method and Its Photocatalytic Activity for the Decomposition of Water. *J. Mater. Chem.* **2002**, *12*, 1782−1786.
(35) Alvarez, C. J.; Leonard, R. L.; Gray, S. K.; Johnson, J. A.; Petford-Long, A. K. Structural and Kinetic Analysis of $BaCl_2$ Nanocrystals in Fluorochlorozirconate Glass-Ceramics. *J. Am. Ceram. Soc.* **2015**, *98* (4), 1099−1104.
(36) Bohley, C.; Wagner, J. M.; Pfau, C.; Miclea, P. T.; Schweizer, S. Raman Spectra of Barium Halides in Orthorhombic and Hexagonal Symmetry: An Ab Initio Study. *Phys. Rev. B: Condens. Matter Mater. Phys.* **2011**, *83* (2), na.
(37) Pfau, C.; Bohley, C.; Miclea, P.; Schweizer, S. Structural Phase Transitions of Barium Halide Nanocrystals in Fluorozirconate Glasses Studied by Raman Spectroscopy. *J. Appl. Phys.* **2011**, *109* (8), 083545.
(38) Tian, X.; Li, J.; Chen, K.; Han, J.; Pan, S.; Wang, Y.; Fan, X.; Li, F.; Zhou, Z. Nearly Monodisperse Ferroelectric $BaTiO_3$ Hollow Nanoparticles: Size-Related Solid Evacuation in Ostwald-Ripening-Induced Hollowing Process. *Cryst. Growth Des.* **2010**, *10* (9), 3990−3995.
(39) Bai, H.; Liu, X. Low Temperature Solvothermal Synthesis, Optical and Electric Properties of Tetragonal Phase $BaTiO_3$ Nanocrystals Using $BaCO_3$ Powder. *Mater. Lett.* **2013**, *100*, 1−3.
(40) Reichmann, M. G.; Bell, A. T. Raman Study of the Preparation of Silica-Supported Titania from Titanium Tetrachloride and Hydrogen Chloride. *Langmuir* **1987**, *3* (1), 111−116.
(41) Bassano, A.; Buscaglia, M. T.; Buscaglia, V.; Nanni, P. Particle Size and Morphology Control of Perovskite Oxide Nanopowders for Nanostructured Materials. *Integr. Ferroelectr.* **2009**, *109* (1), 1−17.
(42) Airimioaei, M.; Buscaglia, M. T.; Tredici, I.; Anselmi-Tamburini, U.; Ciomaga, C. E.; Curecheriu, L.; Bencan, A.; Buscaglia, V.; Mitoseriu, L. $SrTiO_3$-$BaTiO_3$ Nanocomposites with Temperature Independent Permittivity and Linear Tunability Fabricated Using Field-Assisted Sintering from Chemically Synthesized Powders. *J. Mater. Chem. C* **2017**, *5* (35), 9028−9036.
(43) Bernardi, F.; Fecher, G. H.; Alves, M. C. M.; Morais, J. Unraveling the Formation of Core-Shell Structures in Nanoparticles by S-XPS. *J. Phys. Chem. Lett.* **2010**, *1* (6), 912−917.
(44) De Marchi, L.; Pretti, C.; Gabriel, B.; Marques, P. A. A. P.; Freitas, R.; Neto, V. An Overview of Graphene Materials: Properties, Applications and Toxicity on Aquatic Environments. *Sci. Total Environ.* **2018**, *631*−*632*, 1440−1456.
(45) Baer, D. R.; Gaspar, D. J.; Nachimuthu, P.; Techane, S. D.; Castner, D. G. Application of Surface Chemical Analysis Tools for Characterization of Nanoparticles. *Anal. Bioanal. Chem.* **2010**, *396* (3), 983−1002.
(46) Sarma, D. D.; Santra, P. K.; Mukherjee, S.; Nag, A. X-Ray Photoelectron Spectroscopy: A Unique Tool to Determine the Internal Heterostructure of Nanoparticles. *Chem. Mater.* **2013**, *25* (8), 1222−1232.
(47) Fan, Y.; Wang, G.; Huang, X.; Bu, J.; Sun, X.; Jiang, P. Molecular Structures of (3-Aminopropyl)Trialkoxysilane on Hydroxylated Barium Titanate Nanoparticle Surfaces Induced by Different Solvents and Their Effect on Electrical Properties of Barium Titanate Based Polymer Nanocomposites. *Appl. Surf. Sci.* **2016**, *364*, 798−807.
(48) Miot, C.; Husson, E.; Proust, C.; Erre, R.; Coutures, J. P. Residual Carbon Evolution in $BaTiO_3$ Ceramics Studied by XPS after Ion Etching. *J. Eur. Ceram. Soc.* **1998**, *18* (4), 339−343.
(49) Nayak, S.; Sahoo, B.; Chaki, T. K.; Khastgir, D. Facile Preparation of Uniform Barium Titanate ($BaTiO_3$) Multipods with High Permittivity: Impedance and Temperature Dependent Dielectric Behavior. *RSC Adv.* **2014**, *4* (3), 1212.
(50) Alkathy, M. S.; Hezam, A.; Manoja, K. S. D.; Wang, J.; Cheng, C.; Byrappa, K.; Raju, K. C. J. Effect of Sintering Temperature on Structural, Electrical, and Ferroelectric Properties of Lanthanum and Sodium Co-Substituted Barium Titanate Ceramics. *J. Alloys Compd.* **2018**, *762*, 49−61.
(51) Sun, S.; Ding, H.; Zhou, H. Preparation of TiO_2-Coated Barite Composite Pigments by the Hydrophobic Aggregation Method and Their Structure and Properties. *Sci. Rep.* **2017**, *7* (1), 10083.
(52) Wang, Z.; Zou, G.; Luo, X.; Liu, H.; Gao, R.; Chou, L.; Wang, X. Oxidative Coupling of Methane over $BaCl_2$-TiO_2-SnO_2 Catalyst. *J. Nat. Gas Chem.* **2012**, *21* (1), 49−55.
(53) Xu, M.; Lu, Y. N.; Liu, Y. F.; Shi, S. Z.; Qian, T. S.; Lu, D. Y. Sonochemical Synthesis of Monosized Spherical $BaTiO_3$ Particles. *Powder Technol.* **2006**, *161* (3), 185−189.
(54) Hennings, D.; Schreinemacher, S. Characterization of Hydrothermal Barium Titanate. *J. Eur. Ceram. Soc.* **1992**, *9*, 41−46.
(55) Buscaglia, M. T.; Bassoli, M.; Buscaglia, V.; Alessio, R. Solid-State Synthesis of Ultrafine $BaTiO_3$ Powders from Nanocrystalline $BaCO_3$ and TiO_2. *J. Am. Ceram. Soc.* **2005**, *88* (9), 2374−2379.
(56) Buscaglia, V.; Buscaglia, M. T.; Viviani, M.; Mitoseriu, L.; Nanni, P.; Trefiletti, V.; Piaggio, P.; Gregora, I.; Ostapchuk, T.; Pokorný, J.; Petzelt, J. Grain Size and Grain Boundary-Related Effects on the Properties of Nanocrystalline Barium Titanate Ceramics. *J. Eur. Ceram. Soc.* **2006**, *26* (14), 2889−2898.
(57) Rossel, M.; Hoche, H. R.; Leipner, H. S.; Voltzke, D.; Abicht, H. P.; Hollricher, O.; Muller, J.; Gablenz, S. Raman Microscopic Investigations of $BaTiO_3$ Precursors with Core-Shell Structure. *Anal. Bioanal. Chem.* **2004**, *380* (1), 157−162.

DOI: 10.1021/acs.inorgchem.9b00865
Inorg. Chem. 2019, 58, 8120−8129

(58) Catalin, N.; Cernea, M. Characterization of $BaTi_4O_9$ Ceramics by Raman Spectroscopy and XPS after Ion Etching. *J. Optoelectron. Adv. Mater.* **2006**, *8* (5), 1879−1883.
(59) Kohno, M.; Ogura, S.; Inoue, Y. Preparation of $BaTi_4O_9$ by a Sol-Gel Method and Its Photocatalytic Activity for Water Decomposition. *J. Mater. Chem.* **1996**, *6* (12), 1921−1924.

DOI: 10.1021/acs.inorgchem.9b00865
Inorg. Chem. 2019, 58, 8120−8129

Supplementary material

Revealing the Role of the Intermediates during the Synthesis of $BaTi_5O_{11}$

Carmen María Álvarez-Docio[a,*], Julián Jiménez Reinosa[a], Giovanna Canu[b], María Teresa Buscaglia[b], Vincenzo Buscaglia[b], José Francisco Fernández[a].

[a] *Ceramic and Glasses Institute (ICV-CSIC), Ceramics for Smart Systems group, C/Kelsen 5, Madrid, Spain.*

[b] *Institute of Condensed Matter Chemistry and Technologies for Energy (IENI-CNR), Synthesis of Advanced Functional Oxides group, Via de Marini 6, Genoa, Italy.*

*E-mail address: carmenma.docio@icv.csic.es (Carmen María Álvarez-Docio)

EXPERIMENTAL PROCEDURE

Materials: $BaCl_2 \cdot 2H_2O$ (99%), NH_4OH (28% solution), H_2O_2 (30% solution), and NaOH (99%) were supplied by Aldrich. $TiCl_4$ (99.9%) was purchased from Acros Chemical. The water used in the experiments was always freshly distilled water.

Synthesis of $BaTiO_3$ nanoparticles: An acidic $TiOCl_2$ mother solution (3.4728 mol/kg) was prepared by drop-by-drop addition of $TiCl_4$ in water cooled in an ice bath. The precise titanium content of this solution was determined by gravimetric titration. The required amount of the $TiOCl_2$ mother solution was diluted with water, and solid $BaCl_2$ was added in the amount required to have a [Ba]/[Ti] molar ratio of 1.11. An excess of barium in comparison to the stoichiometric amount was always used. The suspension was stirred until dissolution of the solid chloride. The resulting solution was then quickly mixed (20 s) under vigorous stirring with the same volume of a NaOH solution with immediate formation of a gelatinous suspension of titanium hydroxide gel. An excess of NaOH, in comparison to the stoichiometric amount required by reaction 1, was used to guarantee quantitative precipitation of $BaTiO_3$. This excess corresponds to $[OH^-]$ = 1 mol/L (i.e., a pH of about 14) in the final barium titanate suspension. Consequently, the synthesis of barium titanate particles was carried out according to the overall formal reaction:[1]

$$BaCl_2\ (aq) + TiOCl_2\ (aq) + 4NaOH\ (aq) \rightarrow BaTiO_3\ (s) + 4NaCl\ (aq) + 2H_2O\ (l)$$

where (aq) denotes a salt in aqueous solution.

The reaction was carried out in a continuous Segmented Flow Tubular Reactor (SFTR). The SFTR set up was similar to that used by Jongen et al.[2] with a segmenter in which the reaction mixture is separated with an immiscible fluid (nitrogen) into micro-batch volumes or liquid "bubbles" in a continuous mode. The reaction was carried out at 95°C and the residence time in the tubular reactor (length, 12 m, inner diameter, 4 mm) was 10 min. After reaction, the $BaTiO_3$ precipitate was separated by centrifugation, washed until chloride ions were no

longer detected in the supernatant (tested with a 0.1 M silver nitrate solution, detection limit of the order of ppm), and finally dried. The presence of atmospheric CO_2, should be avoided as much as possible during the synthesis and the washing procedure; otherwise, the product will always be contaminated by $BaCO_3$. It is worth noting that the $BaTiO_3$ particles prepared as described above consist of ordered aggregates of primary nanocrystals with a high degree of alignment. Further details on the preparation and properties of the barium titanate templates can be found elsewhere.[3,4]

Preparation of the peroxotitanium (IV) Solution: The required amount of the $TiOCl_2$ mother solution was diluted with water to obtain 75 g of a Ti (IV) solution with concentration of 0.13 mol/kg. During the next preparation steps, the solution was kept at a temperature below 5 °C by an ice bath. A H_2O_2 solution (5 mL) was slowly added to the Ti (IV) solution while stirring. The final clear solution showed a dark orange color, indicative of the formation of the peroxotitanium complex. The ammonia solution was slowly added to the solution of the peroxocompound under vigorous stirring until the pH attained a value of ~9. During the addition, the color of the solution progressively turned into light yellow. The final solution was stable for a few days if kept at a temperature of 5-10 °C. For longer times, the solution became opaque, and formation of a yellow precipitate was observed.

Synthesis of $BaTiO_3$/TiO_2 composite particles: The previous obtained $BaTiO_3$ powder was suspended in the Ti (IV) solution (prepared as described above) at room temperature while stirring. The amount of Ti (IV) solution used for the coating process was determined to have an overall stoichiometry corresponding to Ti/Ba = 5. The suspension was slowly heated to 95 °C and kept at this temperature for 1 h. The solid phase, a yellow powder, was then separated from the liquid by filtration, washed until chloride ions were no longer detected in the supernatant (tested with a 0.1 M silver nitrate solution, detection limit of the order of ppm), and finally dried.

Thermal treatments: The powders consisting of $BaTiO_3/TiO_2$ particles were compacted in cylindrical steel bodies (diameter, 1 cm) by means of cold isostatic pressing and then thermally treated, in a conventional muffle furnace, at different temperatures in the 400ºC to 1000ºC range with a heating rate of 5ºC/min. The hold time at the maximum temperature was 1 minute in each treatment.

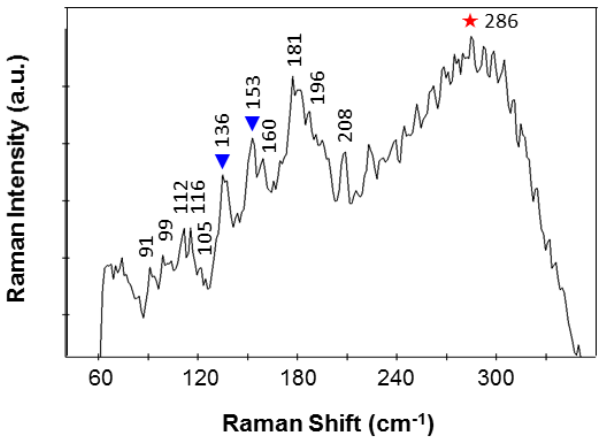

***Figure S1**.- Raman spectrum of as obtained core $BaTiO_3$ particles, showing the $BaCl_2$ phase. Peaks originating from $BaCO_3$ and internal defects are marked by blue triangles (▼) and red stars (★), respectively.*

The Raman spectra of the core $BaTiO_3$ is shown in ***Figure S1***, it presents a Raman band centred at ca. 299 cm^{-1}, which indicates local disorder of titanium atoms in a nominally pseudocubic phase. Moreover, peaks at 136 and 153 cm^{-1} detected for the raw powder are assigned to the $BaCO_3$ phase.[5–7] Finally, the Raman bands at 91, 99, 112, 116, 105, 160, 181, 196, 208 cm^{-1} are assigned to the $BaCl_2$ phase with an hexagonal structure.[8–10]

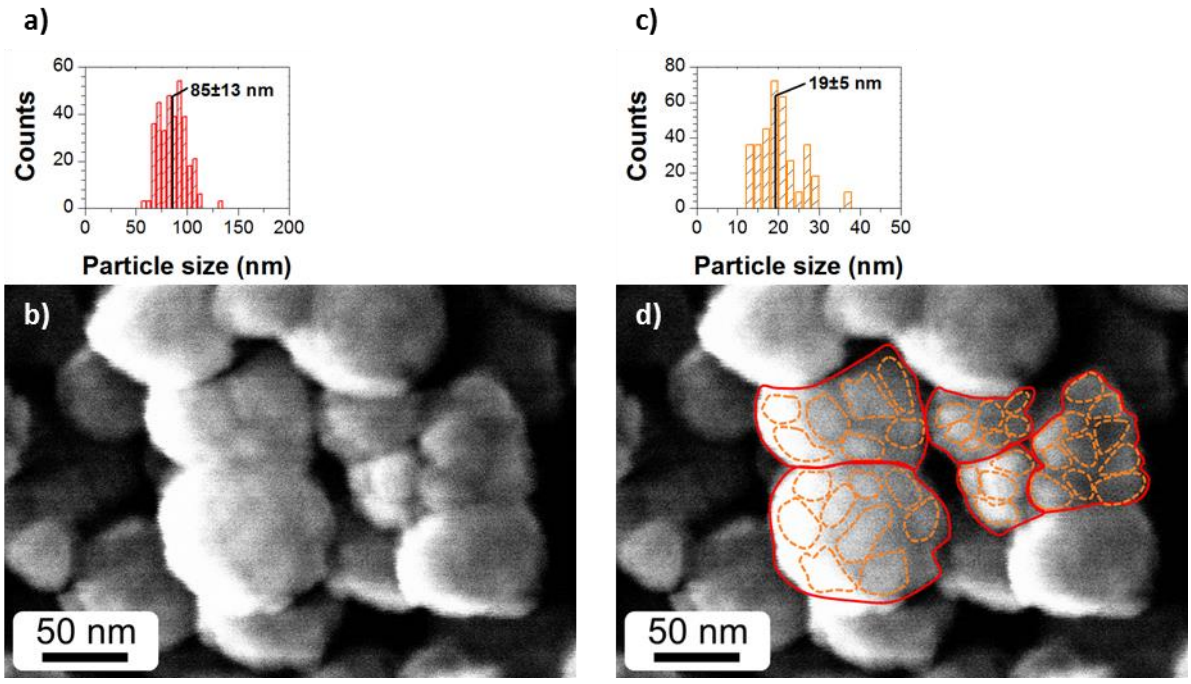

***Figure S2**.- FESEM micrographs of core $BaTiO_3$ particles.*

The morphology of as precipitates $BaTiO_3$ nanoparticles is shown in the ***Figure S2***. The stoichiometric particles have a nearly spherical shape with a diameter of ≈100 nm, whereas it is reported that the nonstoichiometric ones tend to develop a dendritic-like morphology.[11] Moreover, it could be observed that such defined particles are nanostructured and formed from small particles, that is it, primary particles aggregated to build up the so obtained $BaTiO_3$ particles.

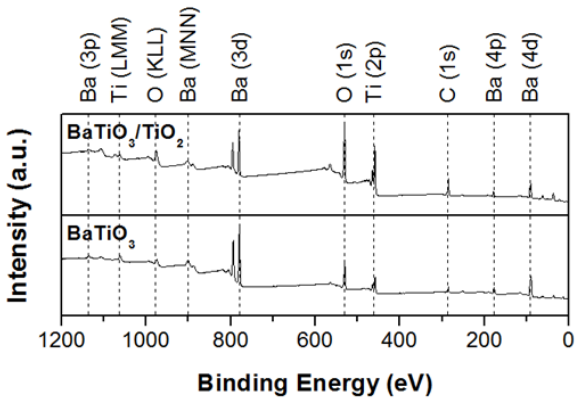

***Figure S3**.- Survey XPS spectrum of: a) as prepared core $BaTiO_3$ and b) aged core-shell $BaTiO_3/TiO_2$.*

A study of the structural changes at the surface of the particles was performed by XPS. A survey scan (shown in ***Figure S3***) from 1300 to 0 eV revealed the presence of Ba, Ti, O and C in both the as obtained core $BaTiO_3$ and 10 days aged core-shell $BaTiO_3/TiO_2$ particles.

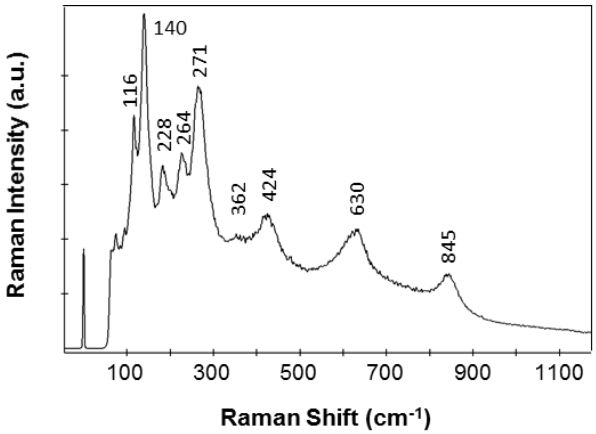

***Figure S4**.- Raman spectrum of $BaTiO_3/TiO_2$ 400ºC, showing the $BaTi_4O_9$ phase.*

Figure S4 shows the Raman spectrum of $BaTiO_3/TiO_2$ after a thermal treatment at 400ºC. It shows Raman peaks at 116, 140, 228, 264, 271, 362, 424, 630, and 845 cm^{-1}). Comparing our results with data from the literature, these Raman peaks correlate with the orthorhombic structure of $BaTi_4O_9$.[12–14]

REFERENCES

(1) Bowen, P.; Donnet, M.; Testino, A.; Viviani, M.; Buscaglia, M. T.; Buscaglia, V.; Nanni, P. Synthesis of Barium Titanate Powders by Low-Temperature Aqueous Synthesis Using a New Segmented Flow Tubular Reactor. *Key Eng. Mater.* 2002, *206–213*, 21–24. https://doi.org/10.4028/www.scientific.net/KEM.206-213.21.

(2) Jongen, N.; Donnet, M.; Bowen, P.; Lemaître, J.; Hofmann, H.; Schenk, R.; Hofmann, C.; Aoun-Habbache, M.; Guillemet-Fritsch, S.; Sarrias, J.; et al. Development of a Continuous Segmented Flow Tubular Reactor and the "Scale-out" Concept – In Search of Perfect Powders. *Chem. Eng. Technol.* 2003, *26* (3), 303–305. https://doi.org/10.1002/ceat.200390046.

(3) Testino, A.; Buscaglia, M. T.; Buscaglia, V.; Viviani, M.; Bottino, C.; Nanni, P. Kinetics and Mechanism of Aqueous Chemical Synthesis of $BaTiO_3$ Particles. *Chem. Mater.* 2004, *16* (8), 1536–1543. https://doi.org/10.1021/cm031130k.

(4) Testino, A.; Buscaglia, M. T.; Viviani, M.; Buscaglia, V.; Nanni, P. Synthesis of BaTiO3 Particles with Tailored Size by Precipitation from Aqueous Solutions. *J. Am. Ceram. Soc.* 2004, *87* (1), 79–83.

(5) Pasierb, P.; Komornicki, S.; Rokita, M.; Rękas, M. Structural Properties of Li_2CO_3-$BaCO_3$ System Derived from IR and Raman Spectroscopy. *J. Mol. Struct.* 2001, *596* (1), 151–156. https://doi.org/10.1016/S0022-2860(01)00703-7.

(6) Yamashita, Y.; Tada, M.; Kakihana, M.; Osada, M.; Yoshida, K. Synthesis of RuO_2-Loaded $BaTi_nO_{2n+1}$ (n = 1, 2 and 5) Using a Polymerizable Complex Method and Its Photocatalytic Activity for the Decomposition of Water. *J. Mater. Chem.* 2002, *12*, 1782–1786. https://doi.org/10.1039/b108722n.

(7) Gajović, A.; Pleština, J. V.; Žagar, K.; Plodinec, M.; Šturm, S.; Čeh, M. Temperature-Dependent Raman Spectroscopy of $BaTiO_3$ Nanorods

Synthesized by Using a Template-Assisted Sol-Gel Procedure. *J. Raman Spectrosc.* 2013, *44* (3), 412–420. https://doi.org/10.1002/jrs.4206.

(8) Alvarez, C. J.; Leonard, R. L.; Gray, S. K.; Johnson, J. A.; Petford-Long, A. K. Structural and Kinetic Analysis of $BaCl_2$ Nanocrystals in Fluorochlorozirconate Glass-Ceramics. *J. Am. Ceram. Soc.* 2015, *98* (4), 1099–1104. https://doi.org/10.1111/jace.13410.

(9) Bohley, C.; Wagner, J. M.; Pfau, C.; Miclea, P. T.; Schweizer, S. Raman Spectra of Barium Halides in Orthorhombic and Hexagonal Symmetry: An Ab Initio Study. *Phys. Rev. B - Condens. Matter Mater. Phys.* 2011, *83* (2). https://doi.org/10.1103/PhysRevB.83.024107.

(10) Pfau, C.; Bohley, C.; Miclea, P.; Schweizer, S. Structural Phase Transitions of Barium Halide Nanocrystals in Fluorozirconate Glasses Studied by Raman Spectroscopy. *J. Appl. Phys.* 2013, *083545* (2011). https://doi.org/10.1063/1.3580281.

(11) Bassano, A.; Buscaglia, M. T.; Buscaglia, V.; Nanni, P. Particle Size and Morphology Control of Perovskite Oxide Nanopowders for Nanostructured Materials. *Integr. Ferroelectr.* 2009, *109* (1 PART 2), 1–17. https://doi.org/10.1080/10584580903432395.

(12) Rossel, M.; Hoche, H. R.; Leipner, H. S.; Voltzke, D.; Abicht, H. P.; Hollricher, O.; Muller, J.; Gablenz, S. Raman Microscopic Investigations of $BaTiO_3$ Precursors with Core-Shell Structure. *Anal. Bioanal. Chem.* 2004, *380* (1), 157–162. https://doi.org/10.1007/s00216-004-2712-0.

(13) Catalin, N.; Cernea, M. Characterization of $BaTi_4O_9$ Ceramics by Raman Spectroscopy and XPS after Ion Etching. *J. Optoelectron. Adv. Mater.* 2006, *8* (5), 1879–1883. https://doi.org/joam.inoe.ro/arhiva/pdf8_5/5Negrila.pdf.

(14) Kohno, M.; Ogura, S.; Inoue, Y. Preparation of $BaTi_4O_9$ by a Sol-Gel Method and Its Photocatalytic Activity for Water Decomposition. *J. Mater. Chem.* 1996, *6* (12), 1921–1924. https://doi.org/10.1039/JM9960601921.

Artículo 4

Pt-based catalysts by mechanical dispersion on non-porous alumina microparticles

C.M. Álvarez-Docio, R. Portela, J. J. Reinosa, F. Rubio-Marcos, J. F. Fernández.

Catalysis Communications (Bajo revision).

Factor de impacto: 3.674 (según JCR Edition Science 2018).

Pt-based catalysts by mechanical dispersion on non-porous alumina microparticles

C.M. Álvarez-Docio[a,*], R. Portela[b,*], J. J. Reinosa[a], F. Rubio-Marcos[a,c], J. F. Fernández[a].

[a]*Instituto de Cerámica y Vidrio, CSIC, C/Kelsen 5, 28049, Madrid, Spain.*

[b]*Instituto de Catálisis y Petroleoquímica, CSIC, Marie Curie 2, 28049, Madrid, Spain.*

[c]*Escuela Politécnica Superior. Universidad Antonio de Nebrija. C/Pirineos, 55, 28040, Madrid, Spain.*

Soot combustion, heterogeneous catalysis, Platinum-based catalyst, nanodispersion

ABSTRACT

A sustainable mechanical method to disperse Pt nanoparticles on the surface of non-porous α-Al_2O_3 microparticles is reported. The hierarchical Pt/α-Al_2O_3 catalyst possesses a specific surface area one order of magnitude lower than state-of the-art reported Pt-based catalysts of similar composition, which are based on the gamma alumina phase with high specific surface area. However, the relatively large size of the Pt nanoparticles seems to favor the catalytic soot oxidation in spite of their relatively low dispersion. As a result, the temperature of half conversion (T_{50} = 440 ºC) is lower when compared with conventional Pt/γ-Al_2O_3 obtained by the impregnation route.

INTRODUCTION

Metal nanoparticles are dispersed on porous supports by different methods [1] to exploit their extraordinary properties in sensors, medical applications, or heterogeneous catalysis. Physical techniques or very sophisticated methods require expensive equipment and/or complicated procedures that are no so easily adapted to the industry and can only be afforded in high-added-value

applications. Therefore, despite the continuous development of methodologies that allow a precise control of the catalyst architecture, the most common synthesis procedures for dispersed metallic catalysts are still wet chemical methods, such as the incipient wetness impregnation [2]. Though the practical execution is apparently simple, a metal precursor is dissolved and then a precise amount of the solution is brought into the pores of a high-specific-surface-area supporting material to fill completely their volume. The fundamental phenomena underlying impregnation and drying are complex [3]. Typically, metal precursor-support interactions are limited, thereby permitting the active phase redistribution over the support body during drying, and the impregnation and drying steps involve mass and heat transfer processes [4] that often do not reach equilibrium, resulting in non-uniform concentration profiles in the solid [5]. Moreover, the presence of the active phases inside the small pores may complicate their accessibility for gaseous, but especially for solid reactants. These reasons justify the interest in alternative efficient and simple nanodispersion strategies.

The mechanochemical synthesis of inorganic materials has been used for years, but its application in the context of heterogeneous catalysis is scarce, and has been largely limited to the processing of the support [6]. The use of mechanical methods for the synthesis of catalysts may improve the atomic efficiency, while reducing the use of solvents and the number of synthetic steps, thus contributing to the catalytic process sustainability. Moreover, there is growing evidence of the advantages of mechanochemical methods for doped metal oxides and mixed oxides synthesis/activation, not only in terms of cost and sustainability, but also in obtaining enhanced catalytic properties due to the creation of defects, particle size reduction, or promotion of interactions between components [7,8]. We have recently demonstrated the mechanical activation by low-energy ball milling of a non-porous $CoAl_2O_4$ spinel to catalyze the oxidation of soot efficiently. A similar procedure is proposed here to obtain supported catalysts based on non-porous solids, thereby reducing the catalyst volume, and thus the required reactor size. Ideally, this technology could be adapted to the

requirements of catalytic microreactors, of less than one microliter [9].The miniaturization of chemical reactors entails benefits as decreased reagent and processing costs, increased safety and control, lower waste volume, and improved process conditions, conversion, and selectivity [10,11]. However, the narrow dimension of microreactors usually restricts the number of sites for the active phase dispersion. Consequently, deposition of efficient catalytic coatings onto the walls of microreactor channels is a sought after goal.

This study proposes a mecanochemical dispersion method to synthetize metal-based catalysts anchored on the surface of a non-porous support. The methodology is based on wet milling using metal oxides with dissimilar composition and size to produce hierarchical nanoparticle-microparticle oxide systems, in which unusual properties arise [12], resulting in superior reactivity of the hierarchal catalysts. The objective is to adapt the wet-milling method to obtain nanodisperse noble-metal particles, with the purpose of generating similar materials to those developed in the form of hierarchical micro-nano oxides by dry milling method [13]. This efficient nanodispersion methodology provides a feasible, low-waste, safe-by-design, mass production solution for practical applications. Pt/Al_2O_3 is a reference catalyst for many reactions, and so far the most widely used catalyst for soot oxidation because of its high activity and durability [14,15]. Soot combustion is a demanding reaction, where the contact between gaseous oxidants, soot, and active sites are key parameters. In addition, the price of the catalyst needs to be reduced, as in all environmental processes, and the advantages of using ball-milled materials have already been demonstrated [16]. Thus, the aim of the present work was to synthesize new low-volume active Pt/Al_2O_3 catalysts by mechanical dispersion and test them for soot combustion with NO/O_2 as benchmark reaction.

METHODS

Catalysts preparation.

A dispersed Pt/α-Al_2O_3 catalyst was prepared by low-energy wet milling incorporating the appropriate amount of PtO_2 nanoparticles (Aldrich) into α-Al_2O_3 micrometric support (Vicar, S.A. Manises, Spain). The α-Al_2O_3 microparticles used as substrate had a purity >99.5% and an average particle size of ~6.0 μm. The PtO_2 nanoparticles had a high purity (>99.9%) and average particle size of ~20 nm, and formed agglomerates larger than 20 μm. First, the as-received PtO_2 powder was introduced in a 60 cm^3 nylon container and milled in 20 cm^3 ethanol during 1 h at 500 rpm to break the agglomerates and facilitate the dispersion. Then, the α-Al_2O_3 microparticles were added and the mixture was homogenized by the same milling procedure for 10 min. The whole milling process was assisted by Al_2O_3 balls (1 mm in diameter), with a ratio of mass of grinding balls:mass of powder equal to 1:1. For comparison, Pt/α-Al_2O_3 and Pt/γ-Al_2O_3 catalysts were prepared by the incipient wetness impregnation technique using the same α-Al_2O_3 as in the mechanical method and γ-Al_2O_3 (Girdler Südchemie, 160 m^2/g), respectively. The corresponding alumina support was impregnated with 1 wt. % Pt using an aqueous solution of tetraammineplatinum (II) nitrate $[Pt(NH_3)_4](NO_3)_2$ (Johnson Matthey, 2.648 wt. % solution). Finally, all the samples were thermally treated at 550 ^oC under N_2-H_2 atmosphere with a heating rate of 20^oC/min in order to reduce the oxide to the metallic phase.

Catalysts characterization.

The crystalline phases were characterized by X-ray diffraction (XRD, D8, Bruker) using a Lynx Eye detector and Cu $K\alpha_1$ radiation.

The particle size and morphology of the powders were evaluated by using secondary electron images of field emission scanning electron microscopy (FE-SEM, Hitachi S-4700).

The Brunauer-Emmett-Teller (BET) equation was used to determine the specific surface areas of the catalysts from N_2 adsorption-desorption data obtained in a Micrometrics ASAP2020 analyzer.

The surface composition was determined using an X-ray Photoelectron Spectrometer (XPS, K-alpha, Thermo Scientific), equipped with a monochromated Al Kα (1486.6 eV) source running at a voltage of 12 KV. Pass energy of 200 eV was used for survey scans, while for high-resolution scans the pass energy was 40 eV. Finally, for charge correction a 1 point scale with the C 1s peak shifted to 285 eV was used.

Catalytic tests.

The catalytic activity for soot oxidation was evaluated by a temperature-programmed reaction in a fixed-bed tubular system with a ramp from 25 to 750 ^{o}C at 5 ^{o}C/min. The soot particles were obtained by burning commercial diesel fuel (British Petroleum, Spain) in a glass vessel. Catalyst (100 mg, 0.125-0.250 μm) and soot (10 mg) were carefully mixed to simulate loose-contact mode [17], diluted with 1000 mg of SiC to avoid pressure drop and favour heat transfer, and placed in the middle part of the reactor (ϕ = 4 mm; bed length = 70 mm). The gas feed comprised 2500 ppm NO_x, 10% O_2, and balance N_2; the total gas flow was 300 mL/min (GHSV 150000 h^{-1}). The operating parameters were fixed to be representative of the relatively high NO_x concentration in diesel emissions, for more information see Supplementary Material (***Table S1***). The fixed-bed reactor outlet composition was analyzed with a Thermo Nicolet FT-IR spectrometer. Blank experiments were also conducted: without catalyst, in order to analyze the non-catalytic soot combustion; and without soot, in order to analyze the NO to NO_2 oxidation capacity of the catalysts.

The catalytic performance of the ball-milled Pt/α-Al_2O_3 catalyst for soot oxidation with only O_2 was evaluated by simultaneous thermogravimetric and differential thermal analysis (STA 6000) connected to a Fourier transform infrared (FTIR) spectrometer (Frontier) equipped with a gas cell, both from PerkinElmer. Around 25 mg of powder was placed in an alumina crucible and subjected to a temperature ramp of 10 ^{o}C min^{-1} up to 950 ^{o}C in air atmosphere. IR spectra were collected from 650 to 4000 cm^{-1} at a resolution of 2 cm^{-1} with 2 accumulations.

The catalytic activity was quantified in terms of T_{10}, T_{50} and T_{90} values, defined as the temperatures for 10%, 50% and 90% soot conversion, respectively. Soot conversion was calculated as the fraction of the total carbon released as CO or CO_2 by the integration of the concentration profiles. The selectivity to CO_2 (S_{CO2}) was calculated as CO_2 outlet concentration divided by the sum of the CO_2 and CO outlet concentration. The generation of NO_2 is expressed as NO_2 fraction of the total amount of NO_x ($NO+NO_2$).

RESULTS AND DISCUSSION

Textural and structural characterization.

Figure 1a illustrates the XRD patterns obtained for the as-received and milled PtO_2 raw material and for the $Pt/\alpha\text{-}Al_2O_3$ sample prepared by mechanical dispersion. The diffraction peaks in the pattern of milled PtO_2 are readily indexed to metallic Pt phase, indicating that during the first step of the milling procedure the reduction of PtO_2 to Pt takes place. The energy released during the ball-milling in presence of ethanol was high enough to cause the transformation of PtO_2 into the highly stable metallic Pt phase, and, probably, the oxidation of ethanol [18–21]. The ball-milled $Pt/\alpha\text{-}Al_2O_3$ catalyst evidences sharp peaks due to the α-alumina support and very low-intensity broad peaks related to the metallic Pt phase that indicate the small amount and size of the crystalline domains. ***Figure S1a*** shows the magnification of the 2θ ranges signaled in ***Figure 1a*** with blue and pink rectangles, where the presence or metallic Pt and also of the PtO_2 phase can be guessed. To verify the chemical state of the Pt active component on the catalyst surface, the sample was characterized by XPS (see ***Figure S1b***). The deconvolution of the spectrum in the Pt 4d region into the individual components revealed the presence of two chemical environments for Pt atoms, attributed to Pt^0 and Pt^{2+}. Hence, in spite of the reduced state of Pt when the support microparticles are added to the ball mill, and of the high-temperature reduction treatment performed, some PtO_2 is present on the surface, which has to be related to strong interaction of Pt with the support. First, the metal

reoxidation has to be induced by the presence of the alumina during the second milling step by formation of strong Pt-O-Al interactions. In addition, the alumina support have high resistance of thermal reduction in H_2/N_2 atmosphere at the temperatures used that also could contribute the partial oxidation of metallic Pt.

The morphology of the as-received and milled PtO_2 raw material and of the Pt/α-Al_2O_3 catalysts prepared by ball milling and impregnation was investigated by field-emission scanning electron microscopy (FE-SEM) and the high-resolution (HR) images are shown in ***Figure 1b-e***. Specifically, the PtO_2 powder morphology at local scale (***Figure 1b***) consisted mainly of flake-like particles of 100 to 200 nm in width and ~20 nm in thickness that formed house-of-card agglomerates related to their electrostatic charge. The milling process of the PtO_2 precursor reduced not only the oxidation state of Pt, but also the size of the agglomerates (see ***Figure S1d***), while at the nanoscale the flake-like morphology is substituted by agglomerates (***Figure S1d***).

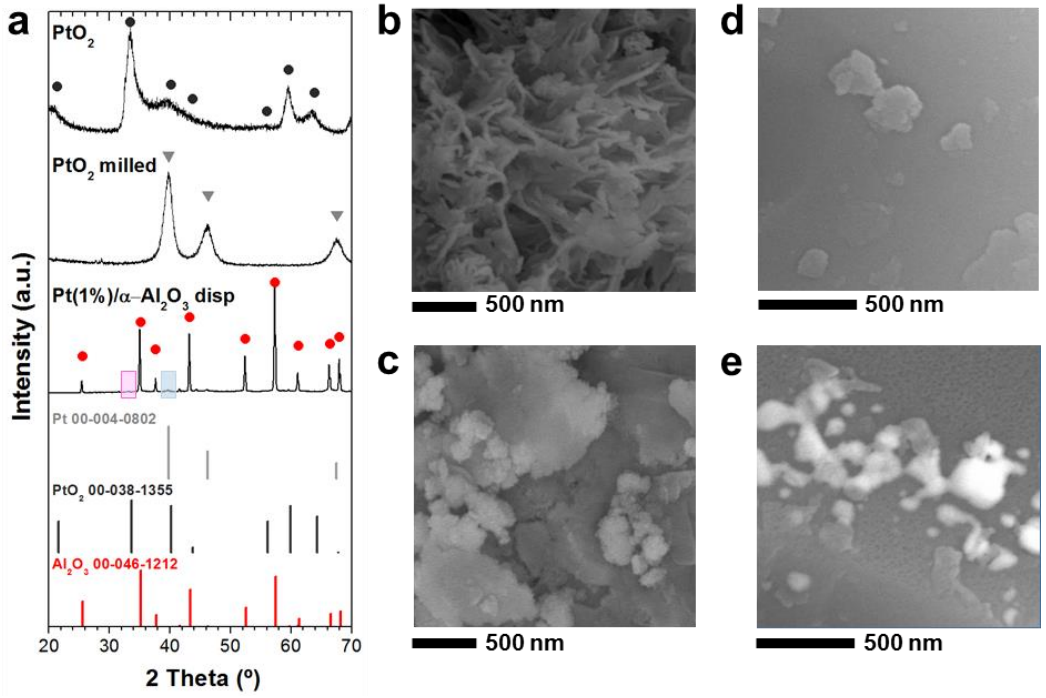

Figure 1.- *(a) XRD patterns of the as-received and milled PtO_2 raw material, the milled Pt(1%)/a-Al_2O_3 catalyst, and JCPD standards for Pt, PtO_2 and a-Al_2O_3. Magnifications in the ranges marked with blue and pink rectangles are shown in Figure S1a. On the right, high-resolution FE-SEM images of PtO_2 nanoparticles: as-received (b) and milled (c), and of Pt/a-Al_2O_3 samples: milled (d) and impregnated (e). Ball-milled Pt-based catalyst on a-Al_2O_3 microparticle shows the alumina surface covered by*

Pt-based particles (d), and impregnated Pt/a-Al_2O_3 shows surface exsolution of Pt-based particles (e). Lower magnification micrographs are shown in the Supplementary Information.

According with FE-SEM images (***Figure 1d,e*** and ***Figure S2a,d***) and EDX mapping (***Figure S2b,e***), in the impregnated sample the platinum particles exsoluted into interconnected, micrometer-sized agglomerates at the surface of the alumina microparticle, which is representative of a low interaction with the non-porous support. Meanwhile, in the ball-milled Pt/α-Al_2O_3 sample, the Pt particles are relatively dispersed on the surface of the α-Al_2O_3. The size of the Pt-based particles in the milled sample is in the 50-500 nm range and the morphology resembles the lamellar shape of the Pt-precursor. The α-Al_2O_3 particles have an average size of ~ 6 μm, in agreement with the specifications of the supporting material, with a nearly hexagonal shape, as shown in ***Figure S2a,d***. Thus, the milling procedure kept the microparticle platelet morphology of the non-milled material [22]. In short, the mechanical methodology used in our research generates a hierarchical catalyst, in which Pt-based particles are dispersed onto the surface of the non-porous alumina microparticles.

Soot combustion catalytic activity.

The results obtained in the temperature-programmed soot combustion experiments carried out under NO_2/O_2 with and without the Pt/Al_2O_3 catalysts are shown in ***Figure 2a-c***. For comparison of the catalytic behavior, ***Table 1*** compiles the temperatures required to achieve 10%, 50%, and 90% soot conversion and the selectivity to CO_2 (calculated by integration of the concentration profiles shown in ***Figure 2b***) obtained in this work, and also for equivalent representative catalysts from the literature. It must be remarked that some of the operating conditions differ in the bibliographic data, so only a tentative, not completely consistent comparison is possible. Therefore, as reference, a Pt/γ-Al_2O_3 sample was prepared by impregnation as well, and tested in the same conditions; the SEM micrograph showing the mesoporous surface of the sample are included in ***Figure S1e,f*** and the catalytic results in the ***Table 1***,

which also summarizes the specific surface areas reported for the different Pt/Al_2O_3 catalysts.

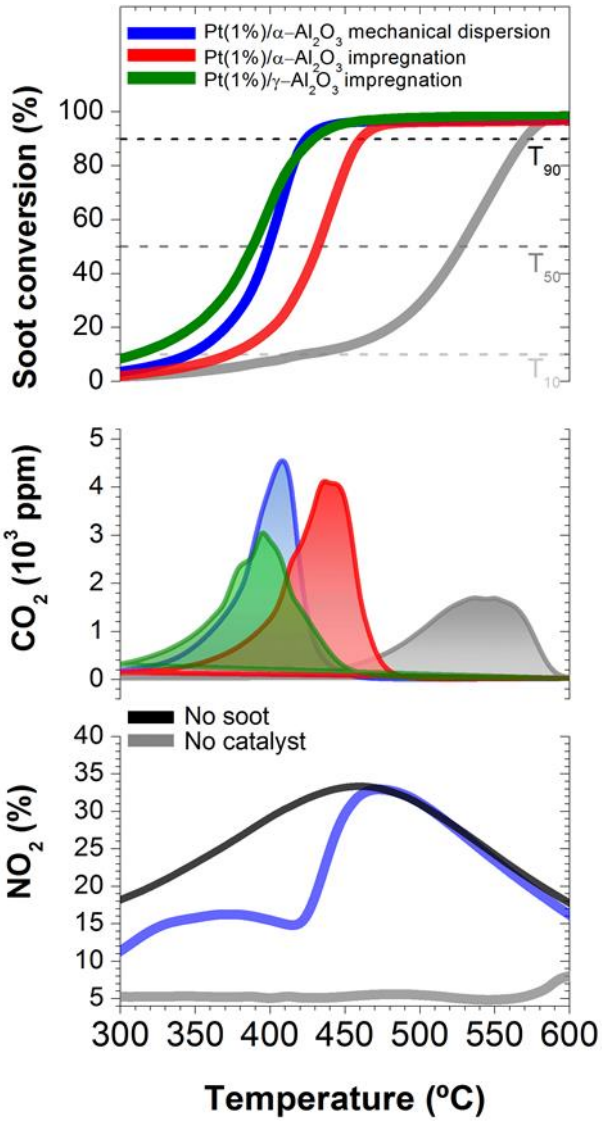

***Figure 2**.- Soot combustion results with the Pt catalysts prepared with a-alumina by wet milling (blue curve) or by impregnation (red curve), or by impregnation of γ-alumina (green curve), and soot combustion results without catalysts (grey curve): (a) Soot conversion profiles, (b) CO_2 generation profiles, and (c) NO_2 to NO_x fraction profiles. Reaction conditions: 100 mg catalyst + 10 mg soot, loose contact, 2500 ppm NO + 10 vol.% O_2 +N_2, 300 ml/min. The black curve in panel (c) is an experiment with the ball-milled Pt/a-Al_2O_3 catalyst without soot (blank experiment).*

Catalyst	S_{BET} (m^2/g)	T_{10} (°C)	T_{50} (°C)	T_{90} (°C)	S_{CO2} (%)	T_{50} (°C) 2nd cycle	Catalyst preparation	Reference
No catalyst		421	527	570	67			This article
Pt/α-Al_2O_3	15.0	345	398	424	100	424	Mechanical dispersion	This article
Pt/α-Al_2O_3	13.8	373	434	465	97	444	Impregnation	This article
Pt/γ-Al_2O_3	160	313	389	429	99	429	Impregnation	This article
Pt/γ-Al_2O_3	138	405	485	490	>98		$Pt(NO_3)_2$ / Impregnation	[24]
Pt/γ-Al_2O_3	137	360	446	500	---		Polyol process/ Impregnation	[25]
Pt/γ-Al_2O_3	160	370	474	550	100		Sigma-Aldrich	[26]

***Table 1**. Comparison of diesel soot combustion catalysts, with the same composition but prepared by different methods, tested in realistic laboratory conditions ("loose" soot-catalyst contact and NO_x + O_2 mixture).*

In the non-catalytic combustion, soot is not consumed completely until the reaction temperature exceeded 600 °C, and 33% of the soot is only partially oxidized to CO. With the synthetized Pt/Al_2O_3 catalysts, the temperature required is lower and the selectivity to CO_2 is complete. The temperature of 10%, 50%, and 90% soot conversion decreased by 76 °C, 129 °C, and 146 °C, respectively, with the ball-milled hierarchical Pt/α-Al_2O_3 catalyst, which shows soot conversion temperatures significantly better that the impregnated Pt/α-Al_2O_3 sample and similar than the impregnated Pt/γ-Al_2O_3 sample, the prepared references. Moreover, the T_{50} of the hierarchical catalyst is lower than that of the most active Pt/γ-Al_2O_3 catalysts obtained by impregnation reported in the literature and 76 °C lower than that of the commercial Pt/γ-Al_2O_3 sample. The evolution of the catalytic oxidation of NO to NO_2 by the mechanically dispersed Pt/α-Al_2O_3 catalyst with and without soot is drawn in ***Figure 2c***. The high NO oxidation capacity of this catalyst, higher than that of the other synthetized samples (results not shown), explains the high soot combustion activity obtained,

because NO_2 is a much stronger oxidizing agent than NO and O_2. In fact, the oxidation profiles obtained in a NO-free atmosphere, illustrated in ***Figure S3***, confirm that the absence of the NO_2-assisted soot combustion mechanism shifts the temperatures towards values similar to the non-catalytic oxidation. In general, samples supported on gamma-alumina, with a larger specific surface area, would favor the dispersion of the active species (i.e. Pt), the adsorption of the gaseous oxidant, and the soot-to-catalyst contact, and thus the catalytic activity. In the hierarchical catalyst, the specific surface area is almost one order of magnitude lower than in the reference ones based on the mesoporous alumina, and the Pt in such a small area is comparatively less dispersed (and therefore it could not be determined by H_2-chemisorption). The explanation for the good performance must be then related to the Pt-based particle accessibility to reactants during soot combustion. Taking into account that the heterogeneously catalyzed NO oxidation is strongly dependent on the Pt particle size, with higher turnover frequencies observed for dispersed but relatively larger Pt nanoparticles [27,28], the hierarchical catalyst, with Pt anchored on the non-porous alpha-alumina surface, seems to have a similar response than impregnated Pt/γ-Al_2O_3 sample that the smaller Pt-metal particles (under FESEM observation Pt-particles are non-detectable in the nanoparticles matrix of γ-Al_2O_3, see ***Figure S1f***). By the contrary the Pt/α-Al_2O_3 by impregnation, fails to produce hierarchical Pt-based catalyst and the agglomeration of Pt-based particles present a worse response. In summary, the mechanically dispersed Pt-based catalyst in alumina shown a behavior in soot combustion similar to the one of standard procedure of impregnation that developed Pt-nanoparticle based catalyst sample. A scheme of the three routes are compared in ***Figure 3***.

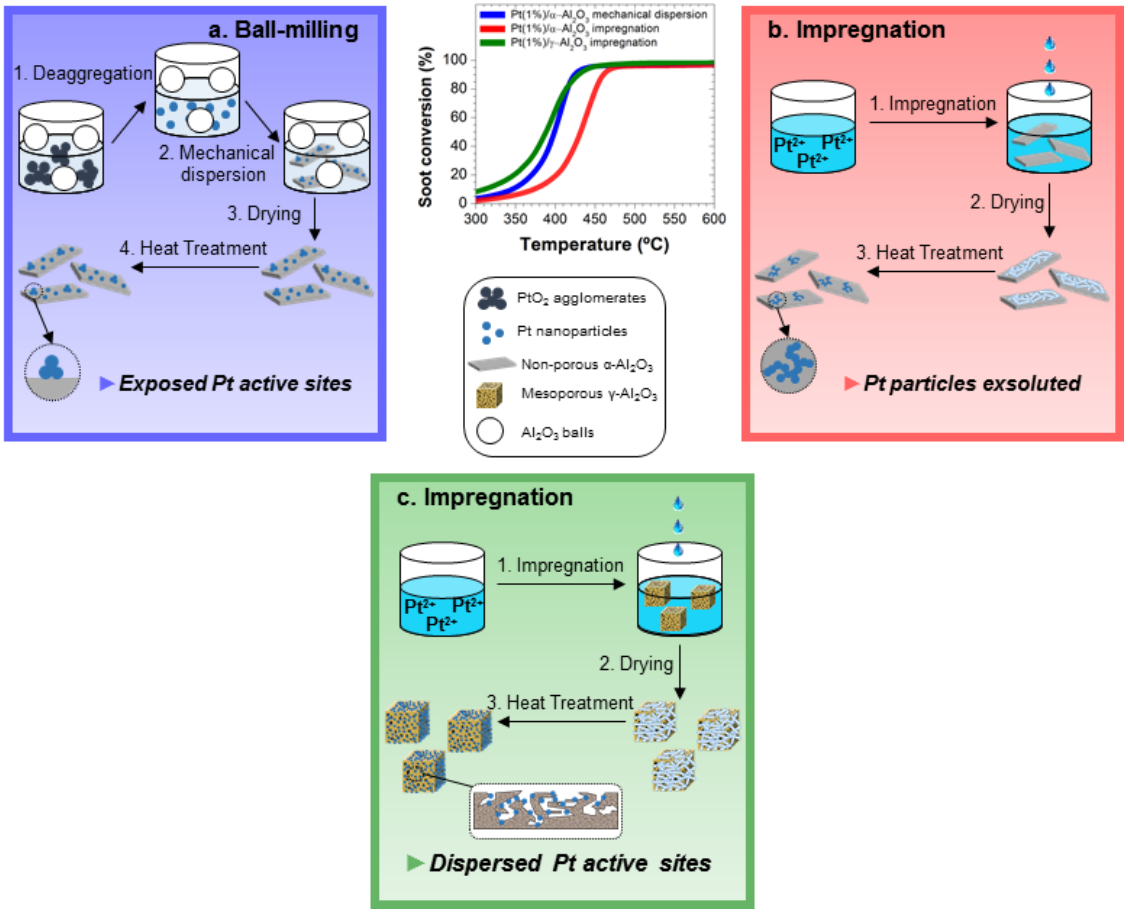

***Figure 3**.- Representation of the attachment of Pt particles to the outer surface of the a-Al_2O_3 support (a and b) or the γ-Al_2O_3 support (c) obtained by using the mechanical dispersion method (a) or the impregnation method (b and c).*

As stability is critical for practical applications, to evaluate the reproducibility of the catalyst performance the used sample was recycled for a second soot combustion test under identical reaction conditions by recharging the soot load. The ball-milled Pt/Al_2O_3 catalyst essentially maintains its initial activity. The slight increase of the T_{50} value in the second soot combustion cycle, of 26 °C, could be mainly attributed to the methodology employed to reload the reactor and the subsequent loss of some of the catalyst mass, although some sintering or defects reconstruction cannot be discarded. Small increases of 10 ºC and 40 ºC were also observed with the impregnated reference samples based on alpha and gamma alumina, respectively, which may be related to the lower stability of the latter phase at the high temperatures achieved in the reactor, 750 ºC.

Finally, our study may lay the groundwork for the integration of the mechanical nanodispersion method in microreactor technology. We have demonstrated that efficient platinum catalysts can be obtained using non-porous low-volume supports. Hence, with the application of the hierarchical catalyst concept, microchannel walls might be effectively covered by active material by direct immersion in wet-milled slurries. The concept here reported would represent a step ahead toward microreactors implementation and a considerable reduction in the channel size.

CONCLUSIONS

A hierarchical catalyst, consisting of Pt particles on α-Al_2O_3 microparticles, was successfully synthetized by a mechanical wet dispersion method. The activity of the hierarchical low-volume Pt(1%)/α-Al_2O_3 catalyst for soot combustion in the presence of NO is better than that of the impregnated counterpart, similar to the reference sample obtained by impregnation of mesoporous alumina, and improved the best results reported in the state-of-the-art literature for this composition. The location of rather large Pt particles well anchored at the small but easily accessible alpha-alumina surface seems to favor the reaction in spite of the relatively low metal dispersion. A further increase in catalytic activity may be expected if the wet-milling process is optimized, and high stability is predicted according to the properties of the alpha phase of alumina, the high metal-support interaction achieved by the milling process, and the similar results obtained when the sample was reused. Thus, the use of a low-energy simple dispersion method seems to be a promising way to reduce the cost of soot oxidation catalysts and improve their performance. We believe that the general strategy described in this study will open new avenues in developing novel catalysts with enhanced properties for a wealth of catalytic reactions.

ACKNOWLEDGMENT

The authors express their thanks to the project NANOMIND CSIC201560E068 and MAT2017-86450-C4-1-R for their financial support. C.M. Alvarez-Docio for a FPI grant BES-2014-069779, which are co-financed with FEDER funds. F. Rubio-Marcos is indebted to MINECO for a 'Ramon y Cajal' contract (ref: RyC-2015-18626), which is co-financed by the European Social Fund. F.R-M also acknowledges support from a 2018 Leonardo Grant for Researchers and Cultural Creators (BBVA Foundation).

REFERENCES

[1]R.J. White, R. Luque, V.L. Budarin, J.H. Clark, D.J. MacQuarrie, Supported metal nanoparticles on porous materials. Methods and applications, Chem. Soc. Rev. 38 (2009) 481–494.

[2]J.R.A. Sietsma, A. Jos van Dillen, P.E. de Jongh, K.P. de Jong, Application of ordered mesoporous materials as model supports to study catalyst preparation by impregnation and drying, in: Sci. Bases Prep. Heterog. Catal., Elsevier Masson SAS, Amsterdam, 2006: pp. 95–102.

[3]F. Liao, T.W.B. Lo, S.C.E. Tsang, Recent developments in Palladium-based bimetallic catalysts, ChemCatChem. 7 (2015) 1998–2014.

[4]M. Komiyama, Design and preparation of impregnated catalysts, Catal. Rev. Sci. Eng. 27 (1985) 341–372.

[5]A. Lekhal, B.J. Glasser, J.G. Khinast, Impact of drying on the catalyst profile in supported impregnation catalysts, Chem. Eng. Sci. 56 (2001) 4473–4487.

[6]K. Ralphs, C. Hardacre, S.L. James, Application of heterogeneous catalysts prepared by mechanochemical synthesis, Chem. Soc. Rev. 42 (2013) 7701–7718.

[7]C. Borchers, M.L. Martin, G.A. Vorobjeva, O.S. Morozova, A.A. Firsova, A. V. Leonov, E.Z. Kurmaev, A.I. Kukharenko, I.S. Zhidkov, S.O. Cholakh, Cu–

CeO_2 nanocomposites: Mechanochemical synthesis, physico-chemical properties, CO-PROX activity, J. Nanoparticle Res. 18 (2016) 344.

[8]C. Tang, B. Sun, J. Sun, X. Hong, Y. Deng, F. Gao, L. Dong, Solid state preparation of NiO-CeO_2 catalyst for NO reduction, Catal. Today. 281 (2017) 575–582.

[9]E. V. Rebrov, A. Berenguer-Murcia, H.E. Skelton, B.F.G. Johnson, A.E.H. Wheatley, J.C. Schouten, Capillary microreactors wall-coated with mesoporous titania thin film catalyst supports, Lab Chip. 9 (2009) 503–506. doi:10.1039/b815716b.

[10] A. Tanimu, S. Jaenicke, K. Alhooshani, Heterogeneous catalysis in continuous flow microreactors: A review of methods and applications, Chem. Eng. J. 327 (2017) 792–821. doi:10.1016/j.cej.2017.06.161.

[11] R. Munirathinam, J. Huskens, W. Verboom, Supported catalysis in continuous-flow microreactors, Adv. Synth. Catal. 357 (2015) 1093–1123. doi:10.1002/adsc.201401081.

[12] F. Rubio-Marcos, V. Calvino-Casilda, M.A. Bañares, J.F. Fernandez, Novel hierarchical Co_3O_4/ZnO mixtures by dry nanodispersion and their catalytic application in the carbonylation of glycerol, J. Catal. 275 (2010) 288–293. doi:10.1016/j.jcat.2010.08.009.

[13] M. Danielis, S. Colussi, C. de Leitenburg, L. Soler, J. Llorca, A. Trovarelli, Outstanding methane oxidation performance of palladium-embedded ceria catalysts prepared by a one-step dry ball-milling method, Angew. Chemie - Int. Ed. 57 (2018) 10212–10216.

[14] J. Oi-Uchisawa, S. Wang, T. Nanba, A. Ohi, A. Obuchi, Improvement of Pt catalyst for soot oxidation using mixed oxide as a support, Appl. Catal. B Environ. 44 (2003) 207–215.

[15] J. Lee, E.J. Jang, J.H. Kwak, Effect of number and properties of specific sites on alumina surfaces for Pt-Al2O3 catalysts, Appl. Catal. A Gen. 569 (2019) 8–19. doi:10.1016/j.apcata.2018.10.004.

[16] C.M. Álvarez-Docio, R. Portela, J.J. Reinosa, F. Rubio-Marcos, C. Granados-Miralles, L. Pascual, J.F. Fernández, Pt-free $CoAl_2O_4$ catalyst for soot combustion with NO_x/O_2, Appl. Catal. A Gen. 591 (2020) 117404.

[17] B.A.A.L. van Setten, J.M. Schouten, M. Makkee, J.A. Moulijn, Realistic contact for soot with an oxidation catalyst for laboratory studies, Appl. Catal. B Environ. 28 (2000) 253–257.

[18] R.W. McCabe, P.J. Mitchell, Reactions of ethanol and acetaldehyde over noble metal and metal oxide catalysts, Ind. Eng. Chem. Prod. Res. Dev. 23 (1984) 196–202. doi:10.1021/i300014a003.

[19] R.D. Gonzalez, N. Masatoshi, Oxidation of ethanol on silica supported noble metal and bimetallic catalysts, Appl. Catal. 18 (1985) 57–70.

[20] L.M. Petkovic, S.N. Rashkeev, D.M. Ginosar, Ethanol oxidation on metal oxide-supported platinum catalysts, Catal. Today. 147 (2009) 107–114. doi:10.1016/j.cattod.2009.02.015.

[21] Y.F.Y. Yao, Catalytic oxidation of ethanol at low concentrations, Ind. Eng. Chem. Process Des. Dev. 23 (1984) 60–67. doi:10.1021/i200024a011.

[22] I. Lorite, M.S. Martín-González, J.J. Romero, M.A. García, J.L.G. Fierro, J.F. Fernández, Electrostatic charge dependence on surface hydroxylation for different Al_2O_3 powders, Ceram. Int. 38 (2012) 1427–1434. doi:10.1016/j.ceramint.2011.09.024.

[23] A. Serrano, O. Llorca-Hernando, A. Del Campo, F. Rubio-Marcos, O. Rodríguez de La Fuente, J.F. Fernández, M.A. García, Ag-AgO nanostructures on glass substrates by solid-state dewetting: From extended to localized surface plasmons, J. Appl. Phys. 124 (2018).

[24] S. Liu, X. Wu, D. Weng, R. Ran, NOx-assisted soot oxidation on Pt-Mg/Al2O3 catalysts: Magnesium precursor, Pt particle size, and Pt-Mg interaction, Ind. Eng. Chem. Res. 51 (2012) 2271–2279. doi:10.1021/ie202239c.

[25] Y. Gao, W. Yang, X. Wu, S. Liu, D. Weng, R. Ran, Controllable synthesis of supported platinum catalysts: Acidic support effect and soot oxidation catalysis, Catal. Sci. Technol. 7 (2017) 3268–3274. doi:10.1039/c7cy01087g.

[26] J. Giménez-Mañogil, A. García-García, Opportunities for ceria-based mixed oxides versus commercial platinum-based catalysts in the soot combustion reaction. Mechanistic implications, Fuel Process. Technol. 129 (2015) 227–235.

[27] B.M. Weiss, E. Iglesia, NO oxidation catalyzed by Pt: elementary steps, structural effects and synergistic effects of NO_2 adsorption sites, J. Phys. Chem. C. 94720 (2007) 94720–94720.

[28] S. Benard, L. Retailleau, F. Gaillard, P. Vernoux, A. Giroir-Fendler, Supported platinum catalysts for nitrogen oxide sensors, Appl. Catal. B Environ. 55 (2005) 11–21. doi:10.1016/j.apcatb.2004.07.005.

Supplementary material

Pt-based catalysts by mechanical dispersion on non-porous alumina microparticles

C.M. Álvarez-Docio[a,*], R. Portela[b,*], J. J. Reinosa[a], F. Rubio-Marcos[a,c], J. F. Fernández[a].

[a]*Instituto de Cerámica y Vidrio, CSIC, C/Kelsen 5, 28049, Madrid, Spain.*

[b]*Instituto de Catálisis y Petroleoquímica, CSIC, Marie Curie 2, 28049, Madrid, Spain.*

[c]*Escuela Politécnica Superior. Universidad Antonio de Nebrija. C/Pirineos, 55, 28040, Madrid, Spain.*

*E-mail address: carmenma.docio@icv.csic.es (Carmen Álvarez)

*E-mail address: raquel.portela@csic.es (Raquel Portela)

We would like to highlight the absence of a standard protocol for these tests. Typically, experimental conditions are specific for each publication and the feed gas composition used changes considerably from one to another reference, as can be observed in the ***Table S1***:

Ref.	Catalyst/soot/SiC weight ratio	Reactor	Gas flow	Feed gas composition
[1]	80/20/300 (loose contact)	Fixed-bed reactor, Ø=1 cm; bed length=1.25 cm	500 ml/min GHSV 30000 h^{-1}	500 ppm NO_x + 5% O_2
[2]	Catalyst 0.2 g	Quartz tube reactor, Ø=6 mm	100 ml/min GHSV 12000 h^{-1}	1000 ppm NO, 1000 ppm C_2H_4, 2% O_2
[3]	100/10/0 (loose contact)	Fixed-bed tubular quartz microreactor, Ø=6 mm	80 ml/min GHSV 6760 h^{-1}	2500 ppm NO_x + 5% O_2
[4]	150/10/0 (tight contact)	Tubular quartz reactor	100 ml/min	5000 ppm NO-O_2-He
[5]	100/10/300 (loose contact)	Tubular quartz reactor	500 ml/min	1000 ppm NO_x + 10% O_2
[6]	100/20/300 (loose contact)	Tubular quartz reactor	GHSV 30000 h^{-1}	500 ppm NO_x + 10% O_2
[7]	80/20/300 (loose contact)	Tubular quartz reactor	500 ml/min GHSV 30000 h^{-1}	500 ppm NO_x + 5% O_2
Our study	100/10/1000 (loose contact)	Fixed-bed reactor, Ø=4 mm; bed length= 7 cm	300 ml/min GHSV 150000 h^{-1}	2500 ppm NO_x + 10% O_2

Table S1. *Experimental conditions of soot combustion catalysts.*

Moreover, the operating parameters were fixed in order to be representative of the relatively high NO_x concentration in diesel emissions, on the basis of the current literature. Accordingly to an inform of the International Council on Combustion Engines, called "*Guide to Diesel exhaust emissions control of NO_x, SO_x, particulates, smoke and CO_2*", the composition of the exhaust gases of the diesel combustion engines contains between 50-1000 ppm of NO_x. McKee et al. reported that the amount of nitrogen oxides, depending on the type of engine and the revolutions, ranges from 15 to 1370 ppm [8]. Jimenez et al. established that diesel engines could emit up to about 3000 ppm of NO_x [9]. Finally, Olsen et al. commented that a Cooper-Bessemer GMV-4TF type engine generates a 5030 ppm peak of NO_2 [10].

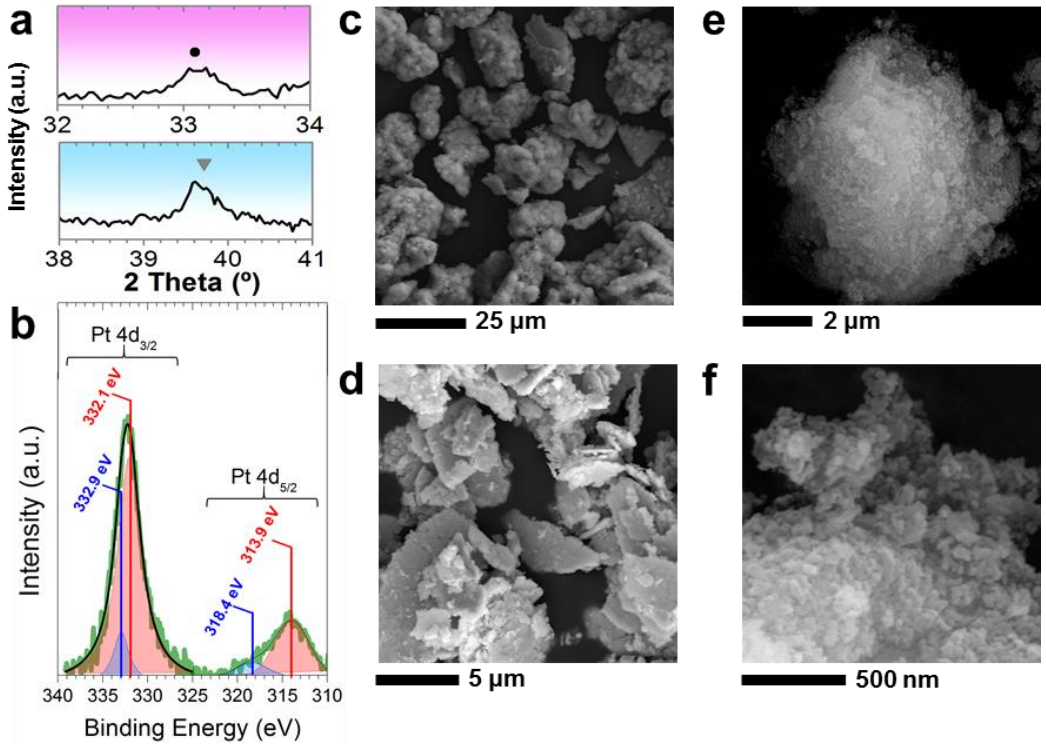

Figure S1.- *On the left, (a) Magnification of the main PtO_2 diffraction peak in the catalyst (pink rectangle) and of the main Pt diffraction peak in the catalysts (blue rectangle). (b) X-ray photoelectron spectrum of the Pt(1%)/Al_2O_3 sample in the Pt 4d region (green curve) and the deconvoluted $4d_{5/2}$ and $4d_{3/2}$ signals for Pt^0 (marked in red) and Pt^{2+} (marked in blue). On the right, low-resolution FE-SEM images of the surface of as-received (c) and milled (d) PtO_2 nanoparticles.*

Figure S1a illustrates the magnification of the main Pt and PtO_2 diffraction peaks in the Pt/Al_2O_3 catalyst prepared by nanodispersion, this XRD peaks have very low intensity and are quite broad, which indicates that the amount and size of the crystalline domains is small.

To verify the emergence of the metallic Pt phase on Pt/α-Al_2O_3 catalyst prepared by mechanical dispersion (*that is, the chemical state of the Pt active components*), the sample was characterized by XPS (see ***Figure S1b***). The Al 2p signal of the support microparticles overlaps with the Pt 4f signal of the active component usually used for the spectroscopic analysis of platinum [11]. Therefore, although the Pt 4d signal is weaker, it was used for the analysis because it is not overlapped by the spectral signals of the other components. ***Figure S1b*** displays the spectral region of the Pt 4d signal, in the range of 310-340 eV. The decomposition of the spectrum into the individual components revealed

the presence of two chemical environments for Pt atoms, the major contribution to Pt $4d_{5/2}$ at 313.9 eV and a minor one at 318.4 eV, attributed to Pt^0 and Pt^{2+}, respectively. Hence, in spite of the reduction treatment performed, some PtO_2 is present on the surface.

The field-emission scanning electron micrographs (FE-SEM) of as-received and milled PtO_2 nanoparticles are shown in ***Figure S1c,d***. The PtO_2 morphology (***Figure S1c***) consisted mainly of flake-like particles of 100 to 200 nm in width and ~20 nm in thickness that formed house-of-card agglomerates related to the electrostatic charge. The agglomerates size is reduced by the milling of the powder (***Figure S1d***).

Finally, as reference, a $Pt/\gamma\text{-}Al_2O_3$ sample was prepared by impregnation as well, and tested in the same conditions; the SEM micrograph showing the mesoporous surface of the sample are included in ***Figure S1e,f***.

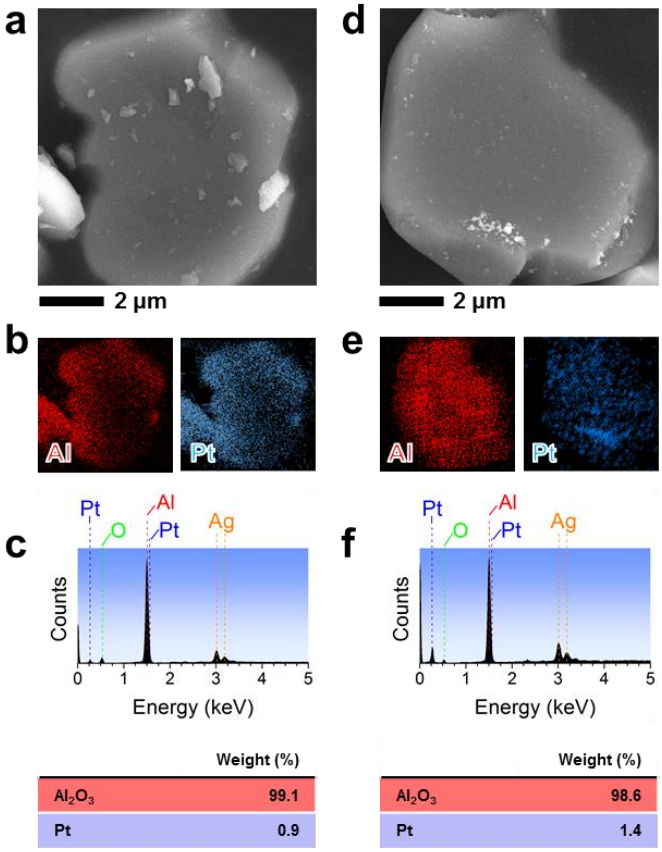

***Figure S2**.- Comparison of the Pt/a-Al_2O_3 catalysts prepared by mechanical dispersion (left) and impregnation (right): a, d) FE-SEM micrograph, b, e) EDX elemental mapping obtained in the same area as a and d), and c,d) Global EDX spectrum and semi-quantitative compositional values obtained.*

The α-Al_2O_3 particles in Pt/α-Al_2O_3 sample (***Figure S2a,d***) have an average size of ~ 6 µm with a nearly hexagonal shape. Milling procedure kept the microparticle platelet morphology (see ***Figure S2a*** in agreement with ref. [12]).

According with EDX mapping (***Figure S2b,e***), in the ball-milled Pt/α-Al_2O_3 sample the Pt particles are relatively dispersed on the surface of the non-porous α-Al_2O_3. The size of the Pt-based particles is in the 50-500 nm range and shown a lamellar type morphology that resemble the one of the Pt-precursor. On the other hand, in the impregnated sample the platinum particles exsoluted into interconnected micrometer-sized agglomerates at the surface of the alumina agglomerate, representative of a low interaction with the non-porous support.

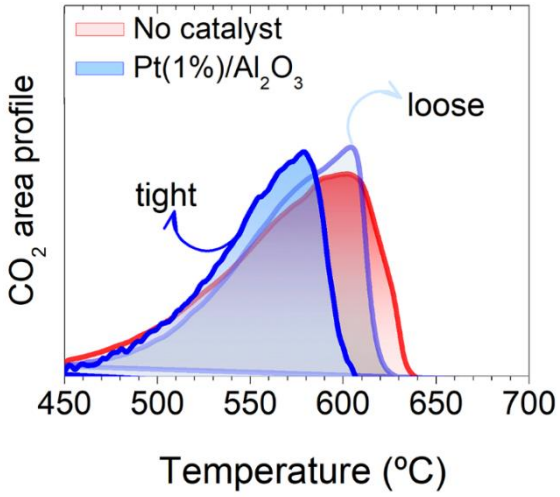

***Figure S3**.- Soot combustion with O_2 in the absence of NO, without (red curve) and with the hierarchical Pt(1%)/Al_2O_3 catalyst, under loose (light-blue curve) or tight (blue curve) soot-to-catalyst contact.*

The profiles obtained under a NO-free atmosphere (containing only 10% O_2 as oxidant) are illustrated in ***Figure S3***. The activity of the hierarchical Pt/α-Al_2O_3 catalyst is different to that found under NO_x/O_2 and, as expected, the curve is shifted towards temperatures similar to the non-catalytic oxidation, due to the absence of the NO_2 assisted soot combustion mechanism. The high activity of the noble metal towards soot combustion originated in the hierarchical catalyst must not only be due to its faster NO_2 production, but also to its efficiency to recycle the NO molecules derived from the NO_2-soot reaction again to NO_2 along the catalyst-soot bed. NO first reacts with the catalyst to generate a much stronger oxidative agent, NO_2, and then the NO_2 can oxidize soot to accomplish the catalysis cycle, in line with the NO_2-assisted mechanism reported in the literature [13,14].

REFERENCES

[1]M. Zawadzki, W. Walerczyk, F.E. López-Suárez, M.J. Illán-Gómez, A. Bueno-López, $CoAl_2O_4$ spinel catalyst for soot combustion with NO_x/O_2, Catal. Commun. 12 (2011) 1238–1241.

[2]X. Chen, A. Zhu, C. Shi, The nature of active sites of Co/Al_2O_3 for the selective catalytic reduction of NO with C_2H_4, Catal. Letters. 133 (2009) 134–141.

[3]J. Wang, G. Yang, L. Cheng, E.W. Shin, Y. Men, Three-dimensionally ordered macroporous spinel-type MCr_2O_4 (M = Co, Ni, Zn, Mn) catalysts with highly enhanced catalytic performance for soot combustion, Catal. Sci. Technol. 5 (2015) 4594–4601.

[4]H. Lin, Y. Li, W. Shangguan, Z. Huang, Soot oxidation and NO_x reduction over $BaAl_2O_4$ catalyst, Combust. Flame. 156 (2009) 2063–2070.

[5]S. Liu, X. Wu, D. Weng, R. Ran, NO_x-assisted soot oxidation on Pt-Mg/Al_2O_3 catalysts: Magnesium precursor, Pt particle size, and Pt-Mg interaction, Ind. Eng. Chem. Res. 51 (2012) 2271–2279.

[6]Y. Gao, W. Yang, X. Wu, S. Liu, D. Weng, R. Ran, Controllable synthesis of supported platinum catalysts: Acidic support effect and soot oxidation catalysis, Catal. Sci. Technol. 7 (2017) 3268–3274.

[7]J. Giménez-Mañogil, A. García-García, Opportunities for ceria-based mixed oxides versus commercial platinum-based catalysts in the soot combustion reaction. Mechanistic implications, Fuel Process. Technol. 129 (2015) 227–235.

[8]H.C. McKee, J.M. Clark, R.J. Wheeler, Measurement of diesel engine emissions, J. Air Pollut. Control Assoc. 12 (1962) 516–546.

[9]J.L. Jimenez, G.J. Mcrae, D.D. Nelson, M.S. Zahniser, C.E. Kolb, Remote sensing of NO and NO_2 emissions from heavy-duty diesel trucks using tunable diode lasers, Environ. Sci. Technol. 34 (2000) 2380–2387.

[10] D.B. Olsen, M. Kohls, G. Arney, Impact of oxidation catalysts on exhaust NO_2/NO_x ratio from lean-burn natural gas engines, J. Air Waste Manag. Assoc. 60 (2010) 867–874.

[11] T. Deng, H. Liu, Promoting effect of SnO_x on selective conversion of cellulose to polyols over bimetallic Pt–SnO_x/Al_2O_3 catalysts, Green Chem. 15 (2013) 116–124. doi:10.1039/C2GC36088H.

[12] I. Lorite, M.S. Martín-González, J.J. Romero, M.A. García, J.L.G. Fierro, J.F. Fernández, Electrostatic charge dependence on surface hydroxylation for different Al_2O_3 powders, Ceram. Int. 38 (2012) 1427–1434. doi:10.1016/j.ceramint.2011.09.024.

[13] S. Liu, X. Wu, D. Weng, M. Li, J. Fan, Sulfation of Pt/Al_2O_3 catalyst for soot oxidation: High utilization of NO_2 and oxidation of surface oxygenated complexes, Appl. Catal. B Environ. 138–139 (2013) 199–211. doi:10.1016/j.apcatb.2013.02.053.

[14] J. Oi-Uchisawa, S. Wang, T. Nanba, A. Ohi, A. Obuchi, Improvement of Pt catalyst for soot oxidation using mixed oxide as a support, Appl. Catal. B Environ. 44 (2003) 207–215.

Artículo 5

Pt-free $CoAl_2O_4$ catalyst for soot combustion with NO_x/O_2

C.M. Álvarez-Docio, R. Portela, J. J. Reinosa, F. Rubio-Marcos, C. Granados-Miralles, L. Pascual, J. F. Fernández.

Applied Catalysis A: General, 591, 2020, 117404.

Factor de impacto: 4.630 (según JCR Edition Science 2018).

Applied Catalysis A, General 591 (2020) 117404

Contents lists available at ScienceDirect

Applied Catalysis A, General

journal homepage: www.elsevier.com/locate/apcata

Pt-free $CoAl_2O_4$ catalyst for soot combustion with NO_x/O_2

C.M. Álvarez-Docio[a,*], R. Portela[b,*], J.J. Reinosa[a], F. Rubio-Marcos[a,c], C. Granados-Miralles[a], L. Pascual[b], J.F. Fernández[a]

[a] Instituto de Cerámica y Vidrio, CSIC, C/Kelsen 5, 28049, Madrid, Spain
[b] Instituto de Catálisis y Petroleoquímica, CSIC, Marie Curie 2, 28049, Madrid, Spain
[c] Escuela Politécnica Superior, Universidad Antonio de Nebrija, C/Pirineos, 55, 28040, Madrid, Spain

ARTICLE INFO

Keywords:
CoAl2O4 spinel
Diesel soot oxidation
NOx
Mechanism
Pt-free

ABSTRACT

Cobalt aluminate spinel compounds prepared by different methods were characterized in terms of crystalline structure, morphology, textural properties and acidity, and evaluated as catalysts for diesel soot combustion in NO_x/O_2 mixtures. The activation of commercial $CoAl_2O_4$ microparticles by ball milling reduced the onset temperature of this material considerably and yielded an efficient catalyst for soot combustion that exhibited a temperature of half conversion, 411 °C, similar to that obtained with the reference Pt/Al_2O_3 catalyst. Moreover, like Pt, the milled $CoAl_2O_4$ suppressed the CO formation observed in non-catalytic soot combustion. The significant modification of the particle size, the emergence of new exposed crystal facets and the creation of defects are responsible for the appearance of new active sites and high acidity that improved catalyst-to-soot contact and reactivity. The findings open a new gate toward the use of efficient Pt-free catalyst for soot combustion.

1. Introduction

Diesel engines generally achieve the highest fuel, energy and thermal efficiency. Their main drawback is the emission of fine black soot particulates, which causes serious problems for human health and the global environment [1,2]. Nowadays, diesel particulate filters (DPFs) that combine separation by size and filter regeneration by catalytic combustion are regarded as the most efficient after-treatment technology for soot particulates elimination to avoid their atmospheric release. Diesel soot is first trapped by the filter and then removed by combustion on the catalytic coating [3,4]. The maximum temperature of diesel engines exhaust gas falls in the range from 260 to 540 °C, and therefore the catalysts must be active enough at these low temperatures. Hence, there is a strong incentive to develop a catalyst for continuous regeneration of DPFs that displays good activity at the temperature of diesel exhausts, with good stability and durability, at a relatively low cost, and, most of all, eco-friendly.

Catalysts based on noble metal active phases such as platinum promote the oxidation of NO, naturally present in the exhausts, to NO_2. The latter is a stronger oxidant than O_2, and thus contributes to decrease the soot combustion onset temperature. However, the cost and scarcity of noble metals has led to the study of other non-critical materials that can be competitive in terms of catalytic activity and price. Among the alternative formulations, cobalt-containing oxidic catalysts have been deeply investigated. Harrison et al. [5] reported a high activity and selectivity for soot oxidation of the CoO/CeO_2 system that was correlated to the strong redox ability of CoO_x [6,7]. Other cobalt oxidic compounds that have been proposed as potential catalysts for the abatement of soot in diesel exhausts are nanostructured spinel-type oxides, such as cobalt aluminates [8] or compounds with the formula AB_2O_4, where A = Co or Mn, and B = Cr or Fe [9]. The catalytic activity of $CoAl_2O_4$ spinel in the simultaneous removal of soot and NO_x, the two prevalent pollutants in diesel exhaust gases in the temperature range of 350–450 °C, can be attributed to its high NO_x chemisorption capacity, which facilitates NO to NO_2 oxidation. To date, however, $CoAl_2O_4$ efficiency is limited by the absence of surface active Co^{3+} species, major actor in catalysing oxidation [10].

In recent years, the controlled synthesis of metal oxide nanoparticles with tailored crystal facets has received tremendous attention, because their different terminated surface atomic arrangements and coordination generally provide diverse sites for adsorption and activation of reactant molecules [11–13]. Therefore, crystal facet engineering offers new perspectives for the fundamental understanding of catalysis and, thus, for surface properties optimization. Also, it has long been known that mechano-chemical surface activation can increase the specific surface area [14], lead to partial amorphization of the surface layer [15], or generate crystalline defects [16], which may improve the performance of solid catalysts [17].

* Corresponding authors.
E-mail address: carmenma.docio@icv.csic.es (C.M. Álvarez-Docio).

https://doi.org/10.1016/j.apcata.2019.117404
Received 11 September 2019; Received in revised form 26 December 2019; Accepted 27 December 2019
Available online 28 December 2019
0926-860X/

In this work, we study the catalytic combustion of soot with NO_x/O_2 on two types of cobalt aluminate spinel: a synthetized nanocrystalline (111) $CoAl_2O_4$ supported on α-Al_2O_3 microparticles [18,19], and commercial $CoAl_2O_4$ microparticles modified by a simple mechanical method to activate the surface. The mechanical creation of defects and several new exposed facets led to a promising low-cost catalyst for soot combustion.

2. Experimental Procedure

2.1. Catalysts preparation

A commercial $CoAl_2O_4$ micrometric pigment, supplied by Manuel Riesgo S.A. (Spain), was mechanically activated by ball milling at 50 rpm, with 1 mm cerium-stabilized zirconia balls, during 3 h in a polyamide type jar (Spex 8000 Mixer mill milling equipment). The $mass_{balls}/mass_{powder}$ ratio was 1:1 and 33 % in ethanol medium. During the wet ball milling the microballs produce collisions or compressive forces in combination with the shear stress forces that promote the creation of particles with reduced size and new crystallographic facets as result of the random ball impacts.

Catalysts with 30 wt.% of Co_3O_4 nanoparticles on α-Al_2O_3 microparticles (hereafter named as 70Al30Co) were prepared by a previously described dry solid-state method and thermally treated at 1200 °C for 5 h with a heating rate of 3 °C/min [20].

2.2. Catalysts characterization

The crystalline phases were characterized by X-ray diffraction (XRD, D8, Bruker) using Cu Kα1 radiation and a LynxEye detector. Quantitative information on the structure and microstructure of the samples was extracted from Rietveld analysis of the XRD data using FullProf Suite [21]. In the refinements, the main phase spinel phase, $CoAl_2O_4$, was described in the Fd-3 m space group (227), with all the Co^{2+} in Td-sites and all the Al^{3+} in Oh-sites. The secondary spinel phase present in the commercial samples was also modelled as a Rietveld phase while the α-Al_2O_3 was described using a Le Bail fit. After deconvolution of the instrumental broadening contribution, the peak profile was modelled as isotropic Lorentzian size-broadening, and volume-weighted average crystallite sizes were obtained from the Scherrer equation [22]. The background was fitted with an orthogonal Chebyshev polynomial of 3 coefficients.

The surface composition was determined using an X-ray Photoelectron Spectrometer (XPS, K-Alpha, Thermo Scientific), equipped with a monochromated Al Kα (1486.6 eV) source running at a voltage of 12 KV. The pass energy was 200 eV for survey scans and 40 eV for high resolution scans. Finally, for charge correction a 1 point scale with the C 1s peak shifted to 285 eV was used.

The Brunauer-Emmett-Teller (BET) equation was used to determine the surface areas of the catalysts from N_2 adsorption-desorption data obtained in a Micrometrics ASAP2020 analyzer.

The morphology of the powders was evaluated by using secondary electron images of field emission scanning electron microscopy (FE-SEM, Hitachi S-4700). An image processing and analysis program (Leica Qwin, Leica Microsystems Ltd, Cambridge, England) was used to determine the microstructural parameters from FE-SEM micrographs, always considering more than 150 particles in each measurement.

Particle size distribution of the catalyst powders were determined by laser diffraction (Mastersizer S, Malvern, U.K.).

The particle size and morphology at the nanoscale were also evaluated using a transmission electron microscope (TEM/HRTEM, JEOL 2100 F) operating at 200 kV and equipped with a field emission electron gun providing a point resolution of 0.19 nm. HRTEM filtering and image processing were performed using Digital Micrograph software.

Raman spectra were obtained using a confocal micro-Raman system (Witec alpha − 300R, Witec, Ulm, Germany) with a 532 nm excitation laser and a 100x objective lens (NA = 0.9). The incident laser power was 0.5 mW for all samples. The final spectra are the result of an average of 10 spectra integrating 30 s each spectrum. Collected spectra were analysed by using Witec Control Plus Software (Witec, Ulm, Germany).

NH_3 temperature-programmed desorption (NH_3-TPD) was performed on a Micromeritics Autochem II 2920 apparatus. Prior to the NH_3-TDP experiments, under He flow the samples (200 mg) were pretreated at 200 °C for 0.5 h and cooled to 100 °C. Then the samples were exposed to a NH_3 flow at 100 °C for 1 h, followed by He purging for 1 h. Finally, the temperature was raised to 850 °C in a He flow at rate of 10 °C/min.

2.3. Catalytic activity evaluation

Soot particles were obtained in one batch by burning commercial diesel fuel (British Petroleum, Spain) in a glass vessel. The soot collected from the vessel walls was dried at 120 °C for 24 h.

Two types of soot combustion tests were performed. Activity tests in NO_x/O_2 atmosphere consisted of heating soot-catalyst mixtures from 25 to 750 °C at 5 °C/min in a plug flow reactor. Catalyst (100 mg, 0.125-0.250 μm) and soot (10 mg) were mixed with a spatula in the so-called loose contact mode, the most representative for diesel particles flowing through a catalytic filter [23]. Afterwards, the mixture was diluted in 1000 mg of SiC (particle size 500 μm) and placed in the reactor (ϕ = 4 mm; bed length = 70 mm). The experiments were performed at atmospheric pressure under a 300 mL/min gas flow (GHSV 150,000 h^{-1}) containing 2500 ppm NO_x + 10 % O_2 balanced with N_2. Gas composition was analysed with a Thermo Nicolet FT-IR spectrometer. Blank experiments under NO_x/O_2 were also conducted: without catalyst, in order to analyse the non-catalytic soot combustion; and without soot, in order to analyse the NO to NO_2 oxidation capacity of the catalysts.

To study the influence of the oxidant and the contact mode, soot combustion with only O_2 was evaluated under loose and tight contact conditions in a simultaneous thermal analyser (STA 6000) connected to a Frontier Fourier-transform infrared (FTIR) spectrometer equipped with a gas cell, both from PerkinElmer. For the tight contact mode, catalyst and soot were mixed in a mortar. This method maximizes the number of contact points and, although less representative of the real contact conditions in a catalytic trap, it is able to discriminate the morphologies better [24]. Around 25 mg of powder were placed in an alumina crucible and subjected to a temperature ramp of 10 °C min^{-1} up to 950 °C in air atmosphere. IR spectra were collected from 650 to 4000 cm^{-1} at a resolution of 2 cm^{-1} with 2 accumulations.

The catalytic activity of the samples was quantified in terms of T_{10}, T_{50} and T_{90} values, defined as the temperatures for 10 %, 50 % and 90 % soot conversion, respectively. Soot conversion was calculated as the fraction of the total carbon released as CO or CO_2 by integration of the concentration profiles. Selectivity to CO_2 (S_{CO2}) was calculated as CO_2 outlet concentration (C_{CO2}) divided by the sum of the CO_2 and CO outlet concentration:

$$S_{CO_2}(\%) = 100\,x\,\frac{C_{CO_2}}{C_{CO_2} + C_{CO}} \quad (1)$$

NO_2 concentration in the outlet is expressed as NO_2 fraction of the total amount of NO_x using the following equation:

$$NO_2(\%) = 100\,x\frac{NO_{2\,out}}{NO_{out} + NO_{2\,out}} \quad (2)$$

where NO_{out} and $NO_{2\,out}$ are NO and NO_2 concentrations, respectively, measured at the reactor outlet.

NO_x removal profiles were determined with the equation:

$$NO_x\ removal\ (\%) = 100\,x\frac{NO_{x\,in} - NO_{x\,out}}{NO_{x\,in}} \quad (3)$$

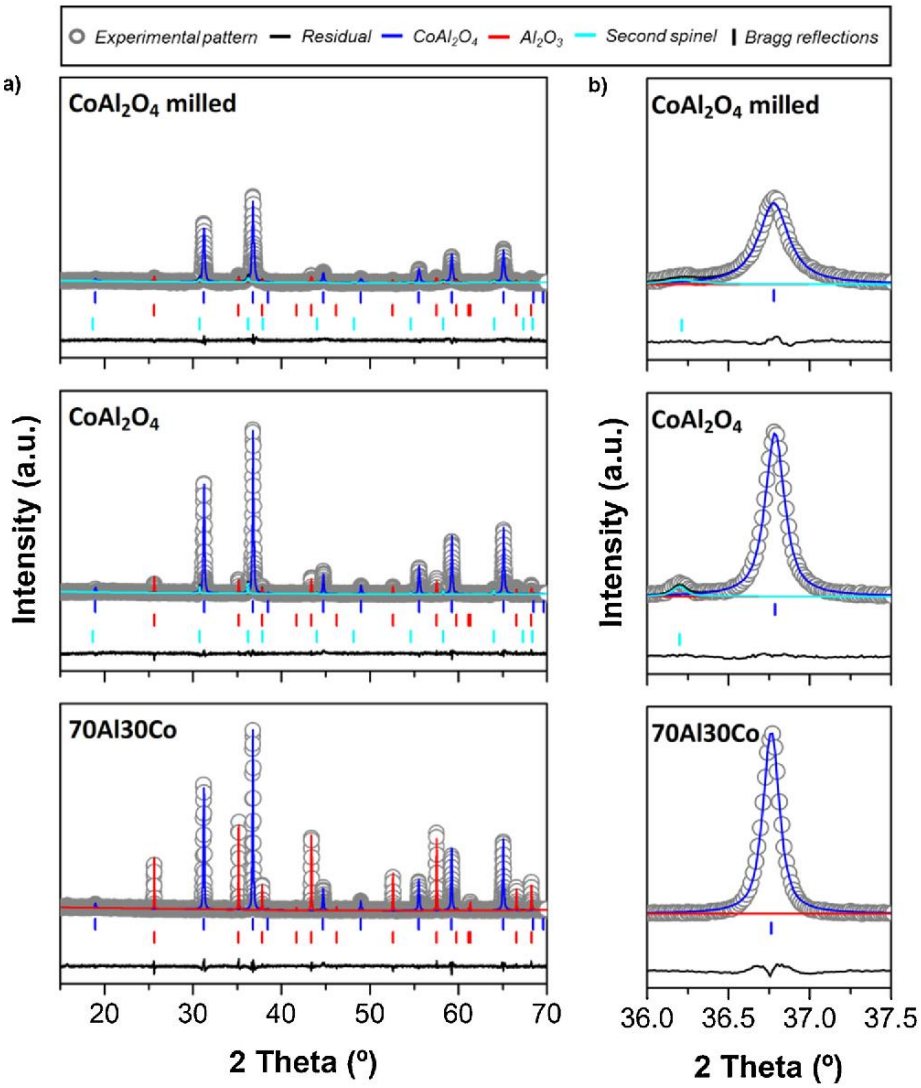

Fig. 1. a) X-ray diffraction patterns of the catalysts along with the corresponding Rietveld models. The open grey circles are experimental data; the blue line corresponds to the CoAl2O4 contribution, the red line to the Al2O3 contribution, and the cyan line to the second spinel contribution. The Bragg positions of the different phases are represented by the vertical ticks underneath the patterns in the corresponding colors. b) Magnification of the main $CoAl_2O_4$ diffraction peak (For interpretation of the references to colour in this figure legend, the reader is referred to the web version of this article).

where $NO_{x\ in}$ and $NO_{x\ out}$ are the concentration of NO_x (NO + NO_2) in the reactor inlet and outlet, respectively, that were continuously monitored by specific analyzers during the experiments.

3. Results and discussion

3.1. Textural and structural characterization

The XRD patterns of the samples, displayed in Fig. 1, exhibit the diffraction peaks of $CoAl_2O_4$ spinel structure and α-Al_2O_3. $CoAl_2O_4$ has a spinel structure (space group Fd3 m). The lattice oxygen is cubic close packed in a unit cell with one-eighth of the tetrahedral sites occupied by Co^{2+} and half of the octahedral sites occupied by Al^{3+} (Fig. S1a). Under equilibrium conditions, $CoAl_2O_4$ naturally exists in the octahedral form, enclosed by the energetically favourable (111) facets rather than the more reactive (110) facets [20] (Fig. S1b-c). The ionic layers stacking in the (111) direction for the $CoAl_2O_4$ lattice may be cleaved into six different surface terminations (see Fig. S1d). Table 1 compiles the results of the Rietveld analysis of the XRD data. It must be highlighted that the $CoAl_2O_4$ commercial sample, and thus the $CoAl_2O_4$ milled sample, contains an additional spinel phase with a larger unit cell parameter (8.22 Å instead of 8.10 Å). The magnification of Fig. 1b shows the peak broadening and intensity reduction caused by the ball milling. Consequently, the crystallite size extracted from the Rietveld refinements decreases from 56.81 nm for the as-received $CoAl_2O_4$ commercial sample to 30.82 nm for the milled one. The quality of the XRD data did not allow for discrimination of the size- and strain contributions to the peak broadening. Therefore, no strain effects are considered in the Rietveld models, although a large amount of defects is presumably generated in the sample during ball milling. Fig. 1 shows good agreement between the XRD data and the Rietveld models.

The field-emission scanning electron micrographs of the catalysts are shown in Fig. 2. The 70Al30Co sample has the characteristic plate-type morphology of α-Al_2O_3 support particles, related to crystal growth in the ab plane, with average particle size $d_{50} \approx 7.8\,\mu m$ (Fig. 2a). $CoAl_2O_4$ crystallizations are envisaged on the α-Al_2O_3 microparticles surface (Fig. 2b). These nanocrystals have an irregular shape, with an average equivalent diameter of 427 ± 118 nm, and present a hole in

Table 1
Refined lattice parameters and volume-weighted average crystallite sizes obtained from Rietveld analysis of the XRD data.

	$CoAl_2O_4$ spinel phase			Secondary spinel phase		
	Cell parameter (Å)	Crystallite size (nm)	Weight fraction (%)	Cell parameter (Å)	Crystallite size (nm)	Weight fraction (%)
70Al30Co	8.10140(4)	76.94(3)	100.0(8)	—	—	–
$CoAl_2O_4$	8.09662(5)	56.81(2)	96.1(6)	8.2233(1)	114.79(1)	3.9(1)
milled $CoAl_2O_4$	8.09830(1)	30.82(1)	93.8(7)	8.2202(5)	25.53(9)	6.2(3)

the middle; they expose the lowest-energy (111) facets represented in Fig. S1c [20,25]. The morphology of the $CoAl_2O_4$ powder before and after ball milling is shown in Fig. 2c–f. The as received material is formed by particles ranging from 0.3–8 µm (Fig. 2c), with an average particle size $d_{50} \approx 2$ µm. A more exhaustive inspection of the morphology reveals pseudo spherical particles with a scarce presence of surface roughness (Fig. 2d). The micrograph of Fig. 2e and the laser diffraction results demonstrate that the ball milling significantly modified the morphology of $CoAl_2O_4$. The primary particle size is reduced to an average particle size $d_{50} \approx 100$ nm, ca. 5 times lower, but the particles agglomerate more easily, leading to a broader bimodal particle size distribution. In addition, the surface of the particles is altered by the impact energy produced during the milling-process; the formation of defects and, therefore, of highly reactive surfaces is signalled with yellow arrows in Fig. 2f.

TEM characterization further clarifies the effect of the milling procedure on the morphological structure of $CoAl_2O_4$. Fig. 3a low-magnification image shows the high agglomeration and heterogeneity of the milled $CoAl_2O_4$ particles. These consist mainly of nanosized grains of 40 nm, which is consistent with the estimates of Table 1, made using the Scherrer formula, but the size distribution ranges from 20 to 200 nm, and this agrees well with the primary particle measurements in FE-SEM images. The magnified micrograph of Fig. 3b reveals well-crystallized nanoregions, with several distinguishable lattice fringes, which are easier to visualize in the filtered HRTEM images of the insets. The figure shows mainly a $CoAl_2O_4$ particle oriented down the [112] zone axis, exposing the (111) facets, which interplanar distances appear at 4.64 Å (Zone III). Nevertheless, three more interplanar distances can be observed in other misoriented areas, where the calculated d-spacing of 2.02 Å (Zone I), 2.86 Å (Zone II), and 2.44 Å (Zone IV) are attributable to the (400), (220), and (311) planes of $CoAl_2O_4$, respectively. These results justify the hypothesis that during the milling procedure

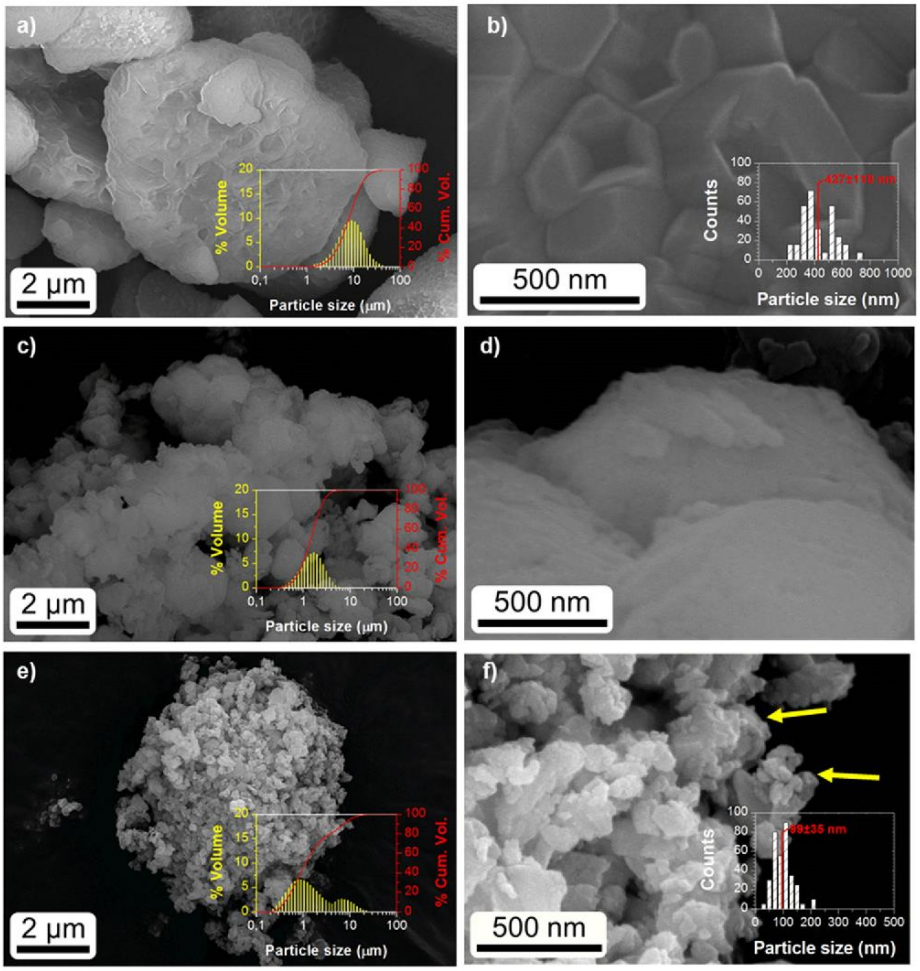

Fig. 2. - FE-SEM micrographs of a–b) 70Al30Co, c–d) as received $CoAl_2O_4$ and e–f) milled $CoAl_2O_4$. Ball milling generates changes in the size, agglomeration state, and surface morphology of the $CoAl_2O_4$ particles: c) FE-SEM micrographs of as received $CoAl_2O_4$, with sizes of 1 − 3 µm, d) detail of the as received $CoAl_2O_4$ particles showing a near flat low-roughness surface, e) FE-SEM micrographs of milled $CoAl_2O_4$, f) Detail of the defects generated by the down-milling technique. The insets of the images on the left (a, c, e) show the particle-size distribution of the samples, measured by laser diffraction, whereas in the images on the right (b, f) the insets reveal the primary particle size measured from the images.

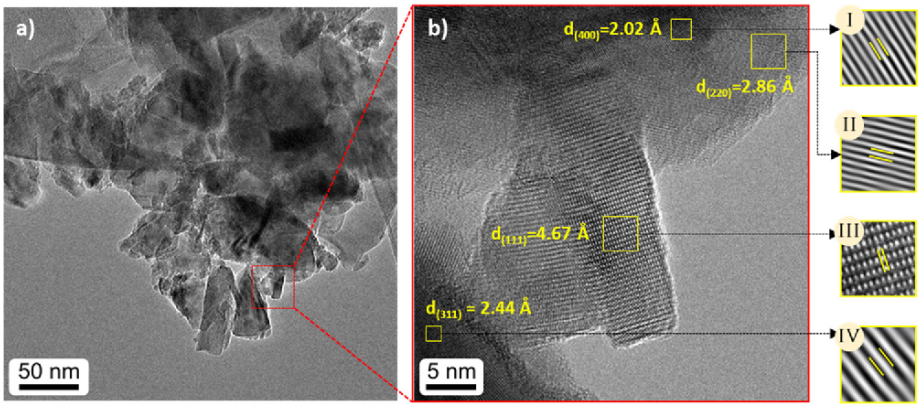

Fig. 3. - TEM images of the milled $CoAl_2O_4$ catalyst. a) Low-magnification image, where the agglomeration of the $CoAl_2O_4$ nanoparticles is evidenced. b) HRTEM image of a detail of the agglomerated particles, the insets show the filtered images of the lattice fringes of the area of interest.

the particles are randomly broken without a preferential direction.

The nature of the introduced crystalline disorder was studied in more detail by XPS analyses of the surface before and after the mechanical activation. The spectra of Co 2p core levels indicate that both samples have a normal spinel structure with Co^{2+} cations in tetrahedral position, evidencing only minor differences (For more details see Supplementary Information Fig. S2). The XPS spectra of O 1s are exhibited in Fig. 4a. The peaks at ~530 and ~532 eV were ascribed to $CoAl_2O_4$ lattice oxygen and chemisorbed oxygen species, respectively [26]. Interestingly, the former shifted to higher binding energy after milling, which reflects a decrease in the electronic density of lattice oxygen that can be related to the generation of anionic defects [27]. Raman characterization is an effective technique to gain insight into the exact structure of cerium-based materials and the formation of oxygen vacancy defects [28,29]. However, in the case of these $CoAl_2O_4$ samples no relevant differences related to such structural defects are obtained (as shown in Supplementary Info, Fig. S3).

The formation of oxygen defects evidenced by XPS can be caused by dehydroxylation processes and should be closely related to the generation of acidity and improved redox properties [30]. NH_3-TPD was performed to investigate the surface acid sites amount and strength of the spinel; the profiles are displayed in Fig. 4b. NH_3 desorption peaks centred at temperatures lower than 400 °C are assigned to weak acid sites, while those centred at temperatures higher than 600 °C originate from strong acid sites [31–34]. Coordinated NH_3 molecules bound to Lewis acid sites are thermally more stable than NH_4^+ ions bound to Brønsted acid sites, and thus need higher temperatures to desorb. Therefore, the low-temperature desorption peak observed for $CoAl_2O_4$ sample (282 °C) is assigned to NH^{4+} ions bound to Brønsted acid sites, while the high-temperature desorption peak of 70Al30Co sample (808 °C) is associated with molecular NH_3 adsorbed on Lewis acid sites [31,32,35]. Interestingly, the ball milling method has a major effect on the acidic properties. The amount of both the Brønsted and the Lewis acid sites in the milled $CoAl_2O_4$ sample, and thus the total acidity, are significantly higher than in the 70Al30Co sample or in the as received cobalt spinel samples. Therefore, the significant modification of the $CoAl_2O_4$ spinel after the milling, as revealed by XRD, SEM, TEM and XPS, is associated with the increase of acid sites. This is a consequence of the higher specific surface area of the milled $CoAl_2O_4$ associated to the particle size reduction obtained by the milling procedure (Table 2). However, the strength of the Lewis acid sites is slightly reduced, according to the downshift of ca. 50 °C of the related ammonia desorption peak. Besides, this peak is broadened, and an additional peak appears at 401 °C, indicating the formation of new types of acid sites are related to surface amorphization and generation of surface kinks. In particular, oxygen defects lead to local unbalanced electron cloud distributions with positive charge. These oxygen defects are electron acceptors or Lewis acid sites [30].

In addition, as the milling process favours the random break of the material, less stable crystal facets are exposed, for example (220), (400) and (311). Moreover, both Al^{3+} and Co^{2+} are exposed, which correspond to the generation of stronger and weaker Lewis acid sites,

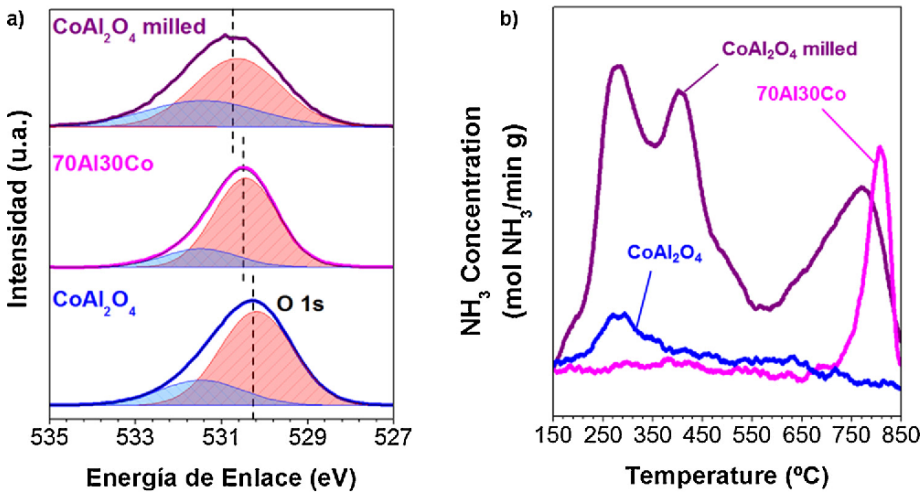

Fig. 4. - a) O 1s XPS spectra of the catalyst samples. b) NH_3-TPD results of the catalyst samples.

Table 2
Physicochemical properties of the different catalysts under study, and soot combustion temperature and selectivity obtained at 50 % conversion. The values obtained without catalyst and with Pt(1 %)/Al_2O_3 [39] in the same experimental set-up and conditions are included as reference.

Catalyst	S_{BET} (m^2/g)	Total acidity (mmol NH_3/g)	T_{50} (ºC)	S_{CO2} (%)
No catalyst			527	67
Pt(1 %)/Al_2O_3 [39]	137.0	0.15	446	> 98
70Al30Co	0.3	1.6	511	97
$CoAl_2O_4$	10.2	2.1	478	97
$CoAl_2O_4$ milled	22.9	11.2	411	100

respectively [36], and, therefore, to a broadening of the Lewis signal. On the contrary, the 70Al30Co sample exhibits the crystalline planes (111) of cobalt aluminate, and on the surface of these planes only Al^{3+} cations are exposed [37]. Accordingly, the surface Co:Al ratio determined by XPS analysis is 1:7, which correlates with a $CoAl_2O_4$ structure that ends with aluminum ions in octahedral positions [25]. Despite the very low specific surface area of the support, the nanodispersion of this spinel results in acid sites available for ammonia adsorption. The fact that the 70Al30Co sample showed only Lewis acid sites indicates that any existing hydroxyls would be eliminated in the subsequent calcination step, forming water and leaving an oxygen vacancy.

In the case of the commercial $CoAl_2O_4$, the size of the microparticles may explain that just some weak acid sites are available. It is worth to mention that the standard procedure used in ceramic pigments manufacture to reduce agglomeration is a low-intensity dry milling, which provokes only a slight attrition of the microparticles. Conversely, during the wet ball milling used in this study, the microballs produce collisions or compressive forces in combination with shear stress forces, providing greater G-forces that result in superior grinding efficiency, with the effects commented above. Therefore, the milled $CoAl_2O_4$ pigment contains Brønsted and Lewis acid sites. On the one hand, the use of ethanol would favour the formation of a high amount of surface hydroxyl groups, with the consequent increase of Brønsted acid sites [38]. On the other hand, the probability of anionic vacancies formation by dehydroxylation is also higher, as the number of adjacent hydroxyls is bigger, and also a proton from ethanol may be available for water formation. Consequently, the wet ball milling reported here is a facile route to create defects and acid sites in $CoAl_2O_4$, and therefore an effective mechanical activation method for this catalyst that may also be adequate for many other systems.

3.2. Catalytic soot combustion activity

Fig. 5 shows the catalytic activity of the three cobalt spinel samples towards soot combustion in loose contact mode with NO_x/O_2 compared to the reactivity in the absence of catalyst. The temperature of 50 % conversion and the selectivity to CO_2 are listed in Table 2, together with the specific surface area of the catalysts.

Soot conversion and CO_2 generation profiles plotted in Fig. 5a and 5b, respectively, evidence that while the nanostructured sample does not significantly reduce the soot combustion temperature, while the microparticles of the commercial $CoAl_2O_4$ pigment are active catalysts in the oxidation of soot. The mechanical activation of this sample boosts the catalytic activity, which is consistent with the promotion of the soot to catalyst contact associated to the smallest particle size (31 vs 56 nm), and thus higher specific surface area (23 vs. 10 m^2/g), of the milled spinel, and with the formation of new active sites. The creation of acid sites may facilitate the interaction with the soot particles, their activation and subsequent oxidation. In this sense, we can state that the catalytic activity increase must be mainly related to the formation of weak acid sites, because the nanostructured 70Al30Co has very low

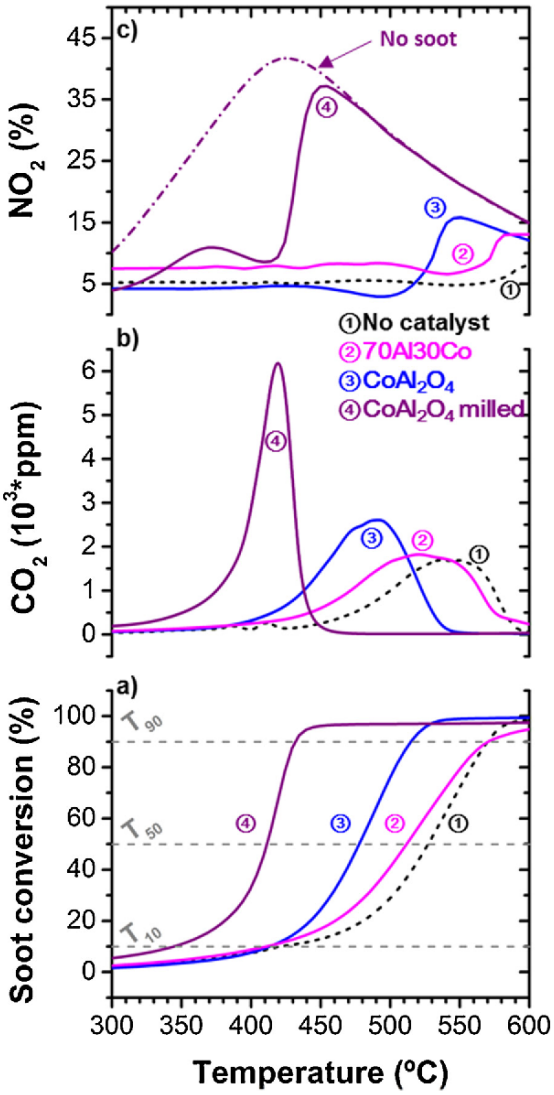

Fig. 5. - Catalytic oxidation tests: a) Soot conversion profiles, b) CO_2 concentration profiles, and c) NO_2 profiles as NO_2 to NO_x fraction. Reaction conditions: 100 mg catalyst + 10 mg soot, loose contact, 2500 ppm NO + 10 vol.% O_2 + N_2, 300 ml/min, 5 °C/min. Solid lines are experiments with soot and catalyst, the dotted line is the uncatalysed soot combustion reference experiment, and the dotted-dashed line in c) is a blank NO oxidation experiment with catalyst but without soot.

activity despite of the significant amount of strong acid sites. Moreover, the specific surface area of the milled sample is doubled with respect to the as-received one, but it is still quite low, almost one order of magnitude lower than that of the reference Pt(1 %)/Al_2O_3 catalyst [39] or other low-activity $CoAl_2O_4$ spinel [8]. Thus, the specific surface area is not expected to be the most relevant parameter of catalytic activation.

The fact that the nanostructured sample (70Al30Co) reduces only a few degrees the soot combustion temperature of the un-catalyzed reaction evidences the low reactivity of the (111) facets exposed by the oxide nanoparticles. The thermal treatment at high temperature promotes the formation of these low-energy facets. The present results support the poor catalytic performance reported by Zawadzki et al. for high-surface-area $CoAl_2O_4$ nanoparticles [8]. The synthesis includes a thermal treatment at 550 °C that promotes crystal defects reconstruction and formation of the most stable surface facets and, therefore, the activity is low in spite of the high specific surface area obtained.

Some studies aimed at elucidating the geometry and relative stability of Co_3O_4 surfaces under oxygen atmosphere [37,40] can help understanding the structure of the (111) surface of $CoAl_2O_4$, with the same spinel cubic (Fd3 m) crystallographic structure. CO can adsorb at the Al^{3+} sites of this surface exothermically, with an energy gain of 0.92 eV, but the high energy barrier to overcome (> 2.10 eV) [41] suggests that the (111) surface does not exhibit catalytic oxidation activity at low temperature, and that the Al^{3+} site is not a key active site.

The efficiency of the mechanically activated $CoAl_2O_4$ its comparable to that of Pt(1 %)/Al_2O_3 catalysts tested in the same experimental conditions [39]. Moreover, like Pt, the milled $CoAl_2O_4$ suppresses the CO formation that is observed in the non-catalytic soot combustion. The wet ball milling is critical for the catalytic activity of the $CoAl_2O_4$ microparticles. On the one hand, the smaller particle size, and thus higher surface area, of the milled $CoAl_2O_4$ sample facilitates the catalyst-soot contact, and also the access of the gaseous species, thus providing more active sites for both soot and NO oxidation [42]. On the other hand, the milling procedure activates a large variety of sites, as evidenced by the wide temperature range of NH_3 desorption, that corresponds to diverse surface energies. Few studies have investigated the importance of the acid properties of the catalyst for soot oxidation [28]. It is reported that the catalytic activity of $CoAl_2O_4$ in deoxygenation is practically zero [43], according to the common exposed facets, (110) and (111) [44]. The low activity of such crystallographic planes is attributed to the fact that tetrahedral coordinated Co^{2+} is not directly exposed to the gas-phase molecules. The (110) plane has two different terminations, usually denoted as A and B: the (110)-A termination exposes both tetrahedral and octahedral ions, whereas the (110)-B termination exposes only octahedral ions [45]. Polarity compensation mechanisms prevent the “polar catastrophe” and stabilize the surface, so it is more covalent than the bulk due to a charge compensation effect [46]. Conversely, when the exposed facet is (100), the tetrahedrally coordinated ions are the terminating species. It has been argued that this fact arise when a minimum number of bonds are broken [46]. The new acid sites generated by mechanical activation are therefore attributed to the crystallographic facet defects that break this compensation effect and allow tetrahedral Co^{2+} sites become active acid sites. These may at least partially contribute to the shift of the peak of CO_2 production towards lower temperatures.

NO_2 plays an important role for soot combustion in these conditions, as it is a much more effective oxidant than NO and O_2. However, the main NO_x species in diesel exhaust gas is NO, and NO_2 is present only in minor quantity. Therefore, its generation *on site* is a rate limiting step. NO_x concentration was monitored during the soot combustion experiments, and also during similar experiments performed in the absence of soot, in order to obtain experimental proofs of the role of NO_2 and the mechanism of soot combustion over these catalysts. The evolution of NO_2 and CO_2, shown in Fig. 5b and c, respectively, are closely related. When the formation of CO_2 reaches the maximum, the concentration of NO_2 is at its minimum, even close to zero for the more active samples. It is clear that the NO_2 produced by NO oxidation acts as the main oxidizer for soot in these systems, because the activity is enhanced in catalysts with higher NO oxidation capacity. Thus, in line with the NO_2-assisted mechanism reported in the literature, NO must react with the catalyst to generate NO_2, and then this can oxidize soot to accomplish the catalysis cycle [47].

The interaction between NO_x and the mechanically activated $CoAl_2O_4$ sample has been studied in a temperature-programmed oxidation blank experiment without soot. The NO_2 to NO_x percent fraction profile obtained in the absence of soot with the most active material, included in Fig. 5c, shows the full capacity for NO oxidation of the catalyst, which overlaps with that obtained in the presence of soot once the latter is consumed. The whole picture of the gas species concentration for the mechanically activated $CoAl_2O_4$ catalyst is shown in Fig. S4. Besides to the NO_2 to NO reduction by soot, the low NO_2 to NO proportion in the presence of soot could also be attributed to the active

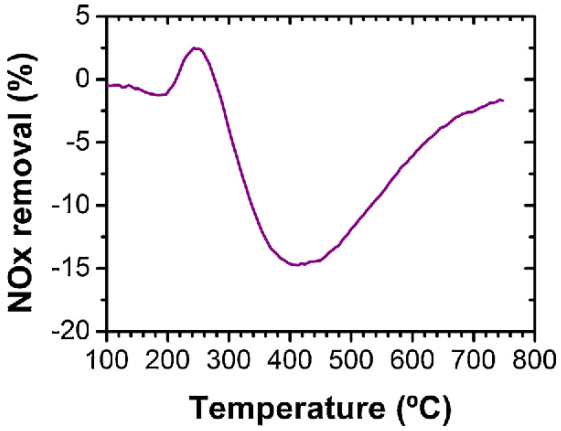

Fig. 6. - NO_x removal profile under NO_x/O_2 for the milled $CoAl_2O_4$ catalyst without soot.

sites blocking by the soot particles and/or the competition of NO and soot for the available oxygen species. The minimization of these effects could further improve the soot oxidation capacity of the catalyst. Moreover, as no N_2O formation is observed, the evolution of total NO_x concentration, with a net consumption coincident with CO_2 generation, suggests that during soot combustion part of the nitrogen oxides is reduced to N_2, and this is of paramount importance, because it indicates that both kind of pollutants, NO_x and soot, could be simultaneously removed.

The total NOx conversion results obtained in the experiment without soot, drawn in Fig. 6 are useful to understand the catalytic activity data. NO_x removal begins at 200 °C and reaches a maximum at 250 °C. Above 300 °C and up to 750 °C, NO_x concentration is higher in the outlet than in the inlet, yielding negative NO_x removal values. This suggests that between 200 and 300 °C the nitrogen oxides are reversibly chemisorbed on the surface of the new facets of the mechanically activated $CoAl_2O_4$ sample, and above this temperature the chemisorbed NO_x species are released.

The analysis of the experiments performed in loose and tight contact conditions in the absence of NO, shown in Fig. 7, offers relevant information. The activity of both as received and activated $CoAl_2O_4$ using only O_2 as oxidant decreases dramatically, to T_{50} values similar to that of the non-catalysed reaction (570 °C). Nevertheless, for the milled $CoAl_2O_4$ sample a slight catalytic activity is still appreciated under tight

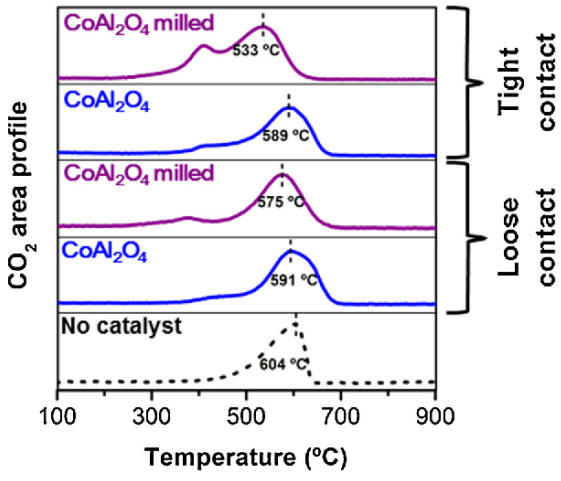

Fig. 7. - Soot combustion with O_2 (in the absence of NO) without catalyst and over the as received and milled $CoAl_2O_4$ catalysts under tight and loose contact conditions. The temperature of maximum CO_2 production is indicated.

contact mode, with T_{50} = 516 °C, a value 43 °C lower than in loose contact mode. This indicates that the surface activation increases the soot-catalyst contact points/surfaces, which are key for the active-oxygen mechanism of soot combustion [48], and are maximized in this contact mode. It can then be concluded that the activity of as received $CoAl_2O_4$ sample only exists in the presence of NO_x (active-oxygen mechanism is negligible), but gas-phase O_2 may be activated on oxygen vacancies and/or defects generated by wet milling and converted into surface active oxygen species (O^{2-}, O^-) so that soot combustion can take place continuously without NO. However, the high catalytic activity of the milled sample in the presence of NO must be mainly attributed to the reaction between NO_2 and soot. This oxygen activation capacity will also contribute to promote NO oxidation, since adsorbed NO_x species can be oxidized by both the generated surface active oxygen species (O^{2-}, O^-) and gaseous O_2. Besides, the higher acidity of the milled $CoAl_2O_4$ catalyst may promote the preferential adsorption of acid NO_x species on the soot surface, which increases the chances of NO_2-soot reaction to form highly active oxygenated complexes. Several authors reported that the acid sites of the catalyst play a key role in the oxidation of soot [49,50], because they can convert soot particles into very active carbon cation radicals that can be oxidized by molecular oxygen at lower temperatures [28].

On the basis of previous literature and the results obtained in this study, a potential mechanism scheme for soot combustion over the milled $CoAl_2O_4$ catalyst in NO-containing atmosphere is proposed in Fig. 8. There are two catalytic reaction pathways for soot combustion [48,51,52], namely, the direct oxidation by oxygen species via oxygen vacancies enabled by the milling procedure (Fig. 8a) and the NO_2-assisted oxidation (Fig. 8b). This work demonstrates that the simultaneous and synergetic contribution of the two oxidation mechanisms improves the catalytic activity of the overall combustion reaction. The catalyst acts as a redox centre, transferring gas-phase O_2 to soot though an oxygen-exchange process. The soot in contact with the catalyst or the adsorbed NO_x species take the active oxygen from the surface for their oxidation and create new vacancies, which are quickly filled by gas-phase or subsurface oxygen. For the NO_2-assisted oxidation of soot, enhanced by the mechanical activation, NO is firstly captured by the catalyst and subsequently oxidized by gaseous O_2 or surface active oxygen species; then NO is regenerated by reaction with nearby soot to produce CO_2. Besides, in some of the active centres, the reduction can proceed to form N_2, and thus neat NO_x removal takes place.

These findings open a new gate toward the use of efficient Pt-free $CoAl_2O_4$ catalysts for soot combustion in which the activation of acid sites can be induced by ball milling in ethanol. The use of common materials and a facile activation process represents a new direction to cost efficient solutions to replace catalyst based on critical raw materials such as noble metals. Moreover, these new mechanically activated catalyst for soot combustion allows directing soot combustion mechanisms that will contribute to reduce the carbon poisoning of Pt-based catalyst.

The used samples were recycled for a second batch test under identical reaction conditions by recharging the soot load. In the second batch reaction, some deactivation has been observed that could be explained by two main effects: a) partial material loss after unloading and reloading the reactor; and b) surface reconstruction at the high temperature reached in the soot catalytic combustion experiments, 750 °C. The surface area and acid sites generated by the milling procedure are reduced as the defects and the less stable crystal facets decrease, and therefore the reactivity enhancement effect disappears. Deactivation tests are in progress in order to ascertain the catalyst stability, as this is a key issue for their industrial applicability. It is expected that the highly reactive crystal facets and surface defects are preserved at lower operating temperatures, keeping the catalytic activity of such mechanically activated Pt-free materials.

4. Conclusions

The high calcination temperature employed in the synthesis of the nanostructured $CoAl_2O_4$ spinel on microstructured α-Al_2O_3 (70Al30Co), 1200 °C, resulted in the formation of low-defective (111) facets, and thus very stable surfaces that had negligible catalytic activity for soot oxidation. On the contrary, the wet milling of a cobalt aluminate commercial pigment successfully reduced the particle size and generated surface defects such as kinks, less stable crystal facets and amorphization. As a consequence, the specific surface area increased, and many new active sites were generated, mainly weak acid sites. The fostered activity of the mechanically activated $CoAl_2O_4$ spinel for soot combustion is related to several combined effects: the soot-to-catalyst contact improvement and the activation of both O_2 and NO on the catalyst surfacepromote both the direct and indirect soot oxidation mechanism. Moreover, the higher acidity of the catalyst favours the interaction of the acid and highly oxidant NO_2 species with soot, and thus the indirect oxidation mechanism, which has been proved to be the most important mechanism for the catalysed reaction with the activated spinel. The excellent results obtained by mechanical activation of the $CoAl_2O_4$ pigment suggest that this cost-effective material is very promising for the purification of diesel exhausts and could be tested for additional applications. Moreover, the simple wet milling method could improve the activity of different catalytic systems.

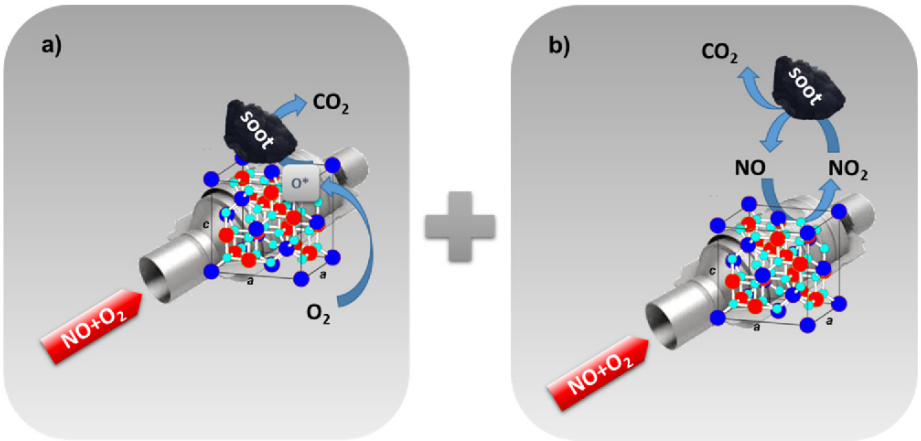

Fig. 8. - a) Active oxygen direct mechanism, b) NO_2-assisted mechanism. Both the active oxygen and the NO_2-assisted mechanisms are not independent and operate in close cooperation.

CRediT authorship contribution statement

C.M. Álvarez-Docio: Methodology, Formal analysis, Validation, Investigation, Writing - original draft, Visualization. **R. Portela:** Conceptualization, Methodology, Validation, Resources, Writing - review & editing, Supervision, Project administration. **J.J. Reinosa:** Conceptualization, Writing - review & editing, Formal analysis. **F. Rubio-Marcos:** Software, Formal analysis, Data curation. **C. Granados-Miralles:** Software, Formal analysis, Data curation. **L. Pascual:** Software, Formal analysis, Data curation. **J.F. Fernández:** Conceptualization, Resources, Writing - review & editing, Supervision, Project administration, Funding acquisition.

Acknowledgment

The authors express their thanks to the project NANOMINDCSIC201560E068 and MAT2017-86450-C4-1-R for their financial support. C.M. Alvarez-Docio for a FPI grant BES-2014-069779, which are co-financed with FEDER funds. F.Rubio-Marcos is indebted to MINECO for a 'Ramon y Cajal' contract (ref: RyC-2015-18626), which is co-financed by the European Social Fund. F. Rubio-Marcos also acknowledges support from a 2018 Leonardo Grant for Researchers and Cultural Creators (BBVA Foundation).

Appendix A. Supplementary data

Supplementary material related to this article can be found, in the online version, at doi:https://doi.org/10.1016/j.apcata.2019.117404.

References

[1] B. Frank, M.E. Schuster, R. Schlögl, D.S. Su, Angew. Chemie - Int. Ed. 52 (2013) 2673–2677.
[2] B. Frank, R. Schlögl, D.S. Su, Environ. Sci. Technol. 47 (2013) 3026–3027.
[3] F.E. Tuler, R. Portela, P. Ávila, E.D. Banús, E.E. Miró, V.G. Milt, Appl. Catal. A Gen. 498 (2015) 41–53.
[4] B.A.A.L. van Setten, M. Makkee, J.A. Moulijn, Catal. Rev. - Sci. Eng. 43 (2001) 489–564.
[5] P.G. Harrison, I.K. Ball, W. Daniell, P. Lukinskas, M. Céspedes, E.E. Miró, M.A. Ulla, Chem. Eng. J. 95 (2003) 47–55.
[6] J. Liu, Z. Zhao, J. Wang, C. Xu, A. Duan, G. Jiang, Q. Yang, Appl. Catal. B Environ. 84 (2008) 185–195.
[7] M.M. Natile, A. Glisenti, Chem. Mater. 17 (2005) 3403–3414.
[8] M. Zawadzki, W. Walerczyk, F.E. López-Suárez, M.J. Illán-Gómez, A. Bueno-López, Catal. Commun. 12 (2011) 1238–1241.
[9] D. Fino, N. Russo, G. Saracco, V. Specchia, J. Catal. 242 (2006) 38–47.
[10] S. Zhang, X. Zhu, C. Zheng, D. Hu, J. Zhang, X. Gao, Aerosol Air Qual. Res. 17 (2017) 2317–2327.
[11] Y. Zhou, Y. Li, W. Shen, Chem. - An Asian J. 11 (2016) 1470–1488.
[12] G. Liu, H.G. Yang, J. Pan, Y.Q. Yang, G.Q.M. Lu, H.M. Cheng, Chem. Rev. 114 (2014) 9559–9612.
[13] J. Wang, F. Cao, Z. Bian, M.K.H. Leung, H. Li, Nanoscale 6 (2014) 897–902.
[14] V.A. Zazhigalov, J. Haber, J. Stoch, L.V. Bogutskaya, I.V. Bacherikova, Appl. Catal. A Gen. 135 (1996) 155–161.
[15] A. Bergmann, E. Martinez-Moreno, D. Teschner, P. Chernev, M. Gliech, J.F. de Araújo, T. Reier, H. Dau, P. Strasser, Nat. Commun. 6 (2015) 8625.
[16] J. Hou, Y. Li, L. Liu, L. Ren, X. Zhao, J. Mater. Chem. A Mater. Energy Sustain. 1 (2013) 6736–6741.
[17] R.A. Buyanov, V.V. Molchanov, V.V. Boldyrev, Catal. Today 144 (2009) 212–218.
[18] L. Martín-García, A. Quesada, C. Munuera, J.F. Fernández, M. García-Hernández, M. Foerster, L. Aballe, J. de la Figuera, Adv. Mater. 27 (2015) 5955–5960.
[19] S.C. Liao, P.Y. Tsai, C.W. Liang, H.J. Liu, J.C. Yang, S.J. Lin, C.H. Lai, Y.H. Chu, ACS Nano 5 (2011) 4118–4122.
[20] C.M. Álvarez-Docio, J.J. Reinosa, A. del Campo, J.F. Fernández, Dyes Pigm. 137 (2017) 1–11.
[21] J. Rodríguez-Carvajal, Phys. B Phys. Condens. Matter 192 (1993) 55–69.
[22] J.I. Langford, J.C. Wilson, J. Appl. Crystallogr. 11 (1978) 102–113.
[23] B.A.A.L. van Setten, J.M. Schouten, M. Makkee, J.A. Moulijn, Appl. Catal. B Environ. 28 (2000) 253–257.
[24] D. Fino, S. Bensaid, M. Piumetti, N. Russo, Appl. Catal. A Gen. 509 (2015) 75–96.
[25] C.M. Álvarez-Docio, J.J. Reinosa, A. Del Campo, J.F. Fernández, J. Alloys. Compd. 779 (2018) 244–254.
[26] M. Piumetti, S. Bensaid, N. Russo, D. Fino, Appl. Catal. B Environ. 165 (2015) 742–751.
[27] Y. Pu, Y. Luo, X. Wei, J. Sun, L. Li, W. Zou, L. Dong, Appl. Catal. B Environ. 254 (2019) 580–586.
[28] P. Sudarsanam, B. Hillary, M.H. Amin, N. Rockstroh, U. Bentrup, A. Brückner, S.K. Bhargava, Langmuir 34 (2018) 2663–2673.
[29] D. Chen, D. He, J. Lu, L. Zhong, F. Liu, J. Liu, J. Yu, G. Wan, S. He, Y. Luo, Appl. Catal. B Environ. 218 (2017) 249–259.
[30] J. González, J.A. Wang, L.F. Chen, M.E. Manríquez, J.M. Dominguez, J. Phys. Chem. C 121 (2017) 23988–23999.
[31] D. Zhang, L. Zhang, L. Shi, C. Fang, H. Li, R. Gao, L. Huang, J. Zhang, Nanoscale 5 (2013) 1127–1136.
[32] R. Nadarajan, W.A.W.A. Bakar, R. Ali, R. Ismail, Appl. Catal. B Environ. 218 (2017) 327–337.
[33] Z. Wu, R. Jin, Y. Liu, H. Wang, Catal. Commun. 9 (2008) 2217–2220.
[34] Y. Shen, S. Zhu, Catal. Sci. Technol. 2 (2012) 1806–1810.
[35] R. Jin, Y. Liu, Z. Wu, H. Wang, T. Gu, Chemosphere 78 (2010) 1160–1166.
[36] N. Dewangan, J. Ashok, M. Sethia, S. Das, S. Pati, H. Kus, S. Kawi, ChemCatChem 11 (2019) 4923–4934.
[37] F. Zasada, J. Gryboś, W. Piskorz, Z. Sojka, J. Phys. Chem. C 122 (2018) 2866–2879.
[38] G. Busca, Microporous Mesoporous Mater. 254 (2017) 3–16.
[39] Y. Gao, W. Yang, X. Wu, S. Liu, D. Weng, R. Ran, Catal. Sci. Technol. 7 (2017) 3268–3274.
[40] X.L. Xu, Z.H. Chen, Y. Li, W.K. Chen, J.Q. Li, Surf. Sci. 603 (2009) 653–658.
[41] H.F. Wang, R. Kavanagh, Y.L. Guo, Y. Guo, G. Lu, P. Hu, J. Catal. 296 (2012) 110–119.
[42] J. Wang, G. Yang, L. Cheng, E.W. Shin, Y. Men, Catal. Sci. Technol. 5 (2015) 4594–4601.
[43] J.-P. Jacobs, A. Maltha, J.G.H. Reintjes, J. Drimal, H.H. Brongersma, J. Catal. 147 (1994) 294–300.
[44] S.C. Petitto, E.M. Marsh, G.A. Carson, M.A. Langell, J. Mol. Catal. A Chem. 281 (2008) 49–58.
[45] J. Chen, A. Selloni, Phys. Rev. B - Condens. Matter Mater. Phys. 85 (2012) 1–9.
[46] M. Ritter, W. Weiss, Surf. Sci. 432 (1999) 81–94.
[47] X. Yu, Z. Zhao, Y. Wei, J. Liu, J. Li, A. Duan, G. Jiang, Cuihua Xuebao/Chinese J. Catal. 36 (2015) 1957–1967.
[48] V. Rico-Pérez, E. Aneggi, A. Bueno-López, A. Trovarelli, Appl. Catal. B Environ. 197 (2016) 95–104.
[49] S. Liu, X. Wu, D. Weng, M. Li, R. Ran, ACS Catal. 5 (2015) 909–919.
[50] S. Liu, X. Wu, H. Luo, D. Weng, R. Ran, J. Phys. Chem. C 119 (2015) 17218–17227.
[51] H. Zhao, X.X. Zhou, L.Y. Pan, M. Wang, H.R. Chen, J.L. Shi, RSC Adv. 7 (2017) 20451–20459.
[52] X. Guo, M. Meng, F. Dai, Q. Li, Z. Zhang, Z. Jiang, S. Zhang, Y. Huang, Appl. Catal. B Environ. 142–143 (2013) 278–289.

Supplementary material

Pt-free $CoAl_2O_4$ catalyst for soot combustion with NO_x/O_2

C.M. Álvarez-Docio[a,*], R. Portela[b,*], J. J. Reinosa[a], F. Rubio-Marcos[a,c], C. Granados-Miralles[a], L. Pascual[b], J. F. Fernández[a].

[a]*Instituto de Cerámica y Vidrio, CSIC, C/Kelsen 5, 28049, Madrid, Spain.*

[b]*Instituto de Catálisis y Petroleoquímica, CSIC, Marie Curie 2, 28049, Madrid, Spain.*

[c]*Escuela Politécnica Superior. Universidad Antonio de Nebrija. C/Pirineos, 55, 28040, Madrid, Spain*

*E-mail address: carmenma.docio@icv.csic.es (Carmen Álvarez)

*E-mail address: raquel.portela@csic.es (Raquel Portela)

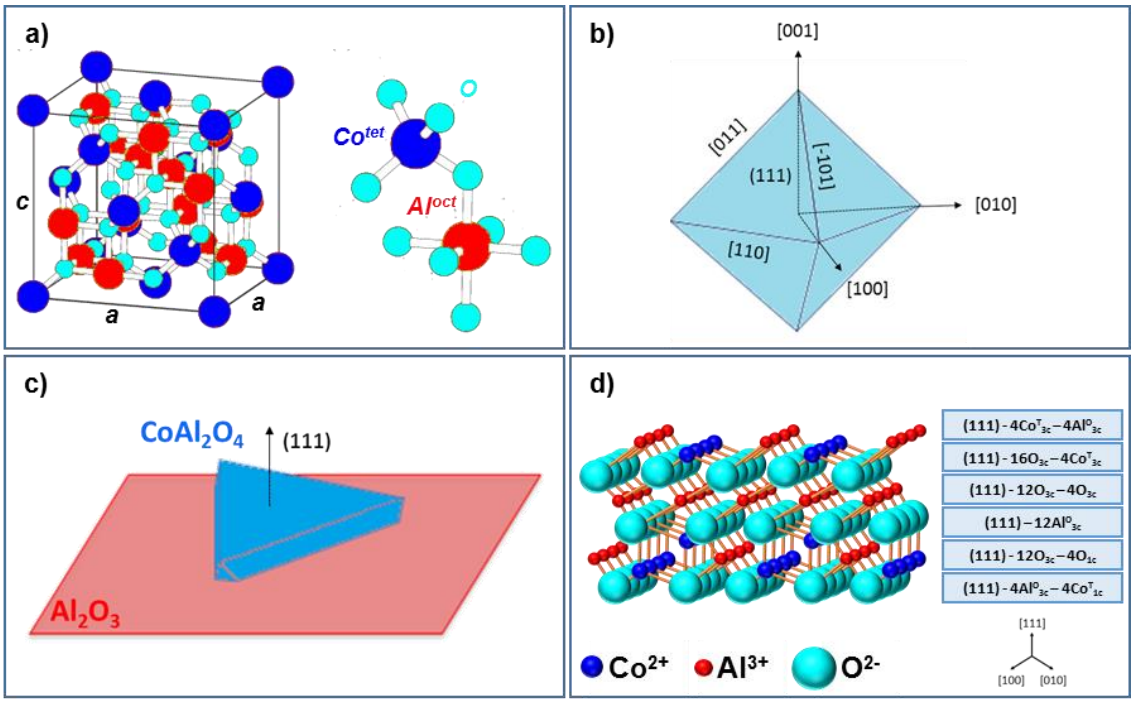

***Figure S1**.- a) Face-centered cubic spinel structure of $CoAl_2O_4$ and magnification of one tetrahedron and one adjacent octahedron sharing an oxygen atom. Large spheres labelled by Co^{tet} and Al^{oct} represent atoms on tetrahedrally and octahedrally coordinated sublattices, respectively. The lattice parameters a in the (001) plane and c in the direction perpendicular to it are identical under equilibrium conditions but differ for tetragonal systems. b) Schematic of the lowest energy surfaces of the $CoAl_2O_4$ crystal. c) Schematic of morphology of the triangular shaped $CoAl_2O_4$ nanoparticles on a-Al_2O_3 surface of 70Al30Co and. d) Surface atomic configurations of the (111) facet for $CoAl_2O_4$ spinel.*

As shown in ***Figure S1a***, $CoAl_2O_4$ is a normal spinel, which exhibits a cubic structure, with Fd3m space group (Z_8). In this structure, the oxygen anions form a cubic close-packed (ccp) sub-lattice surrounded by Co^{2+} and Al^{3+} cations occupying tetrahedral and octahedral sites, respectively. The cations occupy only 1/8 of the tetrahedral sites (8a Wyckoff position) and 1/2 of the octahedral sites (16d Wyckoff position) [1].

The anisotropy of the surface energy provokes that $CoAl_2O_4$ adopts a face-centred cubic crystal structure, and the general sequence for the surface energies of the spinel structure is $\gamma\{111\} < \gamma\{100\} < \gamma\{110\}$ [2]. Consequently, the spinel crystal prefers to form an octahedron with eight (111) surfaces, as shown in ***Figure S1b-c***, because of the lower energy at these planes [3].

The ionic layers stacking in the (111) direction for the $CoAl_2O_4$ lattice may be cleaved into six different surface terminations (***Figure S1d***) [4]. The first termination presented in ***Figure S1d*** exhibits four tricoordinated octahedral ions (denoted Al^{O}_{3c}, where the 3c subscript indicates a trifold coordination) and four tricoordinated tetrahedral Co^{T}_{3c} ions. Thus, this surface may be denoted as (111)-$4Co^{T}_{3c}$-$4Al^{O}_{3c}$. The removal of the most elevated octahedral cations leads to the second termination, with four Co^{T}_{3c} cationic surface ions only, and all of the exposed oxygen anions of the trifold coordination ((111)-$16O_{3c}$-$4Co^{T}_{3c}$). Next, when the remaining tetrahedral cations are removed, the resulting termination contains unsaturated oxygen anions exclusively ((111)-$12O_{2c}$-$4O_{3c}$), and is placed on the monolayer of the Al^{O}_{6c} cations. This layer becomes exposed in the next possible metallic termination, (111)-$12Al^{O}_{3c,}$ placed on the dense packed layer of O_{4c} anions. In an analogous way, the subsequent terminations were produced exposing 12 dicoordinated and 4 monocoordinated anions ((111)-$12O_{2c}$-$4O_{1c}$). The last possible termination is, in turn, of metallic character, with monocoordinated tetrahedral cobalt ions and tricoordinated octahedral aluminium ions, (111)- $4Al^{O}_{3c}$-$4Co^{T}_{1c}$. The removal of highly exposed Co^{T}_{1c} gives back the first facet.

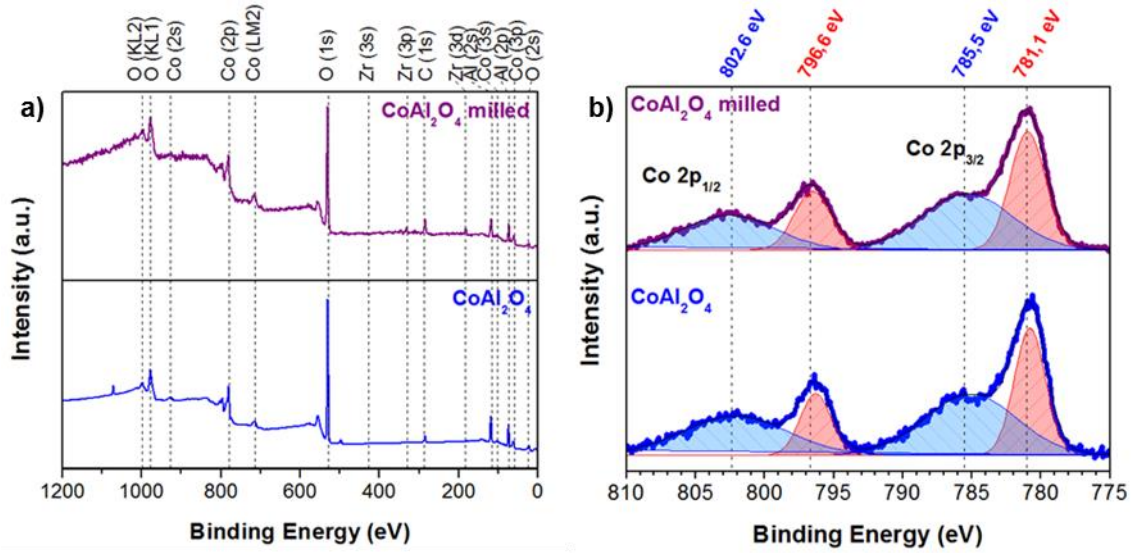

***Figure S2**.- a) Survey XPS spectrum of the samples. b) XPS spectra of Co 2p core levels of samples.*

XPS provides information on the chemical state of the elements in the near-surface region and thus was used to study the possible alteration of the cobalt species by the mechanical activation process. The $CoAl_2O_4$ sample shows the $Co2p_{3/2}$ and $Co2p_{1/2}$ peaks at approximately 781.1 eV and 796.6 eV, together with two peaks at around 785.5 eV and 802.6 eV, respectively. These peaks shape and position were similar for the mechanically activated $CoAl_2O_4$ sample. The relatively narrow peak width, the $2p_{3/2}$ to $2p_{1/2}$ separation of 15.5 eV, and the very flat weak satellite structure found on the high binding energy side of the $2p_{3/2}$ and $2p_{1/2}$ transitions indicated that few Co^{2+} cations occupied octahedral sites in the $CoAl_2O_4$ spinel lattice. Therefore, the samples had normal spinel structure and Co^{2+} was in tetrahedral site for both samples.

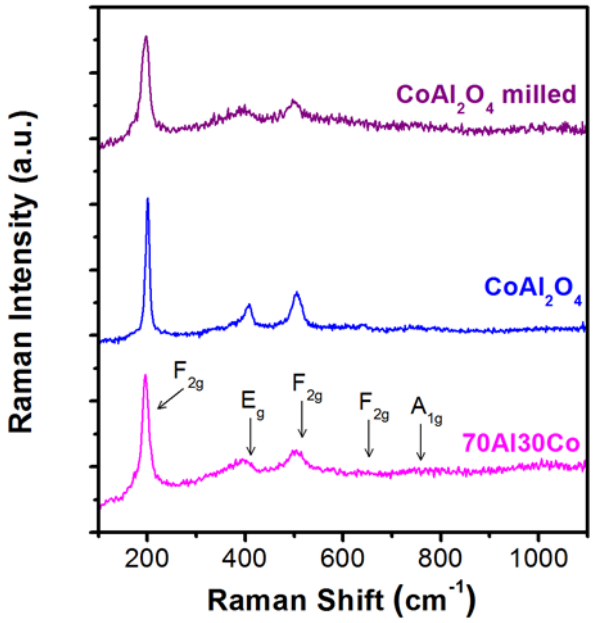

***Figure S3**.- Raman spectra of 70Al30Co, $CoAl_2O_4$ and $CoAl_2O_4$ milled catalysts.*

Raman characterization is an effective technique to study the variation of the lattice oxygen species and thus to gain insight into the exact structure and formation of oxygen vacancy defects within cerium-based materials. However, in the case of the $CoAl_2O_4$ samples, this technique has not provided the desired information. $CoAl_2O_4$ has a spinel structure that belongs to the Fd3m (O_h^7) space group, and therefore it exhibits five Raman active modes: A_{1g} (764 cm-1); F_{2g} (644, 511 and 203 cm-1) and E_g (413 cm-1). No Raman bands of oxygen vacancies are shown in our catalysts Raman spectra.

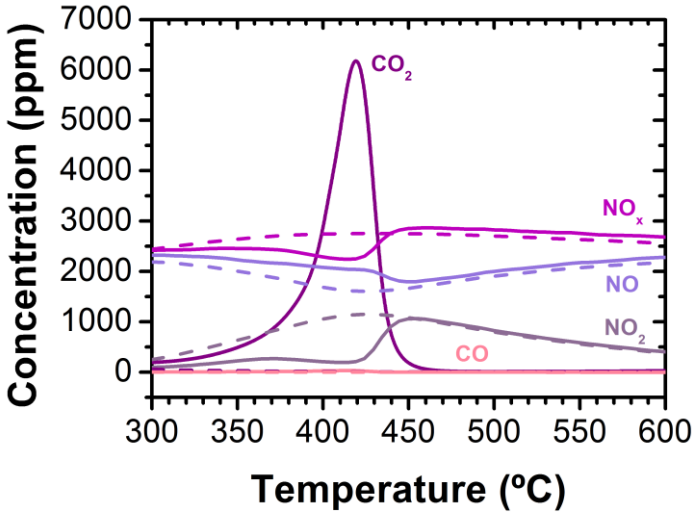

***Figure S4**.- Concentration profiles during heating under NO_x/O_2 obtained with the milled $CoAl_2O_4$ catalyst with soot (solid lines) and without soot (dashed lines). Reaction conditions: 2500 ppm NO + 10 vol.% O_2 +N_2, 300 ml/min, 5 ºC/min.*

The whole picture of the gas species concentration for the mechanically activated $CoAl_2O_4$ catalyst is shown in ***Figure S4***. The low NO_2 to NO proportion in the presence of soot, could also be attributed to, besides to the NO_2 to NO reduction by soot, the active sites blocking by the soot particles and/or the competition of NO and soot for the available oxygen species. The minimization of these effects could further improve the soot oxidation capacity of the catalyst. Moreover, as no N_2O formation is observed, the evolution of total NO_x concentration, with a net consumption coincident with CO_2 generation, suggests that during soot combustion part of the nitrogen oxides is reduced to N_2, and this is of paramount importance, because it indicates that both kind of pollutants, NO_x and soot, could be simultaneously removed.

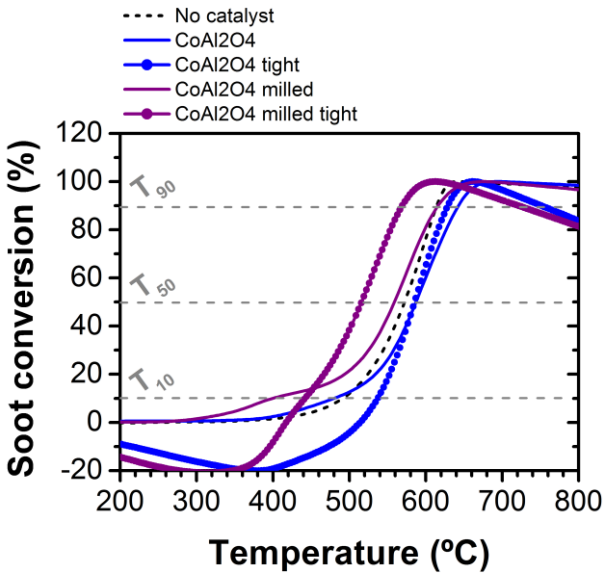

***Figure S5**.- Soot combustion profiles with O_2 (in the absence of NO) without catalyst and over the as received and milled $CoAl_2O_4$ catalysts under tight and loose contact conditions.*

Figure S5 shows the soot conversion profiles obtained from experiments performed in the absence of NO, using only O_2 as oxidant, in loose and tight contact conditions. The activity of both as received and activated $CoAl_2O_4$ decreases dramatically, to T_{50} values similar to that of the non-catalyzed reaction (570 ºC). However, for the activated $CoAl_2O_4$ sample a slight catalytic activity is appreciated. Under tight contact mode the soot-catalyst contact points/surfaces, which according to the literature are key for the active-oxygen mechanism for soot combustion [5], are maximized, and therefore some improvement is observed, with T_{50} = 516 ºC, a value 43 ºC lower than in loose contact mode. This result implies that the activity of as received $CoAl_2O_4$ sample only exists in the presence of NO_x, the active-oxygen mechanism in negligible, but gas-phase O_2 may be activated on oxygen vacancies and/or defects generated by milling and converted into surface active oxygen species (O^{2-}, O^-) so that soot combustion can take place without NO continuously.

REFERENCES

[1]K.E. Sickafus, J.M. Wills, N.W. Grimes, J. Am. Ceram. Soc. 82 (2004) 3279–3292.

[2]H. Zheng, Q. Zhan, F. Zavaliche, M. Sherburne, F. Straub, M.P. Cruz, L.Q. Chen, U. Dahmen, R. Ramesh, Nano Lett. 6 (2006) 1401–1407.

[3]S.C. Liao, P.Y. Tsai, C.W. Liang, H.J. Liu, J.C. Yang, S.J. Lin, C.H. Lai, Y.H. Chu, ACS Nano 5 (2011) 4118–4122.

[4]F. Zasada, J. Gryboś, W. Piskorz, Z. Sojka, J. Phys. Chem. C 122 (2018) 2866–2879.

[5]V. Rico-Pérez, E. Aneggi, A. Bueno-López, A. Trovarelli, Appl. Catal. B Environ. 197 (2016) 95–104.

Artículo 6

Performance and stability of wet-milled $CoAl_2O_4$, $Ni/CoAl_2O_4$ and $Pt\text{-}Ni/CoAl_2O_4$ for soot combustion

C.M. Álvarez-Docio, R. Portela, J. J. Reinosa, F. Rubio-Marcos, L. Pascual, J. F. Fernández.

Catalysis Science and Technology (Bajo revisión).

Factor de impacto: 5.726 (según JCR Edition Science 2018).

Performance and stability of wet-milled $CoAl_2O_4$, $Ni/CoAl_2O_4$ and $Pt\text{-}Ni/CoAl_2O_4$ for soot combustion

C.M. Álvarez-Docio[a,*], R. Portela[b,*], J. J. Reinosa[a], F. Rubio-Marcos[a,c], L. Pascual[b], J. F. Fernández[a].

[a]*Instituto de Cerámica y Vidrio, CSIC, C/Kelsen 5, 28049, Madrid, Spain.*

[b]*Instituto de Catálisis y Petroleoquímica, CSIC, Marie Curie 2, 28049, Madrid, Spain.*

[c]*Escuela Politécnica Superior. Universidad Antonio de Nebrija. C/Pirineos, 55, 28040, Madrid, Spain.*

Diesel soot oxidation, $CoAl_2O_4$ spinel, Platinum-based catalyst, nanodispersion

ABSTRACT

Low-energy wet milling is employed to activate a commercial $CoAl_2O_4$ spinel support and disperse mono- and multi-metallic nanoparticles on its surface. This method yields efficient Pt-Ni catalysts for soot oxidation in simulated diesel exhaust conditions provided that hot spots formation is controlled to avoid the deactivation of the cobalt aluminate. The characterization and activity results indicate that $Ni/CoAl_2O_4$ is highly active, but the presence of Pt is required to provide stability under the operating conditions to the Ni (0.75 wt. %) – Pt (0.25 wt. %)/$CoAl_2O_4$ catalyst. Our work provides important insight for new design strategies to develop high-efficiency low-cost catalysis. Platinum-containing multi-metallic nanostructures can efficiently reduce the amount of the costly but to date non-replaceable Pt noble metal for a large number of industrially important catalytic processes.

INTRODUCTION

Diesel internal-combustion engine emissions could increase between 50% and 250% by 2050[1] despite the increasingly stringent regulations for vehicles in both the EU and the US, and therefore more regulation in this sector is expected to limit their impact on health and the environment.[2] The pressure to comply with the norms has led to misbehaviors such as the "dieselgate" in the automotive industry,[3] and efforts are continuously made to further control and reduce diesel emissions of NO_x and particulate matter, the latter comprising soot and other smaller molecular compounds, mostly toxic.[4–6]

State-of-the-art diesel particulate filters have considerably reduced soot emissions by trapping the carbonaceous particles inside the filter pores and their subsequent oxidation to CO_2.[7] Un-catalyzed soot combustion occurs at around 600ºC, and therefore a catalyst is added to reduce this temperature below that of diesel exhausts.[1,8,9] Noble metals such as Pt achieve high catalytic activity by oxidizing the NO present in the exhaust gas to NO_2, which promotes soot combustion.[10,11] Remaining challenges are to avoid the filter thermal regeneration and to minimize the amount of scarce and costly Pt.[12–14] This drives the quest for improving the activity and reducing the noble metal loading.[15–17] In this regard, several synthetic strategies have been proposed, including the control over particles shape and size,[11,18] the generation of Pt-based materials with hollow interiors,[19] and bi- and trimetallic compositions.[20,21] Multimetallic catalysts have the advantage of tunable electronic and geometric properties through combination of different metal components.[22–25] Ni dispersed on various supporting materials (Al_2O_3, CeO_2, ZrO_2, SiO_2, TiO_2) has been extensively used in hydrogenation, hydro-treating, and steam-reforming reactions due to its good performance and low cost.[26] Moreover, compared to monometallic Ni and Pt, bimetallic Pt-Ni catalysts exhibit higher activity for several reactions.[27] In this sense, the partial substitution of platinum with nickel to form a bimetallic Pt-Ni catalyst may lead to optimized properties for soot combustion with NO/O_2 while reducing the metal content/price.

Active phases activity and stability depends on the material used as support,[28–30] which not only helps in dispersing the active component, but may also participate in some steps of the reaction mechanism.[31] Therefore, supports play an important role in heterogeneous catalysis, especially with metals, and must also be optimized.[32] Al_2O_3 is a widely used support due to its high surface area and thermal stability. However, Al_2O_3 is inert itself for both NO and soot oxidation.[33] Some highly active basic supports like ceria easily suffer from sulfur-poisoning due to their basicity.[34,35] Hence, the use of an appropriate acidic support may give rise to more active and durable catalysts for soot oxidation. Mixed oxides with spinel structure may be advantageous to support metal catalysts. For instance, Pt nanoparticles on the {111} facets of a $MgAl_2O_4$ spinel have shown great dispersion and stability in harsh conditions,[36] and several cobalt spinels efficiently catalyze soot combustion through NO oxidation promotion.[37–39] We have recently reported that the creation of acid sites and defects in commercially available $CoAl_2O_4$ by wet milling yields a low cost active catalyst for soot oxidation.[40] This material could be used as support where the oxygen vacancies serve as strong anchoring sites for metal NPs.[41] Moreover, the metal nanodispersion could also be performed mechanically in the mill used for the support activation, as this method has been used to prepare a Pt/Al_2O_3 catalyst with very good results.[42]

Taking this background into account, the aim of the current work is to disperse Ni and Ni-Pt nanoparticles by low-energy milling onto activated cobalt aluminate spinel to obtain promoted catalytic activity at reduced cost. The performance and stability of the $Pt\text{-}Ni/CoAl_2O_4$ and $Ni/CoAl_2O_4$ catalysts for soot oxidation in diesel exhaust streams is evaluated. As far as we know, the use of $CoAl_2O_4$-supported platinum and/or nickel catalysts has not been previously reported.

EXPERIMENTAL PROCEDURE

Catalysts preparation:

As received $CoAl_2O_4$ spinel microparticles with an average particle size of ~2.0 µm (Manuel Riesgo, S.A., Spain) were mechanically pre-activated by ball milling at 50 rpm, with 1 mm cerium-stabilized zirconia balls, during 3 hours in a polyamide type jar (Spex 8000 Mixer mill milling equipment). The $mass_{balls}/mass_{powder}$ ratio was 1:1 and 33% in ethanol medium. Pt-Ni/$CoAl_2O_4$ with 0.75 wt. % Pt and 0.25 wt. % Ni, and Ni/$CoAl_2O_4$ catalysts with 1 wt. % total metal loading were prepared by mechanical milling in ethanol to incorporate the appropriate amount of high purity (>99.9%) PtO_2 and/or NiO nanoparticles (Aldrich) onto the micrometric $CoAl_2O_4$ support. As received PtO_2 and NiO nanopowders, with an average particle size of ~20 nm, form large agglomerates with diameter >20 µm and >10 µm, respectively, so they were pre-dispersed in a 60 cm^3 nylon container during 1 h at 500 rpm. The process was assisted by the addition of zirconia balls (1 mm in diameter) and 20 cm^3 of ethanol. Then the activated $CoAl_2O_4$ microparticles were added and the mixture was homogenized for 10 min. Finally, the sample was dried and thermally treated at 550 ^oC under N_2-H_2 atmosphere to reduce the oxides to the metallic phase and remove all possible nitrate species from the platinum nitrate.[43] A reference Pt(1%)/Al_2O_3 catalyst was prepared as described elsewhere[42] by a similar low-energy wet milling procedure from PtO_2 nanoparticles and micrometric α-Al_2O_3.

Catalysts characterization:

The crystalline phases were characterized by X-ray diffraction (XRD, D8, Bruker) using a Lynx Eye detector and Cu $K\alpha_1$ radiation.

The Brunauer-Emmett-Teller (BET) equation was used to determine the surface area of the catalysts from N_2 adsorption-desorption data obtained in a Micrometrics ASAP2020 analyzer.

The morphology of the powders was evaluated by using secondary electron images of field emission scanning electron microscopy (FE-SEM, Hitachi S-4700).

The particle size and morphology at the nanoscale were also evaluated using a transmission electron microscope (TEM/HRTEM, JEOL 2100F) operating at 200

kV and equipped with a field emission electron gun providing a point resolution of 0.19 nm. HRTEM filtering and image processing were performed using Digital Micrograph software.

The surface composition was determined using an X-ray Photoelectron Spectrometer (XPS, K-Alpha, Thermo Scientific), equipped with a monochromated Al Kα (1486.6 eV) source running at a voltage of 12 KV. A pass energy of 200 eV was used for survey scans, while for high-resolution scans the pass energy was 40 eV. Finally, for charge correction a 1-point scale with the C 1s peak shifted to 285 eV was used.

Differential thermal analysis (DTA) and thermogravimetric (TG) analysis was carried out from 20 to 1000 ^{o}C with a heating rate of 5 ^{o}C/min in a Netzch STA 409 Thermo-Analyzer.

Catalytic activity evaluation:

Temperature Programmed Oxidation (TPO) of soot was studied under NO + O_2 and O_2 atmospheres. TPO tests under NO/O_2 were conducted in a fixed-bed tubular microreactor (ϕ = 4 mm; bed length = 70 mm) from 25 to 750 °C with a heating rate of 5 °C/min. 100 mg of catalyst were mixed with 10 mg of soot particles obtained by diesel fuel combustion[44] and stirred with a spatula for 5 min, in order to reproduce the loose contact conditions.[45] The mixture was diluted in 1000 mg of SiC (particle size 500 µm) and placed in the center of the tubular microreactor in contact with a k-type thermocouple used to control the catalyst bed temperature. In a typical test, a gas stream of 300 mL/min containing 2500 ppm NO_x in 10% O_2/N_2 was passed through the catalyst-soot diluted mixture at a Gas Hourly Space Velocity (GHSV) of 150,000 h^{-1}. Reference experiments with only catalyst or with only soot were also conducted. The reactor outlet was analyzed in a Thermo Nicolet Fourier transform infrared (FT-IR) spectrometer.

TPO tests with only O_2 were performed under loose and tight contact conditions in a simultaneous thermal analyzer (STA 6000) connected to a Frontier

FTIR spectrometer, both from PerkinElmer. To obtain tight contact catalyst and soot were mixed in a mortar. Around 25 mg of powder were placed in alumina crucibles and subjected to a ramp of 10 ^{o}C min^{-1} up to 950 ^{o}C in air. Gas phase IR spectra were collected from 650 to 4000 cm^{-1} at a resolution of 2 cm^{-1} with 2 accumulations.

RESULTS AND DISCUSSION

Textural and structural characterization:

Figure 1 shows the XRD patterns of the support and the catalysts. Both supported samples exhibit the characteristic peaks of the $CoAl_2O_4$ spinel (JCPDS File Nos. 00-044-0160) and the α-alumina (JCPDS File Nos. 00-046-1212) phases present in the mechanically activated cobalt aluminate. However, the presence of Pt or Ni crystalline phases cannot be determined, due to the low amount and/or high dispersion of the metals. XPS analyses of the fresh and used samples reveal some zirconia contamination attributed to the milling procedure[46] and indicate that all the samples had a normal spinel structure and Co^{2+} cations in tetrahedral sites (***Figure S1***). The intensity of the Pt 4d and Ni 2p peaks was not sufficient to assess the oxidation state before and after reaction by deconvolution of the platinum and nickel spectra into the individual components.

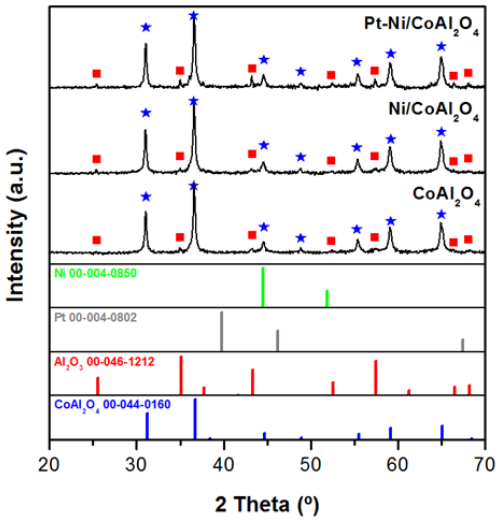

Figure 1.- *a) XRD patterns of the mechanically activated support and the supported catalysts, and JCPD standards for $CoAl_2O_4$, a-Al_2O_3, Pt, and Ni.*

The morphology of the materials is appreciated in the micrographs of ***Figure 2 and 3***. Both Ni/$CoAl_2O_4$ and Pt-Ni/$CoAl_2O_4$ catalysts present agglomerates, <10 μm in size (***a***), formed by metal nanoparticles of ca. 50 nm anchored onto submicronic $CoAl_2O_3$ particles with irregular morphology and average size ca. 500 nm (***b***). The nanoparticles seem to be strongly bonded, as reported for other materials prepared by similar dispersion methods.[47,48] EDX mappings indicate that in both nanostructured samples the metal nanoparticles are uniformly distributed throughout the catalyst agglomerates.

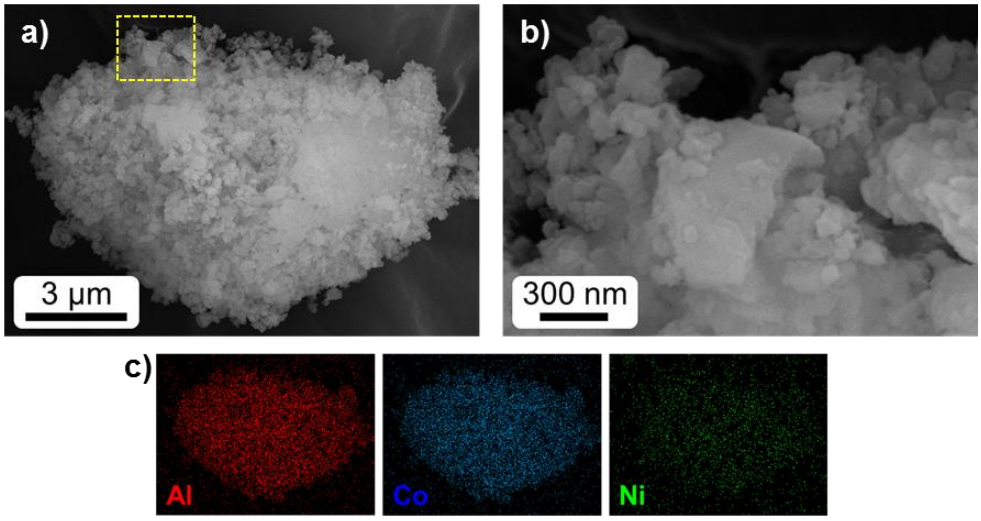

Figure 2.- *a) FE-SEM micrograph of the Ni/$CoAl_2O_4$ catalyst, b) HR-SEM magnification of the area marked in yellow in a), and c) EDX elemental mapping obtained in a).*

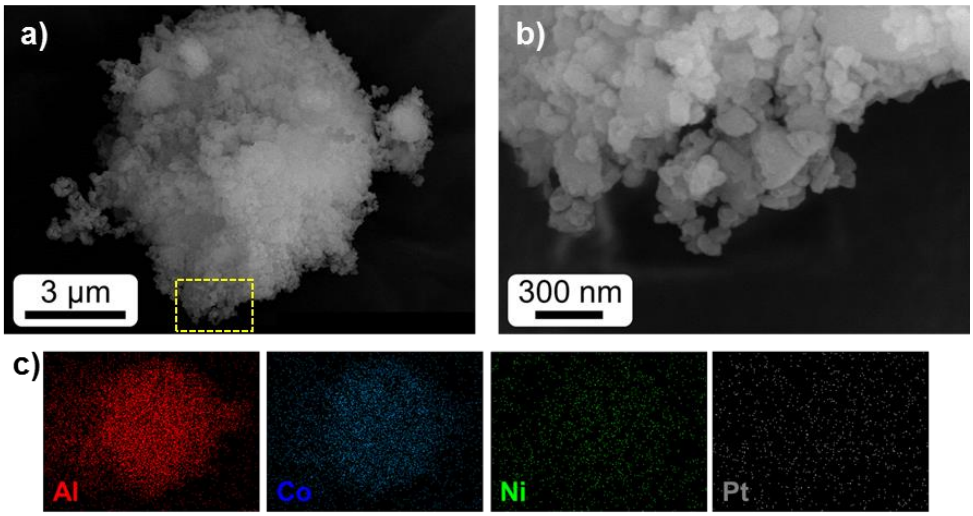

Figure 3.- *a) FE-SEM micrograph of the Pt-Ni/$CoAl_2O_4$ catalyst, b) HR-SEM magnification of the area marked in yellow in a), and c) EDX elemental mapping obtained in a).*

TEM provides more details on the microstructure of the samples. ***Figure 4*** shows representative micrographs of the Pt-Ni/$CoAl_2O_4$ catalyst confirming that dispersed spherical metal nanoparticles are anchored to $CoAl_2O_4$ particles of irregular morphology and different sizes (***Figure 4a***). The dispersed nano-sized Pt and Ni particles are uniformly distributed, either as agglomerates (>20 nm) or as small nanoparticles (~ 3 nm), ***Figure 4b***. The SAED (Selected Area Electron Diffraction) pattern and EDX analysis corresponding to the area of ***Figure 4b*** are shown in ***Figure 4c*** and ***4d***, respectively. The diffraction rings, in which the four first reflections have been marked, can be ascribed to the $CoAl_2O_4$ spinel structure (spatial group Fd3m). Although the EDX analysis detects the presence of Pt and Ni, together with Al and Co, in the SAED pattern no diffraction spots can be indexed as Pt or Ni phases, because of their small size and quantity. ***Figure S2a*** shows an STEM-HAADF (Scanning Transmission Electron Microscopy-High Angle Annular Dark Field) illustrative image of a region with brighter spots dispersed all over the $CoAl_2O_4$ that correspond to Pt and Ni, according to the EDX mapping of these elements in the region. The semi-quantitative distribution of the metals along the $CoAl_2O_4$ support determined by EDX is 65% Pt and 35% Ni. In the STEM-HAADF of another area presented in ***Figure 4e*** two nanoparticles of Ni and Pt have been analyzed in detail to understand their nanostructure. In the case of Ni (***Figure 4f***), the FFT (Fast Fourier Transform) of the HRTEM image can be indexed as a (FM3-M) metallic Ni particle oriented down the [110] zone axis. The Pt nanoparticle is similar, its FFT (***Figure 4g***) can be ascribed to the [112] zone axis of a metallic Pt structure. In the inset of both images a filtered image showing the (111) lattice spacing is included.

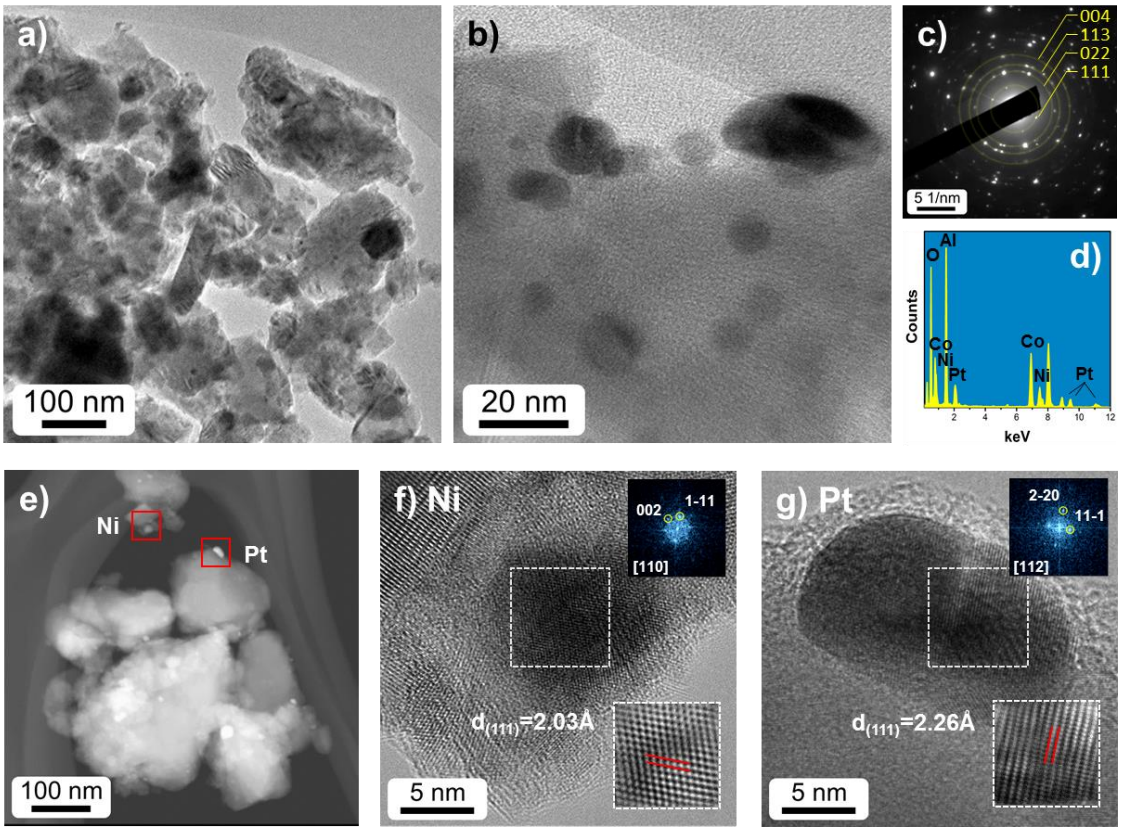

***Figure 4**.- Microstructural analysis of Pt-Ni/$CoAl_2O_4$ catalyst. a-b) TEM images. c) SAED pattern, and d) EDX spectrum, both corresponding to micrograph b. e) HAADF-STEM images. f-g) Magnified micrographs of Ni (f) and Pt (g) nanoparticles; the insets correspond to the marked area of interest: top) filtered images of the lattice fringes, and bottom) FFT used to identify the crystallographic planes and interplanar distances.*

Catalytic activity:

The catalytic soot combustion activity results of the temperature-programmed experiments with NO_x/O_2 are shown in ***Figure 5*** and ***Table 1***. Soot conversion was calculated as the fraction of total carbon in the inlet released as CO or CO_2 in the outlet, CO_2 selectivity (S_{CO_2}) is the CO_2 to $CO+CO_2$ fraction and NO_2 % is the NO_2 to NO_x fraction. T_{10}, T_{50} and T_{90} are the temperatures required for 10%, 50%, and 90% soot conversion, respectively.

Table 1 compiles, besides the values of T_{50} and $S_{CO_2}$of the $CoAl_2O_4$, Ni/$CoAl_2O_4$, Pt-Ni/$CoAl_2O_4$ and Pt/α-Al_2O_3 catalysts, their specific surface area, along with bibliographic data for other spinel-type catalysts or supported-Pt catalysts with the same platinum loading. The $CoAl_2O_4$-supported Ni and Ni-Pt

samples are more active than the bare activated cobalt aluminate spinel and the reference Pt/Al_2O_3, and in the literature, under similar operating conditions, only a bimetallic Pt-Pd(2%)/3DOM-TiO_2 catalyst, with double amount of noble metal, has a better performance. The sample without noble metal, $Ni/CoAl_2O_4$, has the best T_{50}, 156 °C below that of the uncatalysed reaction, 8 °C lower than the T_{50} of α-Al_2O_3–supported Pt, and similar to the values obtained by using other catalyst with spinel structure as $Cu_{1.5}Mn_{1.5}O_4$[49] and $CoCr_2O_4$.[50] In addition, the selectivity of $Ni/CoAl_2O_4$ towards CO_2 formation as soot combustion product is near 100%. In summary, the performance of the mechanically dispersed $Ni/CoAl_2O_4$ sample can be compared to that of the state-of-the-art spinel and supported metal-catalysts reported in the literature that have been tested under similar experimental conditions.

In order to better understand the catalytic behaviour of the samples, the NO_2 to NO_x fraction profiles were measured with and without soot, ***Figure 5c***. The promotion of NO to NO_2 oxidation to conversion values close to the limits of the thermodynamic equilibrium is a key parameter in soot combustion, because NO_2 is a much stronger oxidant than O_2. The bare $CoAl_2O_4$ catalyzes the oxidation of NO to NO_2, which is further accelerated by the presence a metal; the $Ni/CoAl_2O_4$ catalyst produces the highest amount of NO_2. Moreover, the presence of platinum and/or nickel in the spinel structure does greatly increase the concentration of reactive NO_2 species during the reaction with soot. ***Figure S3*** shows that the presence of the metal does not significantly contribute to the direct oxidation mechanism, as the conversion without NOx is similar to that obtained with the bare spinel,[40] and only under tight contact, which maximizes the soot-catalyst interface, slightly different from that of the uncatalysed reaction. The tight contact is less representative of the real conditions in catalytic traps but maximizes the number of contact points, which is key for the active-oxygen mechanism of soot combustion,[51] and thus allows discriminating some effects better.[52] Thus, the soot combustion capacity enhancement takes place via the indirect reaction route.

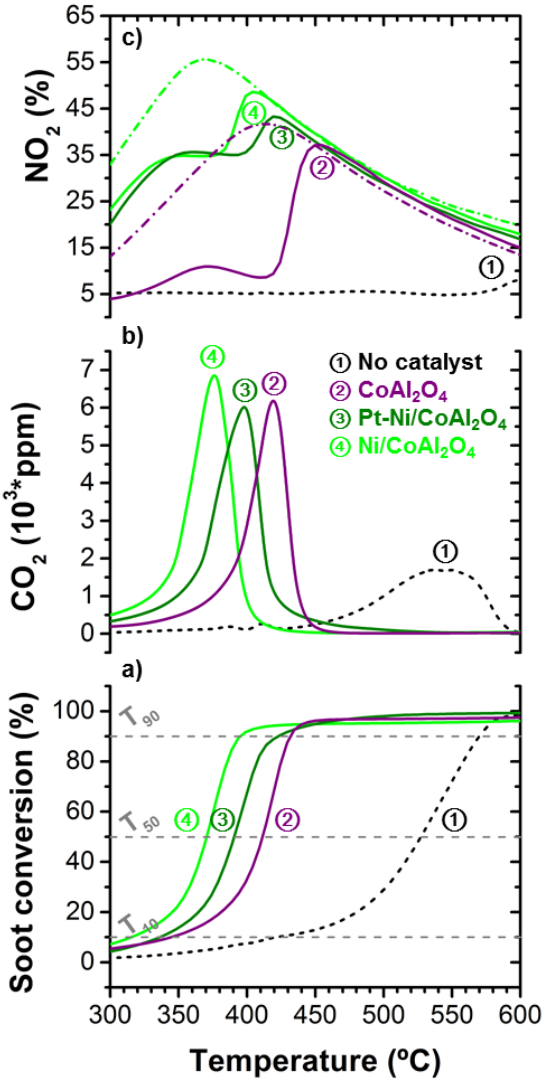

***Figure 5**.- Catalytic oxidation tests: a) Soot conversion profiles, b) CO_2 concentration profiles, and c) NO_2 profiles as NO_2 to NO_x fraction. Reaction conditions: 100 mg catalyst + 10 mg soot, loose contact, 2500 ppm NO + 10 vol.% O_2 +N_2, 300 ml/min, 5ºC/min. Solid lines are experiments with soot and catalyst, the dotted line is the reference experiment of non-catalyzed soot combustion, and the dotted-dashed lines in c) are blank NO oxidation experiments with catalyst but without soot.*

Stability of the catalysts:

To evaluate the performance reproducibility, critical for practical applications, the used samples were recycled for a second soot combustion test under identical reaction conditions by recharging the soot load. The same procedure was followed to evaluate the stability of a reference Pt/Al_2O_3 catalyst. ***Table 1*** contains the T_{50} values obtained in the first and second soot combustion test.

As expected, the reference Pt/Al_2O_3 catalyst essentially maintains its initial activity. The slight increase of T_{50} value in the second soot combustion test, of 24 ºC, could be attributed to the methodology employed to reload the reactor and the subsequent loss of some of the catalyst mass. Similarly, in consecutive runs with the $Pt\text{-}Ni/CoAl_2O_4$ catalyst, ΔT_{50} was 31 ºC. However, the activity of the samples without Pt markedly decreased in the second soot combustion test, with a shift in T_{50} of 84 ºC for the $CoAl_2O_4$ sample (from 411 to 494 ºC), and of 135 ºC for the $Ni/CoAl_2O_4$. (For more details see Supplementary Information ***Figure S5a***).

Catalyst	Metal Content (%)	S_{BET} (m^2/g)	T_{50}-fresh (ºC)	T_{50}-reused (ºC)	S_{CO2} (%)	Reference
No catalyst	---	---	527	---	67	Current study
$CoAl_2O_4$	---	22.9	411	494/441	100	Current study
$Pt\text{-}Ni/CoAl_2O_4$	0.75% Pt 0.25% Ni	19.3	390	421	100	Current study
$Ni/CoAl_2O_4$	1% Ni	22.8	371	506	100	Current study
$Pt/\alpha\text{-}Al_2O_3$	1% Pt	15.0	398	422	100	Current study
$Pt/\gamma\text{-}Al_2O_3$	1% Pt	160	474	---	100	[58]
$Cu/ZnAl_2O_4$	5% Cu	111	600	---	95	[59]
$Pt\text{-}Pd/3DOM\text{-}TiO_2$	2% Pt-Pd	60	338	---	99	[60]
$Cu_{1.5}Mn_{1.5}O_4$	---	---	397	---	---	[49]
$CoCr_2O_4$	---	59	396	---	---	[50]

Table 1*: Comparison of diesel soot combustion catalysts tested in laboratory conditions ("loose" soot-catalyst contact and NO_x + O_2 mixture).*

Figure S5 and ***Figure S6*** analyze the effect of the temperature on the samples. First, the specific surface area of all samples slightly decreases at temperatures higher that 600 ºC (see ***Figure S5b***), which indicates that some active sites are lost during the first catalytic test. This could explain that some deactivation is always observed, but it also may indicate that operation at temperatures lower than 600 ºC might minimize this effect. In addition, TG-DTA results in oxidizing atmosphere also suggest that the metal is partially oxidized, and that the presence of Pt nanoparticles partially improves the thermal stability of the

catalyst. This would explain that Pt-Ni/$CoAl_2O_4$ has the best soot combustion efficiency in the second use, similar to Pt/α-Al_2O with only 25% of the noble metal. The stability of the Pt-Ni/$CoAl_2O_4$ for soot oxidation in diesel exhaust streams could be attributed to lower Ni oxidation due to the Pt-Ni interaction and to the presence of oxygen vacancy defects (demonstrated by XPS analysis, ***Figure S4***), which could serve as strong anchoring sites for metal nanoparticles. Less stable atoms have a greater chemical potential and bind stronger to metal atoms in nanoparticles.[53] For instance, it has been determined that Ag nanoparticles are anchored stronger to a CeO_2 support than to a MgO support,[54] and this may explain the greater sintering resistance of transition metals deposited on CeO_2.[55] It has also been shown that oxygen vacancies stabilize Au atoms, both on TiO_2 and on MgO.[56,57] Thus, the mechanical nanodispersion of Ni-Pt nanoparticles onto the surface of the milled $CoAl_2O_4$ spinel represents a potential way to obtain high catalytic activity and stability, while reducing the amount of platinum. Finally, it must also be considered that high temperatures may promote the $CoAl_2O_4$ structure reconstruction and crystallites sintering and growth. To evaluate the effect of the temperature reached during the catalytic tests on the performance of the mechanically activated $CoAl_2O_4$, the experimental protocol was modified, limiting the temperature during the first run to 500 ºC, and the stability test was repeated. The conversion profiles of both runs and the field-emission scanning electron micrographs of the sample, fresh and after the first run up to 500 or 750 ºC, are shown in ***Figure 6***. In contrast to the catalytic activity decrease of $CoAl_2O_4$-750 in the second test, with a shift of the T_{50} from 411 to 494 ºC, the reused $CoAl_2O_4$-500 sample maintained a high catalytic activity, with T_{50} of 441ºC. This confirms that the deactivation effect can be explained by the high temperature reached in the soot catalytic combustion experiments. The wet ball milling pretreatment of the $CoAl_2O_4$ support modifies the morphology substantially: the particle surface is altered by the impact energy produced during the milling-process, forming defects and highly reactive sites that improve the catalytic behavior for soot oxidation.[40] However, at 750 ºC, the defects generated in the $CoAl_2O_4$ structure are partially reconstructed and grain

boundaries and sintering necks appear (compare ***Figure 6b and 6d***), with the subsequent loss of surface area and acid sites. During the catalytic test run up to 750 ºC, the $CoAl_2O_4$ nanoparticles sintered and formed a more dense and connected structure. $CoAl_2O_4$-500 micrograph in ***Figure 6c*** reveals an intermediate stage, in which a slight densification is also observed, but the rough nanostructured surface is kept. The fact that the maximum temperature of diesel engine exhaust gases falls in the range from 260 to 540 ºC makes the mechanically activated $CoAl_2O_4$ highly attractive for the replacement of traditional platinum catalysts.

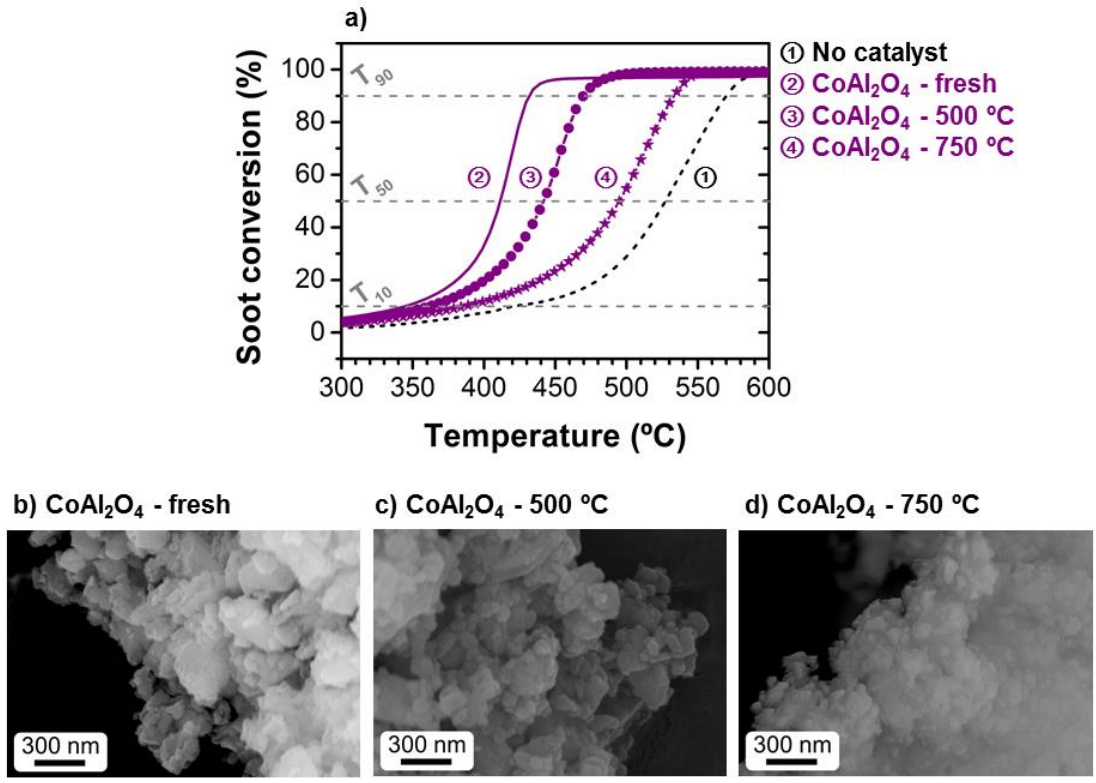

Figure 6.- *a) Soot combustion profiles of $CoAl_2O_4$ sample, fresh (solid line) and after a first use for soot combustion up to 500 ºC (circles) or 750 ºC (stars). The dotted line is the reference non-catalyzed soot combustion experiment. Bottom (b-d): FESEM micrographs of $CoAl_2O_4$ (b) fresh sample, and reused after (c) 500 ºC or (d) 750 ºC.*

CONCLUSIONS

$CoAl_2O_4$ activation and Pt and/or Ni nanodispersion onto $CoAl_2O_4$ can be successfully achieved using a novel mechanical method. These catalysts show

high efficiency for soot combustion in the presence of NO, despite the relatively big size of the metal particles obtained in the low specific surface area of the spinel, due to the easier soot-to-catalyst contact and the efficient generation of oxidant NO_2 by the system. The stability of the activated $CoAl_2O_4$ is maintained up to 500ºC, but care must be taken to avoid hot spots formation, for example in regions where large soot aggregates burn, as this would cause the thermal deactivation of the catalysts. Since the maximum exhaust gas temperature of diesel engines falls in the range from 260 to 540 ºC, the mechanically activated $CoAl_2O_4$ spinel is highly attractive as catalyst and as support for the replacement of traditional platinum catalysts. The highest reaction rates are observed for the samples prepared using Ni as the active metal ($Ni/CoAl_2O_4$), but this high performance is not maintained in successive uses. On the contrary, the substitution by Pt of 1/4 of the 1 wt. % total metal loading seems to hinder the metal oxidation, and the bimetallic Pt-Ni nanoparticles dispersed onto mechanically activated $CoAl_2O_4$ show good stability. These catalysts are therefore promising candidates for catalytic oxidation of diesel soot particles because of their easy synthesis, high activity and low cost.

ACKNOWLEDGMENT

The authors express their thanks to the project NANOMIND CSIC201560E068 and MAT2017-86450-C4-1-R for their financial support. C.M. Alvarez-Docio for a FPI grant BES-2014-069779, which are co-financed with FEDER funds. F.Rubio-Marcos is indebted to MINECO for a 'Ramon y Cajal' contract (ref: RyC-2015-18626), which is co-financed by the European Social Fund. F. Rubio-Marcos also acknowledges support from a 2018 Leonardo Grant for Researchers and Cultural Creators (BBVA Foundation). We acknowledge support of the publication fee by the CSIC Open Access Publication Support Initiative through its Unit of Information Resources for Research (URICI).

REFERENCES

1 B. A. A. L. Van Setten, M. Makkee and J. A. Moulijn, Catal. Rev. - Sci. Eng., 2001, **43**, 489–564.

2 S. S. Dang, A. Serafino, J. O. Müller, R. E. Jentoft, R. Schlögl and S. Fiorito, Environ. Sci. Technol., 2008, **42**, 1761–1765.

3 T. L. Brewer, Energy Policy, 2019, **129**, 1047–1055.

4 D. Q. Rich, H. Özkaynak, J. Crooks, L. Baxter, J. Burke, P. Ohman-Strickland, K. Thevenet-Morrison, H. M. Kipen, J. Zhang, J. B. Kostis, M. Lunden, N. Hodas and B. J. Turpin, Environ. Sci. Technol., 2013, **47**, 9414–9423.

5 B. Frank, R. Schlögl and D. S. Su, Environ. Sci. Technol., 2013, **47**, 3026–3027.

6 B. Frank, M. E. Schuster, R. Schlögl and D. S. Su, Angew. Chemie - Int. Ed., 2013, **52**, 2673–2677.

7 L. Lizarraga, S. Souentie, A. Boreave, C. George, B. Danna and P. Vernoux, Environ. Sci. Technol., 2011, **45**, 10591–10597.

8 D. Fino, P. Fino, G. Saracco and V. Specchia, Korean J. Chem. Eng., 2003, **20**, 445–450.

9 G. Saracco, C. Badini and V. Specchia, Chem. Eng. Sci., 1999, **54**, 3035–3041.

10 R. Matarrese, L. Castoldi, N. Artioli, E. Finocchio, G. Busca and L. Lietti, Appl. Catal. B Environ., 2014, **144**, 783–791.

11 S. Liu, X. Wu, D. Weng and R. Ran, Ind. Eng. Chem. Res., 2012, **51**, 2271–2279.

12 X. Yu, Z. Zhao, Y. Wei and J. Liu, Sci. Rep., 2017, **7**, 1–19.

13 Y. F. Sun, J. H. Li, Y. Q. Zhang, B. Hua and J. L. Luo, ACS Catal., 2016, **6**, 2710–2714.

14 Q. Shi, T. Liu, Q. Li, Y. Xin, X. Lu, W. Tang, Z. Zhang, P. X. Gao and J. A. Anderson, Appl. Catal. B Environ., 2019, **246**, 312–321.

15 M. Hatanaka, N. Takahashi, T. Tanabe, Y. Nagai, K. Dohmae, Y. Aoki, T. Yoshida and H. Shinjoh, Appl. Catal. B Environ., 2010, **99**, 336–342.

16 N. Guillén-Hurtado, A. García-García and A. Bueno-López, Appl. Catal. B Environ., 2015, **174–175**, 60–66.

17 S. Liu, X. Wu, D. Weng, M. Li and H. Lee, Chem. Eng. J., 2012, **203**, 25–35.

18 R. Peng, X. Sun, S. Li, L. Chen, M. Fu, J. Wu and D. Ye, Chem. Eng. J., 2016, **306**, 1234–1246.

19 B. Jin, Y. Wei, Z. Zhao, J. Liu, Y. Li, R. Li, A. Duan and G. Jiang, Chinese J. Catal., 2017, **38**, 1629–1641.

20 T. S. Rodrigues, A. G. M. Da Silva, M. C. Gonçalves, H. V. Fajardo, R. Balzer, L. F. D. Probst, A. H. M. Da Silva, J. M. Assaf and P. H. C. Camargo, Langmuir, 2016, **32**, 9371–9379.

21 X. Liu, Q. Zhang, P. Ning, T. Tang, J. Hu and W. Su, Catal. Commun., 2018, **115**, 26–30.

22 Y. Wei, Z. Zhao, B. Jin, X. Yu, J. Jiao, K. Li and J. Liu, Catal. Today, 2015, **251**, 103–113.

23 N. Nejar and M. J. Illán-Gómez, Appl. Catal. B Environ., 2007, **70**, 261–268.

24 F. Liao, T. W. B. Lo and S. C. E. Tsang, ChemCatChem, 2015, **7**, 1998–2014.

25 H. Zhang, M. Jin and Y. Xia, Chem. Soc. Rev., 2012, **41**, 8035–8049.

26 N. Keghouche, S. Chettibi, F. Latrèche, M. M. Bettahar, J. Belloni and J. L. Marignier, Radiat. Phys. Chem., 2005, **74**, 185–200.

27 W. W. Lonergan, D. G. Vlachos and J. G. Chen, J. Catal., 2010, **271**, 239–250.

28 J. Oi-Uchisawa, S. Wang, T. Nanba, A. Ohi and A. Obuchi, Appl. Catal. B Environ., 2003, **44**, 207–215.

29 J. van Doorn, J. Varloud, P. Mériaudeau, V. Perrichon, M. Chevrier and C. Gauthier, Appl. Catal. B, Environ., 1992, **1**, 117–127.

30 A. Carrascull, C. Grzona, D. Lick, M. Ponzi and E. Ponzi, React. Kinet. Catal. Lett., 2002, **75**, 63–68.

31 W. S. Epling, L. E. Campbell, A. Yezerets, N. W. Currier and J. E. Parks, Catal. Rev. - Sci. Eng., 2004, **46**, 163–245.

32 K. Villani, W. Vermandel, K. Smets, D. Liang, G. Van Tendeloo and J. A. Martens, Environ. Sci. Technol., 2006, **40**, 2727–2733.

33 F. E. López-Suárez, A. Bueno-López, M. J. Illán-Gómez, A. Adamski, B. Ura and J. Trawczynski, Environ. Sci. Technol., 2008, **42**, 7670–7675.

34 Y. Gao, X. Wu, S. Liu, D. Weng and R. Ran, RSC Adv., 2016, **6**, 57033–57040.

35 X. Wu, S. Liu, D. Weng, F. Lin and R. Ran, J. Hazard. Mater., 2011, **187**, 283–290.

36 W. Z. Li, L. Kovarik, D. Mei, J. Liu, Y. Wang and C. H. F. Peden, Nat. Commun., 2013, **4**, 1–8.

37 D. Fino, N. Russo, G. Saracco and V. Specchia, J. Catal., 2006, **242**, 38–47.

38 M. Zawadzki, W. Walerczyk, F. E. López-Suárez, M. J. Illán-Gómez and A. Bueno-López, Catal. Commun., 2011, **12**, 1238–1241.

39 E. Cauda, S. Hernandez, D. Fino, G. Saracco and V. Specchia, Environ. Sci. Technol., 2006, **40**, 5532–5537.

40 C. M. Álvarez-Docio, R. Portela, J. J. Reinosa, F. Rubio-Marcos, C. Granados-Miralles, L. Pascual and J. F. Fernández, Appl. Catal. A Gen., 2020, **591**, 117404.

41 M. Ahmadi, H. Mistry and B. Roldan Cuenya, J. Phys. Chem. Lett., 2016, **7**, 3519–3533.

42 C. M. Álvarez-Docio, R. Portela, J. J. Reinosa, F. Rubio-Marcos and J. F. Fernández, Catal. Commun., , DOI:Under Review.

43 C. Hu, D. Creaser, H. Grönbeck, H. Ojagh and M. Skoglundh, Catal. Sci. Technol., 2015, **5**, 1716–1730.

44 F. E. Tuler, R. Portela, P. Ávila, E. D. Banús, E. E. Miró and V. G. Milt, Appl. Catal. A Gen., , DOI:10.1016/j.apcata.2015.03.019.

45 B. A. A. L. Van Setten, J. M. Schouten, M. Makkee and J. A. Moulijn, Appl. Catal. B Environ., 2000, **28**, 253–257.

46 C. B. Reid, J. S. Forrester, H. J. Goodshaw, E. H. Kisi and G. J. Suaning, Ceram. Int., 2008, **34**, 1551–1556.

47 I. Lorite, M. S. Martín-González, J. J. Romero, M. A. García, J. L. G. Fierro and J. F. Fernández, Ceram. Int., 2012, **38**, 1427–1434.

48 I. Lorite, L. Pérez, J. J. Romero and J. F. Fernandez, Ceram. Int., 2013, **39**, 4377–4381.

49 X. X. Zhou, J. L. Shi, M. Wang, L. Y. Pan, H. Zhao and H. R. Chen, RSC Adv., 2017, **7**, 20451–20459.

50 D. Fino, N. Russo, G. Saracco and V. Specchia, Powder Technol., 2008, **180**, 74–78.

51 V. Rico-Pérez, E. Aneggi, A. Bueno-López and A. Trovarelli, Appl. Catal. B Environ., 2016, **197**, 95–104.

52 D. Fino, S. Bensaid, M. Piumetti and N. Russo, Appl. Catal. A Gen., 2016, **509**, 75–96.

53 C. T. Campbell, Acc. Chem. Res., 2013, **46**, 1712–1719.

54 J. A. Farmer and C. T. Campbell, Science (80-.)., 2010, **329**, 933–936.

55 S. L. Hemmingson, T. E. James, G. M. Feeley, A. M. Tilson and C. T. Campbell, J. Phys. Chem. C, 2016, **120**, 12113–12124.

56 S. Hong and T. S. Rahman, J. Am. Chem. Soc., 2013, **135**, 7629–7635.

57 D. Ricci, A. Bongiorno, G. Pacchioni and U. Landman, Phys. Rev. Lett., 2006, **97**, 1–4.

58 J. Giménez-Mañogil and A. García-García, Fuel Process. Technol., 2015, **129**, 227–235.

59 M. Zawadzki, W. Staszak, F. E. López-Suárez, M. J. Illán-Gómez and A. Bueno-López, Appl. Catal. A Gen., 2009, **371**, 92–98.

60 Y. Wei, Q. Wu, J. Xiong, J. Li, J. Liu, Z. Zhao and S. Hao, Catal. Today, 2019, **327**, 143–153.

Supplementary material

Performance and stability of wet-milled $CoAl_2O_4$, $Ni/CoAl_2O_4$ and $Pt-Ni/CoAl_2O_4$ for soot combustion

C.M. Álvarez-Docio[a,*], R. Portela[b,*], J. J. Reinosa[a], F. Rubio-Marcos[a,c], L. Pascual[b], J. F. Fernández[a].

[a]*Instituto de Cerámica y Vidrio, CSIC, C/Kelsen 5, 28049, Madrid, Spain.*

[b]*Instituto de Catálisis y Petroleoquímica, CSIC, Marie Curie 2, 28049, Madrid, Spain.*

[c]*Escuela Politécnica Superior. Universidad Antonio de Nebrija. C/Pirineos, 55, 28040, Madrid, Spain*

*E-mail address: carmenma.docio@icv.csic.es (Carmen Álvarez)

*E-mail address: raquel.portela@csic.es (Raquel Portela)

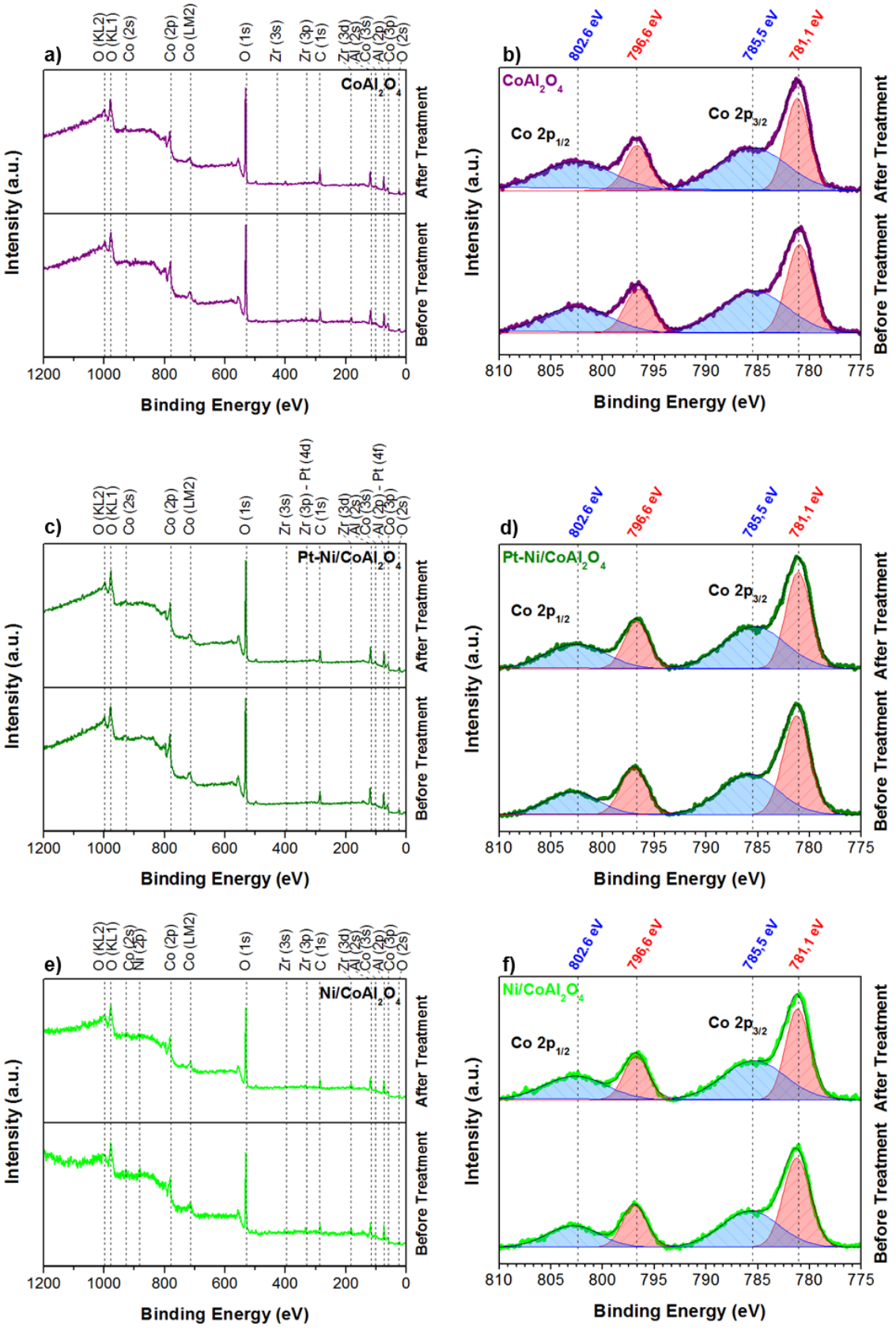

Figure S1.- *a, c, e) Survey XPS spectra. b, d, f) XPS spectra of Co 2p core levels.*

Sample	At % C	At % O	At % Al	At % Co	Co:Al
$CoAl_2O_4$ fresh	17.31	44.43	32.62	5.63	1:6
$CoAl_2O_4$ -700	20.73	44.18	31.06	4.02	1:8
Pt-Ni/$CoAl_2O_4$ fresh	16.17	43.70	35.06	5.07	1:7
Pt-Ni/$CoAl_2O_4$ used	16.43	45.82	33.28	4.46	1:7
Ni/$CoAl_2O_4$ fresh	12.18	43.46	38.15	6.20	1:6
Ni/$CoAl_2O_4$ used	12.91	44.77	37.69	4.63	1:8

***Table S1**: Elemental composition (at %) of the samples based on XPS analysis.*

XPS analyses of the fresh and used samples reveal some zirconia contamination attributed to the milling procedure[3] and indicate that all the samples had a normal spinel structure and Co^{2+} cations in tetrahedral sites (***Figure S1***). ***Table S1*** contains the quantitative elemental analysis obtained from the XPS spectra. The starting Co:Al ratio is in agreement with the $CoAl_2O_4$ structure that ends with aluminum atoms in octahedral positions.[4] The slight variation of the Co:Al ratio after use, from 1:6 - 1:8, confirms that the materials surface is essentially stable. The intensity of the Pt 4d and Ni 2p peaks was not sufficient to assess the oxidation state before and after reaction by deconvolution of the platinum and nickel spectra into the individual components.

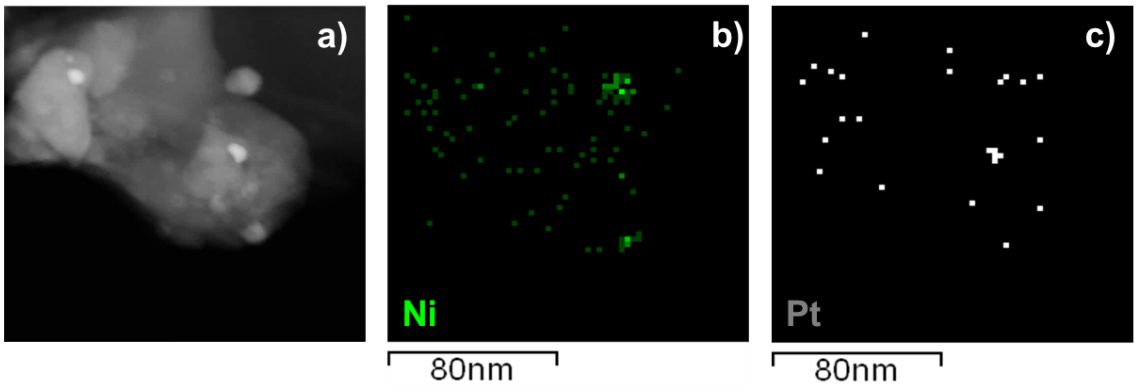

***Figure S2**.- a) HAADF-STEM image of Pt-Ni/$CoAl_2O_4$ catalyst. b-c) EDX mapping analyses for Ni (green) and Pt (gray) of the area.*

Figure S2a shows an STEM-HAADF (Scanning Transmission Electron Microscopy-High Angle Annular Dark Field) illustrative image of a region with brighter spots dispersed all over the $CoAl_2O_4$ that correspond to Pt and Ni, according to the EDX mapping of these elements in the region. The semi-quantitative distribution of the metals along the $CoAl_2O_4$ support determined by EDX is 65% Pt and 35% Ni.

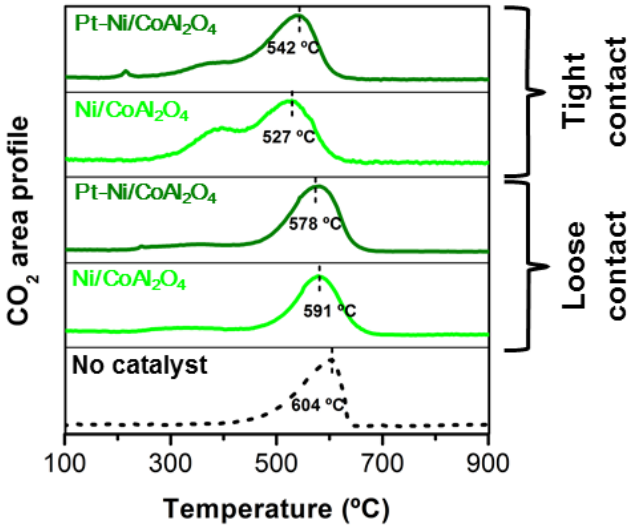

***Figure S3**.- Soot combustion with O_2 (in the absence of NO) without catalyst and over the Pt-Ni/$CoAl_2O_4$ and Ni/$CoAl_2O_4$ catalysts under tight and loose contact conditions. The temperature of maximum CO_2 production is indicated.*

The catalytic performance of the samples in the absence of NO_x, only with O_2, is shown in ***Figure S3***. Apparently, the presence of the metal does not significantly contribute to the direct oxidation mechanism, as the conversion without NOx is similar to that obtained with the bare spinel,[1] and only under tight contact, which maximizes the soot-catalyst interface, key for the active-oxygen mechanism of soot combustion,[2] slightly different from that of the uncatalysed reaction. On the contrary, the presence of platinum and/or nickel in the spinel structure does greatly increase the concentration of reactive NO_2 species during the reaction, and thus the enhancement in the soot combustion capacity takes place via this reaction route.

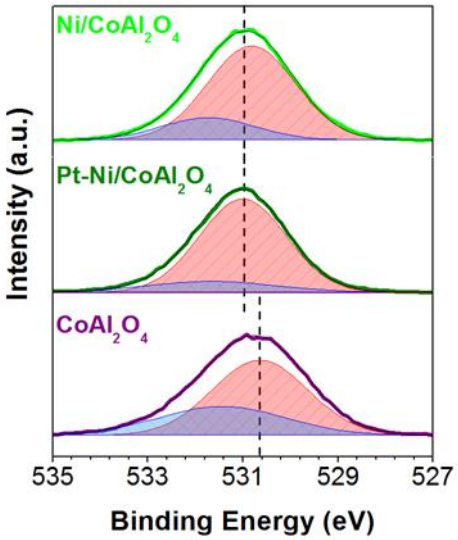

***Figure S4**.- O 1s XPS spectra of the catalysts samples.*

The nature of the introduced crystalline disorder was studied in more detail by XPS analyses of the surface. The XPS spectra of O 1s are exhibited in ***Figure S4***. The peaks at ca 531 and 532 eV were ascribed to $CoAl_2O_4$ lattice oxygen and chemisorbed oxygen species, respectively.[5] Compared to the $CoAl_2O_4$ sample, the position of lattice oxygen in Ni/$CoAl_2O_4$ and Pt-Ni/ $CoAl_2O_4$ is shifted to higher binding energy. This indicates that the introduction of metals reduced the electronic density of lattice oxygen, possibly due to the formation of oxygen defects on $CoAl_2O_4$.[6]

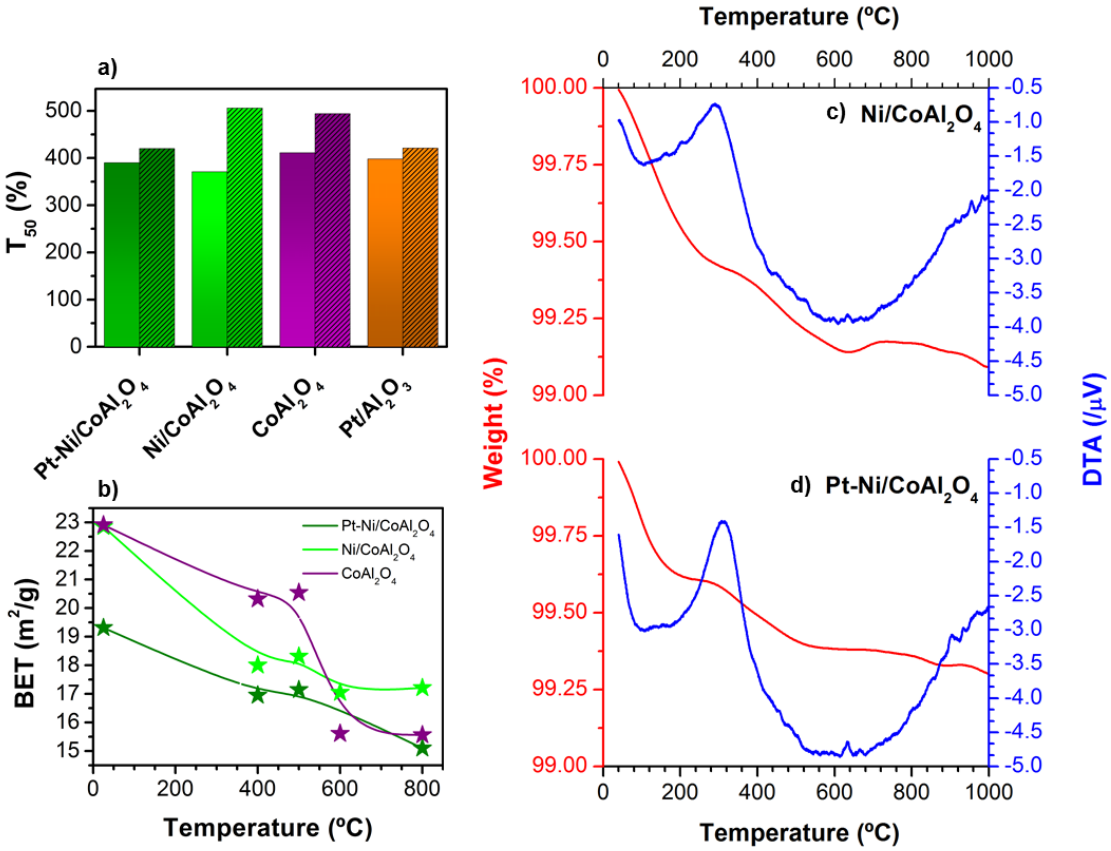

***Figure S5**.- Stability evaluation. a) Temperature needed for 50% soot combustion under loose contact between catalyst and soot with $Ni/CoAl_2O_4$ and $Pt\text{-}Ni/CoAl_2O_4$ catalysts, $CoAl_2O_4$ support, and Pt/Al_2O_3 reference. Solid: first use, dashed: second use. b) Effect of the temperature on the BET specific surface area of the prepared samples. c-d) Thermal analysis in air of the reduced catalysts (c) $Ni/CoAl_2O_4$ and (d) $Pt\text{-}Ni/CoAl_2O_4$.*

Figure S5a shows the T_{50} values obtained in the first and second soot combustion test for easier comparison, together with the BET values obtained as a function of the calcination temperature, ***Figure S5b***, and the TG-DTA results in oxidizing atmosphere, ***Figure S5c***.

The reference Pt/Al_2O_3 catalyst essentially maintains its initial activity. The slight increase of T_{50} value in the second soot combustion test, of 24 ºC, could be attributed to the methodology employed to reload the reactor and the subsequent loss of some of the catalyst mass. Similarly, in consecutive runs with the $Pt\text{-}Ni/CoAl_2O_4$ catalyst, ΔT_{50} was 31 ºC. However, the activity of the samples without Pt markedly decreased in the second soot combustion test, with a shift in T_{50} of 84 ºC for the $CoAl_2O_4$ sample (from 411 to 494 ºC), and of 135 ºC for the $Ni/CoAl_2O_4$.

In order to simulate the effect of the reaction conditions on the textural properties, the S_{BET} of the samples was measured after calcination in air at different temperatures (***Figure S5b***). The specific surface area of $CoAl_2O_4$ is significantly reduced at temperatures higher that 600 ºC, which indicates that active sites are lost; the same effect is expected during the first catalytic test. The loss of surface area can be attributed to the reconstruction of the activated $CoAl_2O_4$ structure and the sintering of the crystallites. This would limit its ability to activate oxygen and the contact with the soot after exposure at temperatures higher than 600 ºC compared with the fresh sample.

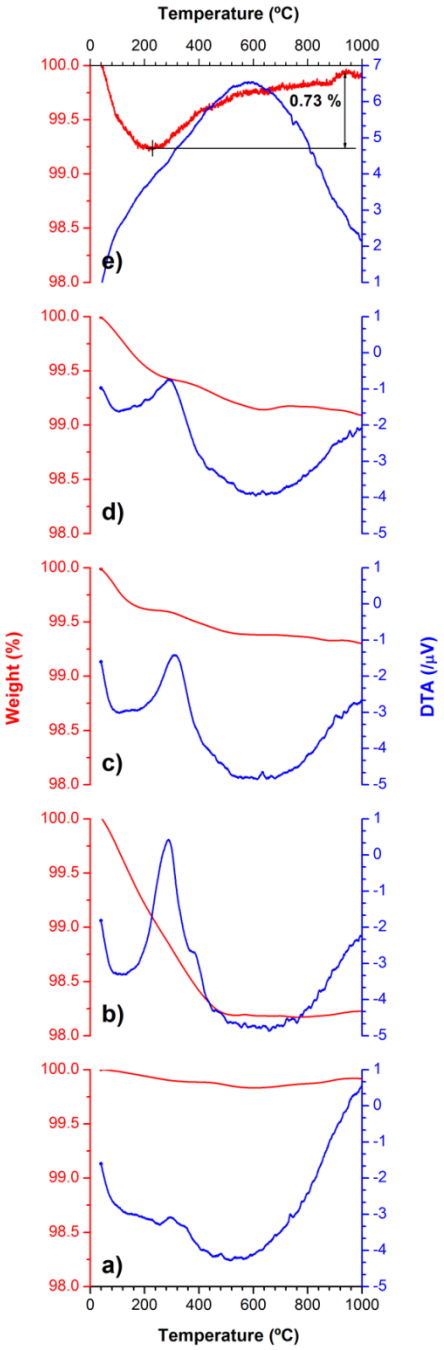

Figure S6.- *Thermogravimetric behavior under air atmosphere of the fresh samples: a) Pt/Al_2O_3, b) $CoAl_2O_4$, c) $Pt\text{-}Ni/CoAl_2O_4$, d) $Ni/CoAl_2O_4$, e) $Ni(5\%)/CoAl_2O_4$.*

The thermal evolution of the $Ni/CoAl_2O_4$ and of $Pt\text{-}Ni/CoAl_2O_4$ catalysts in air up to 1000 ºC shown in ***Figure S5c-d*** (for other samples, see ***Figure S6***) provides further information about the effect of the reaction conditions on the samples. The removal of absorbed water takes place from RT to near 200 °C. From this point, the differential thermal analysis shows an exothermic peak centered at 315

°C, which might correspond to the combustion of organic compounds generated during the milling procedure. The total weight loss of Ni/$CoAl_2O_4$ is 0.89 %, and of Pt-Ni/$CoAl_2O_4$ is 0.69 %. However, the total weight loss of bare $CoAl_2O_4$ is much higher (1.78 %, as observed in ***Figure S6***). This effect is a direct consequence of the weight gain due to the partial oxidation of Ni into NiO, related to the tendency of the secondary metals during annealing to segregate to the surface where oxygen is present,[7] and suggests a possible cause of the catalyst activity loss.[8] The same TG experiment was performed with a similar Ni/$CoAl_2O_4$ sample containing 5 times Ni loading to be able to quantify the extent of the oxidation process (see ***Figure S6***). In this sample, the weight gain between 200 and 950 °C, after water removal is 0.73 %. Even though a masking effect by weight compensation in the first 200 °C cannot be ruled out, this value is much lower than the weight corresponding to the complete oxidation of Ni into the partial oxidation product, NiO (1.4 %), or the total oxidation product, Ni_2O_3 (2.0 %). The supported Pt-Ni/$CoAl_2O_4$ catalyst has lower weight loss than the monometallic Ni catalyst, and thus better thermal stability, despite the decrease in the surface area. This suggests that the Pt nanoparticles can improve both the activity and the stability of Ni-based catalyst.

REFERENCES

(1) Álvarez-Docio, C. M.; Portela, R.; Reinosa, J. J.; Rubio-Marcos, F.; Granados-Miralles, C.; Pascual, L.; Fernández, J. F. Pt-Free $CoAl_2O_4$ Catalyst for Soot Combustion with NO_x/O_2. Appl. Catal. A Gen. **2020**, 591 (2), 117404.

(2) Rico-Pérez, V.; Aneggi, E.; Bueno-López, A.; Trovarelli, A. Synergic Effect of $Cu/Ce_{0.5}Pr_{0.5}O_{2-\delta}$ and $Ce_{0.5}Pr_{0.5}O_{2-\delta}$ in Soot Combustion. Appl. Catal. B Environ. **2016**, 197 (11), 95–104.

(3) Reid, C. B.; Forrester, J. S.; Goodshaw, H. J.; Kisi, E. H.; Suaning, G. J. A Study in the Mechanical Milling of Alumina Powder. Ceram. Int. **2008**, 34 (6), 1551–1556.

(4) Álvarez-Docio, C. M.; Reinosa, J. J.; Del Campo, A.; Fernández, J. F. Investigation of Thermal Stability of 2D and 3D $CoAl_2O_4$ Particles in Core-Shell Nanostructures by Raman Spectroscopy. J. Alloys Compd. **2018**, 779 (3), 244–254.

(5) Piumetti, M.; Bensaid, S.; Russo, N.; Fino, D. Nanostructured Ceria-Based Catalysts for Soot Combustion: Investigations on the Surface Sensitivity. Appl. Catal. B Environ. **2015**, 165 (4), 742–751.

(6) Pu, Y.; Luo, Y.; Wei, X.; Sun, J.; Li, L.; Zou, W.; Dong, L. Synergistic Effects of Cu_2O-Decorated CeO_2 on Photocatalytic CO_2 Reduction: Surface Lewis Acid/Base and Oxygen Defects. Appl. Catal. B Environ. **2019**, 254 (1), 580–586.

(7) Croy, J. R.; Mostafa, S.; Hickman, L.; Heinrich, H.; Cuenya, B. R. Bimetallic Pt-Metal Catalysts for the Decomposition of Methanol: Effect of Secondary Metal on the Oxidation State, Activity, and Selectivity of Pt. Appl. Catal. A Gen. **2008**, 350 (2), 207–216.

(8) Lee, J.; Choi, W. Photocatalytic Reactivity of Surface Platinized TiO_2: Substrate Specificity and the Effect of Pt Oxidation State. J. Phys. Chem. B **2005**, 109 (15), 7399–7406.

Capítulo 3. Discusión Integradora

"Ciencia es todo aquello sobre lo cual siempre cabe discusión"

José Ortega y Gasset

En esta tesis doctoral se han estudiado materiales nanoestructurados basados en aluminato de cobalto. Dicho material posee una estructura de espinela y se emplea actualmente como pigmento cerámico, tanto en forma de micropartículas, como de nanopigmento. Sin embargo, su uso en forma de nanomaterial plantea retos tecnológicos asociados con la dificultad en su caracterización, las limitaciones en su reactividad, la escasez de materias primas de cobalto y su potencial toxicidad. En este estudio se han abordado diferentes rutas de obtención de materiales nanoestructurados basados en aluminato de cobalto que, en base a una caracterización avanzada, han permitido diseñar aplicaciones novedosas. A continuación, y bajo una perspectiva más general, se analizan los resultados obtenidos en los trabajos recogidos en esta tesis.

El tamaño de cristalito y el tamaño de partícula son parámetros fundamentales para determinar las propiedades de los pigmentos (***Figura 3. 1***). Concretamente, las partículas de tamaño micrométrico de la espinela de aluminato de cobalto presentan una elevada opacidad, intenso color azul, un gran poder de recubrimiento y una alta estabilidad frente a la temperatura, que permite su uso como pigmento de grado cerámico [1]. En cambio, las nanopartículas de $CoAl_2O_4$ presentan efectos de transparencia relacionados con tamaños de partícula inferiores a la longitud de onda del espectro visible [2]. Así mismo, el elevado potencial químico de las nanopartículas de aluminato de cobalto favorece su disolución en los esmaltes cerámicos [3]. Además, asociado a la reactividad de las nanopartículas pueden producirse efectos negativos para la salud durante los procesos productivos [4]. Estos factores revelan que, aunque el aluminato de cobalto presenta una estructura estable en su forma micrométrica, la reducción del tamaño hasta el rango nanométrico modifica sus propiedades y condiciona el uso de dicho material [5]. A partir de estas premisas y junto a los resultados experimentales obtenidos en esta tesis doctoral, es posible determinar que el procesamiento del material permite modular de forma efectiva las propiedades de los materiales nanostructurados para adaptarse de forma segura a aplicaciones específicas.

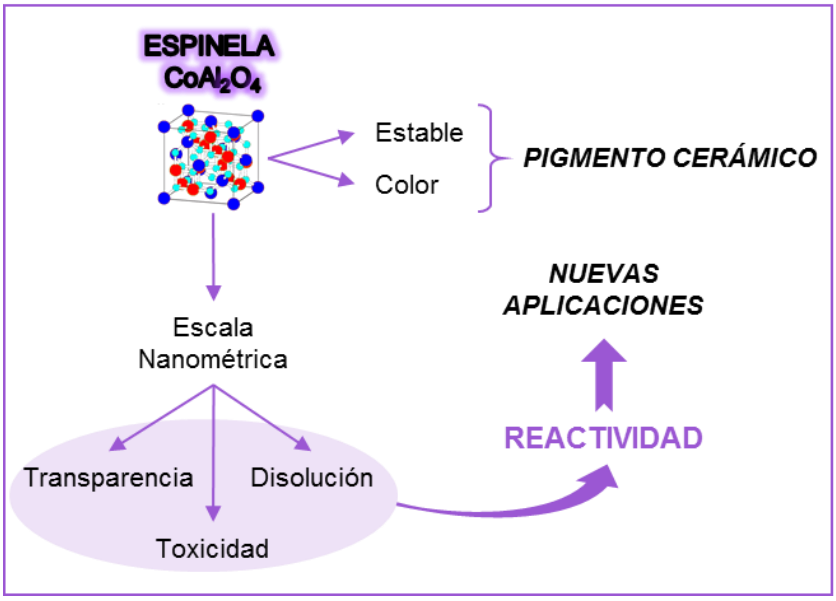

Figura 3. 1 *Esquema de los efectos de la disminución del tamaño de partícula del aluminato de cobalto hasta la nanoescala.*

Para el desarrollo de estos materiales nanoestructurados se han seguido dos rutas: proceso de Abajo-Arriba (*Bottom-Up*, en inglés) y proceso de Arriba-Abajo (*Top-Down*, en inglés). En el primer caso, se ha obtenido una estructura de tipo coraza-núcleo, donde las micropartículas soporte de α-Al_2O_3 se encuentran recubiertas de cristalizaciones nanométricas de espinela de $CoAl_2O_4$. Por el contrario, en el proceso de Arriba-Abajo, se realiza un proceso de micromolturación partiendo de micropartículas de aluminato de cobalto comercial, para generar partículas nanométricas con superficies activas. Con el propósito de facilitar la discusión posterior de los materiales estudiados, a partir de aquí se denominan **$CoAl_2O_4$ soportado** y **$CoAl_2O_4$ molturado**, los materiales generados mediante los procesos de Abajo-Arriba y de Arriba-Abajo, respectivamente. A continuación, se realiza una comparativa y una evaluación de ambos materiales, con el propósito de establecer la influencia de los procesos de obtención seguidos en las propiedades funcionales. En concreto, se estudia la influencia en el rendimiento del color para el $CoAl_2O_4$ soportado y en la respuesta reactiva para el $CoAl_2O_4$ molturado. La ***Tabla 3. 1*** resume las propiedades de ambos materiales y representa una ayuda para comprender cómo influyen las

características físico-químicas en las propiedades del material, tal y como será analizado a continuación.

	$CoAl_2O_4$ soportado	$CoAl_2O_4$ molturado
Microestructura	Cristalizaciones nanométricas con 2 morfologías diferentes. Cristalizaciones con bordes bien definidos y plano de cristalización preferente (111)	Morfología irregular con superficies nanorugosas. Planos cristalinos diferentes al (111)
Superficie específica	Baja: 0.3 m^2/g	Moderada: 22.9 m^2/g
Cristalinidad	Nanoestructuras altamente cristalinas	Pérdida de cristalinidad y generación de defectos $V_O^{\cdot\cdot}$
Sitios ácidos	1.6 mmol NH_3/g Ácidos de Lewis fuertes (Al^{3+})	11.2 mmol NH_3/g Ácidos de Lewis fuertes y débiles (Al^{3+} y Co^{2+}) y ácidos Brønsted
Estabilidad térmica	Partículas 2D: alta estabilidad Partículas 3D: baja estabilidad	Baja estabilidad
Rendimiento Color	Mismo tono que $CoAl_2O_4$ micrométrico para una reducción del 26 % en peso de cobalto	Pérdida del tono debido a una mayor dispersión de la luz
Actividad catalítica	No reactivo	Cataliza la reacción de combustión de la carbonilla

Tabla 3. 1 *Tabla resumen en la que se muestran las propiedades estudiadas de los materiales nanoestructurados basados en aluminato de cobalto.*

El control de la morfología de las nanopartículas es un factor clave para su aplicación en tecnologías emergentes [6]. Por ejemplo, las propiedades ópticas de las nanopartículas de oro, relacionadas con la resonancia de plasmones superficiales, dependen fuertemente de la morfología de las mismas [7]. Aunque, habitualmente, no existen reglas simples para determinar la morfología final de los nanomateriales inorgánicos [8], en este trabajo de tesis, ha sido posible la modificación de la morfología de las cristalizaciones de $CoAl_2O_4$ soportadas mediante la concentración de los precursores, que afecta a los procesos de nucleación, coalescencia y crecimiento cristalino [9]. De esta forma, dependiendo del estado de aglomeración que presentan las nanopartículas precursoras (Co_3O_4) en la dispersión inicial, los mecanismos de cristalización del aluminato de cobalto permiten generar morfologías diferenciadas: partículas 2D y partículas 3D (***Figura 3. 2***). La formación de partículas 2D laminares y con morfología triangular se produce a partir de nanopartículas de Co_3O_4 dispersas en la superficie de alúmina. Las partículas 3D son el resultado de aglomerados

iniciales de nanopartículas de Co_3O_4 con el soporte de α-Al_2O_3. Además, se constató que el tratamiento a alta temperatura favorece el crecimiento de las cristalizaciones de $CoAl_2O_4$ en planos cristalográficos (111), debido a la menor energía de dichos planos cristalinos por su alto factor de empaquetamiento atómico [10,11]. Por el contrario, debido al alto aporte de energía durante los procesos de micromolienda, se produce un importante cambio morfológico del material [12], generándose nanorugosidad en la superficie de las partículas y la rotura de la red cristalina que expone superficies con planos cristalinos diferentes a la dirección cristalográfica [111]. Así, la morfología de las nanopartículas obtenidas en el $CoAl_2O_4$ se ve afectada por la ruta de procesamiento seguida.

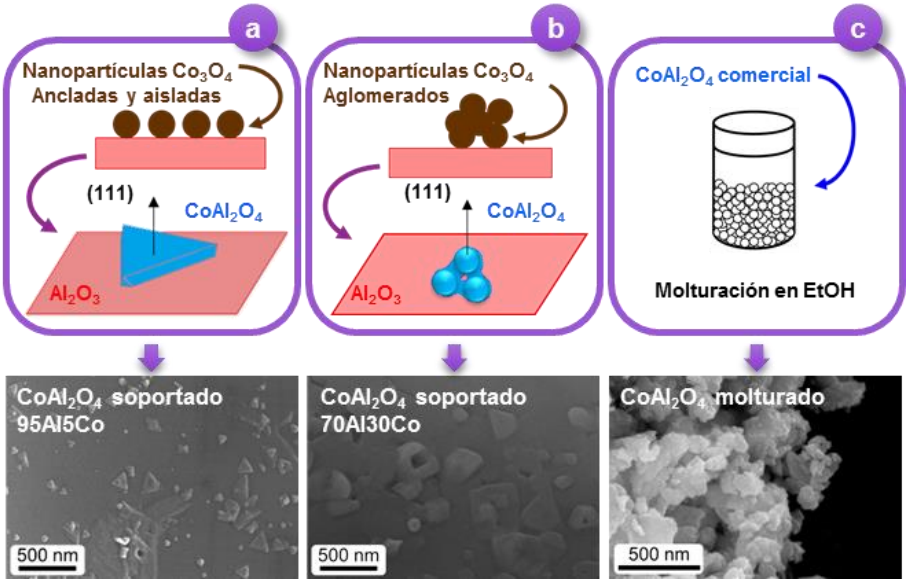

Figura 3. 2 *Morfología de las nanoestructuras en función del proceso de obtención seguido y del estado de aglomeración de los precursores.*

Estas diferencias asociadas a la morfología de las superficies nanoestructuradas tienen un efecto directo sobre los valores de superficie específica de los materiales. Las cristalizaciones del $CoAl_2O_4$ soportado se caracterizan por tener al menos una dimensión (el espesor) en el rango nanométrico. De hecho, las partículas 3D sobresalen más de la superficie de la alúmina que las partículas 2D, pero su rugosidad es < 100 nm. Por lo tanto, como las cristalizaciones son prácticamente planas y se encuentran soportadas sobre un material no poroso, la superficie específica es mínima (0.3 m^2/g). Para el $CoAl_2O_4$ molturado, este valor

aumenta hasta 22.9 m^2/g, debido a una mayor rugosidad de la superficie y a la reducción del tamaño de partícula hasta el rango nanométrico. Estos valores de superficie específica son considerablemente inferiores a los valores encontrados en la bibliografía para síntesis de nanopartículas de espinelas de metales de transición con valores comprendidos entre 70 y 250 m^2/g [13].

En el tratamiento a alta temperatura llevado a cabo para obtener aluminatos metálicos (de fórmula general $MeAl_2O_4$), se produce un proceso de difusión tipo Kirkendall [14], según el cual el mecanismo de formación y crecimiento de los cristales se basa en la contradifusión de los cationes en las interfaces entre Al_2O_3 y CoO, donde el mónoxido de cobalto es el resultado de la reducción térmica del precursor de Co_3O_4 [15]. De esta forma, la difusión del catión Co^{2+} en la interfaz de la alúmina conduce a la formación de la estructura de la espinela. La cristalización de la espinela requiere del transporte de masa por difusión superficial de los cationes de cobalto en la superficie, que precisa una menor energía que los procesos de difusión en volumen. Por lo tanto, el crecimiento cristalino se produce en la dirección cristalográfica que requiere menor energía, esto es en los planos cristalográficos (111). Como resultado, los aluminatos de cobalto nanoestructurados de la presente memoria muestran una alta cristalinidad a pesar de su carácter nanoestructurado y sus superficies específicas son tan bajas como la de óxidos metálicos micrométricos, esto es valores inferiores a 1 m^2/g. Por el contrario, en los materiales de $CoAl_2O_4$ molturado la energía de proceso de molturación por micromolienda genera múltiples superficies de fractura y defectos cristalinos que aumentan el valor de superficie específica respecto del aluminato de cobalto micrométrico precursor.

Se observa que, tras el proceso de molturación, el material conserva su estructura cristalina, correspondiente a la fase espinela del $CoAl_2O_4$. Es importante remarcar este comportamiento ya que durante el proceso de molienda se mantiene la estructura cristalina del material sin producir transformaciones químicas. Sin embargo, si se compara el tamaño de cristalito determinado a partir de difracción de Rayos X (***Figura 3. 3a***) se determina que el

$CoAl_2O_4$ soportado presenta un valor de 77 nm, mientras que para el $CoAl_2O_4$ molturado disminuye el tamaño de cristalito hasta 31 nm. La disminución de tamaño de cristalito lleva asociada una mayor densidad de defectos estructurales de la red cristalina [16] e incluso la amorfización de regiones superficiales [17]. La espectroscopia de fotoelectrones de rayos X (***Figura 3. 3b***) muestra una disminución en la densidad electrónica de la red de oxígeno de la espinela molturada, como resultado de la formación de vacantes de oxígeno [18].

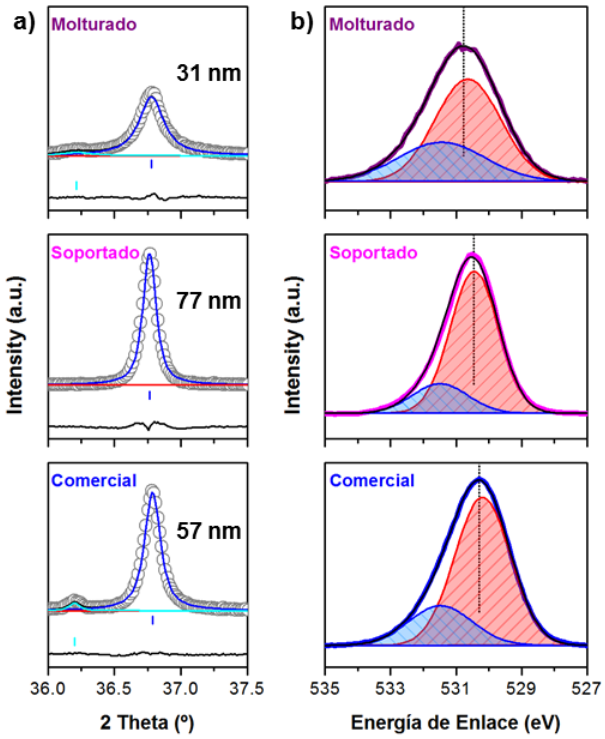

Figura 3. 3 *a) El tamaño de cristalito se calculó mediante la fórmula de Scherrer para el plano cristalográfico más intenso del pido de difracción de Rayos X situado a 36.8º 2θ y correspondiente a la familia de planos (311). b) Espectros obtenidos mediante espectroscopia de fotoelectrones emitidos por rayos X, de la línea correspondiente al O1s.*

La relación entre la presencia de defectos cristalinos en el $CoAl_2O_4$ molturado y la actividad del material se ha evaluado mediante TPD de NH_3. Los valores de acidez correlacionan los defectos con el aumento de grupos hidroxilo en la superficie del material durante el proceso de micromolienda en etanol, y el consecuente aumento de sitios ácidos de Brønsted [19]. Sin embargo, dichos grupos hidroxilo se eliminan parcialmente al producirse la deshidrogenación del etanol y la formación de agua. Este proceso de formación de vacantes de oxígeno

conduce a una distribución de la nube de electrones alrededor de los cationes metálicos desequilibrada y cargada positivamente [20]. Por lo tanto, estos defectos en superficie constituidos por vacantes de oxígeno son aceptores de electrones, es decir, ácidos de Lewis. La ruptura del material de forma aleatoria durante el proceso de molienda posibilita la presencia tanto de sitios Al^{3+} como de sitios Co^{2+} en la superficie, que se corresponden con la generación de sitios ácidos de Lewis fuertes y débiles, respectivamente [21]. Por el contrario, el $CoAl_2O_4$ soportado, solo presenta sitios ácidos de Lewis fuertes, pues los planos cristalinos (111) del aluminato de cobalto son preferentes y en la superficie de estos planos solo se exponen los cationes Al^{3+} [22]. Se ha evaluado también el comportamiento de estos materiales frente a la temperatura para realizar una estimación de su estabilidad térmica. A pesar de que una de las características principales del aluminato de cobalto es la elevada estabilidad de su estructura [23], en este trabajo se ha demostrado una respuesta diferencial a la absorción de fuentes de luz según el estado de aglomeración de las nanopartículas. Mediante espectroscopia Raman la nanoestructuras soportadas de $CoAl_2O_4$ presentan una mayor estabilidad térmica que los aglomerados de nanopartículas en el $CoAl_2O_4$ molturado.

La respuesta estructural de las nanoestructuras de $CoAl_2O_4$ a la absorción de la luz coherente láser depende en gran medida de la morfología de los nanocristales en la coraza sobre el soporte de alúmina micrométrica. Durante el calentamiento la evolución de la estructura de espinela de cobalto se determina a través de la evolución de los modos Raman característicos del material. Los espectros promedio de las muestras presentan una variación significativa en su respuesta frente a la temperatura con la morfología de las partículas, 3D o 2D, que están relacionadas con una diferencia en los procesos de dispersión de fonones de la red. La evolución de los modos Raman con la temperatura indica un desacoplamiento de los modos Raman para las muestras nanoestructuradas en las que predominan las cristalizaciones de las partículas 2D, debido a las diferencias dimensionales entre la superficie y el espesor; así, la energía térmica asociada a los modos de vibración varía según la dirección en la que se

propaguen los fonones de red. En cambio, los procesos de calentamiento están favorecidos como resultado de un confinamiento de los fonones que se correlaciona con una relajación de la red cristalina.

En este sentido, las mejoras en los procedimientos de análisis estructural y mico-nanoestructurales mediante Microscopía Raman Confocal se han trasladado a procesos de síntesis de nanopartículas de $BaTi_5O_{11}$. Este material difiere notoriamente del aluminato de cobalto respecto a su estructura y composición. Sin embargo, sirve como ejemplo de la utilidad de la Microscopia Raman Confocal para la monitorización de reacciones químicas complejas en la nanoescala. Así, ha sido posible optimizar el proceso químico de la síntesis del $BaTi_5O_{11}$, identificar la presencia de intermedios de reacción y de residuos generados durante la síntesis de los precursores para determinar su contribución en la formación final del material. De modo que, la estrategia general y los principios de diseño descritos en este trabajo pueden abrir nuevas direcciones para el estudio estructural y composicional de nanopartículas inorgánicas.

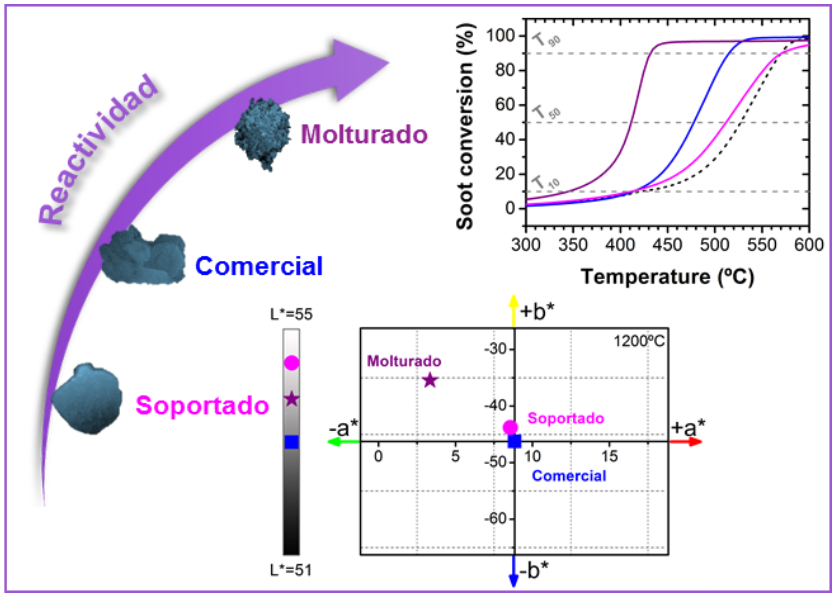

Figura 3. 4 *La reactividad de las superficies nanoestructuradas obtenidas en esta memoria y la variación de las propiedades permite la aplicación de este compuesto en diferentes campos.*

Por otro lado, la nanoestructuración de la superficie también afecta a las propiedades ópticas de los materiales basados en el aluminato de cobalto. En

primer lugar, para el $CoAl_2O_4$ molturado se observó una pérdida significativa de absorbancia en el espectro visible, junto con una mayor dispersión de la luz, que implica una disminución de la intensidad del color, tal y como indican sus coordenadas CIEL*a*b* (***Figura 3. 4***). Este comportamiento se correlaciona con el aumento de defectos en la estructura cristalina como consecuencia del proceso de micromolienda [24]. En cambio, la elevada cristalinidad de las nanopartículas de $CoAl_2O_4$ soportadas hace que se mejore el rendimiento de color del pigmento cerámico. De esta forma se consigue una reducción del 78% en peso en la proporción de CoO empleada, con respecto a la relacción estequiométrica del $CoAl_2O_4$ (***Figura 3. 5***). Igualmente, la efectividad de la coraza en cuanto a la respuesta del color se combina con la buena reflectividad del núcleo de α-Al_2O_3, en particular para la región NIR que posee una mayor capacidad de penetración en la estructura cristalina. El $CoAl_2O_4$ soportado presenta así una reflectividad del espectro solar del 77%, que es superior en 10 puntos porcentuales al pigmento convencional $CoAl_2O_4$ [25,26].

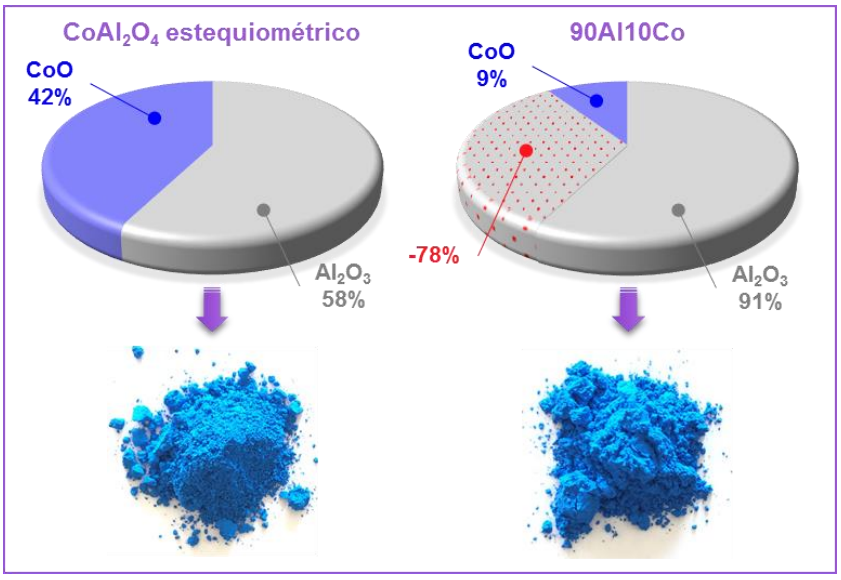

Figura 3. 5 *Composición química estequiométrica del $CoAl_2O_4$ y de la muestra 90Al10Co que presenta las mejores propiedades ópticas.*

El diseño y la fabricación de estructuras de tipo coraza-núcleo es una estrategia prometedora para conseguir un mayor rendimiento del cobalto, mientras que el proceso de deposición en seco disminuye, en parte, la

problemática asociada a la manipulación de las nanopartículas [27]. En este sentido, la inmovilización de las nanopartículas en el soporte, mediante su anclaje a través de una reacción electroquímica a temperatura ambiente permite utilizar las ventajas de las nanopartículas disminuyendo la toxicidad asociada a las mismas [28]. Por otro lado, para la aplicación del material como pigmento cerámico, un factor importante es la elevada estabilidad de estas nanopartículas como consecuencia de la estabilización de las mismas sobre el soporte de α-Al_2O_3, proceso que permite controlar su estado de aglomeración. Además, la reacción a alta temperatura hace que el crecimiento cristalino se encuentre delimitado hacia las direcciones cristalográficas con menor energía [29]. Por lo tanto, este material cumple uno de los requerimientos básicos de los pigmentos cerámicos: mantiene una estructura cristalina estable a elevadas temperaturas [30]. Finalmente, la presencia de las nanopartículas 3D, originadas por la sinterización de aglomerados de Co_3O_4, limita no solo la efectividad en cuanto al color, sino también la estabilidad térmica de la nanoestructura; por lo que el desarrollo de un procedimiento más refinado para maximizar la cantidad de cristalizaciones 2D planas representa un desafío para los pigmentos de tipo coraza-núcleo.

Además de una disminución de la intensidad del color, la generación de defectos durante el proceso de molturación, implica la activación de la superficie, generando una alta inestabilidad térmica. Estos aspectos limitan la aplicación de este material como pigmento cerámico [31]. Sin embargo, en este trabajo, las características obtenidas mediante la molturación del aluminato de cobalto permiten su aplicabilidad en otros campos de la técnica. De esta forma, se obtiene que el $CoAl_2O_4$ molturado presenta una elevada actividad catalítica frente a la reacción de combustión de carbonilla, que contrasta claramente con los valores obtenidos en la literatura para otros catalizadores basados en aluminato de cobalto [32].

La activación de sitios superficiales en el $CoAl_2O_4$ molturado permite abordar un proceso termoquímico para eliminar la carbonilla generada por los motores diésel que supone un gran impacto medioambiental [33] y tiene efectos

nocivos sobre la salud humana [34]. Episodios recientes como el denominado "Dieselgate" ponen de manifiesto las tremendas dificultades que supone para los fabricantes de automóviles cumplir los límites de emisiones impuestas por las normas Europeas [35]. Por ello, el control de las emisiones contaminantes generadas por los coches diésel se ha convertido, en los últimos años, en un tema con un gran impacto en la comunidad científica [36]. Además, este catalizador basado en aluminato de cobalto, con un coste relativamente bajo y activado mediante un proceso de molturación, se presenta como una alternativa apropiada frente al alto precio de los catalizadores de platino [37].

La reactividad catalítica del aluminato de cobalto molturado es consecuencia de una serie de factores que se resumen a continuación. En primer lugar, mediante la molturación se produce la nanoestructuración de la superficie de las partículas. Debido al pequeño tamaño de las nanopartículas, aumentan las zonas de contacto entre el catalizador y la carbonilla, facilitando el acceso a las especies gaseosas reactivas [38]. Esta fenomenología está directamente relacionada con la reducción del tamaño de cristalito, ya que la disminución del dominio coherente cristalino influye en la respuesta catalítica de los materiales [39]. Sin embargo, la eficiencia catalítica del $CoAl_2O_4$ soportado es mínima (***Figura 3. 5***), evidenciando que simplemente la presencia de nanopartículas en superficie no es suficiente para aumentar la reactividad del aluminato de cobalto. Según lo estudiado, la activación de las nanopartículas del $CoAl_2O_4$ molturado se atribuye a la aparición de planos cristalinos diferentes al (111), con una mayor energía superficial [40]. La diferencia en reactividad entre ambos materiales, soportado y molturado, está relacionada con la naturaleza de los cationes en la superficie del material. Como se ha discutido previamente, en el caso del $CoAl_2O_4$ soportado, únicamente se exponen los cationes Al^{3+}, que resultan ser centros poco reactivos, debido a la alta barrera energética que debe superar el CO adsorbido para reaccionar con el O_2 disponible en superficie [41]. En cambio, la presencia de planos cristalinos diferentes al (111), en el caso del $CoAl_2O_4$ molturado, posibilita que las terminaciones atómicas tengan una mayor cantidad de centros reactivos de Co^{2+}, que presentan una mayor reactividad [29].

A pesar de que los resultados obtenidos resultaron ser prometedores, se debe tener en cuenta también la estabilidad de los catalizadores, puesto que es un factor clave para su uso en aplicaciones prácticas [42]. Debido a la baja estabilidad térmica de la superficie nanoestructurada de $CoAl_2O_4$ obtenida mediante este proceso de molturación y a las altas temperaturas alcanzadas durante la reacción de combustión de la carbonilla se produce la sinterización de las nanopartículas de $CoAl_2O_4$, que genera la desactivación de la superficie [43,44]. Para solventar este problema se han estudiado diferentes rutas. En primer lugar, evitar la desactivación del catalizador, evitando que la temperatura no supere los 500ºC. Dado que la temperatura máxima que alcanzan los gases de escape de los motores diésel se encuentra en el rango de 260 a 540 ºC. Por otro lado, se propone el uso del $CoAl_2O_4$ molturado como soporte ácido de nanopartículas metálicas, para obtener catalizadores más activos y duraderos. Se plantea que un aumento de la energía de enlace entre las nanopartículas y el soporte debería disminuir la velocidad de sinterización [45]. Campbell demostró que la energía de adhesión de los metales variaba en función del soporte en el orden: MgO (100) ≈ TiO_2 (110) ≤ α-Al_2O_3 ≤ CeO_{2-x} (111) ≤ Fe_3O_4 y explicó este comportamiento basado en la estabilidad del oxígeno de la red, pues los átomos de oxígeno menos estables tienen un mayor potencial químico y se unen más fuertemente a los átomos metálicos en las nanopartículas [46]. Además, los defectos de vacantes de oxígeno en el soporte pueden servir como sitios de anclaje fuertes para las nanopartículas metálicas. Por ejemplo, mediante calorimetría de adsorción se ha determinado que las nanopartículas de Ag se adhieren más fuertemente sobre un soporte de CeO_2 que sobre un soporte de MgO (100) [47]. Esta observación puede explicar la mayor resistencia a la sinterización obtenida para los metales de transición depositados sobre CeO_2 [48]. Además, se ha demostrado que las vacantes de oxígeno estabilizan átomos de Au, tanto sobre TiO_2, como sobre MgO [49,50]. De este modo, el diseño y la síntesis de nanopartículas de Ni-Pt soportadas sobre la superficie de la espinela $CoAl_2O_4$ representa una vía potencial para mejorar su actividad y estabilidad catalítica en la reacción de oxidación de carbonilla, además de contribuir a reducir la cantidad de platino.

De esta manera, este trabajo de tesis ha supuesto una revisión de las propiedades de la espinela $CoAl_2O_4$ de forma que se han conseguido nuevas aplicaciones y se ha adecuado a las nuevas tendencias científicas actuales, como es la obtención de materiales funcionales a partir del estudio de propiedades y de la modificación de las mismas mediante la variación de la morfología y del tamaño de partícula. Se han adquirido así nuevos conocimientos de un material de uso habitual como pigmento gracias a la aplicación de nuevas técnicas de caracterización, y se abren nuevas rutas de aplicación del mismo en sectores en los que no se encontraba presente.

3.1. Bibliografía

1. Salavati-Niasari, M., Farhadi-Khouzani, M., and Davar, F. (2009) Bright blue pigment $CoAl_2O_4$ nanocrystals prepared by modified sol-gel method. *J. Sol-Gel Sci. Technol.*, **52** (3), 321–327.

2. Rangappa, D., Naka, T., Kondo, A., et al. (2007) Transparent $CoAl_2O_4$ hybrid nano pigment by organic ligand-assisted supercritical water. *J. Am. Chem. Soc.*, **129** (36), 11061–11066.

3. Cavalcante, P.M.T., Dondi, M., Guarini, G., et al. (2009) Colour performance of ceramic nano-pigments. *Dye. Pigment.*, **80** (2), 226–232.

4. Laguna, M., Núñez, N.O., Fernández, M., and Ocaña, M. (2018) Synthesis and optical properties of environmentally benign and highly uniform $NaCe(MoO_4)_2$ based yellow nanopigments. *J. Alloys Compd.*, **739** (3), 542–548.

5. Yüngevis, H., and Ozel, E. (2013) Effect of the milling process on the properties of $CoFe_2O_4$ pigment. *Ceram. Int.*, **39** (5), 5503–5511.

6. Henry, C.R. (2005) Morphology of supported nanoparticles. *Prog. Surf. Sci.*, **80** (3–4), 92–116.

7. Nehl, C.L., and Hafner, J.H. (2008) Shape-dependent plasmon resonances of gold nanoparticles. *J. Mater. Chem.*, **18** (21), 2415–2419.

8. Wu, Z., Yang, S., and Wu, W. (2016) Shape control of inorganic nanoparticles from solution. *Nanoscale*, **8** (3), 1237–1259.

9. Ingham, B., Lim, T.H., Dotzler, C.J., et al. (2011) How nanoparticles coalesce: An in situ study of Au nanoparticle aggregation and grain growth. *Chem. Mater.*, **23** (14), 3312–3317.

10. Liao, S.C., Tsai, P.Y., Liang, C.W., et al. (2011) Misorientation control and functionality design of nanopillars in self-assembled perovskite-spinel heteroepitaxial nanostructures. *ACS Nano*, **5** (5), 4118–4122.

11. Kim, D.H., Yang, J., Kim, M.S., and Kim, T.C. (2016) Structure and magnetic properties of spinel-perovskite nanocomposite thin films on $SrTiO_3$ (111) substrates. *J. Cryst. Growth*, **449** (9), 62–66.

12. Chikhalia, V., Forbes, R.T., Storey, R.A., and Ticehurst, M. (2006) The effect of crystal morphology and mill type on milling induced crystal disorder. *Eur. J. Pharm. Sci.*, **27** (1), 19–26.

13. Dhak, D., and Pramanik, P. (2006) Particle size comparison of soft-chemically prepared transition metal (Co, Ni, Cu, Zn) aluminate pinels. *J. Am. Ceram. Soc.*, **89** (3), 1014–1021.

14. Yin, Y., Rioux, R.M., Erdonmez, C.K., et al. (2004) Formation of hollow nanocrystals through the nanoscale Kirkendall effect. *Science (80-.).*, **304** (4), 711–714.

15. Pettit, F.S., Randlev, E.H., and Felten, E.J. (1966) Formation of $NiAl_2O_4$ by solid state reaction. *J. Am. Ceram. Soc.*, **49** (4), 199–203.

16. Chamarthy, S.P., and Pinal, R. (2008) The nature of crystal disorder in milled pharmaceutical materials. *Colloids Surfaces A Physicochem. Eng. Asp.*, **331** (1–2), 68–75.

17. Popescu, M. (1984) Defect formation in amorphous structures as revealed by computer simulation. *Thin Solid Films*, **21** (4), 317–347.

18. Pu, Y., Luo, Y., Wei, X., et al. (2019) Synergistic effects of Cu_2O-decorated CeO_2 on photocatalytic CO_2 reduction: Surface Lewis acid/base and oxygen defect. *Appl. Catal. B Environ.*, **254** (April), 580–586.

19. González, J., Wang, J.A., Chen, L.F., et al. (2017) Structural defects, Lewis acidity, and catalysis properties of mesostructured WO_3/SBA-15 nanocatalysts. *J. Phys. Chem. C*, **121** (43), 23988–23999.

20. Liu, C., Hou, R., and Wang, T. (2015) Role of acid sites and surface hydroxyl groups in isophthalonitrile hydrogenation catalyzed by supported Ni-Co catalysts. *RSC Adv.*, **5** (34), 26465–26474.

21. Dewangan, N., Ashok, J., Sethia, M., et al. (2019) Cobalt-based catalyst supported on different morphologies of alumina for non-oxidative propane dehydrogenation: Effect of metal support interaction and Lewis acidic sites. *ChemCatChem*, **11** (19), 4923–4934.

22. Zasada, F., Piskorz, W., and Sojka, Z. (2015) Cobalt spinel at various redox conditions: DFT+U investigations into the structure and surface thermodynamics of the (100) facet. *J. Phys. Chem. C*, **119** (33), 19180–19191.

23. Ragupathi, C., Vijaya, J.J., Kennedy, L.J., and Bououdina, M. (2014) Combustion synthesis, structure, magnetic and optical properties of cobalt aluminate spinel nanocrystals. *Ceram. Int.*, **40** (8 PART B), 13067–13074.

24. Liu, B.H., Ding, J., Dong, Z.L., et al. (2006) Microstructural evolution and its influence on the magnetic properties of $CoFe_2O_4$ powders during mechanical milling. *Phys. Rev. B - Condens. Matter Mater. Phys.*, **74** (18), 1–10.

25. Jose, S., Jayaprakash, A., Laha, S., et al. (2016) $YIn_{0.9}Mn_{0.1}O_3$–ZnO nano-pigment exhibiting intense blue color with impressive solar reflectance. *Dye. Pigment.*, **124** (1), 120–129.

26. Hedayati, H.R., Sabbagh Alvani, A.A., Sameie, H., et al. (2015) Synthesis and characterization of $Co_{1-x}Zn_xCr_{2-y}Al_yO_4$ as a near-infrared reflective color tunable nano-pigment. *Dye. Pigment.*, **113** (2), 588–595.

27. He, X., Wang, F., Liu, H., et al. (2018) Synthesis and color properties of the TiO_2@$CoAl_2O_4$ blue pigments with low cobalt content applied in ceramic glaze. *J. Am. Ceram. Soc.*, **101** (6), 2578–2588.

28. Lorite, I., Romero, J.J., and Fernandez, J.F. (2013) Study of the nanoparticle/microparticle powder systems by dry dispersion. *Ceram. Int.*, **39** (2), 1631–1637.

29. Zasada, F., Gryboś, J., Piskorz, W., and Sojka, Z. (2018) Cobalt spinel (111) facets of various stoichiometry - DFT+U and ab initio thermodynamic

investigationssdafsfas. *J. Phys. Chem. C*, **122** (5), 2866–2879.

30. Tomas, G.M., and Monrós, G. (2003) *El color de la cerámica: Nuevos mecanismos en pigmentos para los nuevos procesados de la industria cerámica*, Athenea, Castelló de la Plana.

31. Dondi, M., and Eppler, R.A. (2014) Ceramic Colorants, in *Ullmann's Encyclopedia of Industrial Chemistry*, Wiley Online Library, London, pp. 1–18.

32. Zawadzki, M., Walerczyk, W., López-Suárez, F.E., et al. (2011) $CoAl_2O_4$ spinel catalyst for soot combustion with NO_x/O_2. *Catal. Commun.*, **12** (13), 1238–1241.

33. Thomson, M., and Mitra, T. (2018) A radical approach to soot formation. *Science (80-.).*, **361** (6406), 978–979.

34. Niranjan, R., and Thakur, A.K. (2017) The toxicological mechanisms of environmental soot (black carbon) and carbon black: Focus on Oxidative stress and inflammatory pathways. *Front. Immunol.*, **8** (JUN), 1–20.

35. van Setten, B.A.A.L., Makkee, M., and Moulijn, J.A. (2001) Science and technology of catalytic diesel particulate filters. *Catal. Rev. - Sci. Eng.*, **43** (4), 489–564.

36. Fino, D. (2007) Diesel emission control: Catalytic filters for particulate removal. *Sci. Technol. Adv. Mater.*, **8** (1), 93–100.

37. Sealy, C. (2008) The problem with platinum. *Mater. Today*, **11** (12), 65–68.

38. Wang, J., Yang, G., Cheng, L., et al. (2015) Three-dimensionally ordered macroporous spinel-type MCr_2O_4 (M = Co, Ni, Zn, Mn) catalysts with highly enhanced catalytic performance for soot combustion. *Catal. Sci. Technol.*, **5** (9), 4594–4601.

39. Zanella, R. (2014) Aplicación de los nanomateriales en catálisis. *Mundo Nano*, **7** (12), 66–82.

40. Huang, W., and Li, W.X. (2019) Surface and interface design for heterogeneous catalysis. *Phys. Chem. Chem. Phys.*, **21** (2), 523–536.

41. Wang, H.F., Kavanagh, R., Guo, Y.L., et al. (2012) Origin of extraordinarily high catalytic activity of Co_3O_4 and its morphological chemistry for CO oxidation at low temperature. *J. Catal.*, **296** (12), 110–119.

42. Argyle, M.D., and Bartholomew, C.H. (2015) Heterogeneous catalyst deactivation and regeneration: A review. *Catalysts*, **5** (1), 145–269.

43. Cheng, N., Zhang, L., Doyle-Davis, K., and Sun, X. (2019) *Single-atom catalysts: From design to application*.

44. Liu, L., and Corma, A. (2018) Metal catalysts for heterogeneous catalysis: From single atoms to nanoclusters and nanoparticles. *Chem. Rev.*, **118** (10), 4981–5079.

45. Barbero, J., Peña, M.A., Campos-Martin, J.M., et al. (2003) Support effect in supported Ni catalysts on their performance for methane partial oxidation. *Catal. Letters*, **87** (3–4), 211–218.

46. Campbell, C.T. (2013) The energetics of supported metal nanoparticles: Relationships to sintering rates and catalytic activity. *Acc. Chem. Res.*, **46** (8), 1712–1719.

47. Farmer, J.A., and Campbell, C.T. (2010) Ceria maintains smaller metal catalyst particles by strong metal-support bonding. *Science (80-.).*, **329** (5994), 933–936.

48. Hemmingson, S.L., James, T.E., Feeley, G.M., et al. (2016) Adsorption and adhesion of Au on reduced CeO_2 (111) surfaces at 300 and 100 K. *J. Phys. Chem. C*, **120** (22), 12113–12124.

49. Hong, S., and Rahman, T.S. (2013) Rationale for the higher reactivity of interfacial sites in methanol decomposition on Au_{13}/TiO_2 (110). *J. Am. Chem. Soc.*, **135** (20), 7629–7635.

50. Ricci, D., Bongiorno, A., Pacchioni, G., and Landman, U. (2006) Bonding

trends and dimensionality crossover of gold nanoclusters on metal-supported MgO thin films. *Phys. Rev. Lett.*, **97** (3), 1–4.

Capítulo 4. Conclusiones

"Es débil porque no ha dudado bastante y ha querido llegar a conclusiones"

Miguel de Unamuno

A partir de los resultados obtenidos en este trabajo de investigación se pueden extraer las siguientes conclusiones:

- ✓ Se ha optimizado un proceso para la obtención de un pigmento nanoestructurado, en el que las nanopartículas de $CoAl_2O_4$ se encuentran soportadas sobre micropartículas de α-Al_2O_3; para ello se ha utilizado un proceso de dispersión en seco y un tratamiento térmico a alta temperatura. De esta manera, se ha obtenido una estructura de tipo coraza-núcleo, en la que la coraza está formada por nanocristales laminares de $CoAl_2O_4$, orientados en la dirección [111] y estables térmicamente. El pigmento nanoestructurado coraza-núcleo permite reducir la cantidad de óxido de cobalto (CoO) empleada en un 78 % en peso respecto de la requerida en los pigmentos de composición estequiométrica. Se ha demostrado que una estructura coraza-núcleo es una estrategia útil para minimizar el uso de materiales caros o nocivos.

- ✓ Se ha determinado la efectividad como pigmento frío de las micropartículas formadas por una coraza de $CoAl_2O_4$ y un núcleo de α-Al_2O_3. El pigmento nanoestructurado presenta una mayor reflectividad solar que los pigmentos estándar, gracias a la sinergia existente entre las propiedades de los materiales que constituyen la coraza y el núcleo. De esta forma las cristalizaciones de tamaño nanométrico de $CoAl_2O_4$ aportan el color azul en el rango del espectro visible, mientras que el núcleo compuesto por α-Al_2O_3 de color blanco aumenta la reflectividad solar, principalmente en el rango del espectro correspondiente a la región de infrarrojo cercano.

- ✓ Mediante Microscopia Raman Confocal se ha desarrollado una metodología para la caracterización de los materiales micro-nanoestructurados basados en $CoAl_2O_4$. Los materiales nanoestructurados de $CoAl_2O_4$ soportados, presentan una gran estabilidad térmica. Sin embargo, dicha estabilidad está limitada por formación de aglomerados de nanopartículas que relajan la estructura cristalina y favorecen los procesos de calentamiento.

- ✓ Se ha desarrollo un material de $CoAl_2O_4$ nanoestructurado por activación mediante un proceso de micromolienda. Las nanopartículas de $CoAl_2O_4$ obtenidas por molturación presentan una mayor rugosidad en su superficie y planos cristalinos diferentes al plano cristalino de mayor estabilidad, (111). Como resultado, las nanopartículas de $CoAl_2O_4$ obtenidas por molturación presentan un aumento de los sitios ácidos superficiales. Dichos sitios ácidos promueven la reacción de oxidación de carbonilla de diésel a temperaturas de trabajo similares a las obtenidas por los mejores catalizadores actuales a pesar de presentar una superficie específica netamente inferior.
- ✓ Se ha utilizado el $CoAl_2O_4$ activado mecánicamente como soporte activo de nanopartículas metálicas como una vía para la mejora en la desactivación térmica del catalizador en procesos de combustión de carbonilla por sobrecalentamiento.
- ✓ Los catalizadores basados en aluminato de cobalto, con un coste relativamente bajo y activado mediante un proceso de micromolienda se presentan como una alternativa viable para la sustitución de los catalizadores de platino en reacción de oxidación de carbonilla.

Anexos

Anexo I

Patente. Catalyst for soot combustion

MINISTERIO
DE INDUSTRIA, ENERGÍA
Y TURISMO

Oficina Española
de Patentes y Marcas

Justificante de presentación electrónica de solicitud de patente

Este documento es un justificante de que se ha recibido una solicitud española de patente por vía electrónica utilizando la conexión segura de la O.E.P.M. De acuerdo con lo dispuesto en el art. 16.1 del Reglamento de ejecución de la Ley 24/2015 de Patentes, se han asignado a su solicitud un número de expediente y una fecha de recepción de forma automática. La fecha de presentación de la solicitud a la que se refiere el art. 24 de la Ley le será comunicada posteriormente.

Número de solicitud:	P201930647	
Fecha de recepción:	11 julio 2019, 13:37 (CEST)	
Oficina receptora:	OEPM Madrid	
Su referencia:	ES1641.1457	
Solicitante:	CONSEJO SUPERIOR DE INVESTIGACIONES CIENTÍFICAS (CSIC)	
Número de solicitantes:	1	
País:	ES	
Título:	CATALYST FOR SOOT COMBUSTION	
Documentos enviados:	DescripcionOL.pdf (21 p.) ReivindicacionesOL.pdf (1 p.) DibujosOL.pdf (12 p.) ResumenOL.pdf (1 p.) OLF-ARCHIVE.zip FEERCPT-1.pdf (1 p.) FEERCPT-2.pdf (1 p.)	package-data.xml es-request.xml application-body.xml es-fee-sheet.xml feesheet.pdf request.pdf
Enviados por:	C=ES,O=PONS PATENTES Y MARCAS INTERNACIONAL SL,2.5.4.97=#0C0F56415445532D423834393231373039,CN=50534279 J ANGEL PONS (R: B84921709),SN=PONS ARIÑO,givenName=ANGEL,serialNumber=IDCES-50534279J,descriptio n=Ref:AEAT/AEAT0297/PUESTO 1/40639/21092018091901	
Fecha y hora de recepción:	11 julio 2019, 13:37 (CEST)	
Codificación del envío:	D0:34:D9:E7:CD:B9:FE:4E:FB:8F:E8:A2:55:FD:29:61:AD:DD:E0:EF	

AVISO IMPORTANTE
Las tasas pagaderas al solicitar y durante la tramitación de una patente o un modelo de utilidad son las que se recogen en el Apartado "Tasas y precios públicos" de la página web de la OEPM (http://www.oepm.es/es/propiedad_industrial/tasas/). Consecuentemente, si recibe una comunicación informándole de la necesidad de hacer un pago por la inscripción de su patente o su modelo de utilidad en un "registro central" o en un "registro de internet" posiblemente se trate de un fraude.
La anotación en este tipo de autodenominados "registros" no despliega ningún tipo de eficacia jurídica ni tiene carácter oficial.
En estos casos le aconsejamos que se ponga en contacto con la Oficina Española de Patentes y Marcas en el correo electrónico informacion@oepm.es.

ADVERTENCIA: POR DISPOSICIÓN LEGAL LOS DATOS CONTENIDOS EN ESTA SOLICITUD PODRÁN SER PUBLICADOS EN EL BOLETÍN OFICIAL DE LA PROPIEDAD INDUSTRIAL E INSCRITOS EN EL REGISTRO DE PATENTES DE LA OEPM, SIENDO AMBAS BASES DE DATOS DE CARÁCTER PÚBLICO Y ACCESIBLES VÍA REDES MUNDIALES DE INFORMÁTICA.
Para cualquier aclaración puede contactar con la O.E.P.M.

/Madrid, Oficina Receptora/

MINISTERIO DE ENERGÍA, TURISMO Y AGENDA DIGITAL

Oficina Española de Patentes y Marcas

(1) MODALIDAD: **PATENTE DE INVENCIÓN** **MODELO DE UTILIDAD**	 [✓] [ ]
(2) FORMULARIO 5101. TIPO DE SOLICITUD: PRIMERA PRESENTACIÓN SOLICITUD DIVISIONAL CAMBIO DE MODALIDAD TRANSFORMACIÓN SOLICITUD PATENTE EUROPEA PCT: ENTRADA FASE NACIONAL	 [✓] [ ] [ ] [ ] [ ]
(3) EXP. PRINCIPAL O DE ORIGEN: MODALIDAD: N.º SOLICITUD: FECHA SOLICITUD:	
4) LUGAR DE PRESENTACIÓN:	OEPM, Presentación Electrónica
(5-1) SOLICITANTE 1: DENOMINACIÓN SOCIAL: UNIVERSIDAD PÚBLICA NACIONALIDAD: CÓDIGO PAÍS: NIF/NIE/PASAPORTE: CNAE: PYME: DOMICILIO: LOCALIDAD: PROVINCIA: CÓDIGO POSTAL: PAÍS RESIDENCIA: CÓDIGO PAÍS: TELÉFONO: FAX: CORREO ELECTRÓNICO: EMPRENDEDOR: PERSONA DE CONTACTO: MODO DE OBTENCIÓN DEL DERECHO: INVENCIÓN LABORAL: CONTRATO: SUCESIÓN: PORCENTAJE DE TITULARIDAD:	 CONSEJO SUPERIOR DE INVESTIGACIONES CIENTÍFICAS (CSIC) [ ] España ES Q2818002D C/ Serrano, 117 Madrid 28 Madrid 28006 España ES [ ] [✓] [ ] [ ] 100,00 %
(6-1) INVENTOR 1: APELLIDOS: NOMBRE: NACIONALIDAD: CÓDIGO PAÍS: NIF/NIE/PASAPORTE: DOMICILIO: LOCALIDAD: PROVINCIA: CÓDIGO POSTAL: PAÍS RESIDENCIA: CÓDIGO PAÍS:	 ÁLVAREZ DOCIO CARMEN MARÍA

TELÉFONO:	
FAX:	
CORREO ELECTRÓNICO:	
EL INVENTOR RENUNCIA A SER MENCIONADO:	[ ]
(6-2) INVENTOR 2:	
APELLIDOS:	PORTELA RODRÍGUEZ
NOMBRE:	RAQUEL
NACIONALIDAD:	
CÓDIGO PAÍS:	
NIF/NIE/PASAPORTE:	
DOMICILIO:	
LOCALIDAD:	
PROVINCIA:	
CÓDIGO POSTAL:	
PAÍS RESIDENCIA:	
CÓDIGO PAÍS:	
TELÉFONO:	
FAX:	
CORREO ELECTRÓNICO:	
EL INVENTOR RENUNCIA A SER MENCIONADO:	[ ]
(6-3) INVENTOR 3:	
APELLIDOS:	FERNÁNDEZ LOZANO
NOMBRE:	JOSÉ FRANCISCO
NACIONALIDAD:	
CÓDIGO PAÍS:	
NIF/NIE/PASAPORTE:	
DOMICILIO:	
LOCALIDAD:	
PROVINCIA:	
CÓDIGO POSTAL:	
PAÍS RESIDENCIA:	
CÓDIGO PAÍS:	
TELÉFONO:	
FAX:	
CORREO ELECTRÓNICO:	
EL INVENTOR RENUNCIA A SER MENCIONADO:	[ ]
(6-4) INVENTOR 4:	
APELLIDOS:	JIMÉNEZ REINOSA
NOMBRE:	JULIÁN
NACIONALIDAD:	
CÓDIGO PAÍS:	
NIF/NIE/PASAPORTE:	
DOMICILIO:	
LOCALIDAD:	
PROVINCIA:	
CÓDIGO POSTAL:	
PAÍS RESIDENCIA:	
CÓDIGO PAÍS:	
TELÉFONO:	
FAX:	
CORREO ELECTRÓNICO:	
EL INVENTOR RENUNCIA A SER MENCIONADO:	[ ]
(6-5) INVENTOR 5:	
APELLIDOS:	BAÑARES GONZÁLEZ
NOMBRE:	MIGUEL ÁNGEL
NACIONALIDAD:	
CÓDIGO PAÍS:	
NIF/NIE/PASAPORTE:	
DOMICILIO:	
LOCALIDAD:	
PROVINCIA:	
CÓDIGO POSTAL:	
PAÍS RESIDENCIA:	
CÓDIGO PAÍS:	
TELÉFONO:	

FAX: CORREO ELECTRÓNICO: EL INVENTOR RENUNCIA A SER MENCIONADO:	 [ ]
(7) TÍTULO DE LA INVENCIÓN:	CATALYST FOR SOOT COMBUSTION
(8) NÚMERO DE INFORME TECNOLÓGICO DE PATENTES (ITP):	
(9) SOLICITA LA INCLUSIÓN EN EL PROCEDIMIENTO ACELERADO DE CONCESIÓN SI NO	 [ ] [✓]
(10) EFECTUADO DEPÓSITO DE MATERÍA BIOLÓGICA: SI NO	 [ ] [✓]
(11) DEPÓSITO: REFERENCIA DE IDENTIFICACIÓN: INSTITUCIÓN DE DEPÓSITO: NÚMERO DE DEPÓSITO: ORÍGEN BIOLÓGICO:	
(12) RECURSO GENÉTICO: NÚMERO DE REGISTRO: NÚMERO DE CERTIFICADO DE ACCESO AL RECURSO: UTILIZACIÓN DEL RECURSO GENÉTICO: CONOCIMIENTO TRADICIONAL ASOCIADO A UN RECURSO GENÉTICO:	
(13) DECLARACIONES RELATIVAS A LA LISTA DE SECUENCIAS: LA LISTA DE SECUENCIAS NO VA MÁS ALLÁ DEL CONTENIDO DE LA SOLICITUD LA LISTA DE SECUENCIAS EN FORMATO PDF Y ASCII SON IDENTICOS	 [ ] [ ]
(14) EXPOSICIONES OFICIALES: NOMBRE: LUGAR: FECHA:	
(15) DECLARACIONES DE PRIORIDAD: PAÍS DE ORIGEN: CÓDIGO PAÍS: NÚMERO: FECHA:	
(16) REMISIÓN A UNA SOLICITUD ANTERIOR: PAÍS DE ORIGEN: CÓDIGO PAÍS: NÚMERO: FECHA:	
(17) AGENTE DE PROPIEDAD INDUSTRIAL: APELLIDOS: NOMBRE: CÓDIGO DE AGENTE: NÚMERO DE PODER:	 PONS ARIÑO ÁNGEL 0499/5 20081765
(18) DIRECCIÓN A EFECTOS DE COMUNICACIONES: DIRECCIÓN ASOCIADA AL PRIMER SOLICITANTE DOMICILIO: LOCALIDAD: PROVINCIA: CÓDIGO POSTAL: PAÍS RESIDENCIA: CÓDIGO PAÍS: TELÉFONO: FAX: CORREO ELECTRÓNICO: MEDIO PREFERENTE DE COMUNICACIÓN	

(19) RELACIÓN DE DOCUMENTOS QUE SE ACOMPAÑAN:	
DESCRIPCIÓN EN OTRO IDIOMA:	[✓] N.º de páginas: 21
REIVINDICACIONES EN OTRO IDIOMA:	[✓] N.º reivindicaciones: 7
DIBUJOS EN OTRO IDIOMA:	[✓] N.º de dibujos: 10
RESUMEN EN OTRO IDIOMA:	[✓] N.º de páginas: 1
FIGURA(S) A PUBLICAR CON EL RESUMEN EN OTRO IDIOMA:	[✓] N.º de figura(s):
ARCHIVO DE PRECONVERSION:	[✓]
DOCUMENTO DE REPRESENTACIÓN:	[ ] N.º de páginas:
JUSTIFICANTE DE PAGO (1):	[✓] N.º de páginas: 1
JUSTIFICANTE DE PAGO (2):	[✓] N.º de páginas: 1
LISTA DE SECUENCIAS PDF:	[ ] N.º de páginas:
ARCHIVO PARA LA BUSQUEDA DE LS:	[ ]
OTROS (Aparecerán detallados):	
(20) EL SOLICITANTE SE ACOGE A LA REDUCCIÓN DE TASAS PARA EMPRENDEDORES PREVISTA EN EL ART. 186 DE LA LEY 24/2015 DE PATENTES Y, A TAL EFECTO, APORTA LA SIGUIENTE DOCUMENTACIÓN ADJUNTA:	[ ]
(21) NOTAS:	
(22) FIRMA:	
FIRMA DEL SOLICITANTE O REPRESENTANTE:	50534279J ANGEL PONS (R: B84921709)
LUGAR DE FIRMA:	MADRID
FECHA DE FIRMA:	11 Julio 2019

Anexo II

Currículum obtenido durante el período de Tesis doctoral

PUBLICACIONES O DOCUMENTOS CIENTÍFICO-TÉCNICOS

Artículos incluidos en la tesis doctoral

1. C. M. Álvarez-Docio, J. J. Reinosa, A. del Campo, J. F. Fernández, 2D particles forming a nanostructured shell: A step forward cool NIR reflectivity for $CoAl_2O_4$ pigments, Dyes and Pigments, 137 (2017) 1-11.

2. C. M. Álvarez-Docio, J. J. Reinosa, A. del Campo, J. F. Fernández, Investigation of thermal stability of 2D and 3D $CoAl_2O_4$ particles in core-shell nanostructures by Raman spectroscopy, Journal of Alloys and Compounds, 779 (2019) 244-254.

3. Carmen María Álvarez-Docio, Julián Jiménez Reinosa, Giovanna Canu, María Teresa Buscaglia, Vincenzo Buscaglia, José Francisco Fernández, Revealing the Role of the Intermediates during the Synthesis of $BaTi_5O_{11}$, Inorganic Chemistry, 58, (2019) 8120−8129.

4. C.M. Álvarez-Docio, R. Portela, J. J. Reinosa, F. Rubio-Marcos, J. F. Fernández, Pt-based catalysts by mechanical dispersion on non-porous alumina microparticles, Catalysis Communications (Enviado).

5. C.M. Álvarez-Docio, R. Portela, J. J. Reinosa, F. Rubio-Marcos, C. Granados-Miralles, L. Pascual, J. F. Fernández, Pt-free $CoAl_2O_4$ catalyst for soot combustion with NO_x/O_2, Applied Catalysis A: General, 591, (2020), 117404.

6. C.M. Álvarez-Docio, R. Portela, J. J. Reinosa, F. Rubio-Marcos, L. Pascual, J. F. Fernández, Performance and stability of wet-milled CoAl2O4, Ni/CoAl2O4 and Pt-Ni/CoAl2O4 for soot combustion, Catalysis Science and Technology (Enviado).

Otros artículos realizados durante la tesis doctoral

1. Julián Jiménez Reinosa, Carmen María Álvarez Docio, Víctor Zapata Ramírez, José Francisco Fernández Lozano, Hierarchical nano ZnO-micro TiO_2 composites: High UV protection yield lowering photodegradation in sunscreens, Ceramics International, 44, (2018) 2827-2834.

2. Julián Jiménez Reinosa, Pilar Leret, Carmen M. Álvarez-Docio, Adolfo del Campo, José F. Fernández, Enhancement of UV absorption behavior in ZnO–TiO_2 composites, Boletín de la Sociedad Española de Cerámica y Vidrio, 55, (2016) 55-62.

Patente solicitada

Autores: C.M. Álvarez-Docio, R. Portela, J. F. Fernández, J. J. Reinosa, M. A. Bañares.

Título: Catalyst for soot combustion

Titularidad: 100% Consejo Superior Investigaciones Científicas

Nº registro: P201930647 11-Julio-2019

CONTRIBUCIONES A CONGRESOS

1. C. M. Álvarez-Docio, J. J. Reinosa, J. F. Fernández. "Safe Design of Cobalt Aluminate Nanostructures" XII Reunión Nacional de Electrocerámica, Universidad Politécnica de Madrid, 17-19 junio 2015.

2. C. M. Álvarez-Docio, J. J. Reinosa, J. F. Fernández. "Diseño Seguro de Nanoestructuras de Aluminato de Cobalto" IV Jornadas de Jóvenes Investigadores, Instituto de Cerámica y Vidrio, 9 julio 2015.

3. C. M. Álvarez-Docio, J. J. Reinosa, J. F. Fernández. "Diseño de Superficies Nanoestructuradas Mediante el Crecimiento de Partículas 2D y su Aplicación Como Materiales Reflectivos" LV Congreso de la Sociedad Española de Cerámica y Vidrio, Universidad de Sevilla, 5-7 octubre 2016.

4. C. M. Álvarez-Docio, J. J. Reinosa, A. del Campo, J. F. Fernández. "Study of $CoAl_2O_4$ nanostructured surfaces by Raman Confocal Spectroscopy" 4° Workshop sobre Microscopia Raman Confocal, Instituto de Cerámica y Vidrio, 26-28 abril 2017.

5. C. M. Álvarez-Docio, J. J. Reinosa, J. F. Fernández. "Compuestos jerarquizados de ZnO nano-TiO_2 micro con alta protección UV y reducción de la foto-degradación en protectores solares" VI Jornadas de Jóvenes Investigadores, Instituto de Cerámica y Vidrio, 28 junio 2017.

6. C. M. Álvarez-Docio, J. J. Reinosa, J. F. Fernández. "Design of nanostructured surfaces through the growth of 2D particles and its application as reflective materials" 12th International Conference on Surfaces, Coatings and Nanostructured Materials (NANOSMAT), París, 11-13 septiembre 2017.

7. C. M. Álvarez-Docio, J. J. Reinosa, V. Buscaglia, M. T. Buscaglia, G. Canu, J. F. Fernández. "Phases evolution during the synthesis of $BaTi_5O_{11}$ through the $BaTiO_3$@TiO_2 core-shell particles as intermediate" VII Jornadas de Jóvenes Investigadores, Instituto de Cerámica y Vidrio, 27 junio 2018.